New materials and device architectures for organic solid-state lasers

Hadi Rabbani-Haghighi

UNIVERSITÉ PARIS 13

INSTITUT GALILÉE

LABORATOIRE DE PHYSIQUE DES LASERS

THÈSE

présentée pour obtenir le grade de

DOCTEUR DE L'UNIVERSITÉ PARIS 13

Discipline : Physique

par

Hadi Rabbani-Haghighi

Nouveaux matériaux et architectures de dispositifs pour les lasers organiques à l'état solide

Soutenue le 26 octobre 2011 devant le jury composé de :

M. Alain Siove, LPL, Université PARIS 13 — *Directeur de thèse*
Mme Isabelle Ledoux-Rak, LPQM, ENS Cachan — *Rapportrice*
M. Patrick Georges, LCF, Institut d'Optique Graduate School — *Rapporteur*
Mme Sophie Bouchoule, Laboratoire de Photonique et Nanostructures
M. Jean-Jacques Simon, IM2NP, Université Paul Cézanne Aix –Marseille III
Mme Elena Ishow, CEISAM, Université de Nantes
M. Frédéric du Burck, LPL, Université PARIS 13
M. Sébastien Chénais, LPL, Université PARIS 13

To my beloved family

and

the important persons in my life

Acknowledgements

The current dissertation is the result of a three-year work that has been realized in the organic photonics and nanostructures group, part out of eight groups at *Laboratoire de Physique des Lasers (LPL),* university of Paris 13.

Certainly, this thesis would not have been possible unless the assistance of many people who stood by my side at different stages and supported me at all moments in various ways during three years of the exciting work. I am whole-heartedly indebted to them.

I start by the head of the laboratory; Mr. Charles Desfrançois for giving me the opportunity to realize my research work at the best possible condition under his direction. *Merci beaucoup!*

Words fail me to express my gratitude to my thesis director, Alain Siove and my two great mentors, Sébastien Chénais and Sébastien Forget. During the course of this work they made available their support in a number of ways and have become a role model for my future career. Thank you so much Alain! Not only because of what you thought me in chemistry of organic compounds but also for being so compassionate to me in different occasions. I never forget your kindness, especially in the last days for helping me with the shopping and carrying of the foods and drinks for the thesis defense reception. The two Sébastiens with their distinctive and persistent efforts in doing research and experiments featured the notion of an authentic scientific person to me. They introduced me to the fascinating world of organic photonics and gave me valuable insights into the domain of lasers. All that I know in this field is because of these persons and for this reason I keenly appreciate what they did for me.

Collective and individual acknowledgements are conveyed to my thesis reading committee members. I am so grateful to my thesis referees Mr. Patrick Georges and Ms. Isabelle Ledoux-Rak for accepting this role and reading the thesis manuscript with great care, interest and patience. It was an extreme honor for me to have them as well as other members of the jury, Ms. Sophie Bouchoule, Mr. Jean-Jaques Simon, Ms. Elena Ishow

and Mr. Frédéric du Burck as my thesis board of examiners. I owe a further gratitude to Ms. Ishow for providing me with the novel organic compound for laser characterization. She is an exemplary and kind-hearted person whom I never forget for her favors to me.

I would like to thank Thierry Billeton from the optics workshop for preparing me the silica substrates and for his valuable advice and guidance about the substrate cleaning procedure.

I equally thank Albert Kaladjian and Brahim Kasmi from the mechanics workshop who kindly prepared me the required mechanical pieces within the shortest possible delay.

I am grateful to Fabrice Wiotte and Julien De Lapeyre De Bellair from the electronics workshop for design and fabrication of the signal peak detector circuit which became a crucial tool for laser emission lifetime measurement.

My gratitude also goes to Jeanne Solard and Nathalie Fabre for making it possible to use the clean room facilities whenever it was needed.

I would like to acknowledge the administration of the LPL, Martine Alsters, Solen Guezennec for all their help and support. I also thank Sabine Barbut, the past member of the administration who helped me so much during the first days and months of my arrival to the laboratory.

I am so thankful to Nordine Diffalah, Manal Yewakim and Xin zhang; the students who spent the period of their Master thesis internship at LPL and significantly contributed to the advancement of the realized experiments.

It was an honor for me to know Marie-Calude Castex and Dominique Adès whom I really enjoyed and benefited from discussions during the period of my presence in the laboratory.

It's a pleasure to thank from Mélanie Lebental at ENS Cachan for the fruitful and scientific discussions.

I would like to thank my friends in the organic photonics and nanostructures group, Quentin Ripault, Anthony Coens, François Gourdon, Getachew Ayenew and Tatiana Leang for their friendship and making me joyful moments in and outside of the laboratory

environment. I equally thank from Iryna Gozhyc at ENS Cachan. I wish them all a prosperous continuation with their Ph.D. studies.

I would like to thank all the members of the *Laboratoire de Physique des Lasers* for creating a very pleasant, comfortable and friendly atmosphere and making the laboratory as my second home. *Merci à tous et à toutes !*

I would like to show my special gratitude to a group of my best friends, starting with Roshanak Ashrafnejad who was the very first Iranian whom I met short after moving to the Cité Internationale Universitaire de Paris (CIUP) in September 2008. This acquaintance was a key to meet several others: Mohammad Ghorbani, Maryam Jabbari, Amir Karimi, Amir Besharati and Mohammad-Ali Jenabian. Being at this convivial and vibrant place for two years and having the chance to meet these people forged me unforgettable moments which will stay with me during my entire life. I wish them all success in their studies and every other aspect of their lives and I am very eager to see them again wherever/whenever possible.

Lastly, I cannot forget my dear family. If it was not their unflagging support and encouragement, today I would not be at this stage. To thank them, I would like to say some words in Persian:

پدرومادرعزیزم به خاطر زحمات و پشتیبانیتان همواره از شما قدردان و سپاسگزارم.

Table of contents

Introduction and overview of organic solid-state dye lasers

Introduction

The first demonstration of a laser device in 1960 was the initial step of a major breakthrough in science and technology. Today the impact of such devices in our lives is evident and one can find them throughout everyday life in CD/DVD players, printers, scanners and so on. The gain media in such devices can be in shape of gas, liquid or solid state. Among several varieties, solid-state lasers based on inorganic materials have been of great interest mainly because of their efficiency and compactness. However, for applications such as spectroscopy, these inorganic-based laser sources are only available for limited number of wavelengths. In this regard, materials developments have paved the way in development of new class of lasers based on organic dye compounds. The large gain bandwidth of these materials makes it possible to have tunability ranges extended over the whole visible spectrum. The first demonstration of such devices dates back to mid sixties where they appeared for the first time in liquid phase. However, liquid dye lasers have rather complex and expensive operating systems and one has to deal with toxic dye solvents as they have to be replaced periodically due to dye photodegradation. Therefore, from the early days of development of dye lasers, attempts were made to overcome the problems related to the use of organic solvents by incorporating the dye molecules into solid matrices. Solid-state dye lasers avoid the problems of toxicity and flammability. They are compact, widely tunable and easy to operate and maintain. In addition, they have the potential to be easily processed at very low costs via spin coating or thermal evaporation techniques. Because of these advantages, during the past three decades they have become the main focus of interest and have found applications in different areas such as spectroscopy or bio/chemo sensing. In most of the already realized devices the pump source is generally a bulky and expensive laser source which may be a limiting point toward widespread use of such devices. Therefore, following the successful realization of Organic

Light Emitting Diodes (OLEDs) and then Organic Thin Film Transistors (OTFTs), the people thought of realizing an organic laser diode where the excitation is given by the electrical current. However, despite an enormous amount of effort made for this goal, no direct electrically-driven organic semiconductor laser has been achieved so far mainly because of several loss mechanisms which are led to very high lasing thresholds. The ongoing failure in realization of an electrically-injected organic laser has inevitably led the researchers toward exploration of inexpensive, simple-processed and low-threshold devices where the excitation is given by compact optical sources such as Light Emitting Diodes (LEDs) or inorganic laser diodes. In the context of electrical excitation and also to realize devices which are compatible and operational with the compact optical sources, the main objective has been to lower the lasing threshold. Therefore, structures that enable reaching this goal, such as diffractive resonators and/or vertical microcavities have been extensively addressed. However, using devices with the privilege of lowered lasing thresholds is at the cost of losing some other important emission aspects such as good beam quality and high output energy as they are hardly achievable elements in a single device.

In this thesis, two research axes that consider both of the above issues in optically-pumped devices, which are, low threshold organic devices against those with high output powers and well-defined beam qualities, are defined and developed.

The first subject is treated via exploration, optical characterization and lasing demonstration in a novel organic material that can be easily processed in neat film configuration. This material with its interesting properties can solve many existing problems associated with the optically pumped organic thin film devices such as low absorption, quenching, etc. and can be very promising toward realization of low-threshold devices and perhaps future electrical pumping.

The second axis focuses on some of the less-considered emission aspects of organic solid-state lasers such as the beam quality and output energy in an inexpensive and simple-processed device based on thin films. This has become true through design and realization of an optically-pumped organic Vertical External Cavity Surface Emitting Laser (organic VECSEL) which is fully characterized and optimized through simulations and then proved via experiments. Furthermore, it will be seen how the special emission characteristics of this simple device made it possible to extend the emission wavelengths to the ultraviolet part of the spectrum.

Now, before entering into the main discussion of this thesis, let us have an overview on the current issues within the context of organic solid-state dye lasers.

Overview of organic solid-state dye lasers

Nowadays, organic dye lasers have established their place as one of the most indisputable, successful laser sources among several existing varieties. This is indeed thanks to the numerous available materials incorporated into various laser architectures leading to a class of tunable devices covering a range from near-UV to near-infrared in both pulsed and continuous regimes. The first of these laser sources working in a pulsed regime appeared in 1966 as a result of the work realized by Sorokin and Lankard where a Q-switched ruby laser was used to pump a solution of phthalocyanine [1]. Later on, in 1970, the first continuous-wave (CW) dye laser was demonstrated by Peterson et al. [2]. In that case, a solution of Rhodamine 6G was used as the gain medium excited by an Ar ion laser.

Today, liquid dye lasers are still among the most effective tunable laser sources in the visible, especially, in research laboratories. Before the invention of Titanium-sapphire lasers, they were widely-used sources for femtosecond pulse generation purposes because of their broad emission bands that enable generation of ultra-short pulses as low as 6 fs [3]. However, in these devices we have to deal with filthy laser dye solutions which are carcinogenic and need to be replaced periodically because of the irreversible dye degradation upon optical excitation. Although, the causes of this effect (often referred to as photobleaching) are not completely understood, photo-oxidation of the excited dye molecules together with some other destructive photochemical effects are known as the main possible reasons of this phenomenon [4].

Forgetting about this issue, liquid dye lasers are very cumbersome in size and the technology used in their fabrication seems to be rather complicated. Perhaps, the ensemble of the above-mentioned issues can be accounted as negative points which limit the application of such devices in various occasions and also explain why they have not been able to put a step outside the laboratory environments.

Optically-pumped solid-state dye lasers

Not very late after the invention of liquid dye lasers, it was in 1967 that solid-state dye lasers were introduced by Soffer and McFarland [5]. The medium was based on Rhodamine 6G-doped PMMA (poly (methylmethacrylate)) and was pumped by the second harmonic of Nd laser. This experiment was then followed by the work of Peterson and Snavely in 1968 [6] where in separated experiments two dyes within the Rhodamine family (Rhodamine 6G

and Rhodamine B) were incorporated into PMMA rods and pumped by a flashlamp-excited laser. Solid-state dye lasers are advantageous over their liquid-state rivals by being non-volatile, non-toxic, mechanically stable and compact. Accordingly, they have caught the attention of researchers and have become the subject of growing interest during the past few decades. For several years after their invention, the gain medium in such devices was based on dye-doped polymer matrices such as PMMA, poly (carbonate), poly (styrene) and poly (vinyl alcohol) [7, 8]. These host materials, however, have been shown to be inherently lacking mechanical and thermal resistance, photostability. This reason made people turn toward the use of other host materials with more rigidity. Consequently, several reports with the host medium based on a copolymer (a polymer constituted from two or more monomer units) [9-14] or obtained from sol-gel process (a method by which glass-like, simple oxide or mixed oxide matrices can be obtained through low temperature solution processing) [15, 16], appeared in the literature. In all these reports, the gain media were bulk size ($\sim$ cm).

Following the discovery of electroluminescence in organic semiconducting materials and the considerable interest in the development of optoelectronic devices (specially, the organic light emitting diodes (OLEDs)) based on these materials, in 1996 Tessler et al. [17] reported on an optically-pumped organic microcavity based on vacuum-evaporated, 100-nm-thick film of poly (p-phenylene vinylene) (PPV).

This successful work paved the way for several other reports of this kind. On this basis, there are several reports where the gain medium is based on thin film of an organic semiconductor [18-23], that is, a material with carbon structure having semiconducting properties. These materials fall into two categories of conjugated polymers and small molecules. The gain medium can be also a thin film of neutral or ionic material like Coumarin or Rhodamine [24], without semiconducting properties .

Thus far, organic thin-film devices have appeared in different configurations including diffractive resonators (DFB [25] and DBR [26]), vertical microcavities (VCSEL) [17] and microlasers (microdisk [27], microring [28] and microsphere [29]). In depth case study and comparison of these various laser architectures will be the subject of discussion in chapter 3. Meanwhile, one can make a distinction between devices of this category and the bulk dye-doped lasers being introduced just earlier. This discrimination must be done considering the positive and negative features associated to devices of each kind since one cannot get all the desired points, for instance, high output power together with low lasing threshold within a single device. Bulk dye-doped lasers have shown to be very promising in terms of providing high output powers thanks to rather rigid lasing media which are capable to withstand fast photodegradation under high incident intensities on the order of

tens of $MW.cm^{-2}$ [30]. Furthermore, these devices have well-defined beams and also good conversion efficiencies due to optimum overlap between the pump beam and the cavity mode in the used configurations. In this regard, there exist some works reporting on output energies of more than a hundred mJ and optical slope efficiencies up to 86% [30, 31]. However, the major drawback of such devices is the long and elaborate fabrication process of the gain medium via traditional radical polymerization, sol-gel or copolymerization techniques which sometimes may take several days and up to several weeks. In addition, once the dye-doped matrix is prepared via one of these techniques, it also requires mechanical processing (cutting, grinding and polishing to optical grade quality) prior to its use as a laser gain medium.

On the other hand, there are thin-film based devices which offer inexpensive, fast and simple fabrication via different methods such as thermal evaporation (suitable to small-molecular weight organic semiconductors) spin coating, dip coating, doctor blading and inkjet printing. In terms of lasing characteristics, except high output energies, all other desired features are achievable from devices of this category. For instance, diffractive resonators (DFB and DBR) are viable for the lowest possible lasing thresholds due to efficient feedback while vertical microcavities can provide diffraction-limited beam qualities and modest conversion efficiencies.

Similar to liquid dye lasers and bulk dye-doped solid-state lasers, one unpleasant point about organic thin-film lasers is their limited lifetime because of the dye degradation under optical excitation. However, considering many positive features of such devices (mainly the fabrication simplicity and rapidity with the consequence of considerably reduced setup price), the degradation issue could not have become a real hurdle towards practical applications of these devices. Furthermore, their popularity can be further increased if one considers that steps can be taken to enhance the lifetime. On this regard, one proposed technique has been the application of a rotating system for the solid gain medium as the dye jet flow in liquid dye lasers [32]. In the family of thin film devices, another reported technique has been through device encapsulation in order to prevent formation of non-emissive radical species as a result of the interaction between the excited dyes and oxygen. An example of this kind among several [33-35], is the encapsulated structure realized by Richardson et al. [36] where a 2500-fold improvement was observed in lifetime when compared to non-capsulated device excited at ambient condition.

Thanks to all the advantages discussed above, today we can see that optically-excited organic thin film solid-state lasers have successfully raised as potential candidates for practical applications in spectroscopy domains [37-40], bio/chemo sensing [41-44] and short-haul data telecommunications via plastic optical fibers [45, 46].

One major issue about organic solid-sate lasers in general, is the choice of the excitation source. In most cases that are reported in the literature, the excitation source is an expensive bulky laser such as harmonics of a flashlamp-pumped Nd: YAG laser (picoseconds to nanoseconds), Excimer laser, frequency-doubled Ti-sapphire femtosecond lasers, etc. which certainly impose a limit on final device cost and mainly, its compactness and portability for practical applications like in situ spectroscopy. Therefore, following the successful realization of the Organic Light Emitting Diodes (OLEDs) [47] and then Organic Thin Film Transistors (OTFTs) [48] based on semiconducting organic materials and considering that these materials are also able to be easily incorporated into several resonant configurations, the researchers got enough reasons to go towards realization of an organic laser diode. This means an organic laser where the excitation energy can be simply given through the electrical current, e.g. a battery, as in OLEDs. However, despite an enormous amount of efforts made on this issue, up to date, no electrically-injected organic laser has been reported so far owing to the very high lasing thresholds encountered in the coursework of this goal realization. In the following, it would be interesting to open a window and having an overview of the several existing challenges together with some of the very recent references addressing these problems.

Difficulties toward realization of an organic laser diode

There are two essential requirements in the design of an organic laser diode. First of all, it has to provide for efficient current injection in the optically active material, and second, it has to form an optical resonator with charge-injecting electrodes, whose optical losses are smaller than the gain.

The first problem is related to optical losses in the waveguide structures proposed for the electrical injection which is generally a film (100 – 200 nm) of semiconducting organic gain medium sandwiched between two metallic electrodes. These losses are due to absorption in the electrodes because of the substantial penetration of waveguide modes into the contact layers [49]. Configurations are suggested to resolve this issue but with considerably increased lasing threshold in the presence of the metallic contacts [27, 50-52] with exceptions proposed by Reufer et al [53] and Wallikewitz et al [54]. Recently, optical excitation of an elaborate ambipolar LEFET[1] is also reported as a solution since the emission can be made to occur far from the electrodes upon using this architecture [55].

[1] Light-emitting field-effect transistor

The second problem is the substantial absorption owing to the high density of injected charge carriers, thus increasing losses compared with an optically pumped laser. A molecular ion with an extra charge (electron or hole) has a broad absorption spectrum that efficiently overlaps the emission spectrum of the organic material [56].

The third hurdle in realization of an organic laser diode is that when the opposite charges recombine in an organic semiconductor, they frequently (approximately 75% of the time [57]) form a triplet exciton, that is, an excited triplet state bounded to the ground state in a molecular system of the organic species which is not emissive in fluorescent materials and can also contribute to loss through its absorption. Moreover, created excitons upon charge injection may also dissociate into single charge excitations, or polarons. Finally, in a recent report [58], it is found out that singlet-triplet annihilation (STA), is a major barrier to electrically-pumped lasing.

The fourth problem, which becomes troublesome as the consequence of the above problems, is related to intrinsic low mobility of organic semiconducting materials. Given the above loss sources, very high current densities are required. It is shown that current densities in the range of thousands of amperes per cm^2 [59] are necessary to even approach the lasing threshold. The current density is estimated by $J \approx \mu.(V/d)$ where, μ is the charge mobility, V is the applied voltage and d is the film thickness. Based on this relation, given the low mobility of organic semiconducting materials, high current densities are more easily achievable for thin films. However, having a thin film makes it difficult to pass very high current densities as most of the semiconducting polymers won't be able to withstand such current densities.

"Indirect electrical pumping" approach

Given the above-mentioned challenges in realization of an electrically-injected organic laser and the undergoing keen interest of some researchers on this regard, there exists another group of scientists who came with the idea of "indirect electrical pumping" of organic lasers [60, 61](One of the current leading groups is Samuel et al. at saint Andrews University). That is, an electrically-injected inorganic source mediated between the organic gain medium and the electrical current, served to optically pump the organic laser structure. They believe that reaching the predefined goal of simple, compact and inexpensive devices

operating at low powers can be achievable in this way with much less difficulties in comparison with direct electrical pumping. Their belief might be significantly due to major recent progresses in the technology of solid-state laser sources. On this regard, one approach has been the use of rather compact microchip lasers as the excitation source [38, 62-65]. A further compact and miniaturized device can be obtained upon using inorganic laser diodes. The very first laser diodes were emitting in the infrared part of the spectrum. Using laser diodes to pump the organic dyes is not a novel approach as the first demonstration of diode-pumped dye laser was reported in 1974 in liquid phase where a 50-ns pulsed AlGaAs laser diode operating at 820 nm was used to excite an IR 140 dye solution in a waveguide laser structure [66]. However, the organic dyes are not very good emitters in the infrared part of the spectrum due to their poor fluorescence quantum yield in this region. During the years after, upon gradual development of laser diode technology, the emission wavelength of such sources could be extended to visible part of the spectrum. This achievement became the basis of several reports on optically-excited dye lasers using diode lasers as the excitation source [67-71]. This fact has become even more noticeable after the appearance of powerful InGaN-based blue-emitting laser diodes, being capable to provide output peak powers in the order of few a kW. This makes them ideal sources to easily reach lasing threshold of organic lasers which is typically on the order of few kW/cm^2 . Recently, Riedl et al. [67] reported for the first time on an organic "thin-film" istributed feedback (DFB) laser pumped by an InGaN blue-violet laser. Since then some other reports of this type have been appeared in the literature [68, 69].

The idea of indirect electrical pumping could become even further simplified in the report of Yang et al. [60] where the authors demonstrated a hybrid organic/inorganic device pumped by an inorganic incoherent light emitting diode (LED)(above-illustrated figure). However, one limitation of the LED pumped laser is that the power density from the LED is very limited even when it operates in pulsed regime at high currents. Furthermore, the incoherent emission together with high divergence intrinsic of LEDs, make it difficult to tightly focus the light.

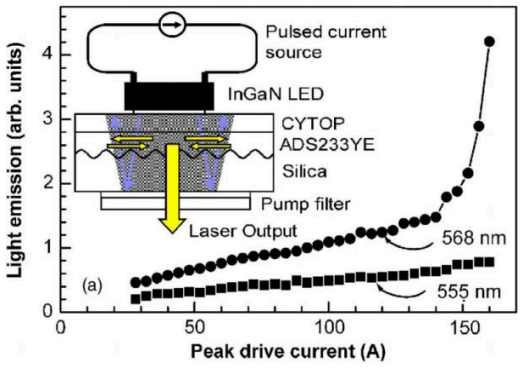

Image of the hybrid organic/inorganic laser configuration realized by Samuel et al at Saint Andrews University (Image taken from [60]).

The above-given review on organic solid-state lasers evidences the amount of realize work done in this area. As one could see, these devices still need to be improved in several aspects. That is one of the goals of the present thesis.

Thesis organization

The present manuscript is structured in the following manner.

In the first chapter, some of the fundamentals on photo-induced intramolecular and bimolecular interactions in organic media are described which gives the necessary tools to proceed throughout the whole text. This is continued by some generalities about amplification and lasing and at the end, development of the rate equations governing the laser operation in a four-level system, adapted to molecular structure of the organic dyes.

Following the given insight on the organic solid-state dye lasers, one can observe the current trend is mainly focused on realization of compact devices with low thresholds for the possibility of diode or LED pumping or even for future electrical excitation. As already said in the introduction, laser geometries such as diffractive resonators (DFB and DBR) and/or vertical microcavities which make it possible to achieve this goal are extensively studied. In the contest of realizing low-threshold devices, some other important emission aspects such as beam quality, conversion efficiency etc. are being less investigated as all these concepts cannot be obtained in a single device. Therefore, in this thesis, two axes that consider both of the above issues in optically-pumped devices, which are, low threshold devices against those with high output powers and well-defined beam qualities, are discussed in detail.

The second chapter is devoted to the exploration of a novel small-molecular weight organic compound called, “fvin”, which was synthesized and provided by Prof. Elena Ishow at ENS Cachan. On the contrary to most of the organic dyes which suffer from concentration quenching with the consequence of small doping rates and thus low absorption within a thin film, the “fvin” with its special geometry showed to be capable of emitting in neat film configuration with very low amount of quenching. This can be very promising in realization of low threshold devices and eventual future electrical excitation thanks to considerable amount of pump absorption that can be achieved within a thin layer (few hundreds of nm). The optical characterization of the “fvin” molecule is carried out via the widely-used Variable Stripe Length (VSL) technique in planar waveguide configuration. At the end of this chapter, the result of lasing operation in this material, in DBR geometry realized by simple optical contact interferometry technique, is presented and discussed. At each stage of the “fvin” characterization, the results are compared with the measurements performed

on DCM-doped PMMA film at the same experimental conditions.

In the third chapter, a new and very simple-built external cavity organic laser based on a layer of Rhodamine 640-doped PMMA matrix is presented and discussed from initial design steps. The laser cavity, inspired from the inorganic VECSEL structure, has the so-called name of VECSOL standing for Vertical External Cavity Surface-emitting Organic Laser. The realized device performance is compared by using two pump sources differing in pulse durations (0.5 ns and 7 ns). The emission is characterized in terms of performance, beam quality, power scaling capability and photostability. Following these characterizations, the emission dynamics are described in theory and then modeled by using the Tang-Statz-De Mars rate equations in pulsed regime. Thanks to these simulations, the performance optimization is carried out.
Following the initial characterization and analysis of the VECSOL, a modified version of the VECSOL architecture which was employed to realize intracavity frequency doubling and extend the emission wavelength to the UV region, is presented. The result of UV emission characterization in terms of performance and photostability are then discussed in detail.
In perspective, the realized VECSOL architecture will be the subject of further optimization such as diode pumping. This can lead to a very compact device toward practical applications such as point-of-care biosensing or in-situ spectroscopy domains.

1 Fundamentals of photo-induced light-matter interaction in organic materials

1.1 Introduction

In the following, some of the generalities which are helpful in the context of this thesis are detailed. This starts with some fundamentals on the photophysical processes related to the organic materials and then description of lasing principles. The laser concept is presented and then the rate equations adapted to molecular structure of the organic dyes are developed. At the end, the issues related to using of organic dyes as the laser gain media are discussed.

1.1.1 Perrin-Jablonski diagram

The molecular structure of the organic materials and the corresponding phenomena happening as a result of optical excitation can be conveniently described by considering a band-like energy level model. A schematic representation of this model, known as the Perrin-Jablonski diagram, is depicted in Figure 1.1.

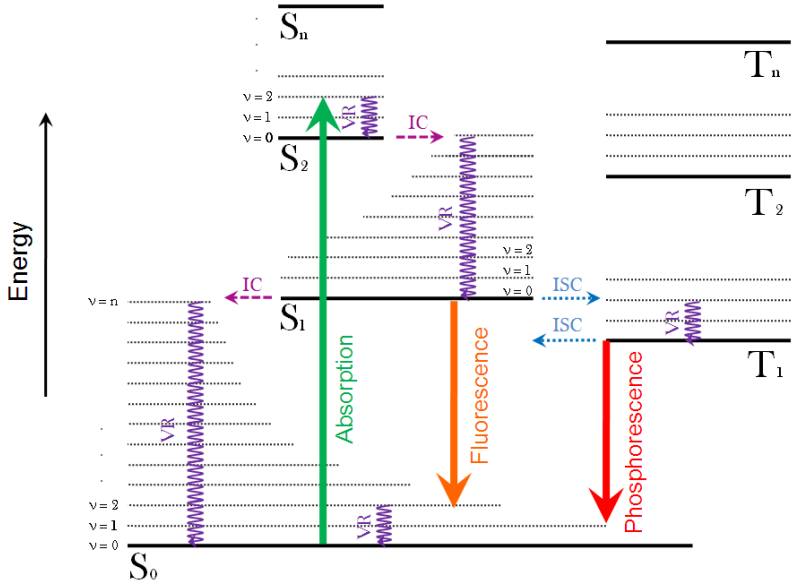

Figure 1.1 - Schematic of the Perrin-Jablonski diagram

Based on this model, the dye molecular structure consists of two main types of energy manifolds, the singlet ($S_i (i = 0,1,2,...,k)$) and the triplet ($T_i (i = 1,2,3,...,k)$) electronic states, designated by bold horizontal lines in the above diagram with energy differences of a few eV between two successive states. S_0 is called the ground state and is the predominantly-populated energy level at thermal equilibrium condition. S_i and T_i with $i > 0$ are referring to excited electronic states with i indicating the excitation order.

Each of the electronic states is associated with a multitude of vibrational sublevels with spacing in the order of ~ 0.1 eV (dotted lines above each electronic state in the Perrin-Jablonski diagram), and to each vibrational sublevel, corresponds a closely-lying manifold of rotational levels (not shown here) with ~ 0.01 eV internal spacing.

The singlet and triplet states are discriminated from each other through their spin multiplicities. In quantum mechanics, the rotation of an electron around itself is characterized through a momentum, called "spin" [72]. For an electron, the spin value can be either $+1/2$ or $-1/2$ with a spin wave function attributed to each value. Furthermore, to each molecular orbital occupied by an electron of a given spin, is attributed an orbital wave function defining a 'spin-orbital' or 'total' wave function together with the electron spin wave function. The total spin of a molecular system with two electrons is determined by the sum of the spin values together with a combination of the corresponding spin wave functions. If the total spin value is $+1 = 1/2 + 1/2$ or $-1 = -1/2 - 1/2$, then the electronic state will be called triplet state and is schematized by two parallel spins as $\underline{\uparrow\uparrow}$ or $\underline{\downarrow\downarrow}$. For a total spin value of zero, the corresponding electronic state is called singlet state and can be simply demonstrated by an electron pair of opposite spins as $\underline{\uparrow\downarrow}$. In practice, the singlet state as is just shown does not exist. What we have is a linear combination of $\underline{\uparrow\downarrow} + \underline{\uparrow\downarrow}$ or $\underline{\uparrow\downarrow} - \underline{\uparrow\downarrow}$ with both cases leading to a total spin value of zero [73].

Based on quantum mechanics electronic transitions between states of the same multiplicity, i.e., singlet-singlet and triplet-triplet are spin-allowed and the electron spin is conserved during the transition process. However, transitions between states of different multiplicity, i.e., singlet-triplet and vice versa are spin-forbidden and thus highly improbable, unless there is a strong spin-orbit coupling[2] [74]. Under this condition, the transition from the triplet excited state to the ground state becomes spin allowed and gives rise to a phenomenon called phosphorescence (see section 1.1.2).

With the above descriptions, now imagine a photon of light is incident on such a molecular

---

[2] In a classical view, the spin-orbit coupling phenomenon can be simply understood by considering the electron movement around the nucleus. This rotational movement around the nucleus generates a magnetic momentum; furthermore, an electron also rotates around itself, which causes generation of another magnetic momentum. The spin-orbit coupling is the interaction between these two magnetic momenta.

system at thermal equilibrium condition where the molecule is at the ground electronic state. The incident photon loses its energy and promotes an electron from the ground electronic state, S_0 , to an electronically-excited state. As this transition may terminate in any of several closely-lying vibrational sublevels of the corresponding excited electronic state, therefore, light absorption in organic materials consists of broad spectral bands instead of sharp peaks.

During the absorption process, the spin inversion is quantum-mechanically forbidden and is therefore highly unlikely to observe the absorption occurring between electronic states with different spin multiplicities (e.g. Singlet $\rightarrow$ Triplet).

Typical timescale for the absorption phenomenon is on the order of 10^{-15} s [74].

1.1.2 Intramolecular deactivation pathways in electronically-excited molecules

Once the molecule is promoted to an excited electronic state via absorption of a photon, it undergoes several decaying mechanisms to find itself back in its fundamental or ground state, S_0 . These decaying mechanisms are of two types; radiative and nonradiative which are detailed in the following.

1.1.2.1 Radiative decays

According to Kasha's rule in photochemistry [74], the downward radiative transition generally takes place between the "lowest vibrational level" of S_1 or T_1 and one of the vibrational sublevels lying within the ground electronic state. If this transition occurs from the first excited singlet state to the ground state, then the spin multiplicity of the initial and final states will remain unchanged, and the emission process is called fluorescence. On the other hand, in case of emissive relaxation from the first excited triplet state to the ground state, a change in spin multiplicity must take place and the corresponding emission phenomenon is called phosphorescence which only takes place in phosphorescent materials.

$$\begin{aligned} &\text{Fluorescence} && S_1(\nu = 0) \rightarrow S_0(\nu = i;\ 0 \le i \le n) + h\nu \\ &\text{Phosphorescence} && T_1(\nu = 0) \rightarrow S_0(\nu = i;\ 0 \le i \le n) + h\nu \end{aligned} \qquad (1.1)$$

$h\nu$ is the emitted photon energy with h being the Planck constant and ν the emission frequency.

The two types of radiative transitions are shown by thick downward arrows in the above-depicted Perrin-Jablonski diagram.

Because the radiative transition from T_1 to S_0 is spin-forbidden, therefore, the first excited triplet state lifetime ($10^{-6} - 1$ s) [74] is bigger in comparison to the first excited singlet state lifetime ($10^{-10} - 10^{-7}$ s) [74].

1.1.2.2 Non-radiative decays

In electronically-excited species, apart from the radiative transition during the relaxation process to the ground state, there exist also several nonradiative mechanisms which are described in the following.

- Vibrational relaxation (VR)

Vibrational relaxation (VR) is a nonradiative transition process that involves release of the excess energy accumulated in the vibrational levels of a given excited electronic state (singlet or triplet) upon excitation, unless the absorption is being occurred between the lowest vibrational level of the ground and the lowest vibrational level of given excited electronic state, that is, $S_0(\nu = 0) \rightarrow S_1(\nu = 0)$ (Figure 1.2). This is also the decaying mechanism to the lowest vibration level of the ground state following a radiative transition (fluorescence or phosphorescence) ended up with one of the vibration levels ($\nu > 0$) of the ground state. Vibration relaxation is also followed after a transition between the isoenergetic vibrational levels of two electronic states with similar or different spin multiplicities. These transition types are called internal conversion and intersystem crossing respectively which are further detailed in the following.

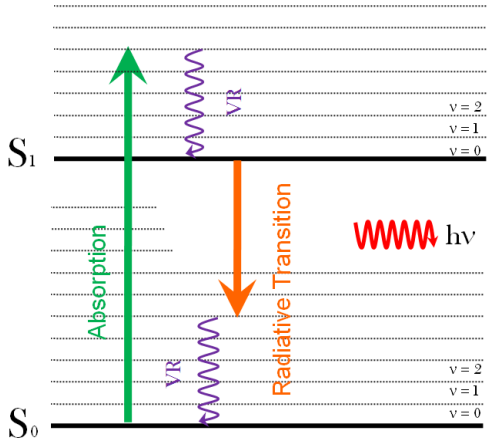

Figure 1.2 – Demonstration of vibrational relaxations in the vibration levels of each electronic state. These relaxations are shown by wavy arrows.

From the laser point of view, thanks to these vibrational levels, the molecular system of the organic dyes is structured in four different levels and as will be described later on, this fact

is an advantageous point towards practical application of these materials as the gain medium in laser systems. In the depicted Perrin-Jablonski diagram vibrational relaxations are shown by downward wavy arrows.

In a given medium, the vibrational energy is dissipated in form of heat. Typical timescales of the VR process are on the order of $\sim 10^{-12}$ s [75].

- Internal conversion (IC)

Relaxation from an upper excited electronic state to a lower excited state of the same multiplicity ($S_n \rightarrow S_m$ and $T_n \rightarrow T_m$, $n > m$) takes place within a spin-allowed radiationless transition process, called internal conversion (IC). Generally, the energy gap between the upper excited electronic states is smaller than the energy gap between the first excited electronic state (S_1) and the ground state (S_0). This makes possible to have an optimum overlap between two isoenergetic states, that is, between the lowest vibrational level of an upper excited electronic state with one of the vibrational levels of underlying electronic state and thus, allowing rapid transition through IC. Internal conversion between higher excited electronic states occurs on the sub ps-timescale ($10^{-14} - 10^{-12}$ s) [75] making other radiative and nonradiative transition mechanisms unsuccessful to compete with it. On the other hand, IC from the first excited singlet state S_1 to the ground state is much slower ($10^{-9} - 10^{-7}$ s) [76] due to much bigger energy gap in this case, making fluorescence possible. This transition type is shown in Figure 1.3 by a horizontal dashed arrow between the second and the first excited singlet states.

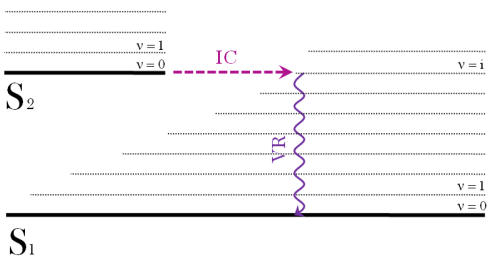

Figure 1.3 – Demonstration of intersystem crossing (IC) between two electronic state with the same spin multiplicity.

- Intersystem crossing (ISC)

Intersystem crossing (ISC) involves an intramolecular radiationless transition between two isoenergetic vibrational levels belonging to two excited electronic states with different spin multiplicities. For example, an excited molecule in the lowest vibration level of the first excited singlet state ($S_1(v = 0)$) is able to cross to one of the isoenergetic vibrational levels of the first excited triplet state ($T_1(v = i, 0 < i \leq n)$) which is then followed by a vibrational

relaxation to the lowest vibrational level of T_1. The ISC transition is shown by dotted horizontal arrow in Figure 1.4.

In general, transition between two electronic states with different spin multiplicities is forbidden. However, as mentioned before, this transition can become possible if the spin-orbit coupling (coupling between the orbital and electron spin magnetic moments) is sufficiently strong. On this regard, the presence of heavy atoms (Ir, Pt) in the molecular structure can considerably increase the probability of spin-orbit coupling with an efficiency that varies by Z^4 (Z= atomic number).

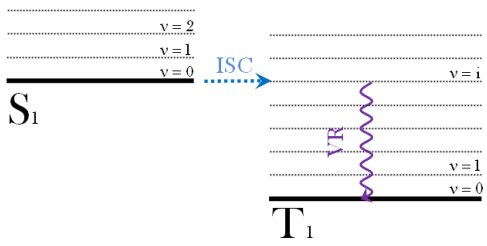

Figure 1.4 - Demonstration of intersystem crossing (ISC) between two electronic states with different spin multiplicities.

Typical characteristic time for ISC transition is on the order of $10^{-10} - 10^{-8}$ s [74].

1.1.3 Excited-state bimolecular interactions

In the following, the bimolecular interactions are described. These interactions can be of useful as in Förster resonant energy transfer, or they can be highly unwanted like the quenching phenomenon, described in the following.

1.1.3.1 Förster resonant energy transfer (FRET)

Förster resonant energy transfer (FRET) refers to a "nonradiative" energy transfer mechanism that requires dipole-dipole interaction (Coulombic interaction) between a donor (D) and an acceptor (A) molecule (Figure 1.5). This transition cannot happen unless there is an overlap between the emission spectrum of the donor molecule (from its singlet excited state) and the absorption spectrum of the acceptor. As a

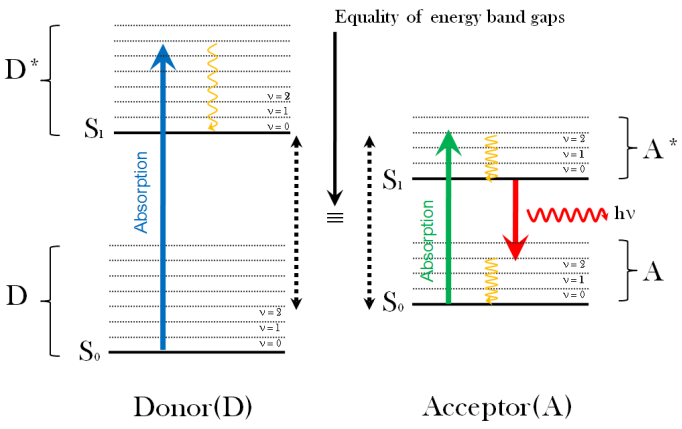

Figure 1.5 - Schematic representation of Förster resonant energy transfer (FRET).

result of this overlap, the donor passes on its energy to the acceptor molecule. After the energy transfer, the excited acceptor molecule can nonradiatively relax to its lowest vibration level, and subsequently, fluorescence can happen. This phenomenon can be simply described via the following relation:

$$D^* + A \rightarrow A^* + D \tag{1.2}$$

Where the "*" superscript denotes the singlet excited-state species.

1.1.3.2 Annihilation (quenching)

Quenching is a highly unwanted phenomenon and is tried to be avoided as much as possible since it reduces the fluorescence quantum yield, that is, the ratio between the number of emitted and absorbed photons. This phenomenon can be the consequence of external stimuli which are present around the excited-state species or dye-overdoped solutions and solid matrices. The latter, which is often referred to as concentration quenching, is a bimolecular interaction and causes that two excited state molecules to be close enough and contribute efficiently in ceasing the emission. To avoid this source of quenching, considerable attention must be paid in choosing the right doping rate in order to have the excited species far enough from each other where this effect is minimized.
In the following, the above-mentioned annihilation mechanisms responsible for quenching of the excited-state species are detailed.

- Singlet-singlet annihilation (SSA)

The SSA is a process happening between two molecules in the first excited singlet state. During this phenomenon the energy from one of the excited molecules is transferred to the second one. As a result, the first molecule falls back to its ground state and the second molecule gets promoted to a higher excited singlet state which then relaxes to the first excited singlet state or triplet state.

- Singlet-triplet annihilation (STA)

The STA is a process where a molecule in the first excited singlet state is quenched by another molecule in the excited triplet state in its vicinity. As a result, the latter is getting

excited to a higher triplet state while the former relaxes to its ground state. The molecule that is raised to an upper excited triplet state will then go down the first excited triplet state which eventually relaxes to the ground state.

- Triplet-triplet annihilation (TTA)

The TTA annihilation is the consequence of interaction between two molecules in the excited triplet state. As a result one molecule relaxes to the ground state while the second one rises to the upper triplet excited state from where it decays down to the first excited singlet state or triplet state.

- Quenching by oxygen and impurities (H_2O,...)

Apart from the above annihilation mechanisms between the excited-state dye species, the presence of oxygen (dissolved in the solution or being existed in the molecular structure of the dyes or the host matrices) and also impurities in the medium are also considered as one of the major parameters in quenching of the fluorescent light and the excited-state species.

1.2 Generalities on light absorption and amplification

1.2.1 Light absorption in a medium

Earlier, the light absorption and the consequent phenomena following this process were described within the molecular structure of an organic material. Here, it would also be interesting to see how the light absorption varies in a medium of a given thickness made of an absorbing material such as an organic dye. In this case, the governing rule is defined by the Beer-Lambert's law. This law states that when monochromatic light passes through a transparent medium, the rate of decrease in intensity with the thickness of the absorbing medium is proportional to the intensity of the penetrating radiation. Consider an infinitesimal layer of the gain medium of thickness $d\ell$ and let I be the intensity of radiation entering it, then the Beer-Lambert's law can be expressed by differential equation as:

$$-\frac{dI}{d\ell} = N\sigma_{abs} I$$

$$\int_{I_0}^{I} \frac{dI}{I} = -N\sigma_{abs} \int_{0}^{L} d\ell \quad \Rightarrow \quad Ln\frac{I}{I_0} = -N\sigma_{abs} L \quad (1.3)$$

$$\Rightarrow \quad I = I_0 e^{-N\sigma_{abs} L}$$

where $\sigma_{abs}(cm^2)$ is the absorption cross section, $N(cm^{-3})$ is the density of molecules, I is the intensity at distance $\ell = L$ and I_0 is the intensity at $\ell = 0$.
Based on this expression the absorption of the incident light reduces exponentially as it travels inside the medium.

1.2.2 Light amplification

If a medium has the capability to amplify light, then it is said to have gain. In the following, the stimulated emission phenomenon which is the basis of light amplification together with a mechanism that uses this concept to amplify the spontaneous emission of light, are described.

- Stimulated emission concept

Stimulated emission, a phenomenon theoretically predicted by Albert Einstein, is a process where an excited-state species interacts with a photon of light with certain frequency and as a result falls back to its fundamental or ground state via emission of a coherent photon, that is, a photon of the same phase, direction, frequency and polarization as the incident one (Figure 1.6). This mechanism which is the reverse of the absorption phenomenon is the fundamental physical process underlying laser operation.

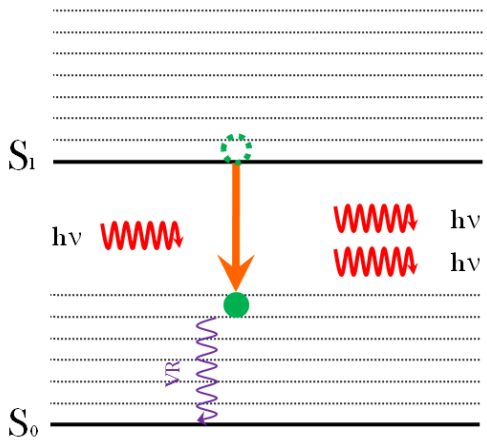

Figure 1.6 - Stimulated emission demonstration.

- Amplified spontaneous emission (ASE)

The ASE is cascade of emission as a result of interaction between fluorescent photons with excited singlet states species along the optical path. Consequently, the spontaneously emitted photons become amplified through coherent stimulated emission process. A signature of amplified spontaneous emission is the fluorescence emission spectral narrowing. An example of ASE observation in thin film DCM dye-doped PMMA is depicted in Figure 1.7. As the pump intensity increases the spectrum changes from a normal fluorescence to pure ASE.

In order to observe ASE, reaching to a condition where a positive net gain (the gain minus losses due to medium absorption or scattering) can be obtained is somehow necessary. This requires having more molecules in the singlet excited state than in the ground state. This condition is referred to as "population inversion" of states. Therefore, as the spontaneously-emitted photons propagate in the medium, there will be more stimulated emission than absorption leading to amplification.

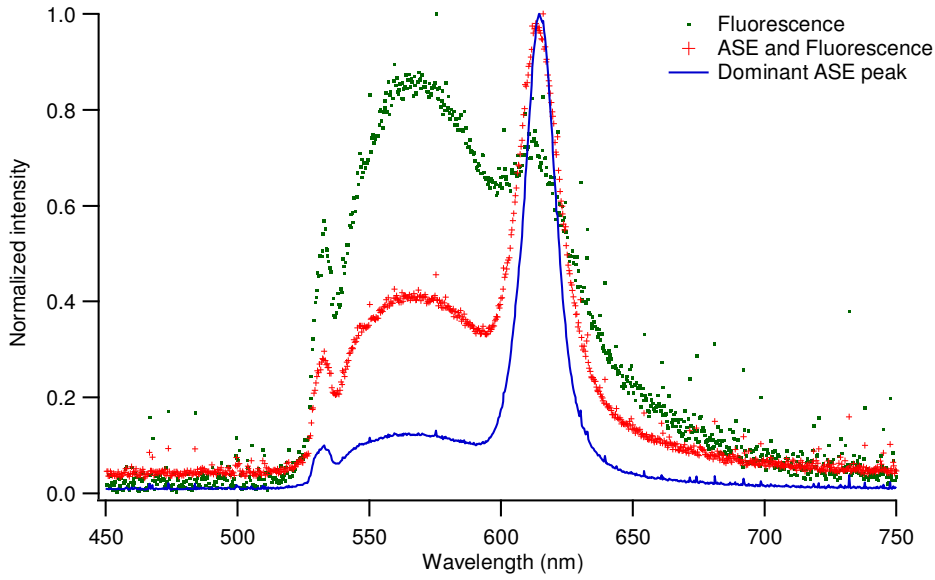

Figure 1.7 – Fluorescence spectral narrowing demonstration as a consequence of pump intensity increase in DCM-doped PMMA film. The small peak before 550 nm is the pump at 532 nm.

1.2.3 Basic principles of lasers

The acronym, "LASER", stands for "Light Amplification by Stimulated Emission of Radiation". A standard laser is a device composed of a "resonator" made of two specially-wavelength-coated mirrors with high reflectivity, hosting a "gain medium" (gas, liquid or solid phase), in which population inversion of the energy levels has to take place for lasing action to happen (Figure 1.8). The laser kinetic equations prove that this situation can be easily obtained in a four-level system upon optical or electrical excitation of the gain medium with certain pump source intensity and finite duration. However, this is more difficult in a three-level system (a system made of pure electronic states or a system without vibrational levels in one of the ground or excited state) and not achievable in a two-level system having no vibrational levels. Once the population inversion is reached, the first spontaneously-emitted photons along the resonator axis bounce back and forth inside the resonator while being amplified by passing through the gain medium. As a result, an increasing intensity emission of light via stimulated emission phenomenon will be built. A fraction of the generated intracavity intensity exiting the resonator builds up the laser emission in shape of a beam. Since this beam-like emission is produced via stimulated emission, therefore, it is privileged to ordinary light sources through its directionality, spatial[3] and temporal[4] coherence, more or less pronounced monochromaticity (made of single wavelength) and polarization.

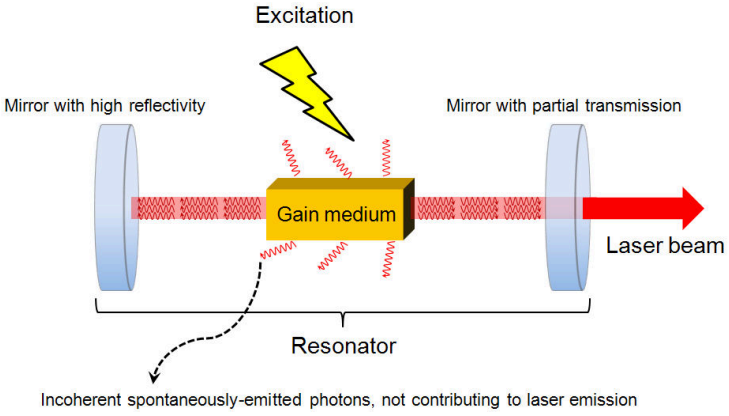

Figure 1.8 - Laser cavity composed of a gain medium in between the two wavelength-coated, highly-reflective mirrors.

[3] Spatial coherence means that a fixed phase relationship exists between two points of the beam cross section.
[4] Temporal coherence means that along the beam, the lightwave has a regularly varying phase during a finite coherence length (ℓ_c) related to the spectral width by $\ell_c = c\tau_c = c/\Delta\nu$ with c being the speed of light and τ_c the coherence time.

1.2.4 Derivation of laser rate equations in a four level system

In this section, laser rate equations of a four-level system comprising two electronic states S_0 and S_1 are developed (Figure 1.9). These equations describe the dynamic behavior of a laser system. For the sake of simplicity, the triplet-state-related transitions (ISC, phosphorescence and triplet state absorption toward higher excited triplet states) are neglected. This is a relevant approximation in our experimental conditions since for the realized works, pulsed sources with durations much smaller than the ISC time constant (on the order of hundreds of ns) are used. This has made us to suppose that excited triplet state accumulation and the subsequent phenomena following this transition are negligible. In addition, emission reabsorption from S_1 to a higher excited singlet state and the stimulated emission at the pump wavelength are also neglected.

As mentioned earlier, each of the electronic levels contains a multitude of closely lying vibrational-rotational levels which are schematized by band of graded colors. Pump laser intensity at wavelength compatible with the $S_0 \rightarrow S_1$ transition, populates a higher vibrational level in the first excited electronic state manifold. This is followed by rapid radiationless transition to the lowest vibrational level of S_1 from where transitions to the vibrational manifold of the ground electronic state give rise to a broadband emission with intensity I. Following the radiative transition to one of the vibrational levels of the ground state, the molecule relaxes back to the lowest vibrational level of the ground state.

Absorption cross section (cm²)	$\sigma_{01\,(0,n)}$
Emission cross section(cm²)	$\sigma_{e\,(0,v)}$
reabsorption cross section(cm²)	$\sigma'_{01\,(v,0)}$
Radiationless transition rates (1/s)	$\gamma_{1\,(n,0)}$ $\gamma_{0\,(n,0)}$
Excited-state lifetime (s)	τ_{10}
Emission intensity (photons/s/cm²)	I
Pump intensity (photons/s/cm²)	Ip

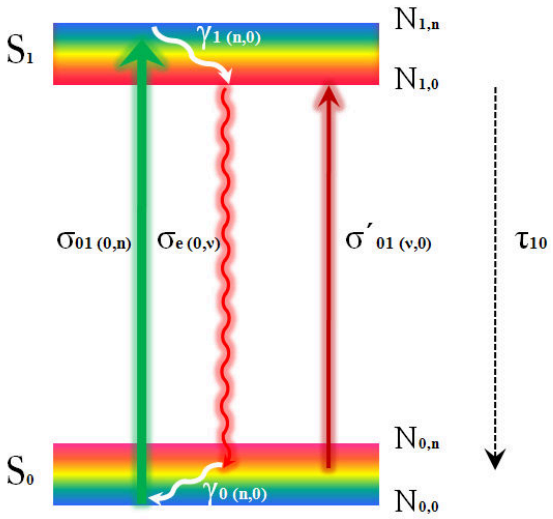

Figure 1.9 - (Right) Four-level system, (left) table of different characterizing parameters corresponding to various transition types.

Considering the above assumptions, the dynamics of the energy levels within the electronic states can be described by the following set of equations:

$$\left\{\begin{array}{l} N = N_{0,0} + N_{0,n} + N_{1,0} + N_{1,n} \\ \dfrac{dN_{0,0}}{dt} = -\sigma_{01(0,n)} I_p N_{0,0} + \gamma_{0(n,0)} N_{0,n} \\ \dfrac{dN_{0,n}}{dt} = -\gamma_{0(n,0)} N_{0,n} - \sigma'_{01(\upsilon,0)} I N_{0,n} + \sigma_{e(0,\upsilon)} I N_{1,0} + \dfrac{N_{1,0}}{\tau_{10}} \\ \dfrac{dN_{1,0}}{dt} = \gamma_{1(n,0)} N_{1,n} - \sigma_{e(0,\upsilon)} I N_{1,0} + \sigma'_{01(\upsilon,0)} I N_{0,n} - \dfrac{N_{1,0}}{\tau_{10}} \\ \dfrac{dN_{1,n}}{dt} = \sigma_{01(0,n)} I_p N_{0,0} - \gamma_{1(n,0)} N_{1,n} \end{array}\right\} \qquad (1.4)$$

$N(cm^{-3})$ is the total density of molecules and $N_{i,j}$ with $i = 0,1$ and $j = 0,n$ represents the distributed density at different energy levels. The subscript "i" is the electronic state and "j" is a vibrational level within a given electronic state. Ground state is denoted by i=0 and the excited electronic state is precised by i=1. $\sigma_{01(0,n)}$ and $\sigma'_{01(v,0)}$ are the absorption cross section and the reabsorption cross section at the emission wavelength, respectively. Absorption cross section defines the absorption probability of one photon per molecule under the I_p pump intensity. In the used notation, the subscript "01" denotes a transition from the ground state to the excited state and the characters inside the parenthesis show the transitions within different vibrational levels. Similarly, $\sigma_{e(0,v)}$ is defined as the emission cross section from the lowest vibrational level of the excited state to one of the vibrational levels of the ground state. $\gamma_{0(n,0)}$ and $\gamma_{1(n,0)}$ are the vibrational relaxation rates in the ground state and excited electronic state.

In practice, $\gamma_{0(n,0)}$ and $\gamma_{1(n,0)}$ transition rates are far superior (10^{12} s^{-1}) to the radiative transition rate $1/\tau_{10}$ ($10^{7} - 10^{10}$ s^{-1}). Thus $N_{0,n}$ and $N_{1,n}$ tend to be zero at a given time as the corresponding energy levels depopulate almost instantaneously.

$$\left\{\begin{array}{l} N_{0,n} \to 0 \\ N_{1,n} \to 0 \end{array}\right. \quad \Rightarrow \quad \left\{\begin{array}{l} \dfrac{dN_{0,n}}{dt} = 0 \\ \dfrac{dN_{0,0}}{dt} = 0 \end{array}\right. \qquad (1.5)$$

By these assumptions, (1.4) is simplified as:

$$\left\{\begin{array}{l} N = N_{0,0} + N_{1,0} \\ \dfrac{dN_{0,0}}{dt} = -\sigma_{01(0,n)} I_p N_{0,0} + \sigma_{e(0,\upsilon)} I N_{1,0} + \dfrac{N_{1,0}}{\tau_{10}} \\ \dfrac{dN_{1,0}}{dt} = \sigma_{01(0,n)} I_p N_{0,0} - \sigma_{e(0,\upsilon)} I N_{1,0} - \dfrac{N_{1,0}}{\tau_{10}} \end{array}\right\} \qquad (1.6)$$

The set of equations in (1.6) are the simplified rate equations governing a four-level system dynamical behavior. These equations will be employed in chapter three as the basis of further analysis.

1.3 Organic dyes as laser gain media

In the following, the originality of the organic materials with respect to other gain media is discussed by considering the following points:

- In first approximation, the organic materials are known to have the molecular structure of a four- level system.

- By using these materials, the laser operation is limited to the pulsed regime, in the absence of special initiatives such as dye jet flow system as in liquid dye lasers.

1.3.1 Four-level system

In Figure 1.10, a complete excitation and emission cycle in an organic dye, seen in laser operation, is described by using the so-called Morse diagram. In this schematic representation, the ground state and the first excited electronic state with the corresponding vibrational levels to each state are drawn. To each vibrational level is associated a wavefunction as illustrated in the figure.
At thermal equilibrium condition, the molecule is in the lowest vibration level of the ground sate and upon absorption of a photon of necessary energy, it makes a transition to

an upper excited electronic state. According to Franck-Condon principle in quantum chemistry, because of the lower mass of the electrons compared to the nuclei, the electronic transitions (absorption or emission) occur in a timescale ($\sim 10^{-15}$ s) much faster than the nuclear response. Based on this principle, the transitions are vertical and are favored between vibrational levels corresponding to a minimal change in nuclear coordinates. A transition happens when there is an overlap between the vibrational wavefunctions of the ground state and final electronic state. The geometry of the excited state is not necessarily the same as the ground state. This fact is shown in the above figure by a shift in nuclear coordinates between the S_0 and S_1 state and is indicated by Δr. In the particular illustrated case, the transition probability is the strongest between $\nu = 0$ and $\nu = 2$. Once in $\nu = 2$, the electron decays down to the lowest vibration level of the first excited singlet state and then an emission to one of the vibration levels of the ground state (here, $\nu = 2$) based on the Franck-Condon principle takes place. This transition is followed by a non-radiative relaxation to the lowest vibrational level of the ground state by which an absorption-emission cycle becomes completed.

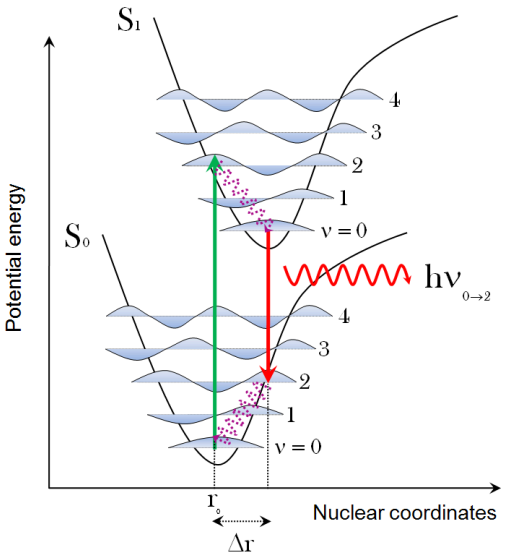

Figure 1.10 - Morse energy diagram.
Since electronic transitions are very fast in comparison to nuclear motions, vibrational levels are favored when they correspond to a minimal change in the nuclear coordinates. The potential energy curves are shown favoring transitions between v = 0 and v = 2.

According to what described in the above, one can observe that thanks to the vibrational levels (VR), the molecular system of the organic dyes is structured in shape of four different energy levels, thus, named as four-level system. Since the emission is always happening from the lowest vibrational level of the first excited electronic state, the emission maximum is red-shifted with respect to the absorption band maximum and thus, the reabsorption losses, i.e. the absorption losses at the emission wavelength, are considerably reduced. The red-shift is known as the Stokes shift and varies from 0.1 eV to 1 eV [77] in most organic compounds. Generally, having large Stokes shifts are highly desirable because of the further decreased reabsorption losses leading to low thresholds for lasing applications.

1.3.2 Pulsed operational regime

Solid-state lasers in which organic dyes are used as the gain medium are not able to operate in continuous regime mainly, because of ISC followed by triplet absorption or STA. In organic compounds the triplet absorption is a spin-allowed transition and the corresponding absorption band is broad and effectively overlaps with the fluorescence emission spectrum which in this case becomes a major issue for laser operation.

Continuous wave (CW) excitation leads to population of the triplet state that finally quenches any available excited singlet state for laser operation. In this respect, attempts to construct a continuous wave (CW) dye laser have led to efforts which are basically aimed to prevent significant accumulation of the triplet state. One common method for liquid dye lasers is to add a second molecule to the dye solution to act as a so-called triplet quenching agent. This technique is helpful in a way that it reduces the excited triplet state lifetime through collisional de-excitation [78].

Since the very beginning after the invention of liquid dye lasers, rapid flow of the dye solution has been another method to control triplet state accumulation and thus, achieving the CW operation. Another advantage that can be obtained through dye jet flow system is the reduced photo chemical/thermal degradation rate of the dye molecules as different dyes are exposed to pump excitation within a given time.

For solid-state dye lasers, rotation of the gain medium to mimic the dye jet flow system as in liquid dye lasers can be a solution [79]. However, the setup would be the subject of strong vibrations and thus output emission instability.

Another solution to the above problems is the use of pulsed excitation regime in order to have fewer amounts of molecules in the excited triplet state and to make the lasing become possible.

2 Lasing characterization of a novel organic small molecule compound

2.1 Introduction

In this chapter, the issues concerning the realization of low threshold laser devices are addressed and discussed. In terms of geometry, waveguide structures are very promising to achieve this goal. From the material point of view, the challenges toward this goal are the subject of the following discussion.

In solid-state films based on conventional laser dyes significant luminescence quenching resulting from a strong interaction of excited-state molecules (singlet-singlet annihilation (SSA), singlet-triplet annihilation (STA) and triplet-triplet annihilation (TTA)) is normally preventing efficient stimulated emission process required for lasing [50, 80]. Therefore, in order to avoid quenching, small doping rates must be carefully chosen while making dye-doped solutions or solid matrices (generally a few percent of dye with respect to the solution or solid mass). However, if these thin solid films have to be used for laser applications, using this technique may lead to an increased lasing threshold and an inefficient device as in this case a small fraction of the pump beam passing through the thin film can be absorbed in single-pass geometry. In this regard, one might think of a thicker film where the absorption can be considerably increased. However, this will be at cost of increasing the lasing threshold and a multimode device. Another solution can be to use multi-pass configuration for the pump beam. But, this may become rather complicated especially when the pump beam has to be focused onto a small spot size diameter.

One proposed solution to stay with thin-film based devices while avoiding the above difficulties, has been the use of guest-host systems based on Förster resonant energy transfer (FRET) (section 1.1.3.1). One can find several reports in the literature based on

this principle [49, 81-85]. A very common example of a guest-host system can be given by 4-dicyanomethylene-2-methyl-6-(p-dimethylaminostyryl)-4H-pyran (DCM) doped into tris (8-hydroxyquinolinate) aluminum (III) (Alq_3). The main advantage of the FRET is the strong pump absorption by the host material and reduced quenching due to diluted guest dispersed in the medium. In FRET, the self-absorption is efficiently circumvented by shifting the emission of guest to a wavelength band where the host material is transparent, leading to very low laser thresholds. However, in order to have an emission in the visible part of the spectrum, an excitation in the UV region is required. This may lead to a reduced emission lifetime of the device because of the higher degradation rate that can be resulted in this way due to very energetic UV photons compared to visible photons getting into the sample.

The solution in this case can be the use of neat films (non-doped matrices) of organic compounds, capable of being excited and then emit in the visible region, where by different means in the molecular structure design, the quenching and the reabsorption losses are considerably reduced. So far, stimulated emission and lasing have been demonstrated in neat films of π-conjugated polymers [86-89] as well as in some low molecular weight organic compounds (small molecules) [22, 90]. Among these two types, the latter are of especial interest as they exhibit a well-defined molecular structure and can be thermally evaporated, leading to a precise control over the layer thickness and a better film quality. One can find reports on lasing in devices based on neat films of small molecules such as sexiphenyls [91], oligothiophenes [90] or spiro-linked[5] conjugated moieties [92-94]. However, in most cases the reported emission wavelengths are essentially in the violet or blue part of the spectrum with some rare exceptions in the orange-red [90]. This is in fact because long-wavelength emission is generally achievable under the condition of extended π-conjugation lengths. But this will increase the probability of π-π stacking as a result of favorable overlap between the π molecular orbitals. However, this may be helpful where high conductivities are needed (e.g. in OLEDs), but on the other hand, long conjugation lengths can efficiently quench the fluorescence. Consequently, efficient red-emitting laser (or OLED) based on neat materials is still a challenge.

In this chapter, a novel small molecular weight organic compound, so-called "fvin", is presented and characterized. The full chemical name of this molecule is "4-di (4'-tert-butylbiphenyl-4-yl) amino-4'-dicyanovinylbenzene" and it was developed by Prof. Elena

[5] Spiro linkage is a technique where a spiro center introduces a twisted unit between two different or similar conjugated moieties. This prevents π-π stacking and improves their processability and morphological stability while maintaining the electronic and optical properties of the non-spiro segments before linkage. The spiro-linked compounds form stable nonpolymeric organic glasses with high glass transition temperatures.

Ishow at ENS Cachan. This material with its unique structural design is capable of emitting in the deep-red part of the spectrum in neat film configuration while the problems related to π-π stacking, concentration quenching and reabsorption losses are considerably reduced. The suitability of this material for stimulated emission is demonstrated by optical pumping of a thin neat film forming an optical waveguide. This technique determines the existence of ASE and is the basic principle of material gain measurement via Variable Stripe Length (VSL) technique. This experiment is then followed by examining this material in a simple resonant distributed feedback (DBR) configuration. At each stage of the experiment the results are compared with the measurements carried out under the same experimental conditions for a film of PMMA doped with the classical DCM laser dye (see appendix 1 for DCM molecule structure). Furthermore, the viability of this novel material under electrical injection was also tested in OLED configuration which is not included in the context of this thesis [95].

In the following, the fundamentals of waveguiding in planar geometry are described and then the Variable Stripe Length (VSL) technique principle and the related theory, used for material gain measurement, are detailed. It is shown how the waveguide losses can be measured by using the realized ASE setup for gain measurement. Then, the experimental part starts by presenting the "fvin" molecular structure and its properties, the sample fabrication procedure and presentation of the realized ASE experimental setup. This is followed by discussion on the gain and loss measurement results in "fvin" neat film configuration and comparing these results with the same measurements carried out on DCM-doped PMMA film. Finally, the last parts are devoted to lasing demonstration in material under investigation incorporated into Distributed Bragg (DBR) geometry and then, demonstration of random lasing effect in "fvin" neat film.

2.2 Planar (slab) waveguide principles

A waveguide is a structure that confines the light in a medium by total internal reflection phenomenon at the medium interfaces with the surrounding media. For light to be trapped and guided, the refractive index of the propagating medium must be superior in comparison to the surrounding media. The amount of light confinement is determined by the refractive index contrast between the propagating medium and the surrounding media. The bigger the difference, the more the light is confined and guided within the structure. One of the most encountered waveguide structures is the planar (slab) geometry where a thin film of a material with refractive index of n_{film} is sandwiched between the up and down claddings. If the claddings have the same refractive indices, then the structure configures a symmetric planar waveguide. A very simple case that we are dealing with in this context is an asymmetric waveguide where the lower cladding is made of fused silica (Sio_2) with $n_{sub} \approx 1.45$ and the upper cladding is the air with the refractive index of $n_{cladding} = n_{air} = 1$. A schematic representation of an asymmetric waveguide structure is shown in the Figure 2.1.

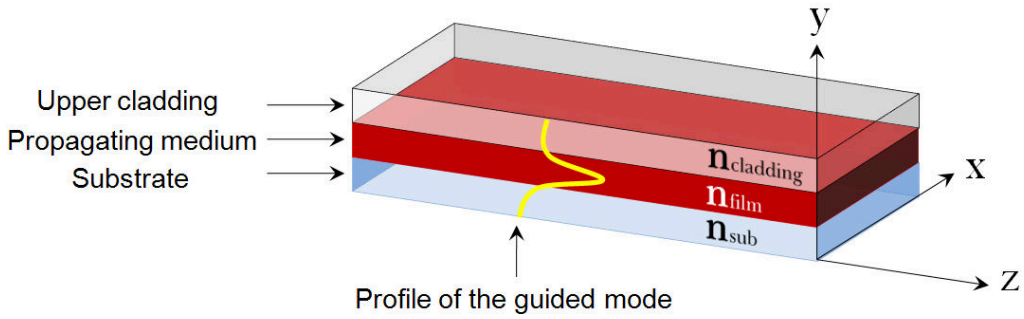

Figure 2.1 – Three dimensional representation of planar waveguide geometry. For light to be guided one should have $n_{film} > n_{sub} \geq n_{cladding}$.

The propagation of light (λ) in the above-illustrated structure composed of a medium with a dielectric constant of ε_r can be described by the Helmholtz equations for the electric and magnetic field components of light as are given in the following:

$$\nabla^2 \vec{E}(r) + k_0^2 \varepsilon_r \vec{E}(r) = 0$$
$$\nabla^2 \vec{H}(r) + k_0^2 \varepsilon_r \vec{H}(r) = 0 \qquad (2.7)$$

where $k_0 = 2\pi/\lambda$ is the wave vector, $\varepsilon_r = n^2$ with n being the refractive index of a given material and $\vec{E}(r)$ and $\vec{H}(r)$ are the electric and magnetic fields, respectively. The solutions to the above equations for an electromagnetic field of light propagating along the z direction are complex and are given by:

$$\begin{aligned}\vec{E}(r,t) &= \vec{E}(x,y)e^{j(\omega t-\beta z)} \\ \vec{H}(r,t) &= \vec{H}(x,y)e^{j(\omega t-\beta z)}\end{aligned} \tag{2.8}$$

where β is the propagation constant and is defined as:

$$\beta = \frac{\omega}{c} n_{eff} = \frac{2\pi}{\lambda} n_{eff} \tag{2.9}$$

with n_{eff} being the effective refractive index, that is, the refractive index seen by the waveguide light along the propagation direction and c is the speed of light. The n_{eff} value lies between the refractive index of the substrate and the refractive index of the material used for the propagating medium.

Generally, in waveguide problems only the TE (transverse electric) modes are considered since the treatment of TM (transverse magnetic) modes is similar. In addition, the field variation along the x direction is assumed to be negligible ($(\partial/\partial x) = 0$) as the waveguide is considered to be infinite at x direction.

Considering the above assumptions, the expansion of the Helmholtz equations in (2.7) for the electric field propagating along the z direction will be in the form of:

$$\frac{\partial^2}{\partial y^2} E(y) + (k_0^2 n^2 - \beta^2)E(y) = 0 \tag{2.10}$$

Solving this equation for each of the media within the waveguide structure (upper cladding, film and the substrate) with application of appropriate boundary conditions at the interface layers will determine the confined guided modes. These imposed conditions are:

- Continuity of the transverse electric profile and its derivative at the layer boundaries. This condition together with the Helmholtz equation given in (2.10) for different layers provide given number of the guided modes.

- A guided mode has a sinusoidal shape in the confining film with exponential decay at the cladding layers.

The full description of the waveguide theory will not be given here, but it can be easily found in any waveguide textbook [96].
In order to assess the suitability of a new material for efficient lasing operation, optical gain measurement is crucial. In the following, the method we applied for gain measurement in thin films waveguides of organic materials is therefore described.

2.3 Gain measurement technique in slab geometry

For the purpose of gain measurement, Variable Stripe Length (VSL) technique is the widely-used method in waveguide configuration [50, 97-102]. This technique involves pumping the sample with a stripe of variable length and monitoring the edge-emitted intensity as a function of the pump stripe length (Figure 2.2). The material gain is then determined by fitting the results by an appropriate function that will be developed in the following.

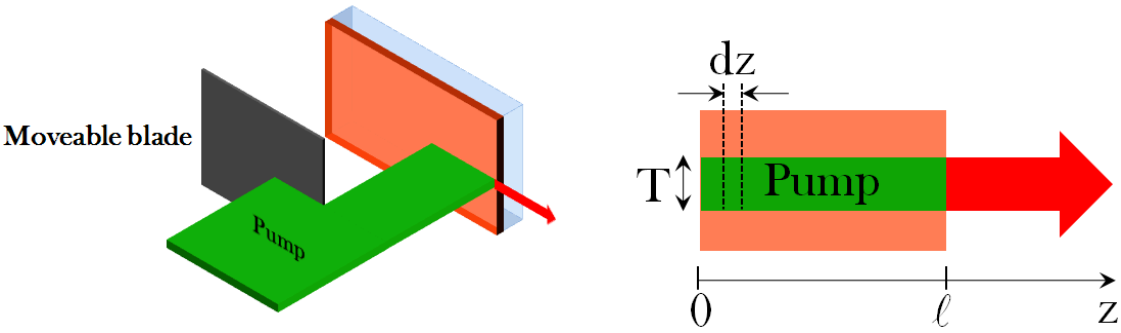

Figure 2.2 - (left) VSL method representation, (right) Close-up over the pumped region from a view normal to waveguide surface.

2.3.1 Gain fundamentals applied to VSL technique

First of all, let us consider a gain material, that is, a material with the potential of light amplification. Now, imagine that a thin film of this material is deposited on a transparent substrate with a lower refractive index to form a planar (slab) waveguide. If a pump stripe of homogeneous intensity profile with a certain thickness T and a variable length of ℓ

($T << \ell$) is incident on such a structure, the ASE will take place within the excited stripe. The local gain (g_{local}), that is, the gain within a given tiny volume of this medium pointed by the r vector is given by

$$g_{local}(x,y,z) = \sigma_{e(0,\nu)} \Delta N\left(\vec{r}\right) \tag{2.11}$$

where $\sigma_{e(0,\nu)}$ (cm^2) is the emission cross section and ΔN (cm^{-3}) represents the inverted population at the given infinitesimal region of the gain medium. As the length of the pump stripe and/or the pump intensity increases, the edge-emitted ASE intensity will grow exponentially. In a mathematical expression, the ASE intensity variation within an infinitesimal slice of dz along the z direction can be written as:

$$\frac{dI}{dz} = \left[\left(\iint_{x,y} g_{local} \underbrace{f(x,y)}_{\substack{\text{propagating} \\ \text{mode profile}}} \overbrace{p(x,y,z)}^{\text{pump profile within the gain medium}} dxdy \right) - \alpha \right] I(z) + \eta_{spont.} \tag{2.12}$$

Where f(x,y) is the propagating mode profile, p(x,y,z) is the pump profile within the film thickness which takes into account the exponential decay as a result of absorption (Beer-Lambert's law), α is the loss coefficient and $\eta_{spont.}$ is a term related to the power density of the spontaneously- emitted photons into the stripe solid angle. The term under the integral defines the modal gain as:

$$g_{modal}(z) = \iint_{x,y} g_{local} \underbrace{f(x,y)}_{\substack{\text{propagating} \\ \text{mode profile}}} \overbrace{p(x,y,z)}^{\text{pump profile inside the gain medium}} dxdy \tag{2.13}$$

If the pump profile is considerably elongated in the z direction, one can consider that for small stripe lengths the variation of the pump intensity profile in the z direction is negligible. Then we have the expression of g_{modal} in the z direction as the following:

$$g_{modal} = \iint_{x,y} g_{local} \underbrace{f(x,y)}_{\substack{\text{propagating} \\ \text{mode profile}}} \overbrace{p(x,y)}^{\text{pump profile inside the gain medium}} dxdy \tag{2.14}$$

Then, the integration of (2.12) over the excited length of ℓ with the boundary condition of $I(0) = 0$ gives:

$$I = \frac{\eta_{spont.}}{g_{modal}}(e^{(g_{modal})\ell} - 1) \qquad (2.15)$$

Derivation of the equation (2.15) is performed under the very important assumptions which are the homogeneous pump intensity profile along the excited region and no gain saturation. In addition, it is supposed that the pump stripe is almost one dimensional. This means the stimulated photons propagate preferentially along the stripe direction if $T << \ell$. At steady state when absorption and stimulated emission rates become equal, gain saturation refers to a condition where the ASE intensity, built along the excitation axis, becomes so strong that it depletes the excited-state population (ΔN) to half of its unsaturated value. Since the local gain is defined as $\sigma_{e(0,v)}\Delta N$, this can be translated as a decrease in the gain value by a factor of two. An example of the gain saturation effect is shown in Figure 2.3.

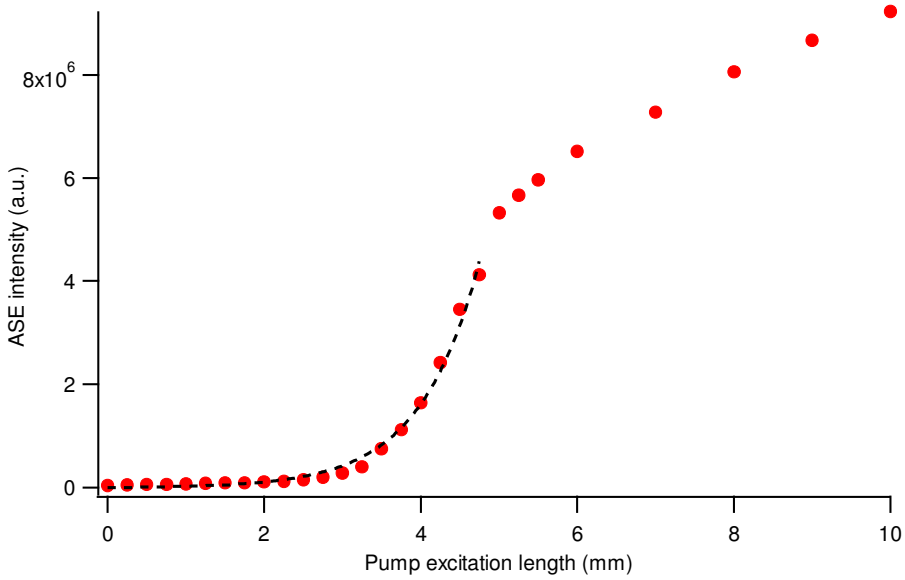

Figure 2.3 - Gain saturation demonstration. The dashed line is a fit to the experimental data by using the expression in (2.15).

In the beginning, the ASE intensity grows exponentially according to (2.15) and then as the pump length increases, the gain saturates and the ASE intensity decreases.

To conclude from the above discussion, one can understand that the gain measurement through the VSL method becomes elaborate for long excitation lengths because of the gain saturation phenomenon. This adds another adjustable fitting parameter (the saturation intensity or I_{sat}) to the given relation in (2.15). Therefore, in order to avoid the consequent complexities as a result of gain saturation and to be able to use the simple relation given in

(2.15), the gain measurement must be carried out at small signal regime, that is, for excitation lengths and pump fluences where there is no gain saturation effect. For a high-gain material, in order to avoid gain saturation, the pump length can be even limited to less than a millimeter under the excitation fluences on the order of few hundreds of $\mu J/cm^2$.

2.3.2 Waveguide propagation losses measurement technique

The gain coefficient measured through VSL technique is the net gain which is the gain minus the waveguide propagation losses. These losses, denoted by (α) in the last section, might be due to scattering, reabsorption losses at the emission wavelength and/or concentration quenching.

The ensemble of the above-mentioned losses can be determined through pump stripe displacement method using VSL arrangement. In this technique the sample is pumped with a stripe of constant length and the edge-emitted intensity is monitored while the set of sample and the emission detector, mounted on the same support, are translated laterally in the normal direction with respect to the pump beam. This resembles the condition when the pump stripe gradually moves away from the edge of the sample (Figure 2.4).

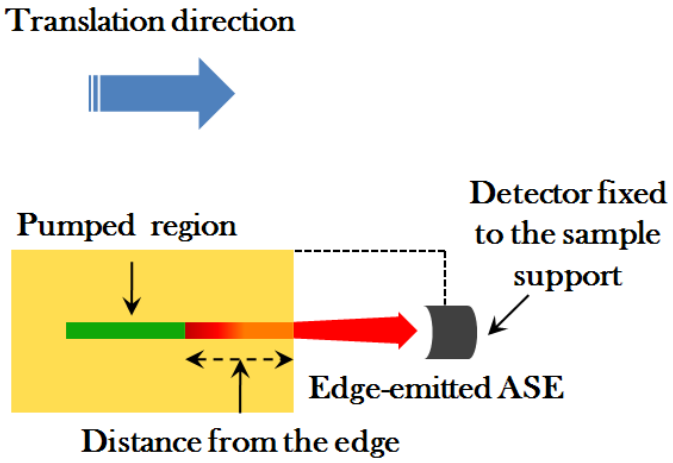

Figure 2.4 - Waveguide propagation losses measurement technique in VSL method.

In this configuration, the emission from the end of the stripe is assumed to be constant. Therefore, as the distance between the end of the pump stripe and the sample edge increases, the edge-emitted ASE decreases since it has to travel across an increasing unpumped length before reaching the sample edge. The intensity reduction is ascribed to losses that occur within the unpumped region. The ASE intensity should depend on the

distance from the sample edge as follows:

$$I_{out} = I_0 e^{(-\alpha x)} \tag{2.16}$$

where x is the length of the unpumped region between the edge of the sample and the end of the pump stripe, I_0 is the intensity at the end of the pump stripe and α is the waveguide loss coefficient.

The above descriptions on the fundamentals of gain and loss measurements in slab geometry will give us the necessary tools to carry out the related experiments on the material under investigation which its molecular structure and properties are described in the following part.

2.4 Experimental

2.4.1 Material under study

The small molecular weight compound under test is called "fvin". This molecule whose chemical structure is depicted in Figure 2.5, has a full name of "*4-di (4'-tert-butylbiphenyl-4-yl) amino-4'-dicyanovinylbenzene*" and was synthesized and provided by Dr. Elena ISHOW from PPSM laboratory (Laboratoire de Photophysique et Photochimie Supramoléculaire et Macromoléculaire) at ENS de Cachan [103].

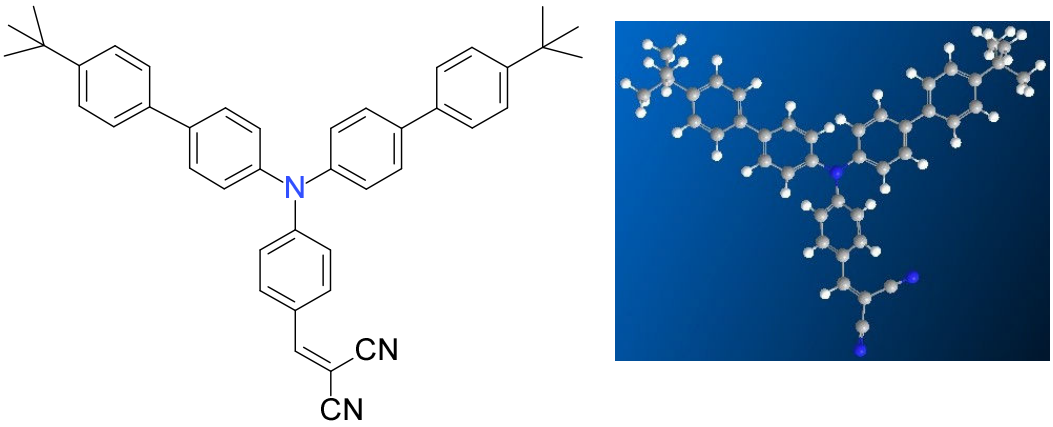

Figure 2.5 – (left) Molecular structure of the so-called "fvin" molecule, (right) three dimensional image of the "fvin" molecular structure.

The normalized absorption and emission spectra of "fvin" molecule in thin film configuration (100-nm-thick neat film) are shown in Figure 2.6. This molecule has two absorption maxima at 319 nm and 479 nm with an emission peak in the red part of the spectrum at 631 nm when excited with a source at 343 nm. In design of this molecule the red emission is obtained via creation of large Stokes shift in a push-pull molecular structure. In this way the solid-state emission is tuned by the strength of intramolecular charge transfer (ICT) while the absorption band and the main structural backbone remain unchanged. This has become possible thanks to the 4-tert-butylbiphenyl substituents at the left and right side of the structure, coupled to the electron-donating triphenylamino core in the middle that have led to a distorted geometry in the excited state relative to the ground state revealed by femtosecond transient absorption spectroscopy done at ENS de Cachan facilities. The advantage is twofold: first, a Stokes shift as wide as 152 nm which is favorable to obtain a true four-level system where the reabsorption is efficiently circumvented at

emission wavelengths; second, it has the consequence of achieving red emission with relatively short conjugation length which limits the intermolecular π-π interaction that can lead to fluorescence quenching.

The bulky tetrahedral tert-butylphenyl groups are also advantageous from another point of view as they cumber the mobility of molecules in film configuration and avoid π-π stacking as well. Thanks to the steric hindrance exerted by these groups and also twisting of the triphenylamino core, quenching is considerably reduced in "fvin" compound. These geometrical characteristics allow to obtain an amorphous material (T_g = 86° C) without any microcrystalline domains. The formation of these domains can lead to high optical losses at the interfaces between different grain boundaries [104].

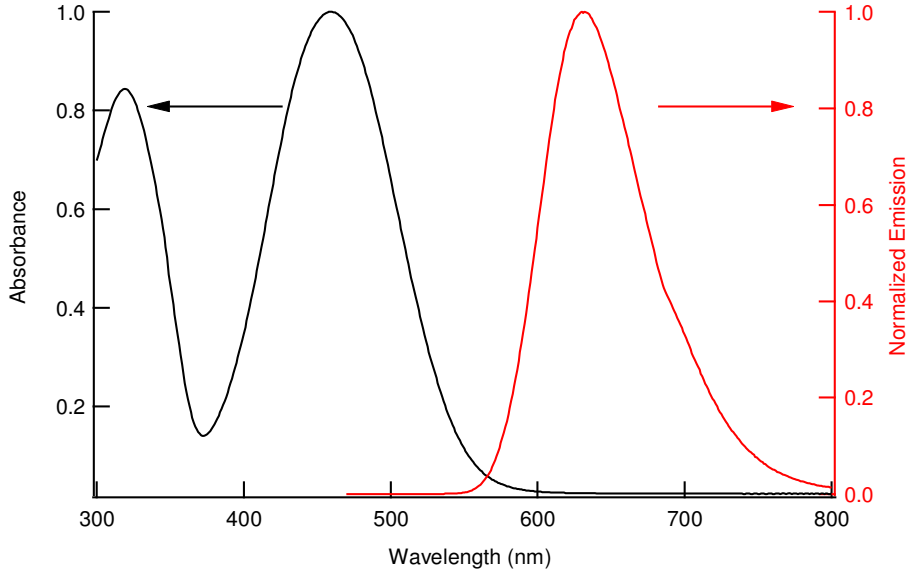

Figure 2.6 - Absorption (left) and emission (right) spectra of the "fvin" molecule in neat film configuration.

An important parameter of the "fvin" compound needed to be determined was the refractive index. This was determined by using the ellipsometry technique at ENS de Cachan facilities[6]. The refractive index showed to be very dispersive by wavelength. A very approximate refractive index of $n \approx 1.85$, corresponding to the refractive index at 631 nm (the emission peak wavelength) is deducible from the measurement.

Following the presentation of the material under investigation, the next step is to examine the suitability of this material as an optical gain medium via VSL method. For this purpose, samples in slab configuration must be fabricated. The next part will be the description of the sample fabrication procedure and the characterization techniques.

[6] I would like to thank Dr. Melanie Lebental for her help in ellipsometry measurement.

2.4.2 Sample fabrication and characterization

Fabrication of a sample is a multi-stage process starting by the required film thickness calculation, substrate preparation followed by active layer deposition and finally its characterization. In the following, these steps are discussed in detail.

2.4.2.1 Film thickness calculations

For the ASE measurements, having waveguide structures with thicknesses that only allow the propagation of the fundamental transverse electric mode (TE_0) are preferential. In this case the whole power is accumulated within an intense peak where the maximum of the field is centered in the middle of the propagating layer and decays exponentially at the cladding layers. For this purpose, in order to have a rough estimation about the required film thickness in our case, the dispersion curves of an asymmetric planar waveguide were calculated and plotted based on the refractive indices of the considered substrate for the film deposition (fused silica with $n \approx 1.458$ at ~ 600 nm) and the material under investigation ("fvin" with $n \approx 1.85$) (Figure 2.7). These curves are showing the effective refractive index (n_{eff}) as a function of the ratio between the film thickness and the wavelength of the propagating field. The method for tracing the waveguide dispersion curves can be easily found in any waveguide textbooks [96].

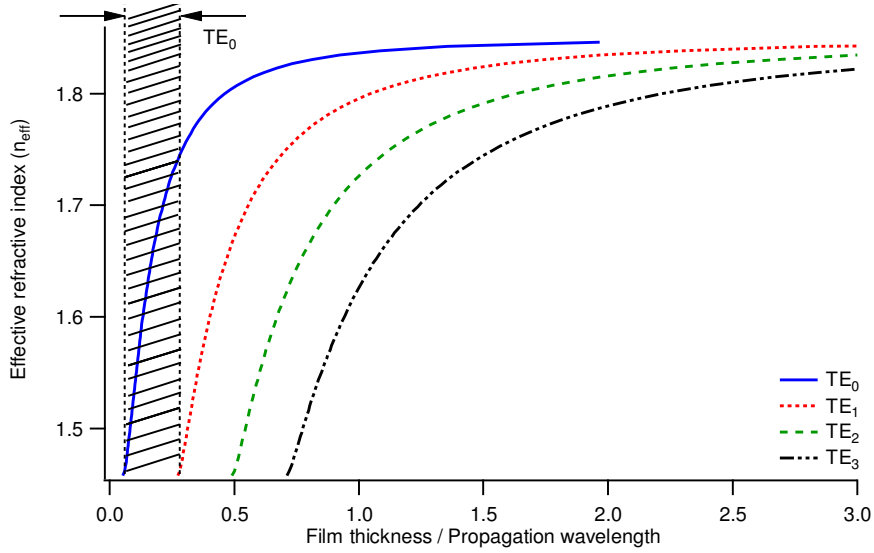

Figure 2.7 - Dispersion curves corresponding to the asymmetric waveguide made of "fvin" layer on silica substrate. The hachured area corresponds to the case where only the TE_0 can propagate.

Considering that ASE happens where the material net gain is maximum, that is, somewhere around the fluorescence emission peak (for "fvin" $\lambda_{max} = 631$ nm in neat film configuration), then based on these curves for film thicknesses from ~ 33 nm to ~ 170 nm realized on fused silica substrate, only the fundamental TE_0 mode would be able to propagate within the structure. Below 33 nm no mode can exist. This thickness is known as the cut-off thickness of the waveguide.

As we intended to compare the gain measurement results of the "fvin" compound with the DCM-doped film of PMMA, then we also calculated the necessary thickness for the propagation of the fundamental TE_0 mode via the dispersion curves in this case. For this rough calculation, the refractive index of dye-doped PMMA was determined to be $n \approx 1.52$ through the technique described in appendix 2. On this basis, the dispersion curves for DCM-doped PMMA films deposited on fused silica substrate are presented in Figure 2.8.

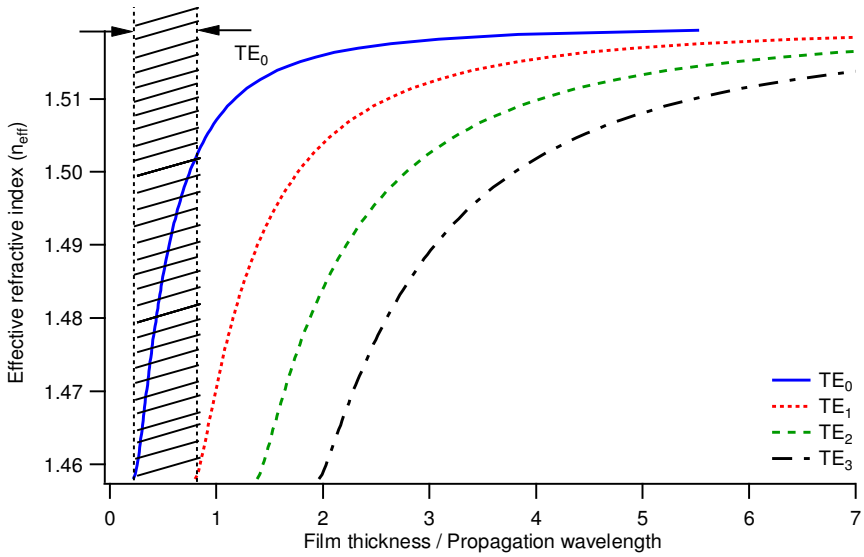

Figure 2.8 - Dispersion curves corresponding to the asymmetric waveguide made of DCM-doped PMMA layer on silica substrate. The hachured area corresponds to the case where only the TE_0 can propagate.

The fluorescence emission peak of DCM-doped PMMA is around 560 nm [105]. Therefore, based on the dispersion curves a film thickness of ~ 600 nm would assure the propagation of TE_0 mode. In this case the cut-off thickness is ~ 123 nm.

In order to have similar experimental conditions for both cases of "fvin" and DCM dye, film thicknesses of 600 nm were chosen even if in case of "fvin", this thickness does not correspond merely to the propagation of the TE_0 mode. As measured later on, this film

thickness could absorb 84% of the pump beam at 532 nm. Considering this high absorption, reducing the film thickness to have the propagation of the fundamental mode, might not seem troublesome in case of "fvin". However, in DCM-doped PMMA, as small doping rates (~ 5%) are required because of the concentration quenching, the pump absorption is limited to very low amounts. As will be seen later, 600-nm-thick film of DCM-doped PMMA (5% doping rate) was measured to absorb 13% of the pump beam.

- **Substrate cleaning procedure**

The cleaning procedure described here is used for all kinds of substrates including glass slides, silica and also the dielectric mirrors used during the whole set of experiments in this thesis. As of glass slide, simply the microscope slides were used, where it needed. The silica substrates were prepared from bulk, cut into pieces and then polished to optical quality in our laboratory workshop[7].

Adequate cleanliness of the substrates prior to film deposition is an important step for having high quality coatings. Any contamination of the surface affects the adhesion of the coating and leads to defects. Therefore it is necessary to remove all the possible dirt and impurities which lies on the surface of the substrates and might be due to dust, grease or organic/inorganic solvent residues. For this reason, a simple procedure is taken as the following in order to have proper substrates:

- Preparing a bath of soapy water.
- Use a lint free wipe to gently rub the surface and make it clean of dirt and residues. Rinse thoroughly in distilled water.
- Transferring the substrates into the bath of pure acetone and let them soak for 15 minutes.
- Drying the substrates by rubbing them against a lint free wipe.

To recover the already-used substrates, immersing the substrates in bath of Tetrahydrofuran (THF) for 15 minutes to remove the already deposited layer is preceding the above-mentioned steps.

[7] I would like to thank Thierry Billeton for preparing the silica substrates.

2.4.2.2 Active layer fabrication methods

Thermal evaporation technique was used to prepare a neat film of "fvin" on silica substrate. On the contrary, this method can't be applied for "DCM" since like the majority of the organic dyes, it is suffering from concentration quenching phenomenon that consequently requires a small doping rate in an inert matrix. In this case, an alternative solution for film deposition would be through spin coating technique.

For this purpose, a small quantity of DCM (Exciton Inc.) was dispersed in a solution of 495000 molecular weight in anisole (PMMA A6 from MicroChem Corp., see appendix 3 for more detail on this PMMA type and the corresponding spin speed curve) in a way that it constitutes 5 wt% of the solid PMMA after solvent evaporation. This PMMA type allows having film thicknesses on the order of few hundreds of nm. A homogeneous blend was obtained after 2 hours of alternating sonication and hot-plate magnetic stirring using stir bars.

In the following, two of the above-mentioned methods which are used in the course of this work for deposition of the organic films are briefly discussed.

- **Thermal evaporation**

This technique allows deposition of extremely uniform films of desired thickness. The apparatus is called thermal evaporator in which an electric resistance heater is used to meltdown the target material which then turns into vapor and finally is condensed back onto the substrate under vacuum condition (Figure 2.9). A Quartz crystal sensor is continuously monitoring the evaporation rate and thus the film thickness. For our gain measurement purpose, a 600-nm-thick film of "fvin" (controlled and measured by the quartz microbalance) was deposited onto a silica substrate under vacuum condition (9×10^{-6} mbar) at 160-180°C. The film optical quality was excellent as is usually expected for thin films realized by this technique.

The "fvin" evaporation process was performed at the ENS Cachan[8].

[8] I would like to thank Prof. Elena Ishow for making it possible to use the evaporator machine and helping us during the evaporation process.

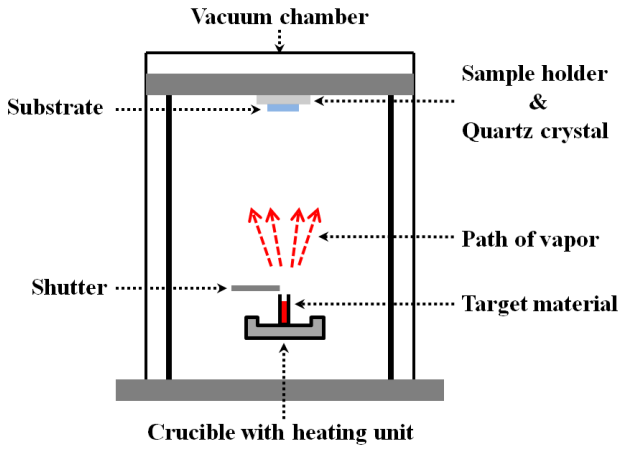

Figure 2.9 - Thermal evaporator chamber

- **Spin coating**

In this method the substrate is placed on the spin coater vacuum chuck and is vacuum clamped for spinning. In order to assure wetting the whole substrate surface, an excess amount of the solution compared to what is finally required is dispensed on the center of the substrate. As the spin coater speeds up according to predefined program, the centrifugal acceleration causes the solution to spread to, and eventually off, the edge of the substrate leaving a thin film of solution on the surface. The resulting film thickness depends on solution viscosity and the spin speed. On this basis and for our gain measurement purpose, the spin coater was programmed to obtain films of ~ 600-nm-thick from the solution of PMMA: DCM already prepared as just being described in the above. The samples obtained by this technique were transferred to the oven and annealed at 50°C during 1 hour to evaporate the solvent and to densify the film. Figure 2.10 is schematically showing different steps in spin coating process.

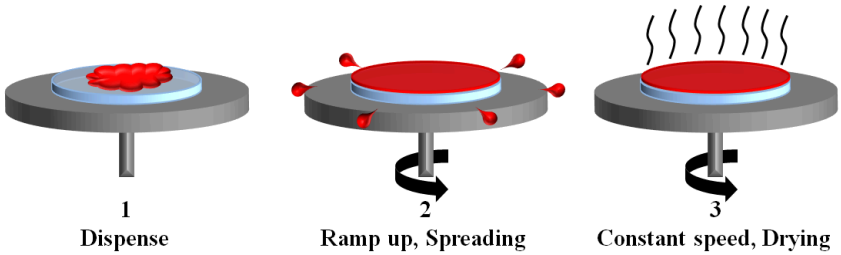

Figure 2.10 – Demonstration of different steps during spin coating process

2.4.2.3 Thin film characterization apparatuses

Once the films were prepared, their thickness was verified by Alpha-Step IQ surface profiler (KLA Tencor). For this purpose, a scratch was made on the sample surface down to the substrate. Then the sample was put at the measurement position under the ultra-fine surface profiler tip which was lightly dragged across the sample surface perpendicular to the scratch. The film thickness was determined by the change in tip elevation as it dropped from the film surface down onto the substrate surface. In this way, film thicknesses of 600 nm and 620 nm were measured for neat film of "fvin" and "PMMA-DCM" film respectively.

The film absorption was measured using a UV-Visible spectrophotometer Varian (Cary 100 series). Absorption amounts of 84% in 600-nm-thick film of "fvin" and 13% in the case of 620-nm-thick film of DCM-doped PMMA were measured at the pump wavelength (532 nm).

An Atomic Force Microscope (AFM) was at disposal to be used for further characterizations such as film surface roughness when it was required.

2.4.3 VSL measurement setup

The VSL experimental arrangement exploited for optical gain and loss measurements in films of organic materials is shown in Figure 2.11.

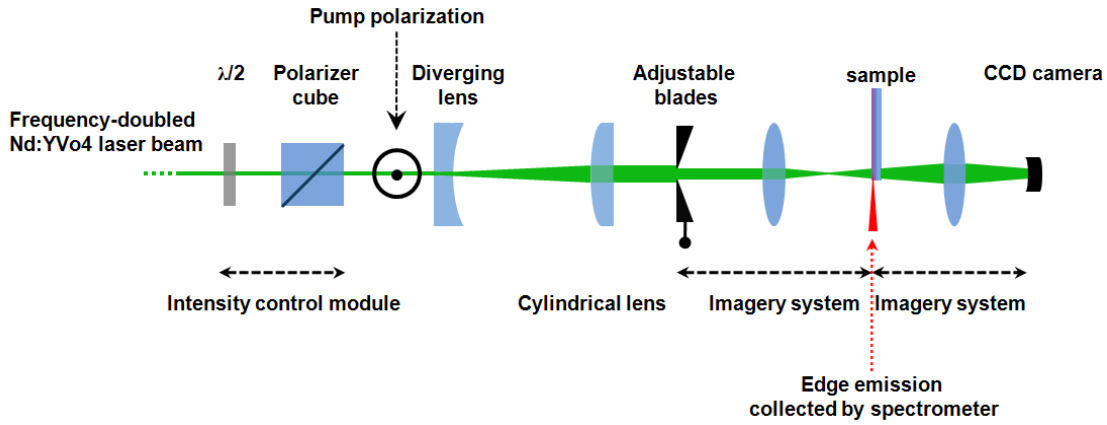

Figure 2.11 - Variable Stripe Length (VSL) technique experimental setup

The laser source was a Q-switched $Nd:YVO_4$ laser generating pulses of 500 ps long at 10 Hz repetition rate and 1064nm (PowerChip, Teem Photonics). The output train of pulses was passed through a frequency-doubling crystal (Lithium triborate) to reproduce pulses at 532 nm which was the required wavelength to pump the samples. A combination of half wave plate and polarizer cube were used to adjust the beam intensity. At this stage since the beam diameter was very small (~ 1 mm) for our purpose which was a stripe of variable length as is required for the VSL technique, a diverging lens was used to grow the beam size which was then focused by a cylindrical lens into a stripe of 320 µm wide measured at $1/e^2$ by a beam analyzer (Spiricon SCOR 20 camera, 1600 by 1200 pixels having the size of 4.4 µm by 4.4 µm each). The length of the stripe was controlled by a pair of adjustable blades selecting the central part of the stripe to assure a uniform intensity along the length of the pump stripe profile. We noticed that the strip arriving into the blades undergoes diffraction effects at the edges which consequently affect the incident stripe shape at its two ends when it reaches the sample. In order to have a well-defined stripe shape with abrupt edges at the ends, the blades and the sample were optically conjugated by means of an imagery system with one-time magnification. Figure 2.12 is demonstrating images of both cases obtained by Spiricon beam analyzer. This imaging is an original improvement in comparison with the widely-used classical method reported in the literature and greatly enhances the accuracy of the system. A second imagery system was following the first one

to have the image of the slit onto a CCD detector (Spiricon). The samples were pumped in transverse configuration resulting in ASE radiation perpendicular to the incident beam, collected by an optical fiber close to the sample edge and sent to a spectrometer (SPEX 270-M with two gratings of 150 and 1200 lines/mm, corresponding to the resolutions of 8 nm and 1 nm, respectively) followed by an Andor technologies DH 720 charge-coupled device (CCD) camera.

The polarization of the incident beam determines whether the ASE radiation is generated and emitted horizontally or perpendicular to the stripe direction. This is explained by the orientation of the dye molecules absorbing a particular pump polarization. Vertically polarized light is more likely to be absorbed by dye molecules whose dipole moment is oriented vertically and thus emit in horizontal direction and vice versa. In our experimental condition, pump polarization was vertical relative to the optical table (Figure 2.11) and the resulting ASE radiation showed to have mainly the same polarization type.

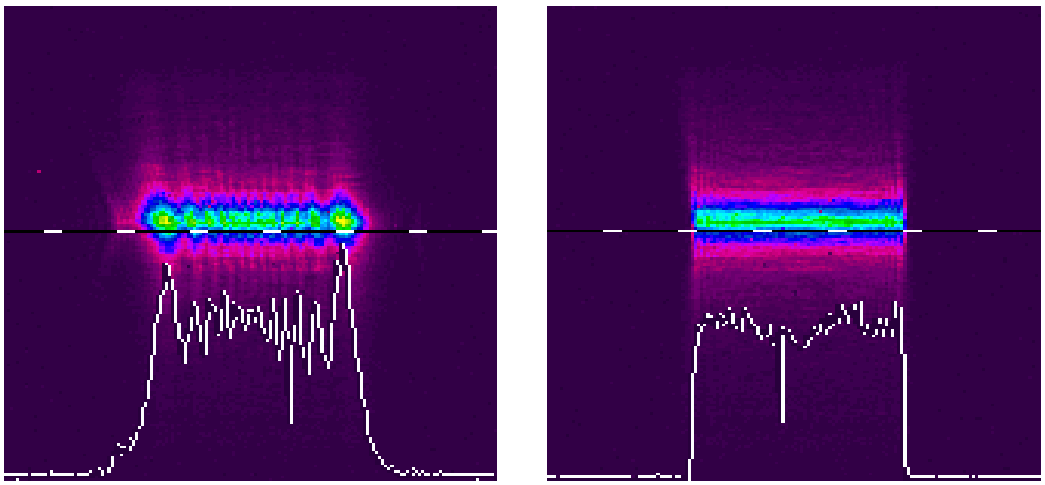

Figure 2.12 – Homogeneity of the pump profile (left) without imaging (right) with imaging system. These images are corresponding to a length scale of 10 mm.

2.4.4 Gain measurement

The VSL technique is applied for gain measurement in thermally evaporated neat film of "fvin" and the result is compared to gain values obtained at similar conditions in DCM-doped PMMA film obtained via spin coating.

Figure 2.13 is showing experimental result in 600-nm-thick neat film of "fvin" for three different pump fluences. We observed a superlinear increase in intensity versus the pump length, combined with a clear spectral narrowing (not shown here), establishing the first experimental evidence of stimulated emission in this material. The inset is showing a typical ASE spectrum of "fvin" with a peak at 660 nm. Each series of experimental points were obtained for a given pump fluence and different pump lengths where a single point yielded through integration over ASE emission peak.

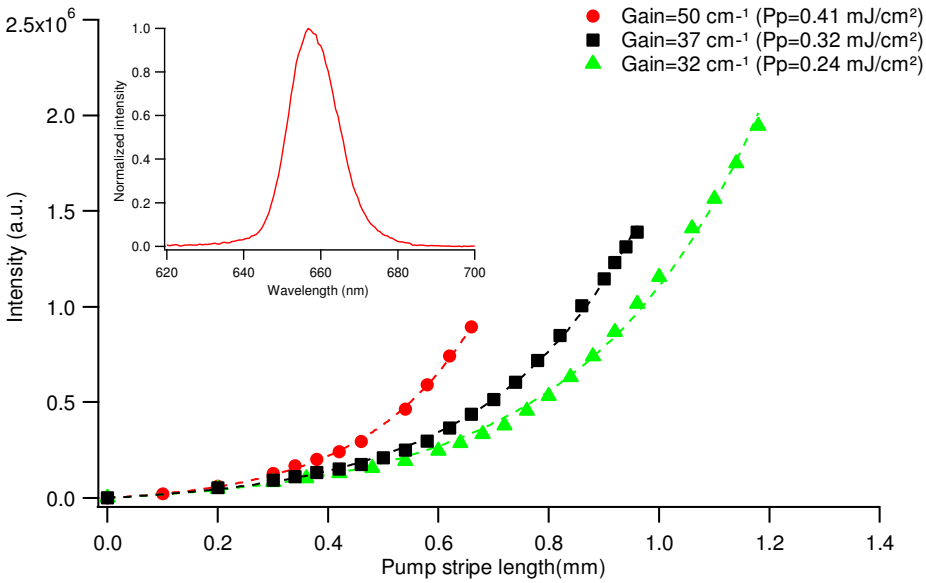

Figure 2.13 - Net modal gain measurement through the VSL technique in neat film of "fvin".

In non-saturated regime, fitting the experimental points with the gain formula in (2.15), resulted in a net modal gain (g_{modal}) value as high as 50 cm^{-1} for an incident pump fluence of 0.41 $mJ.cm^{-2}$.

The gain measurement experiment carried out at same pump fluences for 620-nm-thick film of DCM-doped PMMA, resulted in lower gain values. As one can see in Figure 2.14, for the same pump fluence of 0.41 $mJ.cm^{-2}$, a net modal gain value of 40 cm^{-1} was obtained. In this case, the ASE peak appeared at 613 nm.

It is somehow interesting to notice that a neat film exhibits a higher gain than a low-doped system, specially the DCM dye known for its high efficiency. The opposite case is usually observed due to strong concentration quenching.

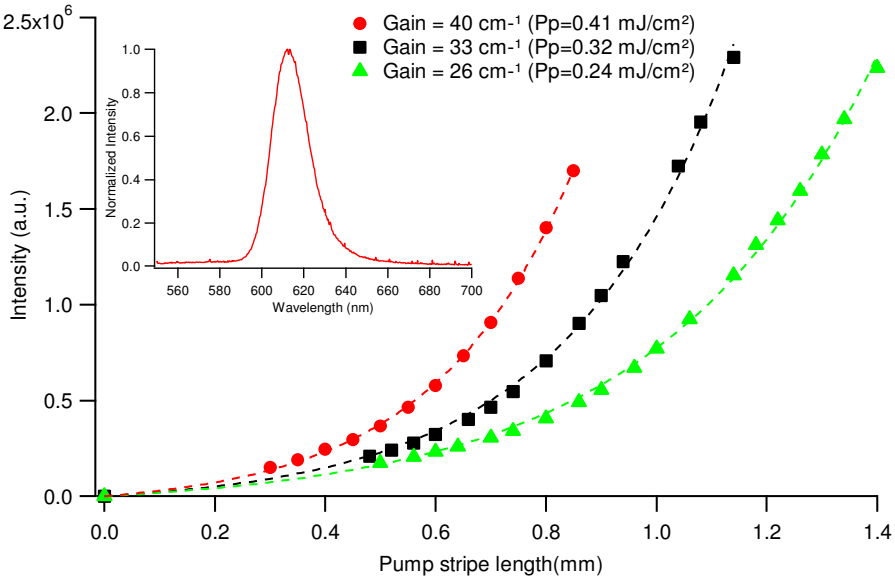

Figure 2.14 - Net modal gain measurement through the VSL technique in DCM-doped PMMA film.

From the above gain comparison, we can then conclude that high gain values obtained for neat film of "fvin" are due to reduced concentration quenching phenomenon thanks to the special geometry of "fvin" molecule as described earlier. What we observed here is a rare example of very efficient and red-emitting laser material in neat film configuration.

The gain values, obtained experimentally, are the net modal gains. To determine the material gain, the waveguide propagation losses should be taken into account. The following section is the result of waveguide loss measurements.

2.4.5 Waveguide loss measurement

To more fully characterize the novel "fvin" compound as a powerful gain material, we have measured the waveguide loss coefficient (α) through the widely-used variable stripe displacement method described earlier. This measurement was carried out on a sample with dimension of ~ 2.5 cm × 2 cm. The result is shown in Figure 2.15. Each point is obtained following the integration over the ASE emission peak for different pump stripe distances from the edge. As one can see the intensity of the guided light decays

exponentially for the first millimeters and then it is followed by a slight increase and finally a decrease to zero. We may explain this anomalous behavior as the following. As the pump stripe is translated away from the sample edge where the light is collected, once it is placed somewhere in the middle, the collected light becomes the contribution of the guided light in both directions. That is, the light which is guided from one end of the pump stripe directly toward the sample edge where the detector is located, added to the light guided in the opposite direction and reflected back by the sample edge into the stripe region and become amplified. At this condition, two guided light intensities are added together and cause an increase in intensity of the collected light. As the stripe advances further from the middle of the sample toward the opposite direction of the collection edge, the intensity will decrease as the propagation distance becomes long with respect to the collection edge for lights guided in both directions. To avoid entering into all these complexities, in order to have an estimation of the waveguide loss coefficient, the first experimental points were fitted by an exponential function. These points correspond to short distances of the pump stripe from the collection edge and far from the opposite sample edge. In this way, the light reflected from the opposite edge is rather weak or negligible considering the length of the sample. The exponential fit resulted in waveguide loss coefficient of ~ 9 cm^{-1}.

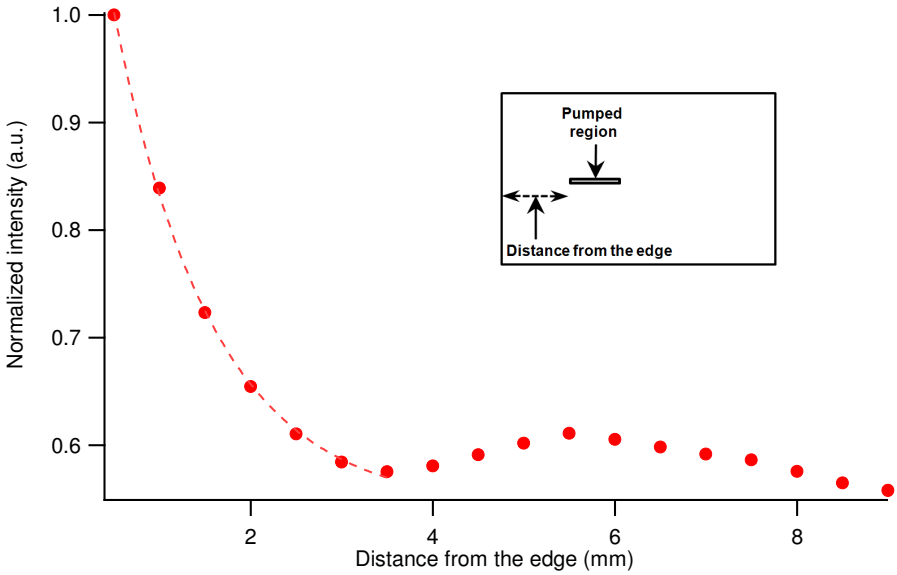

Figure 2.15 – Loss measurement in neat film of "fvin" via variable stripe displacement method. The dashed line is an exponential fit to the experimental data.

For sake of comparison, the same method was also applied for loss measurement in DCM-doped PMMA film (Figure 2.16). Given the above explanation and the complexities

encountered following the displacement of the pump stripe over long distances, in this case, the pump stripe was displaced from the sample edge for 3 mm. In this way, a loss coefficient of ~ 11 cm^{-1} was measured by a simple exponential fit.
The above-measured loss coefficients are comparable to some of the reported values in the literature which are determined by this technique [106, 107] .

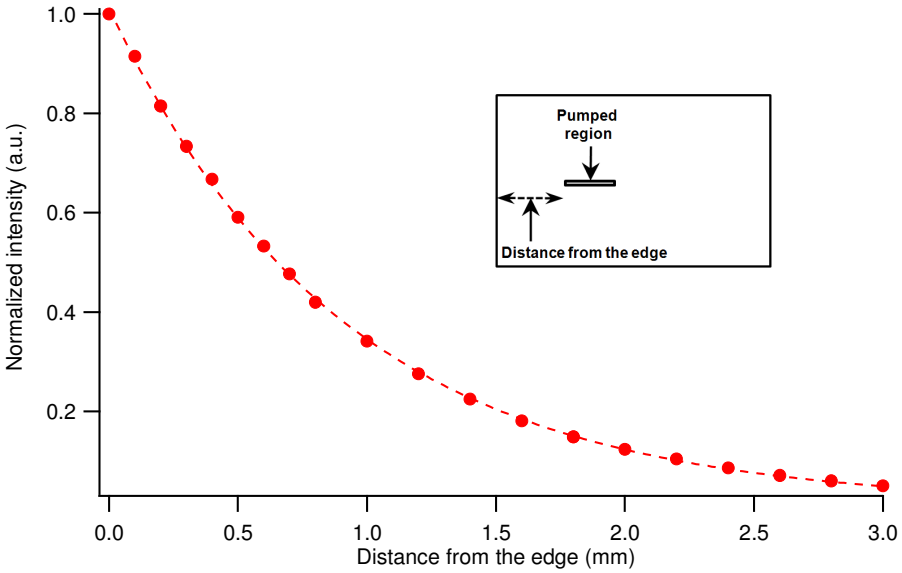

Figure 2.16 - Loss measurement in neat film of DCM-doped PMMA film via variable stripe displacement method. The dashed line is an exponential fit to the experimental data.

The stripe displacement method for waveguide loss measurements is a widely-used technique, employed by several people working on gain measurement and materials optical characterization. However, the loss coefficients measured by this technique are very approximate values and precautions must be taken when using these quantities. In fact, several factors are responsible for considerable uncertainty of this method. The first problem is the diameter of the detector surface that must be larger than the pump stripe diameter to collect all the edge-emitted light. This puts a limit on the diameter of the pump stripe. However, this was not a limiting factor in our case since the pump stripe diameter was 320 μm and the diameter of the fiber spectrometer, used for this measurement (Ocean Optics USB 2000), was 600 μm . The second problem is the very diffractive sample edge due to amorphous nature of the organic materials even after sample cleavage. As the pump stripe moves away from the sample edge, the solid angle becomes wider and thus the fraction of the edge-scattered light, seen by the detector, is varying for each

distance. This fact is schematically represented in Figure 2.17.

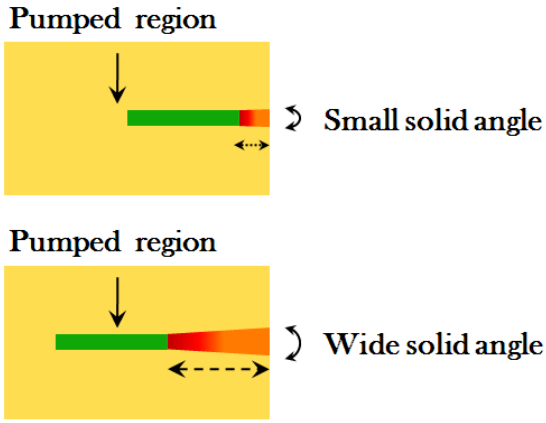

Figure 2.17 – (top) the pump stripe is close to the sample edge and thus, the solid angle is small. (bottom) the solid angle becomes wider as the pump stripe moves away from the sample edge.

Given the above limitations, depending on how the detector is positioned at the sample edge, the edge emitted intensity would be different from one measure to the other, leading to different loss coefficients for a given waveguide structure. Therefore, we investigated for an alternative method of loss measurement that can be repeatable, further reliable and avoid the above-mentioned difficulties. Very recently we found out the proper solution to determine the loss coefficient is to image the guided light, scattered from the film surface. As the light propagates along the pump stripe inside the medium, the intensity of the guided light will decay exponentially from the end of the pump stripe. Therefore, if the guided light intensity profile is imaged and fitted by an exponential, it can determine the waveguide loss coefficient in a precise manner. In this way, the problems related to the light collection method can be resolved and the loss measurement will be further reliable and repeatable. Later on, we found out that this technique is already described in very few reports [108, 109].

We examined the proposed technique of the waveguide loss measurement on a 6-μm-thick film of PMMA doped with the classical Rhodamine 640 laser dye(doping rate: 1% of the total solid matrix weight) spin coated onto the silica substrate.

The image of the guided light along the pump stripe and the corresponding intensity profile are shown in the following figures.

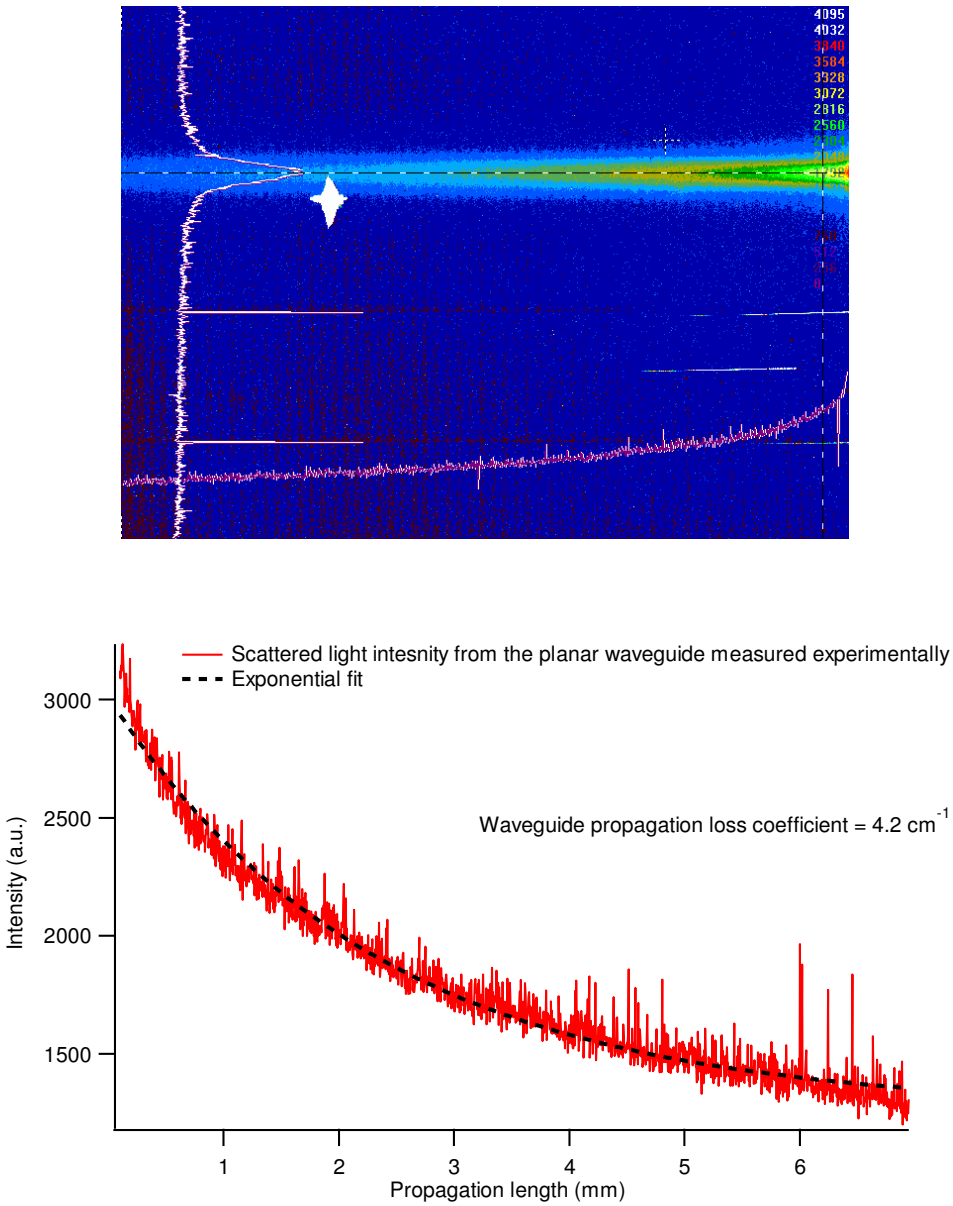

Figure 2.18 - (top) image of the guided light along the pump stripe obtained by Spiricon camera. (bottom) the intensity profile of the guide light. The dashed line is an exponential fit to the experimental data. The white zone in the image corresponds to the damaged pixels of the camera.

On this basis, a waveguide loss coefficient of 4.2 cm^{-1} was measured. Although, in this measurement the realized waveguide was based on a layer of different thickness and different dye in comparison with the preliminary measurements ("fvin "neat film and DCM-doped PMMA film), but at least it showed us a simple, powerful and reliable technique for further loss coefficient determination with the big advantage of measurement repeatability.

Quantification of the waveguide loss coefficient let us to know what is the potential material gain value. The material gain is the net modal gain added to the waveguide loss coefficient. On this basis, by using the measured net modal gain values and the waveguide loss coefficients (9 cm^{-1} and 11 cm^{-1} for "fvin" neat film and DCM-doped PMMA film), an approximate material gain can be obtained, given the uncertainty of the loss coefficients determined by pump displacement method.

Plotting the material gain as a function of the incident pump fluence evidenced a linear relation beween the three experimental points in both cases of "fvin" and DCM-doped PMMA film (Figure 2.19 and Figure 2.20, respectively). These results are in agreement with theory as the local gain is given by $\sigma_{em(0,v)}\Delta N$ and ΔN is linearly proportional to the pump intensity at the condition far from the saturation regime.

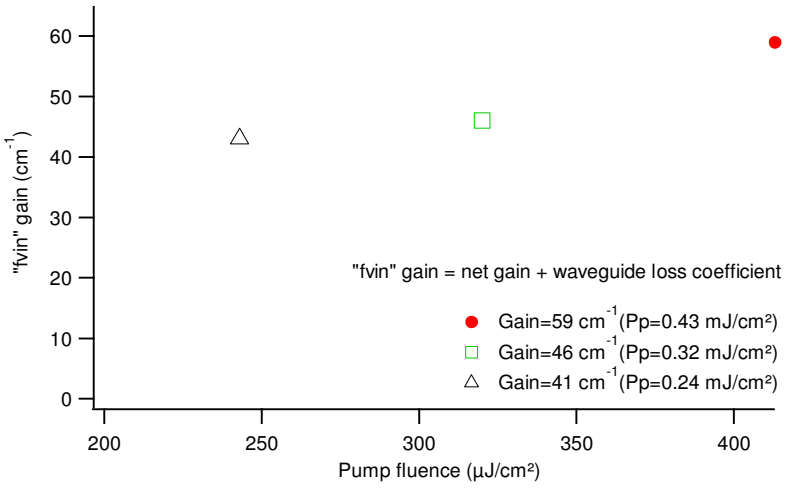

Figure 2.19 - "fvin" gain as a function of three different pump fluences

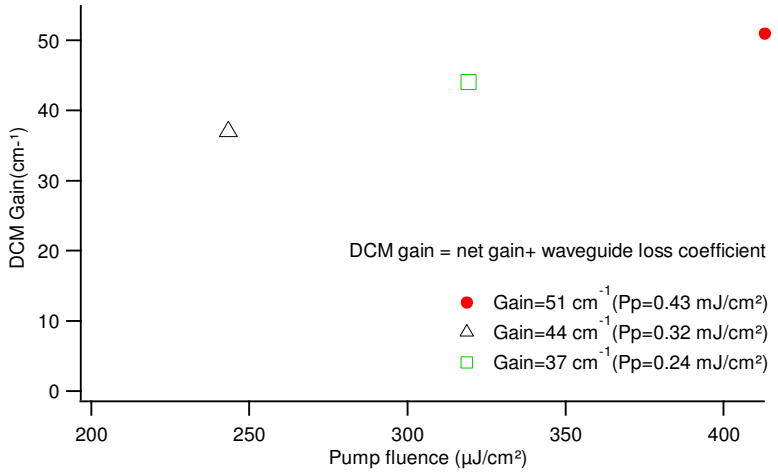

Figure 2.20 - "DCM" gain as a function of three different pump fluences

2.4.6 Photostability

One of the very interesting issues concerning the organic laser dyes is their stability upon optical excitation. For this purpose, we have studied the stability of the "fvin" compound in neat film configuration and we compared the result with the emission lifetime in DCM-doped PMMA film at the same experimental condition (Figure 2.21). The experiment was carried out at an incident pump fluence of ~ 0.4 $mJ.cm^{-2}$ and 10 Hz repetition rate.

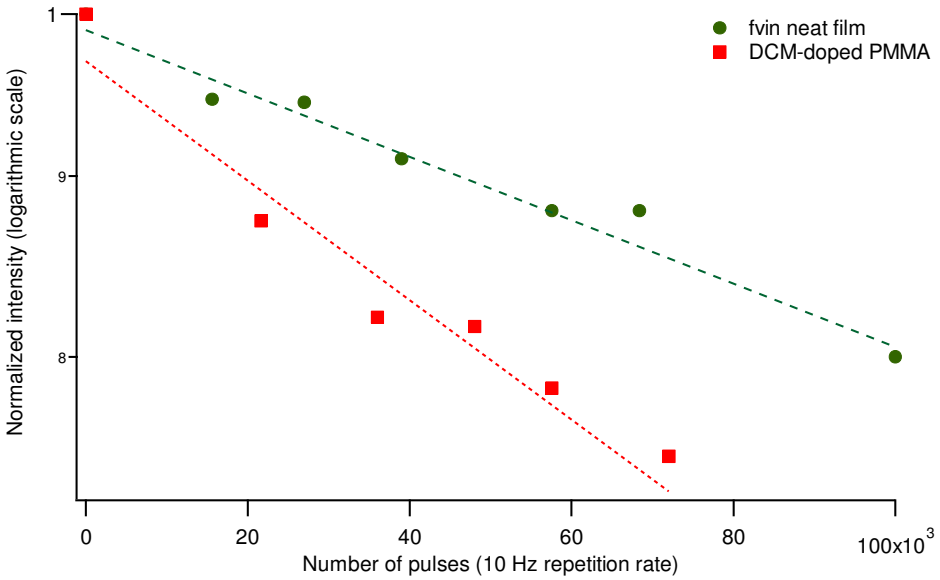

Figure 2.21 – Photostability of "fvin" neat film in comparison to DCM-doped PMMA film.

As one can see in the above graph, higher stability obtained for "fvin" neat film in comparison to DCM-doped PMMA film at the same experimental condition. In case of "fvin", it took around 100000 pulses for the emission intensity to drop to 80% of its initial value. For DCM-doped PMMA film, this happened after around 60000 pulses.
Considering that one of the possible reasons of photodegradation is the thermal effects and the fact that "fvin" neat film absorbs 80% of the pump beam against 13% in case of DCM-doped PMMA, one may conclude good stability of "fvin" molecules against heat problems (The higher the absorption amount, the more the generated heat).

2.4.7 Incorporation of the studied material into one-dimensional resonant structure

Once the existence of gain was proven in the "fvin" compound, we were interested to examine its lasing potential in a simple resonant structure. At the end, the lasing result is compared to the lasing obtained from DCM-doped PMMA film. For this purpose, within the already realized slab geometries, introduction of the in-plane optical feedback seemed to be a very promising technique. It has been shown by Kogelnik and Shank that the optical feedback in a waveguide can be achieved through spatial modulation of the refractive index (or the optical gain) of the active medium [110]. Based on this concept, two kinds of laser structures are distinguishable; DFB and DBR standing for distributed feedback and distributed Bragg reflector respectively. So far, there have been several reports of such devices using the organic materials as the gain medium [25, 111-116] . In the following, the working principles of such devices are briefed.

- **Distributed feedback lasers (DFB)**

A schematic representation of this kind of laser is sketched in Figure 2.22. In this case, the pump beam is incident normal to the surface of the corrugation pattern created within the amplifying medium. Spatial periodic modulation introduces scattering to the guided waves in the slab waveguide. Optical feedback is the result of coupling between the guided modes and the constructively interfered back-scattered waves traveling in the opposite direction along the optical path. The constructive interference is achieved if the Bragg condition is fulfilled:

$$m\lambda_{Bragg} = 2n_{eff}\Lambda \qquad (2.17)$$

where n_{eff} is the effective refraction index of the waveguide, Λ is the corrugation period , m is the feedback order and λ_{Bragg} is the Bragg wavelength at which the lasing occurs. Lasing happens where the coupling between the two counterpropagating waves is the strongest. A comprehensive theoretical study of the DFB geometry would require the implication of coupled-wave theory [110].

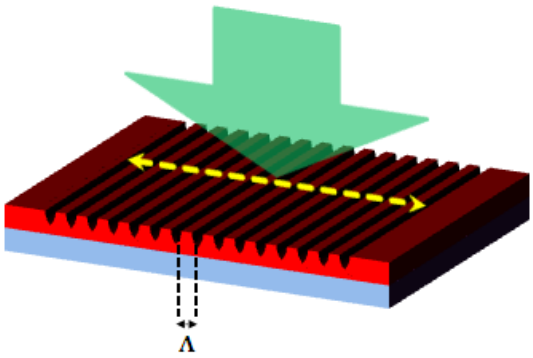

Figure 2.22 – Distributed feedback (DFB) laser structure

- **Distributed Bragg reflector lasers (DBR)**

Distributed Bragg reflector (DBR) lasers are class of devices using a similar principle as the DFB lasers based on Bragg scattering concept. In these devices, the pump is normal incident on the surface of the "uncorrugated" gain medium extended between two in-plane distributed Bragg gratings at its two ends providing the necessary optical feedback (Figure 2.23). Again, the resonance frequency is achieved upon fulfillment of the Bragg condition. DBR lasers might be advantageous relative to DFB devices in such a way that lower lasing threshold can be achieved due to reduced level of losses [117]. These losses are ascribed to the incoherent scattering due to surface non-uniformity of the organic gain medium following the fabrication process and/or the imperfect corrugation pattern [69]. On this basis, in our case the lasing was carried out in DBR geometry. For this mean, two similar corrugation patterns facing each other were created by optical contact interferometry technique described in the following.

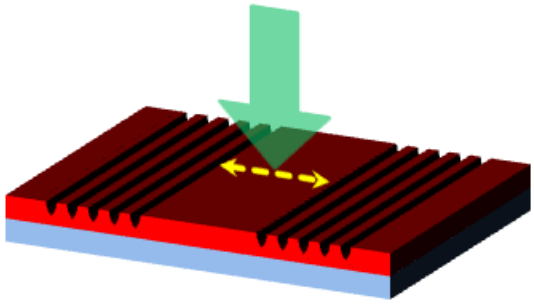

Figure 2.23 - Distributed Bragg reflector (DBR) laser structure

2.4.7.1 Simple realization of Bragg grating through optical contact interferometry technique

Optical contact interferometry technique [118] using a phase mask (pitch=1090 nm) and UV laser beam was applied to create surface relief patterns on a uniform 2.5-μm -thick film of PMMA deposited onto the glass substrate via spin coating above which a 695-nm-thick layer of "fvin" was evaporated. This strategy was taken since direct illumination of "fvin" molecules with highly energetic UV photons could damage the dye molecules with the consequence of hindering the lasing effect. However, in the case of spin-coated DCM-doped PMMA film the gratings were directly engraved within the PMMA film containing the DCM dye.

An Excimer laser (λ=193 nm, energy per pulse = 300 μJ, repetition rate of 10 Hz, Neweks Ltd., PSX-100) was incident normal to the phase mask above which an ultrathin protective film of quartz (thickness on the order of 80 microns) was placed between the coated surface and the phase mask to avoid fall down of the ablated material residues on the phase mask during surface patterning. The schematic representation of the experimental setup is depicted in Figure 2.24. The scheme shows that the ultraviolet light passes through and is diffracted by the periodic corrugation of the phase mask. The number of diffracted orders can be calculated based on the following relation:

$$0 \le \mathrm{Sin}(\theta_m) = \frac{m\lambda}{\Lambda_{\text{Phase mask}}} \le 1 \qquad (2.18)$$

where m is the diffraction order, θ_m is the diffracted beam angle with respect to the grating pane normal, λ is the incident wavelength onto the phase mask (here, $\lambda = 193$ nm), and $\Lambda_{\text{Phase mask}}$ is the phase mask pitch (here, $\Lambda_{\text{Phase mask}}$=1090 nm). On this basis, 5 diffraction orders are recognizable. However, high diffraction orders have a rather weak intensity within the interference zone and thus, have less contribution in creation of the pattern. Therefore, we can say the diffracted light is "mostly" contained in the 0, +1 and -1 diffraction orders. In this case, the fabricated grating pitch was almost equal to the phase mask grating period (1090 nm).

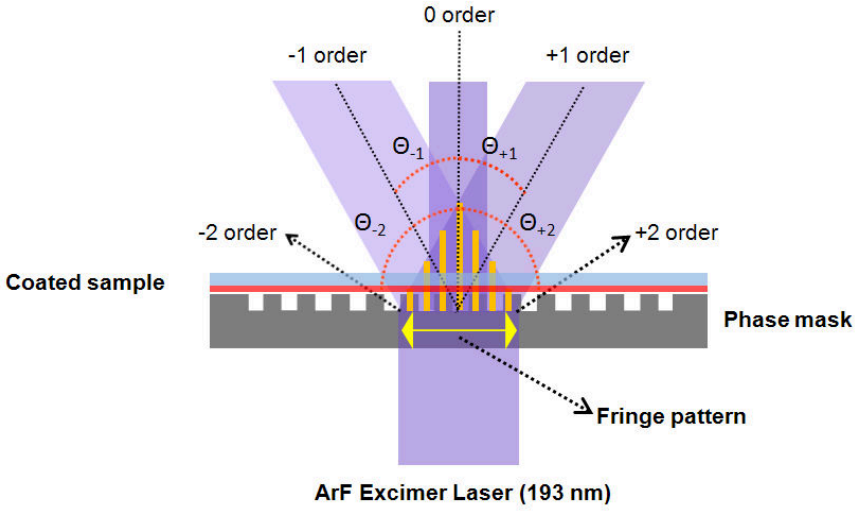

Figure 2.24 – Optical contact interferometry setup. In our experiments, the number of diffraction orders was 5. In the above figure, the 0, 1st and the 2nd diffractions orders are demonstrated.

As just described, the optical contact interferometry technique is based on direct material ablation by using a laser source generating energetic UV photons. What makes this technique to be very interesting is the simplicity of the procedure in comparison to other methods such as lithography in clean room lithography process.

2.4.7.2 Realized grating characterization

The created corrugation pattern was characterized using an Atomic Force Microscope (AFM). Figure 2.25 and Figure 2.26 are showing the AFM images of the used phase mask and the grating pattern created on PMMA-coated glass substrate with the periodicity extended over few millimeters, respectively. The grating structure appeared to be smooth, free of ablation debris and groove defects. The incident energy and the exposure time used to create such a pattern and its characteristic features are briefed in the following table. The structured layer was then used to thermally evaporate a film of "fvin". Further investigation revealed that the evaporated film had followed the surface pattern on the regions that the gratings were present.

Incident energy	0.42 mJ
Exposure time	80 sec.
Grating period	~ 1090 nm
Modulation depth	~ 200 nm

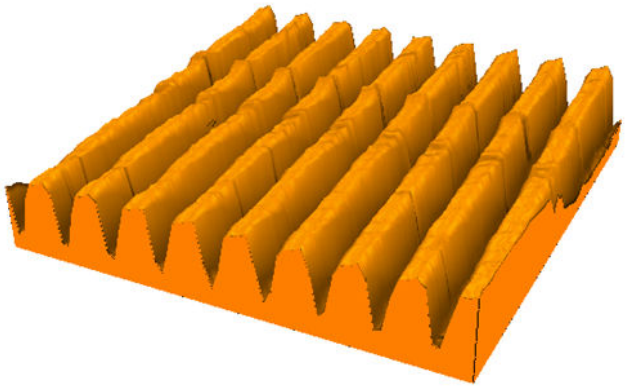

Figure 2.25 – AFM image of the used phase mask in our experiment.

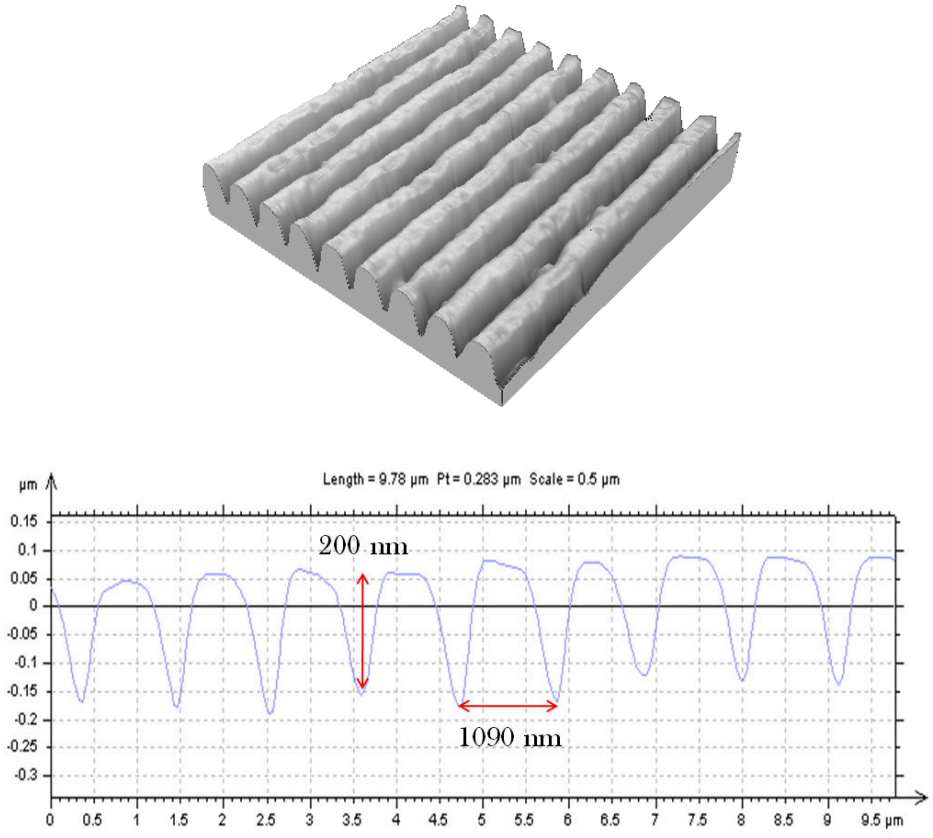

Figure 2.26 – (top) AFM image and (bottom) the corresponding profile of the created pattern on 2.5-µm-thick film of PMMA. This pattern was used for evaporation of the "fvin" layer.

2.4.7.3 Laser performance

The evolution of the laser intensity with pump power in neat film of "fvin" followed by the corresponding laser emission spectrum superimposed with the ASE and fluorescence spectra are shown in the following graphs (Figure 2.27 and 2.28). The VSL experimental setup was used to pump the samples with a stripe length of ~ 2 mm limited between two realized gratings in DBR geometry. Laser emission wavelength is governed by the grating pitch (~ 1090 nm) and the effective refractive index (n_{eff}). On this basis, the laser emission peak was measured to be at 647 nm. Using this information and considering the evaporated "fvin" neat film thickness of 695 nm, the effective refractive index for different waveguide-supported TE modes can be precisely determined from the dispersion curves. However, it should be noted that in the present case the dispersion curves were recalculated by taking into account that the substrate is now a 2.5-µm-thick layer of PMMA ($n \approx 1.49$), onto which the "fvin" film ($n \approx 1.85$) was evaporated. Then by entering the experimentally-measured laser emission wavelength (647 nm) into the equation (2.17), we looked for the integer number corresponding to the Bragg order (m). The result is detailed in the following table.

	n_{eff}	m
TE_0	1.83	6.16
TE_1	1.80	6.06
TE_2	1.73	5.82
TE_3	1.65	5.55
TE_4	1.54	5.18

Based on the above table, as m has to be an integer, the condition seems to be satisfied for propagation of TE_1 mode seeing the effective refractive index of 1.80. This corresponds to a Bragg order of m=6. The very small fraction of 0.06 seen in the calculated m value is considered to be due to measurement uncertainties concerning the realized grating pitch via material ablation and also the "fvin" refractive index value, determined by ellipsometry technique.

By taking into account 84% absorption amount of the pump beam by the "fvin" film, then a lasing threshold of 60 $\mu J.cm^{-2}$ (absorbed pump fluence) is deducible from the input-output characteristic curve.

➢ Lasing in “fvin” neat film

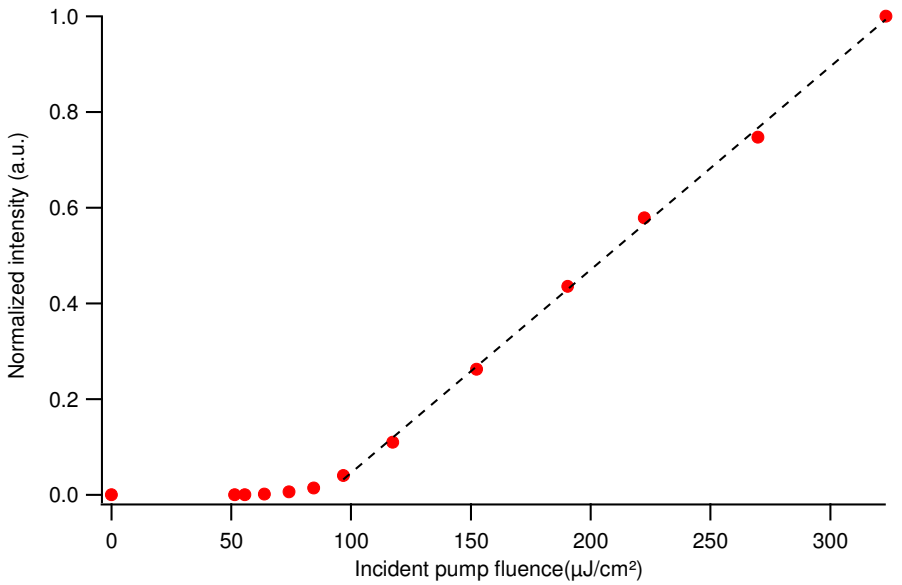

Figure 2.27 – “fvin” laser emission input-output characteristic curve in neat film configuration

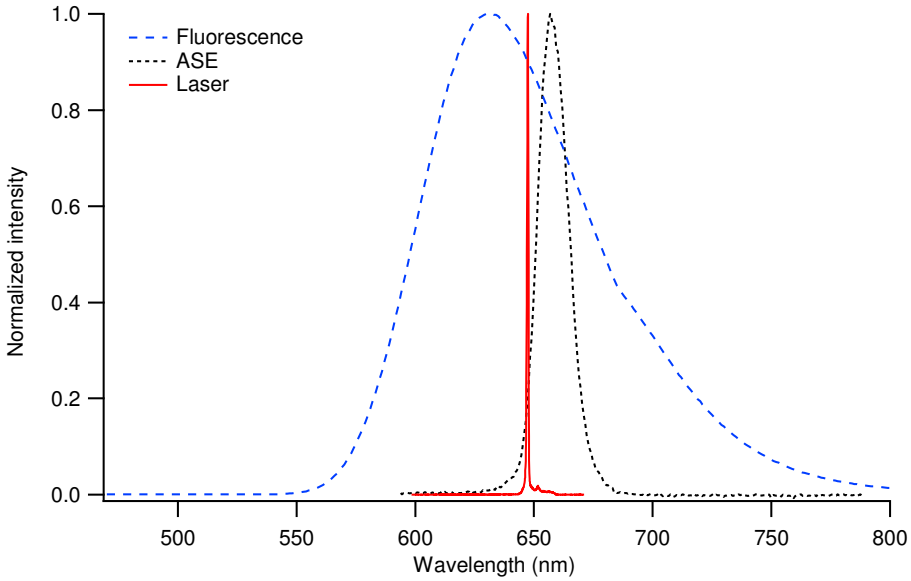

Figure 2.28 – Superimposed spectra of fluorescence, ASE and laser emission in “fvin” neat film

The obtained results for lasing in neat film of "fvin" are compared in the following with the lasing operation in DCM-doped PMMA film (Figure 2.29 and 2.30).

- Lasing in DCM-doped PMMA film

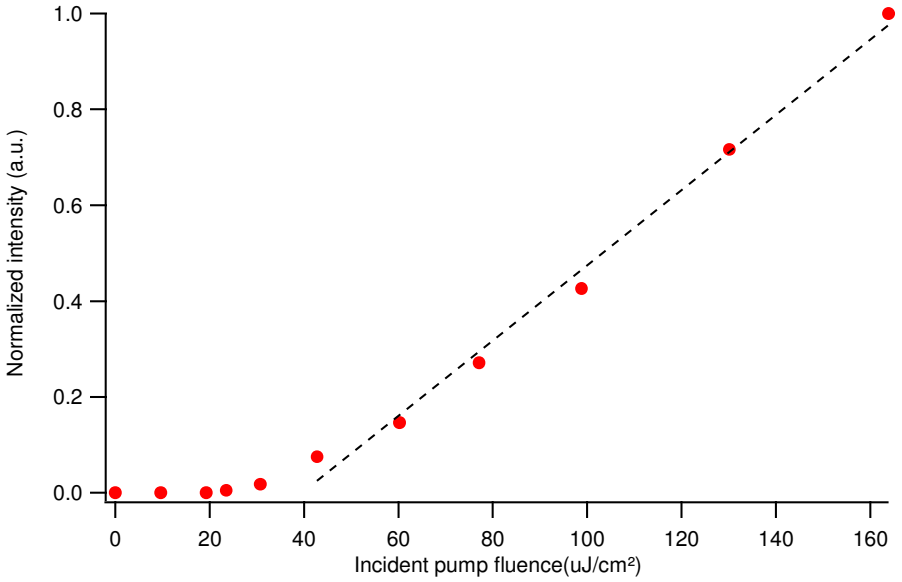

Figure 2.29 - Laser emission characteristic curve of DCM-doped PMMA film

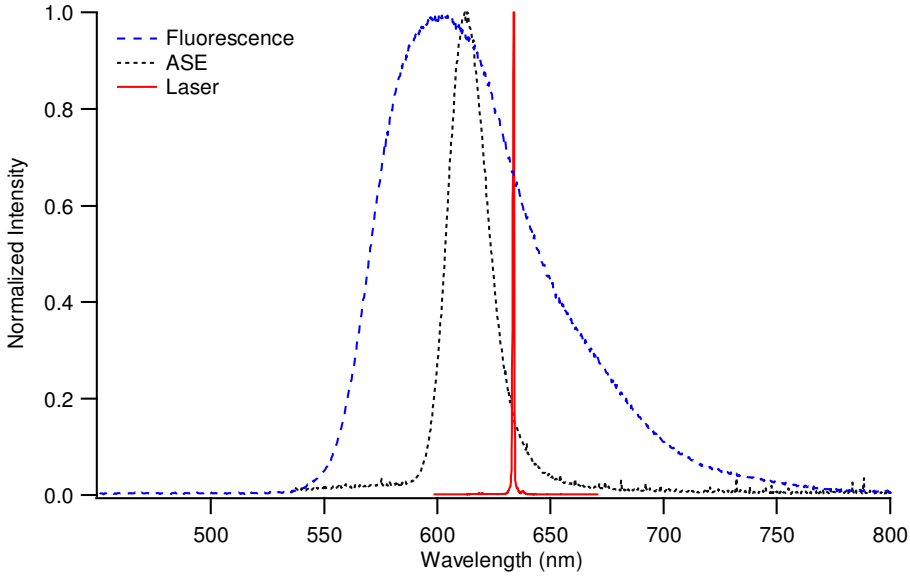

Figure 2.30 - Superimposed spectra of fluorescence, ASE and laser emission in DCM-doped PMMA film

In this case the laser peak observed at ~ 630 nm. Considering a refractive index of ~ 1.52 for the dye doped-PMMA (see appendix 2), then this lasing wavelength corresponds to m=5 diffraction order. For the lasing threshold in this case, if we consider the 13% absorption amount by DCM-doped PMMA film, then a lasing threshold as low as 6 $\mu J.cm^{-2}$ (absorbed pump fluence) can be deduced from the corresponding input-output characteristic curve.

The lasing thresholds obtained in both cases are comparable to several works reporting on the same laser geometry [26, 117]. However, we are not challenging the result of the above lasing experiments with some other works having similar operating principles but with nJ-order lasing thresholds [119]. The reason is because we are not using the optimized phase mask in our case and thus, the resonance condition is achieved under high diffraction orders that have led to rather elevated lasing thresholds.

Another discussable point is the anomalous ASE red shift in comparison to the fluorescence peak in both cases. As just mentioned, the lasing wavelength is defined by the grating pitch and the diffraction order. However, the ASE peak should correspond to the maximum of the gain curve (the fluorescence emission peak). This red shift in case of DCM-doped film can be explained by the overlap between the absorption and emission curves. In this case, due to reabsorption losses, it might be normal that ASE peak appears at longer wavelengths in comparison to the fluorescence emission peak were the absorption becomes negligible. However, in case of "fvin", the reabsorption losses are considerably reduced due to large stokes shift as it can be seen in Figure 2.6. Therefore, this may not be reason in this case. The "fvin" ASE peak shift has not been completely understood so far.

2.4.8 Random lasing observation in neat film of "fvin"

During the gain studies in neat films of "fvin", we observed that under high excitation pump fluences there were positions on the sample for which the amplified spontaneous emission spectrum was highly structured with sharp spikes having the spectral width of 1 nm, limited by the spectrometer resolution. The narrow peaks showed to be stable over time for a given excited region of the sample (Figure 2.31). In addition, we noticed a threshold-like behavior for the appearance of these peaks. This fact can be clearly seen in the typical superimposed spectra presented in Figure 2.32 where for the incident pump fluence below 0.3 mJ/cm^2 no spike is appeared. Similar effects were also noticed for DCM-doped PMMA film. Following the above observations, these narrow peaks are believed to be due to what is referred to as random lasing effect.

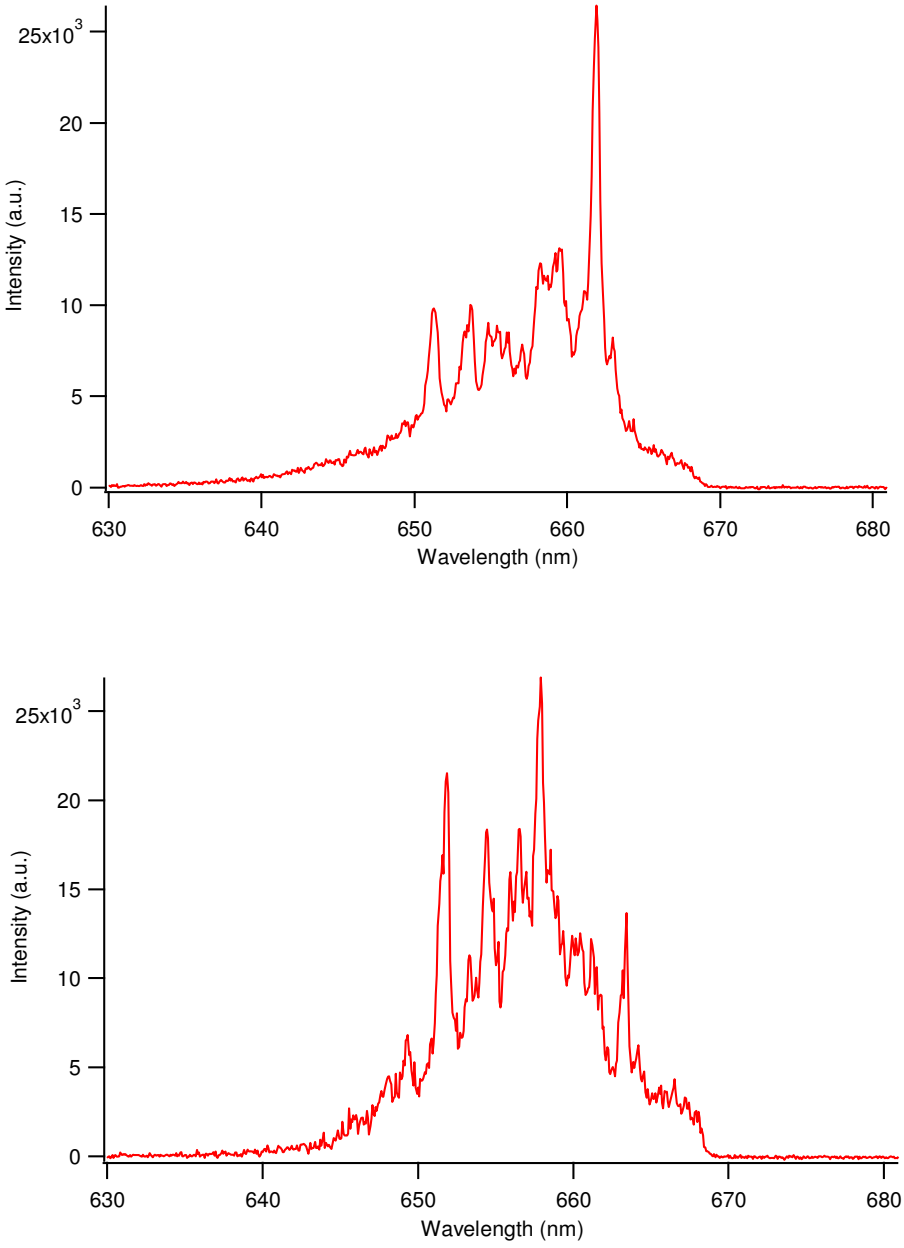

Figure 2.31 –Typical emission spectra of random lasing effect in neat film of "fvin". The spectra correspond to two different positions of the pump stripe on the sample. The pump fluence was ~ 1 $mJ.cm^{-2}$ and the stripe dimension was around 100 μm × 3 mm.

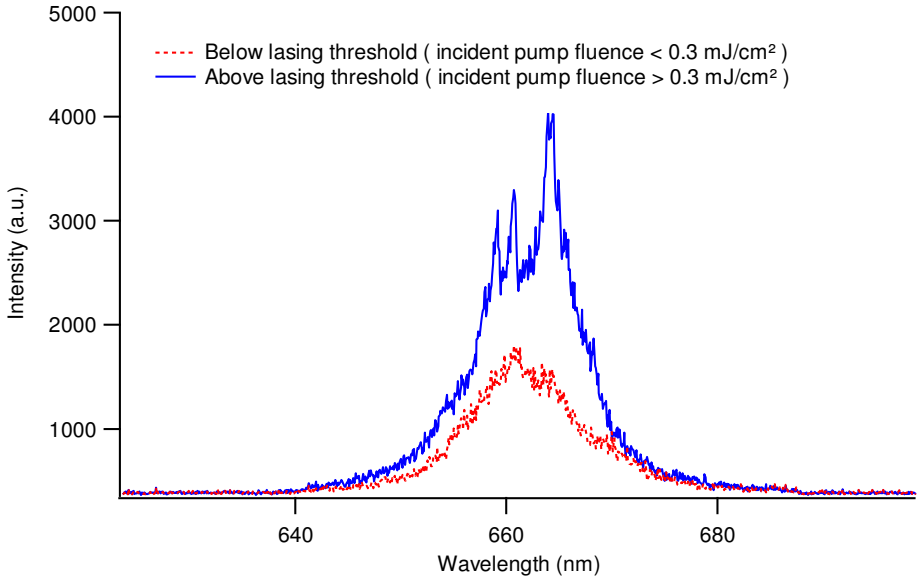

Figure 2.32 – Demonstration of threshold-like behavior of random lasing effect in neat film of "fvin"

Random lasing is a term used for a class of "mirror-less" lasers whose optical feedback is provided through multiple scattering in disordered media that has gain. These media include neodymium powders [120], dyes and polymers mixed with scatterers in films and solutions [121, 122], films of π-conjugated polymers [123], semiconducting powders [124, 125] and synthetic opals infiltrated by π-conjugated polymers and dyes [126, 127]. Unlike conventional lasers where a cavity determines the modes of a laser, in such systems, the spontaneously emitted photons undergo a random walk between several scatterers dispersed in the gain medium. During this propagation, the light is amplified through stimulated emission and may reach the lasing threshold. The resulting laser emission is omnidirectional (Figure 2.33). These lasers are expected to be used in applications such as coding of clothing [128], detection of dangerous materials [44] and distinguishing healthy tissues from cancerous ones [129].

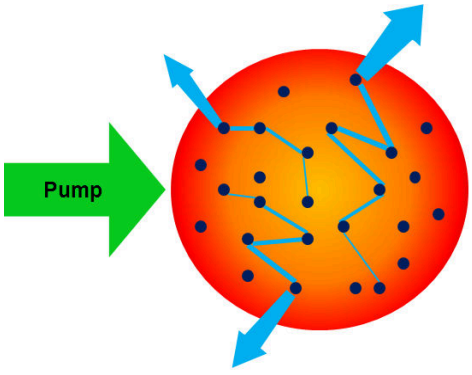

Figure 2.33 - Demonstration of random lasing effect. The dark spots are the scattering centers in the gain medium.

Random lasing effect within the organic media, in the absence of intentionally introduced scatterers such as ZnO and TiO_2 particles into the medium, is related to some morphological defects such as thickness fluctuations [123], nanopores on the film surface [130].

To elucidate the feedback origin in thermally-evaporated neat films of "fvin", the film morphology was studied over a surface of 50 µm by 50 µm by an AFM. The result of the scan, shown in Figure 2.34, revealed an average surface roughness of 5 nm over 700 nm film thickness but with occasional defects having amplitudes of up to 50 nm which might be due to dust or surface imperfections. Therefore, we have speculated that the source of feedback in our case might be due to surface defects.

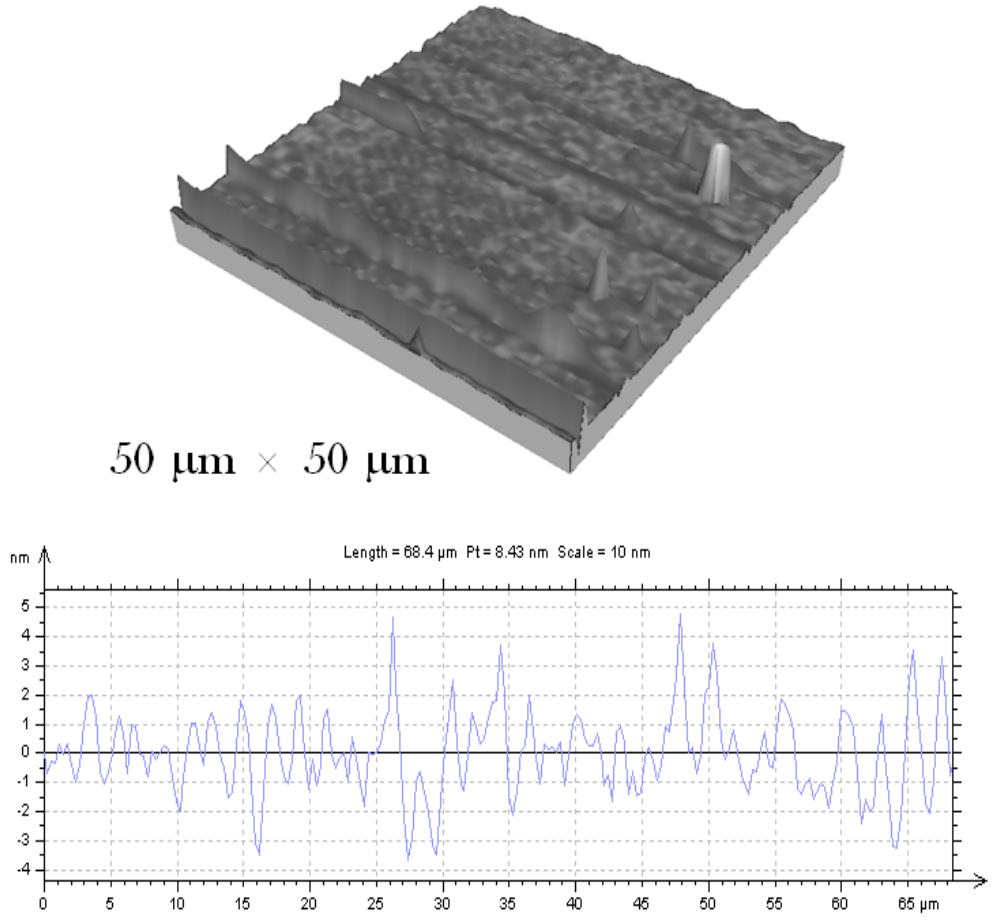

Figure 2.34 - (Top) AFM image of the "fvin" film. (bottom) corresponding surface profile of the scanned region. The surface roughness is ~ 5 nm with occasional defects having amplitudes up to 50 nm.

2.5 Chapter conclusion

In conclusion, we have shown that concentration quenching, a problem associated to most of the organic dyes, was considerably reduced in the novel deep-red emitting "fvin" compound due to its special molecular geometry. This demonstration was carried out by employing the widely-used variable stripe length (VSL) method to measure the material gain. On this basis, for about 600-nm-thick neat evaporated film of "fvin", net modal gain value of 50 cm^{-1} was measured for an incident pump fluence of 0.41 $mJ.cm^{-2}$. This result was compared with the gain value obtained from DCM-doped PMMA film (doping rate: 5% of the total solid matrix weight) of around 620-nm-thick which resulted in net modal gain of 40 cm^{-1} for the same pump fluence and at the same experimental conditions. Given the considerably reduced quenching in "fvin" neat film and thanks to the high absorption amount that can be achieved in this way (84% at 532 nm in 600-nm-thick film in comparison to 13% in DCM-doped PMMA film of almost the same thickness), very low threshold optically-pumped devices can be potentially fabricated. Furthermore, since the "fvin" molecule is a π-conjugated small molecule, it can be also a very promising candidate toward potential future electrical excitation.

The waveguide losses were determined through stripe displacement technique, using the VSL experimental setup. On this basis, loss coefficients of 9 cm^{-1} and 11 cm^{-1} were measured in neat film of "fvin" and DCM-doped PMMA film, respectively. Due to measurement problems related to this loss measurement technique, an alternative loss coefficient determination method was described.

At the end, lasing operation was demonstrated in "fvin" neat film by using a simple DBR geometry, created by optical contact interferometry technique. The result was compared with lasing in DCM-doped PMMA film in DBR geometry fabricated by the same method. Since the phase mask at disposal was not adapted to achieve lasing under the first order Bragg condition, therefore, lasing was observed for higher Bragg orders (m=6 and m=5 in "fvin" and DCM-doped PMMA film, respectively). This fact led to rather elevated lasing thresholds (60 $\mu J.cm^{-2}$ in "fvin" neat film vs. 6 $\mu J.cm^{-2}$ in DCM-doped PMMA, based on absorbed pump fluence) in comparison to lasing thresholds in devices with the same working principles. Therefore, one can conclude that by taking advantage of the "fvin" high gain together with the great possibility of having lasing in neat film due to reduced

quenching, single-mode waveguides are possible and very low lasing thresholds can be achieved through an optimized grating.

During the ASE studies in "fvin" neat film and DCM-doped PMMA film, highly structured ASE peaks with narrow spikes were observed under high excitation densities (~ 1 $mJ.cm^{-2}$). Further studies revealed that these peaks were related to random lasing effect. This effect was understood to be due to some morphological defects within the film thickness or at the surface, revealed by the AFM studies.

3 Design of a compact tunable organic solid-state laser structure

3.1 Introduction: state of the art of existing organic laser architectures

In chapter one, the existing challenges and the corresponding possible strategies that can be adopted for lowering the lasing threshold toward development of the electrically-pumped organic diode laser were discussed. Meanwhile, this goal has not become a reality yet, realization of compact and performant laser sources having "good efficiency" together with "high beam quality" fabricated via "fast" and "inexpensive" techniques is of great importance for practical applications and has been somewhat bypassed or unfortunately has got little attention so far. Furthermore, if such a device turns out to be wavelength tunable within the emission spectrum of a given organic material and/or be capable of generating wavelengths in a range not directly or easily accessible with the current organic materials (for example in the UV and infrared part of the spectrum where the organics are not good emitters), then perhaps the effort put in this way will be worthwhile to be considerably valued.

On this regard, in the following, we have performed a comparative study of the already existing optically-pumped organic solid-state laser architectures (irrespective of the exploited organic material, semiconductor or not) with advantages and negative points associated with each kind. At the end of this discussion we will be able to define the adapted geometry with which we can eventually fulfill the above mentioned goals.

To proceed in our study, we have distinguished the current geometries for organic solid-state lasers into two major categories:

First group are devices based on **thin films of organic materials**; Fabry – Perot waveguides, diffractive resonators (Distributed feedback (DFB) and Distributed Bragg (DBR)), vertical microcavities, microlasers (microdisks and microrings) are falling within this category. In all

these devices either the gain medium with the system providing the optical feedback are somehow integrated and embedded within each other or in case of microcavities they are in direct contact together.

Second group are the **external resonator devices** where the gain medium and the resonator are considerably separated from each other in comparison with the previous rank.

The first distinction between the two categories can be already made here by noticing the fact that in devices of the second group, the external cavity can potentially enable the insertion of optical elements inside the cavity for further purposes such as frequency doubling via a nonlinear crystal, wavelength tuning, etc.

3.1.1 Thin-film-based devices

3.1.1.1 Fabry-Perot Waveguide

We start our discussion by characterization of perhaps the simplest possible geometry that can be imagined for the organic solid-state lasers, that is the Fabry-Perot waveguide (Figure 3.1). In this geometry the light is confined and guided inside a medium sandwiched between two up and down claddings having lower refractive indices than the medium. If the gain medium possesses a high refractive index (n) compared to the surrounding medium (generally, air with n=1), then the medium reflectivity at the edges, given by $\left((n-1)/(n+1)\right)^2$, will be high enough to partially reflect the guided light back into the medium and shape a mirrorless laser. This technique is widely used in technology of the inorganic semiconductor laser diodes thanks to the high refractive index of these materials ($n \sim 2$ - 4) together with crystalline structure of the inorganic material which allows obtaining smooth facets upon cleavage with reflectivities as high as 30%. In organic materials, however, polishing the facets to optical quality seems a kind of difficult due to the amorphous nature of these materials. Furthermore, because of the lower refractive index of organics in comparison to inorganic materials, the reflectivity is limited to a few

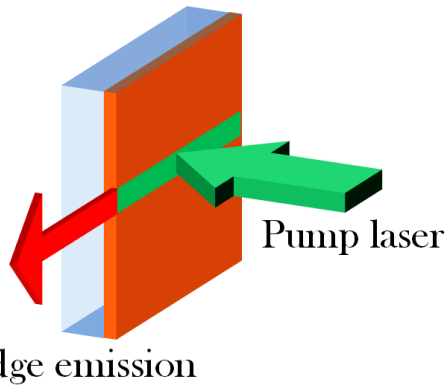

Figure 3.1 - Fabry-Perot waveguide where the light is guided and then emitted from the edge of the sample upon excitation by a pump stripe.

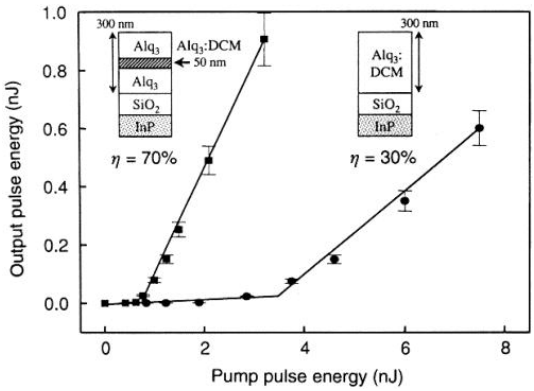

Figure 3.2 - Schematic representation of the waveguide structures realized by Kozlov et al [84]. together with the corresponding input-output characteristic curves.

percents. Despite all these difficulties, Kozlov et al. [84] reported on a Fabry-Perot laser structure (Figure 3.2) based on a vacuum-deposited film of $Alq_3:DCM$ (n = 1.7) with end facet mirror reflectivities of 7% obtained naturally during evaporation process. In that experiment high-level losses imposed by low mirror reflectivities were compensated by choosing a rather long (~ 1 mm) Fabry-Perot waveguide. In such a structure, a quantum slope efficiency[9] of 30% was obtained that could be improved to the highest value of 70% with considerably reduced lasing threshold of $1\,\mu J.cm^{-2}$ using a double-heterostructure device where a film of $Alq_3:DCM$ was sandwiched between two Alq_3 cladding layers (Figure 3.2). Despite excellent slope efficiency, the output energy was less than a nJ per pulse and the emission was suffering from low spatial quality with great divergence[10] due to sub-wavelength edge-emission aperture.

3.1.1.2 Diffractive resonators (DFB & DBR)

The second class of structures attributed to the family of thin film devices are the diffractive resonators. The devices on this basis fall into two categories of Distributed feedback (DFB) and Distributed Bragg (DBR) lasers (Figure 3.3). The working principles of such devices are already described in chapter 2 and as we saw the latter was demonstrated by using "fvin" neat film and DCM-doped PMMA film as the gain media. In such structures, light is also confined and guided within the plane of the film but the problems associated with low mirror reflectivities observed in the previous case are resolved to a great extent using an in-plane distribution of Bragg reflectors extended fully over the whole surface in case of DFB or partially at the two ends of the gain medium in case of DBR, assuring very high

[9] The quantum slope efficiency (η_q) is a criterion for laser performance assessment and is determined by measuring the slope of the laser input-output characteristic curve expressed in terms of photon numbers instead of energy. Expression of the slope efficiency in terms of energy is known as the energy slope efficiency (η_e) and is defined by $\eta_e = (h\nu_{laser}/h\nu_{pump})\eta_q$.

[10] The beam divergence angle θ in radians is expressed as $\theta \simeq \lambda/d$ (imposed by diffraction) where λ is the emission wavelength and d is the diameter of the confined beam by the waveguide.

reflectivities for a narrow band of wavelengths.

Generally, DFB fabrication is easier than DBR since only one continuous corrugation pattern is required. However, in organic-based devices, sometimes DBR might be advantageous over DFB structures due to a lower level of losses as a result of a shorter interaction length of the in-plane confined light with Bragg gratings. These losses are either because of out of plane diffraction induced by the grating and/or due to incoherent scatterings by defects, scratches or any high-spatial frequency modulation in the gain medium [69].

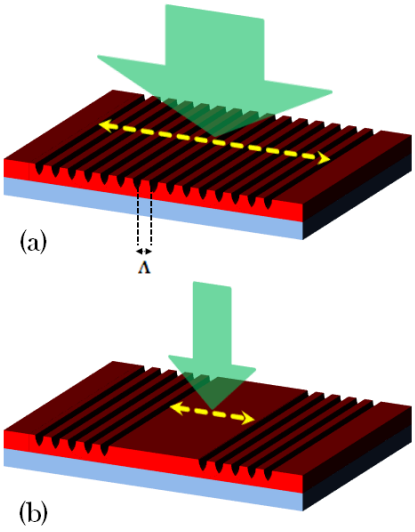

Figure 3.3 - a) Distributed feedback (DFB), (b) Distributed Bragg (DBR) laser structure.

The resonant mode for laser oscillation corresponds to the wavelength that satisfies the Bragg condition: $m\lambda_{Bragg} = 2n_{eff}\Lambda$ where Λ is the grating pitch, n_{eff} the effective refractive index of the guided mode and m is an integer, indicating the diffraction order. The Bragg scattering can be obtained by means of a periodic effective refractive index perturbation of the active material through either dynamic gain or static thickness modulation. The latter is achievable via common different techniques such as electron-beam lithography [131], replica molding [132], room-temperature imprinting [25] or direct laser interference ablation [63, 133], while in the former, periodic gain modulation is obtained through a technique called holographic dynamic grating [134]. For this purpose, an interference pattern is created on the sample surface without fabrication of any static corrugation pattern in contrary to the previous case. Depending on whether the optical feedback is provided in one or several directions within the plane of the film, one and two-dimensional DFB configurations are distinguishable respectively. In case of one-dimensional (1D) DFB, the lowest lasing threshold can be obtained if the grating pitch is designed in such a way to make the device operate under the first-order Bragg condition (m=1) since the out-coupling diffraction losses are the lowest in this case [135]. However, as 1D-DFB resonators provide optical confinement only in one direction perpendicular to the grating axis, the edge-emitted beam divergence in a plane normal to the grating grooves and along the grating axis is large [132, 136]. Moreover, an efficient extraction of light oscillating within the corrugation pattern is difficult mainly because of the highly reflective Bragg reflectors allowing small fraction of light to come out laterally as the laser beam. A solution to this problem can be the use of 1D-DFB structures functioning under higher order Bragg conditions, e.g. m=2. In this approach, the Bragg

condition imposes an emission normal to the corrugation surface resolving the problem encountered with the first-order Bragg grating. The strategy of using 1D-DFB operating under second-order grating is also attractive from the technical point of view since increasing the Bragg order by a factor of m means decreasing the spatial resolution of grating by the same factor and thus simplifying the fabrication process (i.e., through surface ablation technique). These advantages, however, are generally at the cost of increasing the lasing threshold due to a higher level of induced diffraction losses [135]. However, special cases also exist as we can see that in a clever approach, Karnutsch et al. [119] reported on a 1D-DFB structure treating both the lasing threshold and the beam extraction issues in a single device. The realized structure was based on mixed-order of first and second-order Bragg gratings where the strong in-plane feedback was provided by two first-order regions in both sides of a second-order grating for efficient vertical outcoupling. Using this technique, a lasing threshold as low as 45 pJ / pulse (36 $nJ.cm^{-2}$) was obtained. Apart from this exception, the common technique to have an out of plane emission normal to the surface corrugation while maintaining or even lowering the lasing threshold, is the employment of two-dimensional 2D-DFB structures. These devices can be either in the form of concentric circular grating [137, 138] where the optical feedback is omnidirectional within the plane of the film or in the shape of the more complicated, so-called two-dimensional photonic bandgap crystals [139, 140] with feedback in several directions (depending on the lattice type) in the plane of the film. In a particular case of square lattice, the feedback is applied in two orthogonal directions in the plane of the film. By exploiting these devices, Riechel et al. [88] reported on a 2D-DFB laser where the lasing threshold could be reduced by 30% in comparison with 1D device. In another work, Heliotis et al. [136] could achieve 20 times lower lasing threshold in 2D-DFB than in 1D-DFB. Generally, for polymer-based DFB lasers, reported thresholds are typically in the range of 1-10 $\mu J.cm^{-2}$ [141].

Traditionally, diffractive resonators are devices with discrete tunability upon modification of the grating period. Interesting examples of this kind are tunability ranges achieved via the use of segmented grating [85], that is, several DFB gratings on the same substrate separated by a small distance from each other. On this basis, Schneider et al. reported on a largest tuning range of 115.3 nm [142]. However, continuous wavelength tuning is also achieved via changing the grating pitch in devices with holographic dynamic grating [143], in a wedge-shape DFB structure [144] and very recently, in an elastically tunable device [145]. In all these devices the tunability was extended over few tens of nm.

Despite the wavelength tunability and all the extensive efforts for improving the lasing threshold along with finding an easy way to decouple the light from these structures; the

poor-defined spatial beam quality of all devices within this category still has remained a big issue. The far-field emission pattern of a 1D-DFB is reported as "fan-shaped" [136, 146] and the corresponding far-field pattern of a 2D-square-lattice photonic crystal is forming a cross shape following the orthogonal grating groove pattern [88]. The far-field emission of a concentric circular grating demonstrates doughnut-like profile which is due to cylindrical boundary conditions provided by circular grating [138]. On this issue, Turnbull et al. has quantified the quality of the laser beam emitted from a 2D-DFB and has reported a twice diffraction-limited beam (M^2=2.2) [65]. However, this appears to be among the minimum reported value for DFB lasers. The beam quality of such devices, despite very rare reports, seems to be much greater than this amount.

In addition, apart from beam quality issue, the diffractive resonators are not very efficient devices in terms of the energy slope efficiency. A proving signature of this claim is the very few reports characterizing these devices from this aspect. In none of the reports on DFB lasers the energy slope efficiency could exceed few percents [65, 116, 132, 136, 147].

3.1.1.3 Vertical microcavity

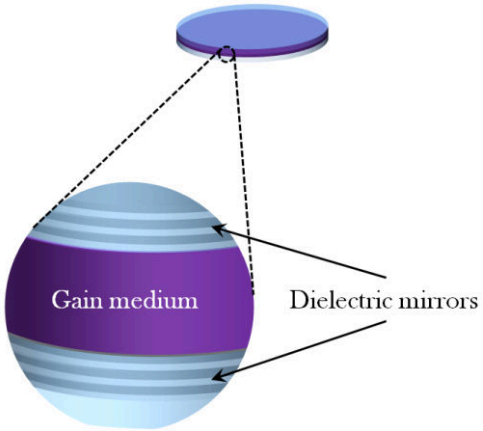

Figure 3.4 - Vertical microcavity composed of a gain medium sandwiched between two Bragg mirrors.

The problem linked to the poor beam quality of diffractive lasers is resolved in the Organic Vertical Cavity Surface Emitting Lasers (OVCSEL) or the so-called vertical microcavities that are another class of devices belonging to the family of thin-film based architectures. In such structures a layer of an organic material is sandwiched between two highly-reflective mirrors (Figure 3.4). The first of these devices was demonstrated by Tessler et al. [17] in 1996 where a 100-nm-thick layer of PPV was sandwiched between a Bragg mirror at the bottom and a 60-nm-thick film of evaporated silver as the top mirror. Since then there have been several reports on the successful realization of the organic microcavities and their performance optimization [18, 20, 23].

Organic VCSELs are characterized by their low oscillation threshold combined with almost diffraction-limited emission normal to the surface of the structure. The threshold in these devices is normally much higher in comparison with DFB devices since the gain medium is

extremely thin and thus a very high gain per unit length is required [141].
In terms of tunability, in a recent work Schütte et al. [148] has reported on continuously tunable laser emission from a wedge-shaped organic microcavity where depending on the position of the excitation beam over the varying film thickness a tuning range, extended from 595 nm to 650 nm, could be obtained.
From the efficiency point of view, similarly to diffractive resonators, organic VCSELs are not very promising devices and the efficiency values can barely exceed few percents. Moreover, the very thin gain medium produces very low output energies.

3.1.1.4 Other microlasers

Microlasers including microdisks and microrings are the last set of devices within the category of thin-film devices (Figure 3.5). A microring consists of a thin polymer waveguide casted around a cylindrical dielectric or metallic core (silica optical fiber or metal wire) by dipping the core into a viscous solution of polymer [149]. In a microring cavity the light is confined by total internal reflection at the interface between the polymer and the surrounding medium. Pumping of these lasers can be either transverse or longitudinal through the fiber core. As the diameter of the fiber is typically around several micrometers, light travels through a long path to make a round trip. As a consequence very low thresholds can be achieved in such structures (1 $\mu J.cm^{-2}$) [27, 28].

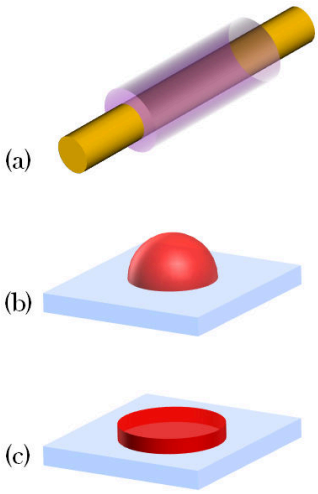

Figure 3.5 - (a) Microring (b) Microsphere (c) Microdisk

Microdisks are realized through photolithographic methods to create disks of organic films that are typically few wavelengths thick and tens of μm wide [150]. As in the case of microrings, in microdisks light is trapped within the disk by total internal reflection at the disk boundary. Apart from disk-shape microlasers, several other geometries (square, pentagon, stadium....) are also reported [151, 152] which provide a good tool to study some fundamental aspects such as chaotic lasing.
The microspheres are another type of resonators within the family of microlasers that cannot be really included or seen as of thin-film devices. They are fabricated from microdisks by melting down and resolidification of the organic semiconductors in the form of three dimensional droplets on a lyophobic surface [29].
All these devices are characterized by their low lasing threshold however for practical

applications their usefulness is limited mainly because of the omnidirectional emission. The lasing modes are numerous indicating an overall low quality factor. In addition, the output power is radially distributed along the emission direction leading to an unpractical device.

3.1.2 External-cavity resonators

Back to the major classification performed in the beginning of this discussion concerning the organic solid-state laser architectures, the second group was the external-cavity-based devices where an organic gain medium is inserted inside a few-mm/cm-long cavity leading to macroscopic-size resonator. These devices are appealing as they provide very efficient output energy extraction possibility due to an optimum overlap between the pump beam and the cavity mode. In addition, they have excellent spatial beam quality and have the potential of being tunable power-scalable devices.

In this respect, in 1993 Hermes et al. [30] reported on a pulsed, organic external resonator device with a slope efficiency as high as 85% and an output energy of 128 mJ. A lasing threshold of ~12 $mJ.cm^{-2}$ is deducible from the input-output characteristic curve. In that experiment, the gain medium was a bulk plastic (hydroxypropyl acrylate/methyl methacrylate) cylindrical rod doped with Pyrromethene 570, placed inside a cavity with flat dichroic mirrors separated by 7.2 cm and end-pumped with a frequency-doubled Nd: YAG laser. Despite that excellent slope efficiency, the output beam was highly divergent as the authors measured a beam quality (M^2) value of 100. They attributed this high beam divergence to the use of flat/flat oscillator combined with the effect of a 2 m positive focal length lensing in the rod itself. Following that success on the high laser efficiency, it was in 1997 that Faloss et al. [31] reported on a 10-cm-long plano-concave resonator enclosing a Pyrromethene-doped cylindrical rod of solid gel (Xerogel) obtained within a process called, sol-gel technique. This technique involves phase transformation of a "sol" obtained from metallic alkoxides or organometallic precursors. The sol, which is a solution containing particles (in our discussion is an organic laser dye, however, this method is not limited to organic materials) in suspension, is polymerized at low temperature to form a wet gel. This one will be densified through a thermal annealing to give an inorganic product like a glass or a dry gel. Using the gain medium obtained in this way incorporated in the above-mentioned architecture, Faloss et al. could achieve a nearly diffraction-limited emission (M^2 ~1.2) with a slope efficiency value of 86%. In addition the authors could tune the emission wavelength of their device by introducing a prism inside the cavity leading to a

tuning range extended over tens of nm. The laser was highly photostable and showed an excellent lifetime over hundreds of thousands of pulses when excited at 20 Hz repetition rate with pump energy of 1 mJ per pulse. The lifetime could further be improved to millions of pulses in oxygen-free Pyrromethene-doped samples.

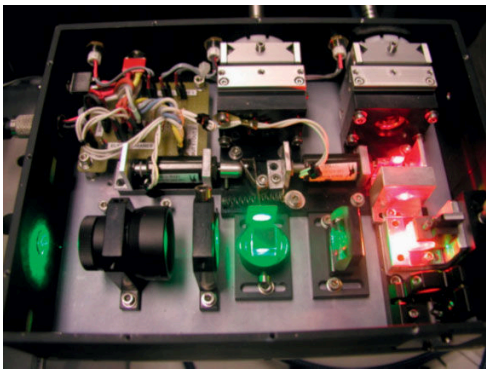

Figure 3.6 - Image of the organic solid-state laser prototype based on an external cavity developed by the Spanish company MONOCROM S.L. [153].

Given all the above-mentioned advantages for such devices in terms of beam quality, efficiency and photostability, the recent work of Garcia-Moreno et al. [153] has triggered development of an organic solid-state laser prototype based on new organic materials incorporated into an external cavity (Figure 3.6) which can be considered as one of the first examples in its own type.

All of the above-mentioned lasers are based on bulk organic gain blocks. One thing that we have not spoken so far about these kinds of lasers is the complicated multi-stage gain medium preparation process that sometimes can take even up to few weeks. For example one of the methods for this purpose is the free-radical bulk polymerization technique used also in ref. [153]. In this technique the dye material and a free radical initiator are added to a monomer and the resulting mixture is agitated in an ultrasonic bath until complete dissolution of the dye is achieved. Then the resulting solution is filtered into appropriate cylindrical mold having an appropriate pore size filter. At this point the polymerization process starts upon careful increase of the temperature in discrete steps during several days. Then the temperature that is risen to several tens of degrees has to be reduced slowly to the room temperature during several days where at that time the sample is ready to be unmolded. The sample is not still ready to be used until it is cut parallel to the axis of the cylinder and the surface ends are delicately polished to optical-grade quality. Some other methods reported in the literature are sol-gel [15], hot-press molding technique [154] and use of epoxy matrices [155] that are also complex in their own kind. Perhaps, this has been one of the reasons that made people think of realizing an “external-cavity” laser keeping all the advantages associated with this class of devices but the long, laborious sample fabrication process was alleviated to a great extent. On this regard, one example is the nice work reported by Bornemaan et al. on a continuous-wave solid-state dye laser [79] (Figure 3.7). Their setup was organized in shape of a folded cavity comprising of two concave mirrors and an output coupler together with a 50 to 100-μm-thick film of Rhodamine 6G-

doped polymer sandwiched between two commercial DVD substrates as the gain medium and a birefringent filter for wavelength tuning. The gain medium was obtained through drop casting of a dye-doped photoresist solution and then curing the photopolymer by UV radiation. The disk-shape gain medium was mounted on a combined rotating/shifting translation stage at the Brewster angle and pumped longitudinally with a vertically-polarized laser diode. The continuous-wave operation was achieved thanks to the disc rotation since exciting the organic dyes in continuous regime fills the long-lived triplet state that is detrimental to laser operation and eventually extinguishes the laser emission. Shifting the sample was due to irreversible photodegradation where in this way fresh regions could be exposed at each time. Using this technique, they could achieve a low slope efficiency of 2% and a laser emission that could last for 30 minutes but with strong fluctuations (~300%) attributed to mechanical imperfections and spatial inhomogeneities in the gain layer thickness. The wavelength tuning range was extended over 40 nm. The strategy adopted in this work to achieve continuous operation and avoid fast photodegration (mimicking the dye jet flow behavior in liquid dye lasers) can be somehow considered as a milestone in the family of organic solid-state lasers but regarding the low slope efficiency of this device, it still keeps a distance from the objectives described in the beginning of this discussion.

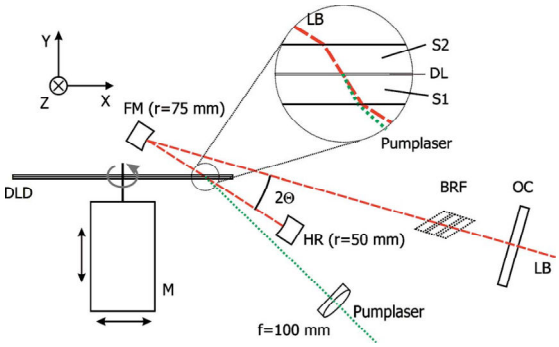

Figure 3.7 - Thin-film solid-state laser based on a rotating disk gain medium sandwiched between two DVD substrates [79].

A thin-film-based external-cavity device with really simple prepared gain medium can be observed in the report of Zavelani-Rossi et al. [90]. In this work, a plano-concave resonator, containing a 500-nm-thick neat film of electroluminescent oligothiophenes, deposited directly onto the high reflector via the fast and simple spin coating technique, was examined. The whole structure was end-pumped with 150-fs-long pulses from the second harmonic of Ti: sapphire laser. Using this configuration, they reported on a nearly diffraction-limited beam with small efficiency value of 1.7% and a tunability range that was achieved over 30 nm by varying the resonator length that could be increased up to ~ 6 μm . No lasing was observed for cavity lengths exceeding 6 μm . This short cavity length limit can be due to the low available gain of the material and the pump length duration which govern the laser pulse buildup time in relation with the cavity length as will be fully described during this chapter. Considering the very modest efficiency value together with the short cavity length obtained in their work, the setup resembles a microcavity device.

Before this work in 1998, Schülzgen et al. [156] reported on a similar structure based on a conjugated polymer where the cavity length was also limited to 9 μm. At the end in a reasonable analogy the authors compared and challenged their work with the "microcavity" reported by Tessler et al. [17].

Following the aforementioned efforts, our present work is a step in the direction of combining the advantages of bulk organic lasers (output power, beam quality, slope efficiency, potential tunability) together with the advantages that can be obtained from thin film devices (fabrication simplicity, low cost).

Our idea is to approach the inorganic VECSEL[11] geometry but made of an organic-based gain medium with a macroscopic cavity length together with an increased efficiency in comparison to organic VCSELs. Whatever comes in the following of this context is the effort made in this way.

[11] VECSEL=Vertical External Cavity Surface Emitting Laser

3.2 The VECSOL concept

The acronym "VECSOL" stands for Vertical External Cavity Surface-emitting Organic Laser. The idea is based on a geometry that resembles the inorganic VECSEL (Vertical External Cavity Surface Emitting Laser)[157] architecture. It consists of a dielectric plane mirror onto which an organic thin film, playing the role of the gain medium, is deposited via a simple deposition technique (i.e. spin coating) and a remote meniscus (concave) mirror closes the cavity. The whole setup is end-pumped with a spot size that matches the cavity mode which allows an efficient extraction of the pump energy along with a circular TEM_{00} emission as they are the characteristic features of the VECSEL configuration. A schematic representation of such laser geometry is sketched in Figure 3.8.

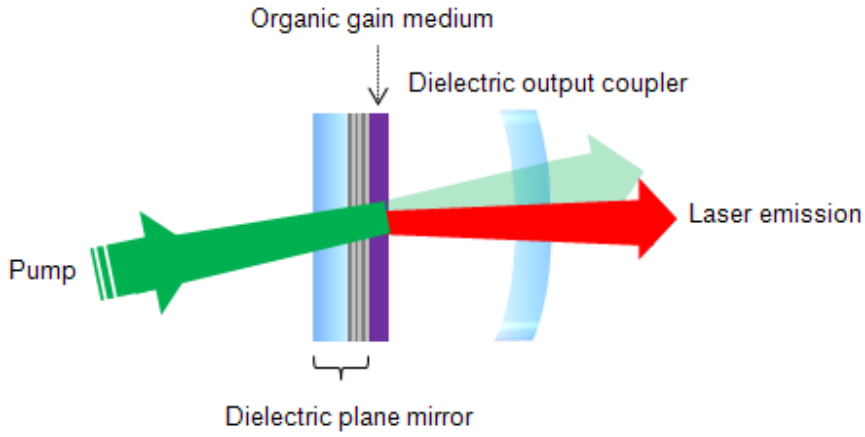

Figure 3.8 - Schematic representation of the VECSEL concept

3.2.1 Approximate initial design

As the first step toward realization of the VECSOL, the analytical assessments in terms of required gain and pump power to make such laser architecture operational were carried out. Whatever comes in the following are the approximate estimations that are done for this matter by having an overview on the gain measurement results in the previous chapter.
To implement the idea of the VECSOL, the well-known "Rhodamine 640" laser dye (see appendix 1) was chosen to be used as the gain material. This material has shown good optical stability [14] and because of its emission wavelength at 650 nm which is very close to the second low-loss window of typical plastic optical fiber (POF) materials, it has been widely characterized due to potential applications that it may find in data telecommunications devices [106, 158]. These extensive studies may facilitate the access to the photophysical parameters of this material (absorption/emission cross sections, radiative lifetime, etc.) studied elsewhere, which is not the case for all the laser dyes.
As many other organic dyes, Rhodamine 640 is suffering from concentration quenching phenomenon. Therefore it must be dispersed in an inert matrix (i.e. PMMA) with a small doping rate. By searching through the commercially-available PMMA solutions, it was found out that uniform film thicknesses of up to a maximum of 20 μm were feasible via spin coating technique. In order to have a useful pump absorption coefficient of ~ 80% over this thickness (for a first try, an excess amount of absorption is not desirable as passive losses due to defects, scattering etc. may cause a fraction of the gain medium at the rear side of the film to be uninverted) a satisfactory doping rate of 1wt% in PMMA would be adequate. Therefore, with a film of Rhodamine 640-doped PMMA, the minimum gain required to reach lasing threshold in the VECSOL configuration is calculated from the following equality:

$$R_1 R_2 e^{2g\ell} = 1 \qquad (3.19)$$

This equation expresses the steady-state laser threshold condition which is achievable when the gain becomes equal to the losses after a round-trip inside the cavity. Here, R_1 and R_2 are the mirror reflectivities and g and ℓ stand for the linear gain and the thickness of the medium, respectively. This expression is valid under the assumption of a constant g over the film thickness. However, the intensity of the pump beam as it propagates into the gain medium decays exponentially so as the gain of the material. The emission intensity variation dI, in a slice of dz within the gain medium would be:

$$\frac{dI}{I} = g_0 e^{-\sigma_{abs} N z} dz \qquad (3.20)$$

where I is the emission intensity, $g_0(cm^{-1})$ is the gain at position $z = 0$, $N(cm^{-3})$ represents the density of dopants (dye molecules) and finally $\sigma_{abs}(cm^2)$ stands for the absorption cross section. If we consider I_0 and I_ℓ are the emission intensities at positions $z = 0$ and $z = \ell$ respectively, then integration of the above equation over the film thickness ℓ gives:

$$Ln\frac{I_\ell}{I_0} = \frac{g_0}{\sigma_{abs} N}(1 - e^{-\sigma_{abs} N \ell}) \qquad (3.21)$$

For sake of simplicity, hereafter in this context the term $(1 - e^{-\sigma_{abs} N \ell})/(\sigma_{abs} N)$ is called the effective length (ℓ_{eff}) and it represents the equivalent length over which the gain is assumed to remain constant (Figure 3.9).

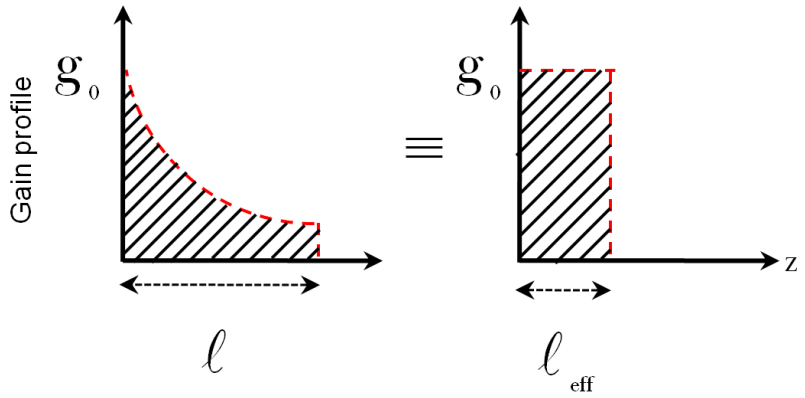

Figure 3.9 - (Left) exponential gain profile evolution over a physical film thickness, ℓ, (Right) constant equivalent gain profile over the distance ℓ_{eff}.

In the case of 20-μm-thick film of PMMA doped with 1wt% of Rhodamine 640, N and σ_{abs} are ~ 1.22×10^{19} cm^{-3} and ~ 0.7×10^{-16} cm^2, respectively (see appendices 1 and 4). Therefore, ℓ_{eff} is estimated to be ~ 10 μm .

Back to the steady-state threshold condition equation, considering that high reflectivity dielectric mirrors up to ~ 99.5% are achievable by simple techniques and reasonable prices, the minimum gain required to reach the lasing threshold would be approximated ~ $5\,cm^{-1}$.

Now the question that might arise is, what would be the necessary pump fluence to have a gain of ~ 5 cm^{-1} and achieve the lasing threshold in the VECSOL geometry? To have a

rough estimation to the answer of this question, we have referred back to the VSL measurements exposed in the previous chapter. However, it has to be mentioned that here we are using Rhodamine 640 laser dye which is different from DCM dye used in VSL measurement, but at least we can have an approximation of the necessary order of magnitudes for different parameters to make the VECSOL operational.

In the VSL configuration, the modal gain value of 40 cm^{-1} was measured in DCM-doped PMMA film of ~ 620-nm-thick for an incident pump fluence of ~ 0.4 $mJ.cm^{-2}$. Considering 13% of the pump absorption over the film thickness, this pump fluence corresponds to an absorbed pump energy density of 0.8 $J.cm^{-3}$, averaged over the pumped volume. One may consider that for small pump intensities, the gain value (g) is a quantity proportional to the absorbed pump energy density ($g \propto$ absorbed energy density). This statement can be written as the following:

$$g \approx k\eta_{abs.} \frac{E_{inc.}}{V} \qquad (3.22)$$

where k is a constant, $\eta_{abs.}$ is the absorption coefficient, $E_{inc.}$ is the incident energy and V is the volume. The k value can be easily calculated from the above-mentioned values in VSL geometry. This gives k=0.046 (cm^2 / mJ).

In the VECSOL geometry, we assume that the pump beam is focused onto a spot size diameter of around 100 μm. With this consideration, we use the above-obtained k constant to find the minimum required incident energy in the VECSOL geometry to have a gain of 5 cm^{-1}, necessary to reach the lasing threshold in a film with $\ell_{eff} = 10\ \mu m$ that absorbs 80% of the pump beam. Using (3.22) gives a required incident energy of around 10 nJ (corresponds to an absorbed energy density of 0.12 $J.cm^{-3}$, averaged over the pumped volume). This amount of energy is easily achievable with the pump source at disposal (PowerChip, Teem photonics), given the maximum available output energy of around 16 μJ from this source.

In terms of degradation, as we saw in VSL measurement, for an absorbed pump energy density of 0.8 $J.cm^{-3}$, the laser intensity dropped to 80% of its initial value after about 60000 pulses. Therefore, we do not have to be much worried with an absorbed energy density of 0.12 $J.cm^{-3}$, calculated in above.

Now, after settling with the pump source, we are interested in the cavity design. For this purpose, we will calculate how much should be the necessary output coupler reflectivity, given the above-estimated parameters. This can be easily verified by writing the oscillation condition above threshold:

$$R_2 > \frac{1}{R_1 e^{2g\ell_{eff}}} \tag{3.23}$$

Thus, with $R_1 = 99.5\%$, $g = 5\ cm^{-1}$ and $\ell_{eff} = 10\ \mu m$, R_2 must be superior to ~ 99.5%. However, considering that there is factor of ~ 8 in the above-calculated absorbed pump energy densities (0.8 $J.cm^{-3}$ against 0.12 $J.cm^{-3}$ in VSL and VECSOL geometry, respectively) and the low degradation rate in VSL measurement for 0.8 $J.cm^{-3}$, one may conclude that the pump energy can be further increased in the VECSOL geometry to have higher gain value and thus, less mirror reflectivity. With this assumption, as the first try we used an available output coupler with 98% reflectivity.

The required curvature radius can be easily calculated from the following relation giving the Gaussian beam size at different positions along the propagation direction [159]:

$$R(z) = z\left[1 + \left(\frac{\pi\omega_0^2}{\lambda z}\right)^2\right] \tag{3.24}$$

where, R(z) is the beam curvature radius, ω_0 is the beam waist (in a plano-concave resonator the beam waist is on the plane mirror), z represents the distance from the waist and finally λ is the wavelength. As the propagating mode curvature inside a cavity should be matched with the mirror curvature, then for a supposed cavity length of 10 mm, a waist diameter of 100 μm and a wavelength of ~ 650 nm within the Rhodamine 640 fluorescence emission spectrum, the required mirror curvature radius that can match the cavity mode is calculated to be ~ 200 mm.

In conclusion, based on the above estimations, as the first try we chose an output coupler having reflectivity of 98% and 200 mm radius of curvature with precise specifications described in the following section.

3.2.2 VECSOL experimental arrangements and emission characterization tools

3.2.2.1 Experimental setup

To realize the so-called VECSOL, the cavity dielectric mirrors were purchased with specifications upon our request. To be able to pump the structure from both sides and mainly because it might be needed to resort a multipass geometry for the pump, the plane mirror and the output coupler were designed in such a way to be transparent at the pump wavelength (T > 90% at 532 nm). The former had a reflectivity more than 99.5% (R > 99.5%) in the range between 600 - 660 nm overlapping the central part of Rhodamine 640 emission spectrum whereas the latter had 98% reflectivity in the range between 600 - 680 nm and a curvature radius of 200 mm. As mentioned earlier, this was an appropriate theoretically-assessed output coupler that the experiment could start with. However, several other output couplers with different reflectivities (80% - 90% - 95% - 98% - 99% - 99.5%) varying around the roughly estimated reflectivity(R > 93%) and with various curvature radii (50 – 100 - 200 mm) were also purchased from different suppliers (Altechna, CVI, RMI).
To build the laser cavity, the standards mirror mounts were used to hold the cavity mirrors parallel to each other. The mirror mounts were positioned on the xyz translation stages making possible lateral as well as longitudinal movement along the cavity axis. The resonator alignment was performed by means of a He-Ne laser. To avoid the path coincidence between the VECSOL emission and the pump beam, the optical axis of the cavity was inclined by few degrees in the xy plane (parallel to the optical table).
The VECSOL resonator was end-pumped using a flash-pumped Nd: YAG laser (SAGA 230, B.M.I., Thomson CSF) generating pulses at 532 nm and 10 Hz repetition rate with pulse duration of $\Delta t \simeq 7$ ns. Furthermore, comparative studies are done when pumped with pulses of ~ 1 order of magnitude shorter in duration. For this purpose, the second harmonic of the Q-switched $Nd:YVO_4$ laser source (PowerChip, TEEM Photonics) generating train of pulses at 10Hz repetition rate, 1064 nm and pulse duration of $\Delta t < 0.5$ ns was used. The second harmonic was generated through single-pass in a 5-mm-thick lithium triborate crystal. This source was the same as the pump source employed for series of measurements presented in chapter 2.

3.2.2.2 Sample preparation procedure

The VECSOL gain medium was a film based on 1 wt% of Rhodamine 640 (Exciton Inc.) in PMMA. For this purpose, a PMMA-anisole solution with molar weight of 950000 corresponding to 15 wt% of PMMA powder in anisole was purchased from MicroChem Corporation. This product which is known with the commercial name of PMMA A15, assures uniform film thicknesses in the range between ~ 4 to 20 μm due to its high degree of viscosity. It was observed that this pre-dissolved PMMA solution gave much better results (in terms of film homogeneity and optical transparency) than a home-made solution of PMMA powder in anisole (may be due to low molar weight in the ready-to-use solution). Rhodamine 640 is a perchlorate salt and is not easily soluble in PMMA/anisole solution since anisole is a weak polar solvent. Thus, it was first dissolved in few droplets of Methanol and then this mixture was added to PMMA/anisole solution. Again like the case of DCM dye, a homogeneous blend was obtained after 2 hours of alternating sonication and hot-plate magnetic stirring using stir bars. The solid gain medium was obtained through spin casting a film of Rhodamine 640-doped PMMA solution directly onto the plane mirror. The spun cast film then transferred to the oven for about 1 hour at 50°C to evaporate the solvent and solidify the film. The spin coating machine was programmed in such a way to obtain a uniform film that can have a satisfactory pump absorption in single-pass geometry. Therefore, according to the PMMA spin speed curve (see appendix 3) and the trial and error method, a 18-μm-thick homogeneous film (measured by Alpha-Step IQ surface profiler, KLA-Tencor Corp.) was obtained that could absorb ~ 80% of the pump beam at 532 nm (verified by UV-Visible spectrophotometer Varian - Cary 100 series). In both cases, the laser beam was focused onto the PMMA-Rhodamine 640 film with a spot size diameter of ~ 140 μm.

3.2.2.3 Excitation / emission characterizing tools

The VECSOL emission spectrum was detected by an optical fiber-coupled spectrometer (SPEX 270-M with two gratings of 150 and 1200 lines/mm, corresponding to the resolutions of 8 and 1 nm respectively (verified by a beam of He-Ne laser) followed by an Andor technologies DH720 charge coupled device camera).
The spatial profile size measurement of the pump and the emitted beam were carried out by means of a Spiricon (LBA-FW) camera.

The pump power/energy measurement was carried out by the following detectors:

PM3Q (Coherent Inc.): amplified thermopile, detecting powers in the range of 0.5 μW – 2 W with a resolution of 50 μW within the wavelength range of 0.3 – 3 μm.
J3-09 (Coherent Inc.): pyroelectric energy detector, measuring pulsed energies from 0.4 μJ to 2 mJ within the spectral range of 0.15– 12 μm.

J8LP-4 (Coherent Inc.): pyroelectric energy detector, measuring pulsed energies from 2 μJ to 20 mJ within the spectral range of 0.15– 12 μm.

The VECSOL output energy was detected through a Labview-controlled silicon energy probe (DSJ-10 with delta-DPM, Spectrum Detector Inc.) measuring pulsed energies from 100 pJ to 1 μJ within the spectral range of 0.19 – 1.1 μm. For energy values exceeding 1 μJ, the above-listed J3-09 energy detector was used.

The VECSOL emission degradation studies (and related phenomena) were carried out with a Silicon photodiode (Thorlabs, PDA100A, 400-1100 nm) linked to a LabView acquisition card controlled by a home-made acquisition program, developed during this Ph.D. thesis.

3.3 VECSOL emission characterization and lasing performance

After all the analytical estimations and the experimental arrangements, realization of a solid-state external cavity laser based on an organic thin film became a reality and fulfilled our expectations. In the following, the performance of the realized VECSOL geometry are presented and discussed.

3.3.1 Efficiency curve

Figure 3.10 is showing the input-output characteristic curve of the VECSOL cavity with an output coupler of 98% reflectivity and 200 mm curvature radius when pumped with 7-ns-long pulses.

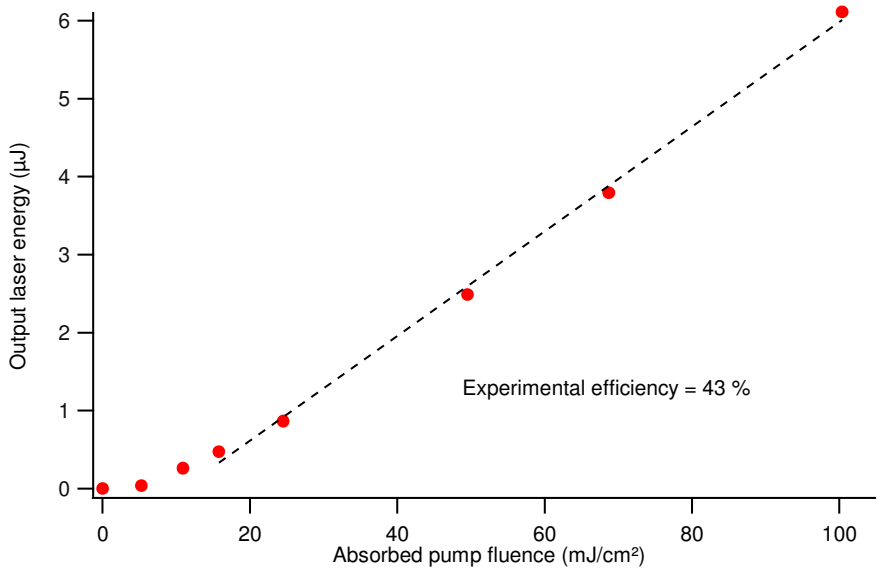

Figure 3.10 - VECSOL output energy vs. absorbed pump fluence for a 4-mm-long cavity under 7-ns-long pulse excitation regime. The dashed line is a linear fit to the experimental data.

For a cavity length of ~ 4 mm, a clear lasing threshold at ~ 1.8 μJ (corresponding to 11.7 mJ/cm^2 absorbed pump fluence) followed by a linear increase as a function of the excitation fluence was obtained. At this experimental condition, an output energy as high as 6.1 μJ was measured. In order to assess this value, in an optically pumped laser the criteria that quantifies the laser performance in terms of the efficiency is called the optical-optical

conversion efficiency and is defined as the ratio between the highest output energy value to the corresponding incident or absorbed pump energy. Similarly, measuring the slope of the laser input-output characteristic curve defines another term known as the laser slope efficiency. On this basis, an optical-optical efficiency as high as 43% and a slope efficiency of 52% (based on absorbed pump energy) are deducible from the input-output characteristic curve. Comparing this slope efficiency with the highest reported slope efficiency for a thin-film-based device, realized by Kozlov et al. (~ 35%) [84], manifests an efficiency record obtained from the VECSOL geometry. It should be noted that this efficiency value was achieved for the cavity parameters chosen based on very approximate initial estimations. As will be seen later on in section 3.4.3, the conversion efficiency could be optimized to 57% by playing on the cavity length and the mirror reflectivity.

For sake of comparison, the cavity was excited with 0.5-ns-long pulses (Figure 3.11). For a cavity length of 4 mm as the previous case, the input-output characteristic curve exhibited a clear lasing threshold at 0.95 μJ (corresponding to 6.2 mJ/cm^2 absorbed pump fluence). In this case, the maximum output energy was limited to 0.7 μJ for an absorbed pump fluence of 75 mJ/cm^2. In terms of lasing and slope efficiencies, the values of 6.3% and 7% (based on absorbed pump energy) are deducible respectively from the input-output characteristic curve.

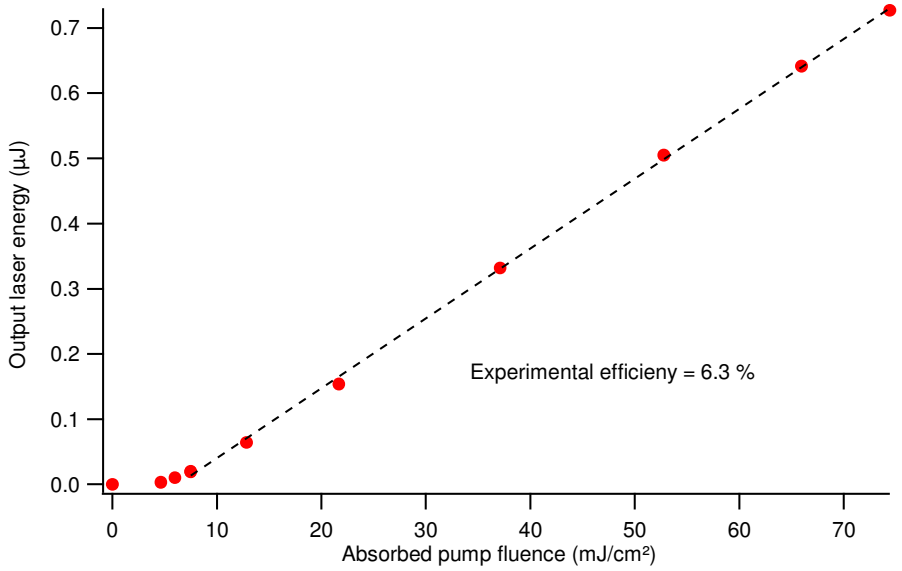

Figure 3.11 - VECSOL output energy vs. absorbed pump fluence for a 4-mm-long cavity under 0.5-ns-long pulse excitation regime. The dashed line is a linear fit to the experimental data.

What is evident from the above input-output characteristic curves is that in both cases the VECSOL lasing thresholds are not differing very much from each other in terms of energy.

The very baffling point in comparison of both graphs is the very distinct efficiency values obtained for the same pump fluences and cavity lengths in both experiments. Considering the same experimental conditions for both measurements, the difference in efficiency values manifests a clear dependence of the laser efficiency to the pump pulse duration.

Apart from the effect of the pump pulse duration on the output energy level and the conversion efficiency, another factor playing a key role in this story is the output coupler reflectivity. One might expect an increase in the output energy by decreasing the mirror reflectivity. However, this fact can be true to some extent but it also leads to a shortened intracavity photon lifetime and thus less amplification. Therefore, there is a compromise between the intracavity photon lifetime and the conversion efficiency that must be respected while choosing the output coupler in order to obtain the optimum efficiency. In this regard, the input-output characteristic curves of a 10-mm-long VECSOL when excited by 7-ns-long pulses are compared together for four different output couplers having reflectivities of 80%, 90%, 95% and 98% (Figure 3.12).

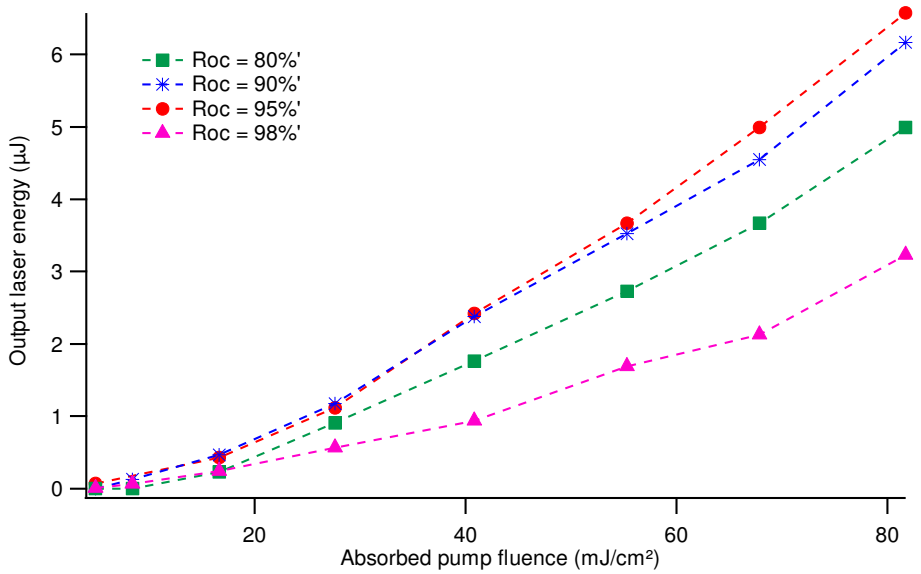

Figure 3.12 - VECSOL output energy vs. absorbed pump fluence under 7-ns-long pulse excitation regime for output coupler with different reflectivities. The cavity length is 10 mm.

Based on the above graph, the optimum coupling is achieved for an output coupler with 95% reflectivity as the highest energy level is achieved in this case within the set of the used couplers.

Other important information that can be deduced from the above graph is the decrease seen in the output energy level when the cavity length is increased. This can be simply verified by comparing the lowest curve within the set of characteristic curves for a 10-mm-

long cavity (Figure 3.12) and the input-output characteristic curve obtained earlier for a 4-mm-long cavity (Figure 3.10). For a given absorbed pump fluence, the latter had a twice higher energy per pulse in comparison to the 10-mm-long cavity structure.
The complete and deep understanding of all these issues such as the efficiency dependence on pump pulse duration, cavity length and the output coupler reflectivity is preserved for a later time in this context (section 3.4) after presentation of some theory followed by the relevant modeling governing the VECSOL behavior in each case. For the moment we continue our discussion by some other emission characterizations that are described in the following.

3.3.2 Emission spectrum

Typical VECSOL emission spectrum for a 4-mm-long cavity together with the Rhodamine 640 fluorescence emission spectrum are shown in Figure 3.13.

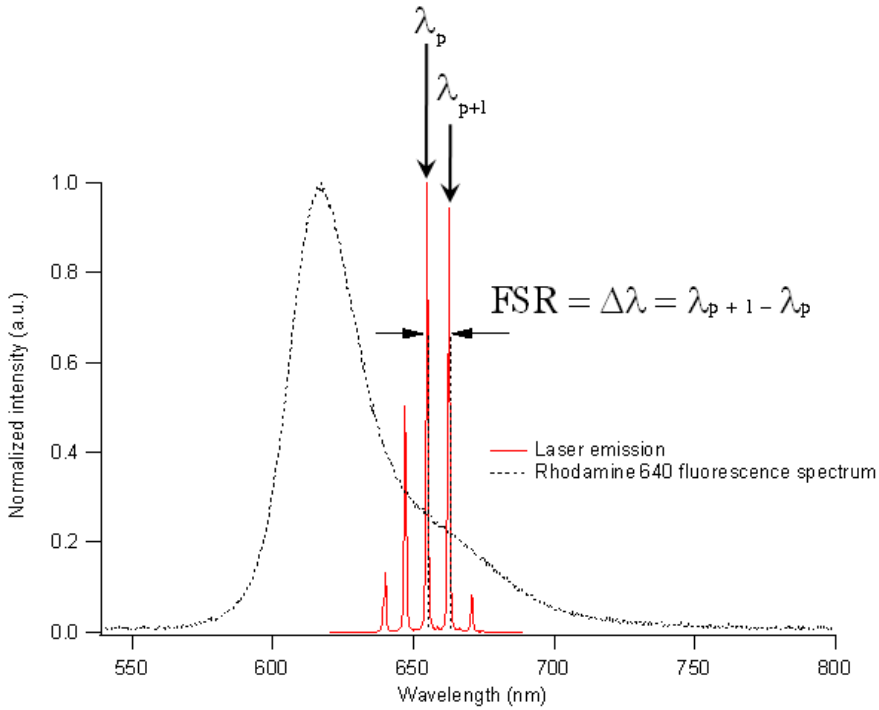

Figure 3.13 - Typical emission spectrum of a 4-mm-long VECSOL cavity when excited by 7-ns-long pulses. The dotted line is the Rhodamine 640 fluorescence emission spectrum in solid film configuration.

As it is seen, several evenly-spaced peaks are residing within the Rhodamine 640-doped PMMA emission spectrum. These emission peaks are related to the peaks of a Fabry-Perot

etalon[12] formed by the ~ 18-µm-thick gain medium. In a Fabry-Perot etalon the free spectral range (FSR) between two successive peaks is given by the following equation:

$$FSR = \lambda_{p+1} - \lambda_p = \frac{\lambda_p \lambda_{p+1}}{2n\ell} \qquad (3.25)$$

where λ_p and λ_{p+1} are the $(p)^{th}$ and $(p+1)^{th}$ emission modes, respectively, n is the refractive index of the medium, ℓ stands for the film thickness and λ is the wavelength.
The film thickness was determined by Alpha-Step IQ surface profiler (KLA-Tencor Corp.) on a coated silica substrate (round shape with standard size of mirror) prepared under the same experimental condition as the VECSOL sample had been prepared (PMMA solution of the same viscosity, doping rate and with the same spin speed). This sample was then inserted inside the spectrophotometer (Varian - Cary 100 series) and its transmission curve was monitored as a function of spectroscopic wavenumber $(1/\lambda)$. As for long wavelengths the sample becomes transparent, the ~ 18-µm-thick film forms a Fabry-Perot etalon for the incident wavelengths leading to a sinusoidally-modulated transmission curve. This curve was fitted by a sinusoidal function with index and wavenumber dependant phase parameter which then determines the optical length ($n\ell$ where n is the refractive index and ℓ is the film thickness) of the doped PMMA film in a rather precise manner from which the refractive index of the doped film could be extracted after measuring the film thickness via profilometer (see appendix 2 for result of the fit).
On this basis, the refractive index was measured to be around n=1.52. This gives a FSR of ~ 7.8 nm at the VECSOL emission wavelength and the sample film thickness which perfectly corresponds to peak intervals in the obtained VECSOL emission spectrum.
Now, the question is, if the observed emission peaks are defined by the Fabry-Perot etalon then what will be the role of the external cavity? To answer this question, if we calculate the FSR corresponding to the longitudinal mode spacing in a mm-thick Fabry-Perot etalon made of air $(n=1)$, it will be a fraction of a nm. This will lead us to the conclusion that in fact each of the above-mentioned peaks is containing the external cavity longitudinal modes which are not resolved with the resolution of the spectrometer (~ 1 nm) at disposal. In fact, we consider that the VECSOL emission spectrum is a consequence of two coupled cavities in which the emission from the external cavity is filtered through the 18-µm-thick Fabry-Perot etalon formed by the gain medium.

[12] The term « etalon » refers to a pair of flat parallel reflective surfaces at fixed spacing.

According to the FSR equation, if the film thickness is reduced in such a way to have only one mode of the Fabry-Perot etalon under the gain spectral region of the Rhodamine 640, then we should observe single-peak laser emission from the VECSOL structure.

As expected, the number of peaks decreased gradually as the FSR ($\Delta\lambda$) increased until a single peak obtained for a film thickness of ~2.3 µm (Figure 3.14). The observed single peak still contained the external cavity modes inside of it. This film thickness was achieved through a mixed solution based on PMMA A15 and PMMA A6 (lower-viscosity PMMA/anisole solution, see appendix 3 for more detail on this PMMA type and the corresponding spin speed curve) with equal weight ratios (50% - 50%) to fill the thickness gap (~ 1-4 µm) that couldn't be obtained merely with each of these PMMA types. The set of graphs in the following figure are showing the decrease in peaks number by reducing the film thickness toward appearance of a single peak.

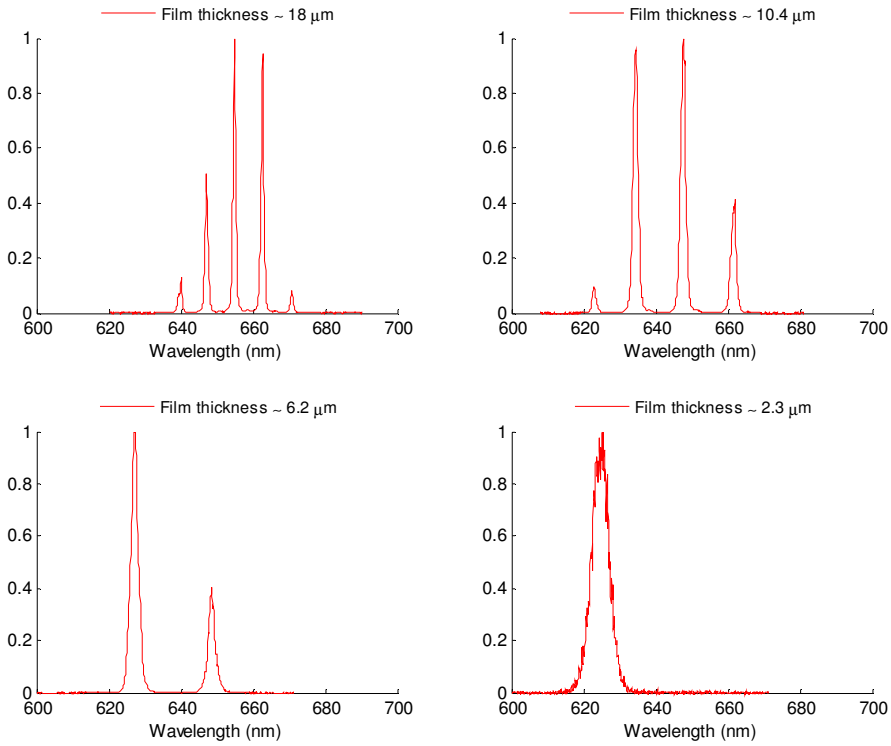

Figure 3.14 - Different emission spectra corresponding to Rhodamine 640-doped-PMMA samples of various thicknesses. Single-peak emission was achieved in a sample with thickness of ~ 2.3 µm (bottom right).

One can notice in the above figure that film thickness reduction has led to a reduced number but broadened emission peaks. This is explained by the fact that film thickness reduction results in a reduced available gain and thus less spectral narrowing through the material gain.

3.3.3 Wavelength selection via film thickness variation

Interestingly, we noticed that the VECSOL emission spectrum could be shifted upon moving the pump spot onto the gain medium. This spectral modification turned out to be due to thickness variations, as they were especially strong at the sample edges. This fact led to one of the most interesting features of the VECSOL emission, that is, the wavelength tuning possibility. The intrinsic characteristic of films realized through spin coating is a flat zone in the middle and then a gradual increase as it goes toward the edge due to the high viscosity. This fact was verified experimentally by measuring the deposited film thickness with a surface profiler from the center to the edge on a PMMA-coated silica substrate with a standard size, as in a plane mirror (diameter = 25.4mm) (Figure 3.15).

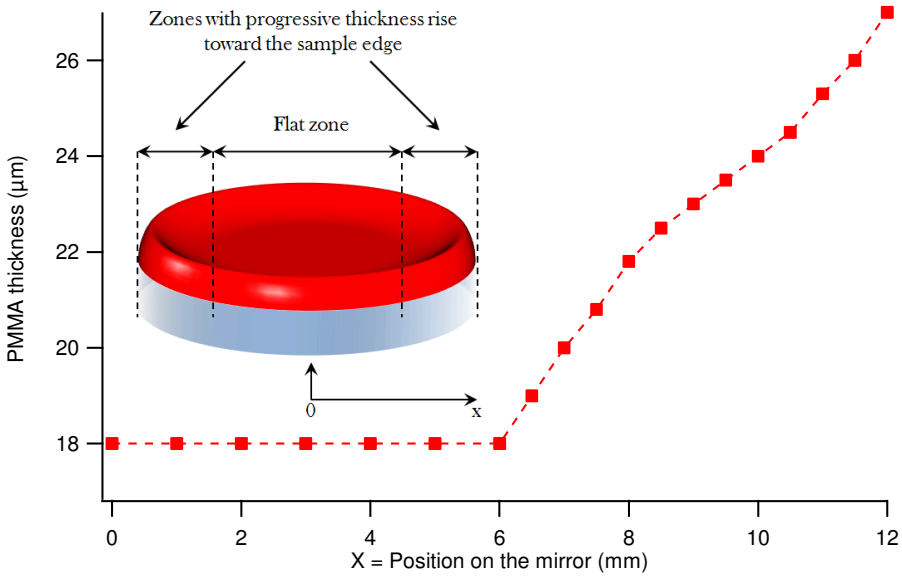

Figure 3.15 - Thickness scan profile of PMMA-coated silica substrate from the center to the edge. The inset is the schematic representation of the film thickness variation by going toward the sample edge.

For the purpose of wavelength tuning demonstration, a 2.3-µm-thick sample was prepared to operate in single-peak regime. When the coated plane mirror moved transversely to the pump beam, as it approached to the edge, the continuous film thickness variation led to a tuning range of around $\Delta\lambda$=40 nm (from 615 nm to 655 nm), limited by the gain spectrum and the mirror reflectivities (see appendix 5) (Figure 3.16).

Several methods (dip-coating, changing the spin coating parameters such as time, ramp, spin speed etc.) were examined in order to realize determined film thicknesses with the

possibility of eventual controlled tunability. This study was carried out during a Master degree internship by Manal Yewakim whom I would like to acknowledge here. Unfortunately, none of the methods resulted in a clear way to achieve the goal of controlled wavelength tuning.

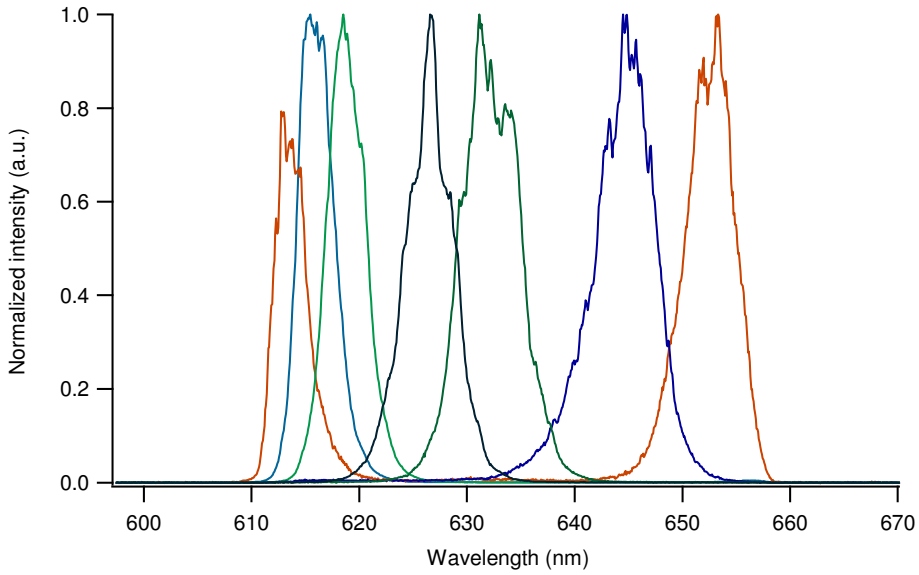

Figure 3.16 - Emission spectrum of a 2.35-µm-thick sample in a 6-mm-long cavity when translated normal to the pump beam from the centre to the edge.

3.3.4 Laser beam quality (M^2)

One of the important aspects of the external-resonator lasers is the high beam quality that can be achieved from such devices. This made us interested to quantify this parameter in the case of the VECSOL emission.

The quality of the beam is the measure of its focusability and is determined by a parameter called M^2 factor. Consider a Gaussian beam propagating along the z direction being focused onto a spot size diameter of $2\omega_0$ at the position $z = z_0$. As this beam propagates along the z axis, the width of the intensity profile will be symmetrically increased from $2\omega_0$ at $z = z_0$ with an axis of symmetry being defined at this position. This position defines the beam waist at which the phase front is planar. The spot size at distance z from the beam waist expands as a hyperbola which has the following form [159]

$$\omega(z) = \omega_0 \sqrt{1 + \left(\frac{\lambda (z - z_0)}{\pi \omega_0^2} \right)^2} \qquad (3.26)$$

where ω_0 is the beam waist radius at position $z = z_0$, λ is the beam wavelength. For a non-perfect (non-TEM_{00}) beam, the divergence will be higher than the divergence governed by diffraction for a given waist radius ω_0. The ratio between the actual divergence and the diffraction-limited divergence is referred to as M^2 factor which intervenes in the above formula and gives:

$$\omega(z) = \omega_0 \sqrt{1 + \left(\frac{M^2 \lambda (z - z_0)}{\pi \omega_0^2} \right)^2} \qquad (3.27)$$

This relation defines how close to "perfect-Gaussian" a laser beam is. A diffraction-limited beam has a perfect Gaussian profile with $M^2 = 1$, while any distortion in the shape leads to higher M^2 values.

In the following, in order to determine this parameter for the VECSOL emission, the output beam was focused onto a beam profile analyzer (Spiricon, 1600 by 1200 pixels with 4.4 µm by 4.4 µm size of each) via a converging lens. The CCD analyzer was mounted on a translation stage easily moving on an optical rail along the laser emission direction. The output beam radius was measured at different positions on both sides of the created waist and fitted through the given relation in (3.27).

As a result, the beam quality measurement experiment led to a perfect diffraction-limited TEM_{00} emission with $M^2 = 1.01$ (Figure 3.17). The measurement was carried out for a cavity length of ~ 4 mm.

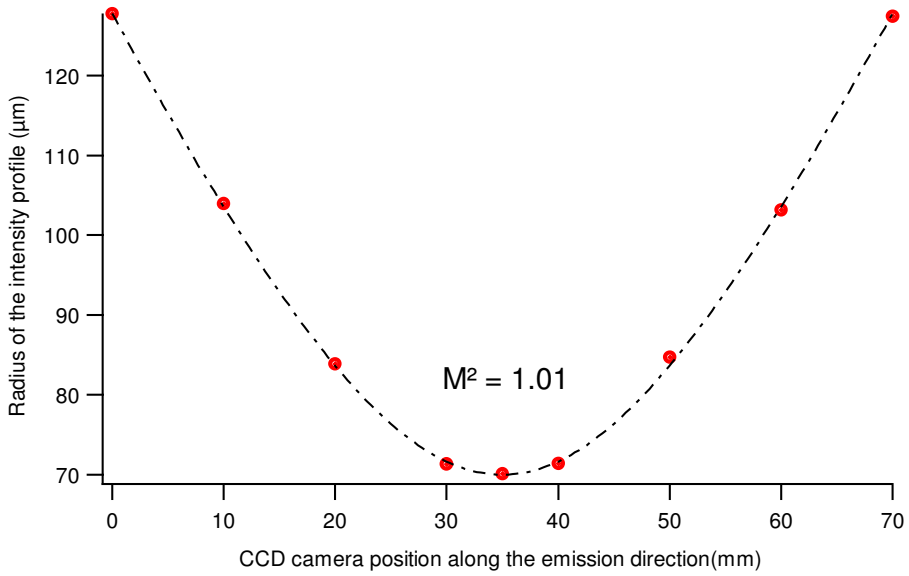

Figure 3.17 - VECSOL emission beam size evolution at both sides of a created beam waist. The dotted line is a fit to the experimental data.

TEM_{00} operation was observed when the size of the pump beam was less than equal the cavity mode size ($\omega_p \leq \omega_0$). It is easy to obtain highly multimode operation with larger pump spots and higher energies as well.

A typical image of the output TEM_{00} beam intensity profile is depicted in Figure 3.18.

Other Hermite-Gaussian modes (TEM_{nm}, where "n" and "m" are the number of nodes in the horizontal and vertical directions respectively) were easily attained by fine misalignment of the laser cavity through the adjustment screws of the mirror mounts.

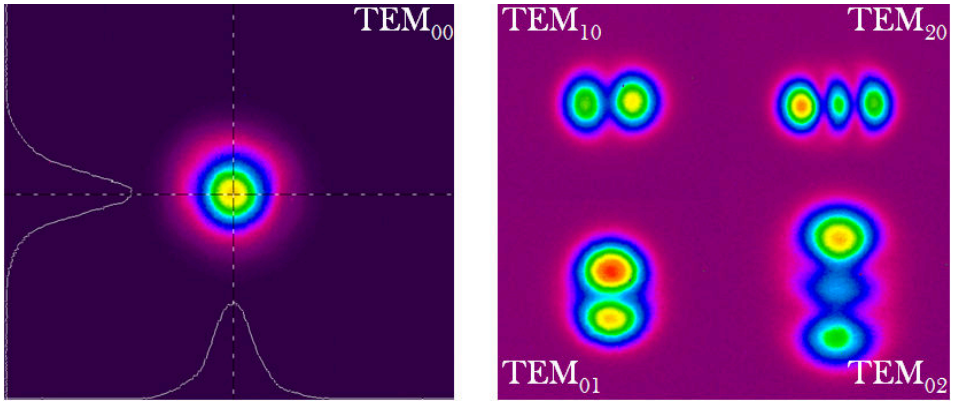

Figure 3.18 - (left) TEM_{00} beam profile of the VECSOL emission. (right) Hermit-Gaussian modes obtained upon fine misalignment of the VECSOL cavity.

3.3.5 Power scaling

Power scaling is one of the most attractive features of inorganic VECSELs [160], and it is also a major advantage of the VECSOL configuration over other organic laser architectures. The concept means the possibility to increase the output power at constant pump fluence. In context of organic lasers, it will be very interesting to achieve this goal without decreasing the laser emission lifetime which is of particular importance, where long-lived devices are highly desirable. As an example, we demonstrated in the following that the output energy can be doubled when the VECSOL is pumped by a twice higher incident energy while the incident pump fluence and consequently the degradation rate were maintained constant. For this purpose, we started the experiment with an output coupler of 98% reflectivity with 50 mm radius of curvature.

In a half-symmetric resonator in which one mirror is planar, and the other spherical, the TEM_{00} fundamental mode spot size radius ω at the plane-mirror end of the cavity is given by [159]:

$$\omega = \sqrt{\frac{L\lambda}{\pi}\sqrt{\frac{g}{(1-g)}}} \tag{3.28}$$

where L is the resonator length, λ the oscillating wavelength and g is a parameter defined as the following:

$$g \equiv 1 - \frac{L}{R} \tag{3.29}$$

where R denotes the mirror curvature radius. This gives ω= 58 μm for R = 50 mm and a cavity length of L = 6 mm, the condition at which the experiment is carried out. Therefore, a pump spot radius of ~ 60 μm was chosen (measured by Spiricon beam analyzer) in order to have only a predominant pump area over the TEM_{00} fundamental cavity mode and not the higher order transverse modes. In another experiment, the pump radius size of ~ 85 μm was chosen in order to enlarge the pump surface area by a factor of two. Thus, the output coupler was replaced with an output coupler of 98% reflectivity and R = 200 mm to match this pump size and the fundamental TEM_{00} cavity mode (having in this case a spot size radius of 84 μm) together. The experimental results depicted in Figure 3.19 are showing the identical degradation rates in accordance with our expectation for an incident pump fluence of 20 mJ.cm^{-2} which is roughly two times above the lasing threshold in the case of pumping the VECSOL with 7-ns-long pulses. It would be also useful to estimate the

maximum attainable output energy of the VECSOL at the same pump fluence with a maximum pump beam diameter of 4 mm for example (for larger diameters, the beam spatial quality is likely to be disturbed by thermal effects) and a relevant output coupler that could match this pump beam size to TEM_{00} fundamental mode. In this condition, we estimate that output energies up to ~ 1 mJ are attainable all by assuring the degradation rate constant.

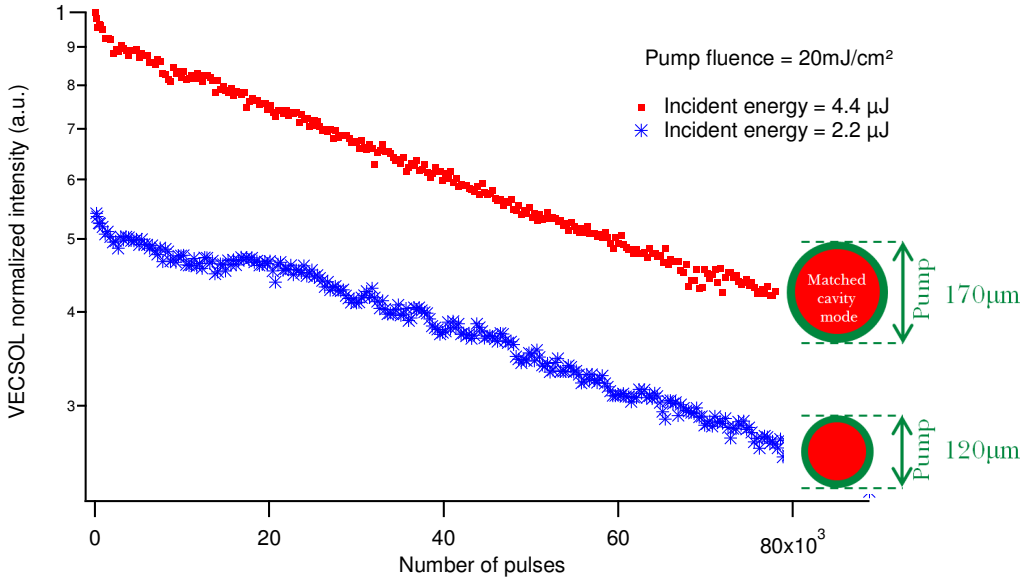

Figure 3.19 - Demonstration of the VECSOL power scaling capability upon excitation with 7-ns-long pulses at 10 Hz repetition rate. (right) Illustration of the corresponding pump size diameters used in each case to match the cavity mode size.

3.3.6 Photodegradation and lasing lifetime

As mentioned earlier, organic dye lasers undergo an irreversible photochemical/thermal degradation and thus, they have a limited lifetime [161].

On this regard, a small part of this thesis is dedicated to measure the laser emission lifetime of the realized VECSOLs. For this purpose, we developed a LabView program which allowed us to carry out lifetime measurements with great ease thanks to automatic data acquisition that could be achieved in this way. In the following, a set of several degradation curves obtained at different conditions for the two previously-used pump sources of 0.5 ns and 7 ns pulse durations are presented and discussed.

3.3.6.1 Degradation measurement procedure

The used strategy for the VECSOL emission lifetime measurements is as the following. A photodiode (Thorlabs, PDA100A, 400-1100 nm, active area = 75.4 mm^2) was capturing the VECSOL emission intensity after being reduced through neutral density filters. After assuring that the photodiode was operating in its linear regime, the captured signal by the photodiode was sent to an analog peak detector circuit (specifically designed and realized at the LPL Electronics workshop). The peak detector circuit was capable to generate a constant signal, blocked between two pulses and varying at each laser pulse following the detected signal level. A LabView-based acquisition system was sampling and then digitizing the blocked signal between two pulses (in order to avoid registration of too many data points for further data processing, the sampling frequency was lower than the repetition rate) (Figure 3.20). As the VECSOL emission decays in time, so as the photodiode signal intensity, sampling the blocked peak level between two emission peaks would give the degraded emission intensity over time. The LabView program was registering the data in an Excel file for further data processing.

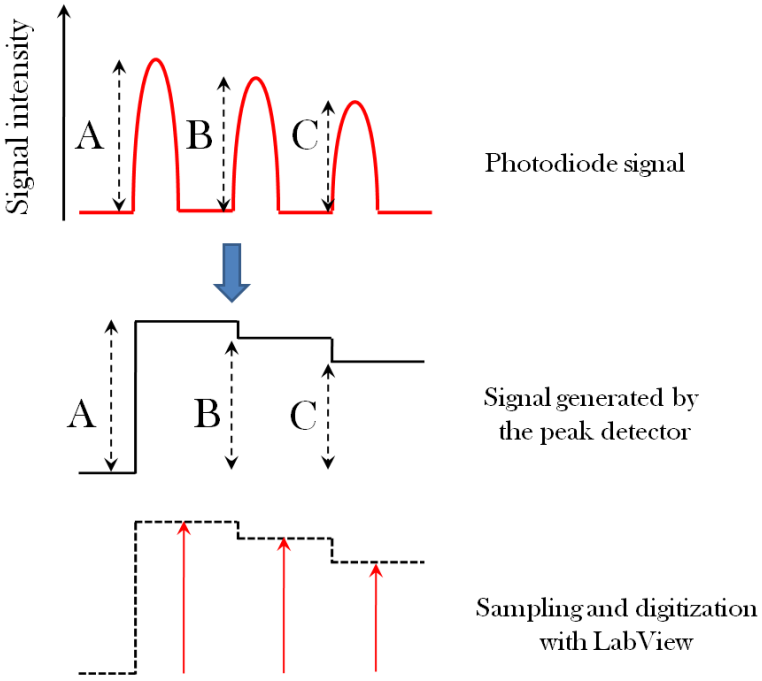

Figure 3.20 – Schematic representation of the used procedure for the VECSOL emission degradation studies.

3.3.6.2 VECSOL degradation curves under 0.5-ns-long pulse excitation regime

For degradation studies under 0.5-ns-long pulse excitation regime, a solution of PMMA A15 doped with 1 wt. % of Rhodamine 640 was made to prepare a coated mirror sample with ~ 18 μm thickness.

For the measurement, the cavity length was set to 6 mm and the pump beam was focused onto the sample with a spot size diameter of ~ 140 μm (measured at $1/e^2$ by Spiricon LBA-FW camera). Figure 3.21 is showing the degradation curves at different pump energy levels.

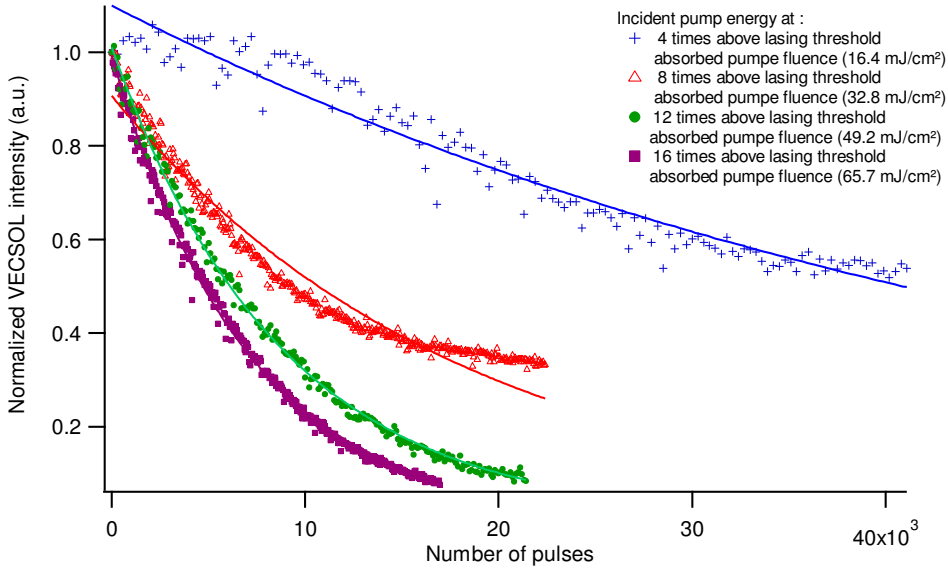

Figure 3.21 - VECSOL degradation curves under 0.5-ns-long pulse and 10 Hz repetition rate excitation regime for several pump energy levels.

One can see from the above curves that higher pump intensities have led to faster degradation rates. Following the measurements, we observed that a monoexponential fit function as $I(t) = I_0 \exp(-t/\tau)$ matches the experimental degradation data. In the given fit function, τ is the characteristic time during which the emission intensity decays to 1/e of its initial value.

By tracing the degradation rate $(1/\tau)$, obtained from a monoexponential fit, as a function of the absorbed pump fluence we observed that they are linearly proportional as shown in Figure 3.22.

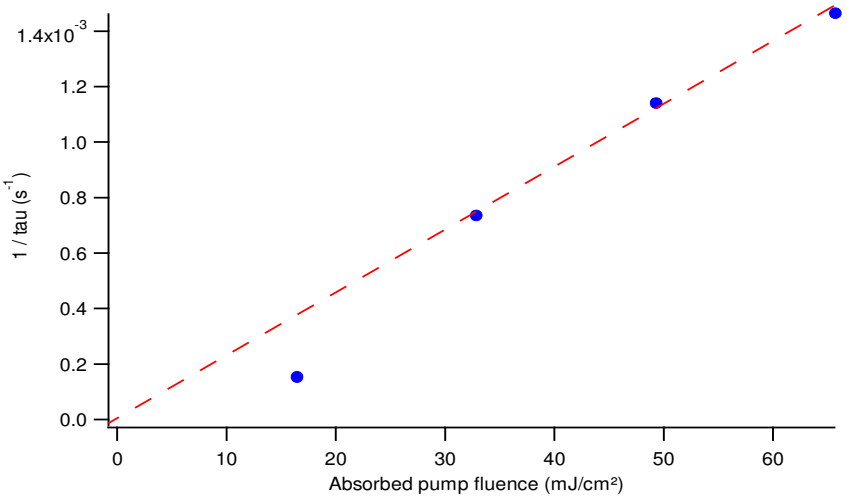

Figure 3.22 - Degradation rate ($1/\tau$) versus absorbed pump fluence.

In this text, for sake of coherence with the existing literature, we define the emission lifetime criterion as the half-lifetime, that is, the time during which the emission intensity drops to half of its initial value. The half-lifetime ($\tau_{1/2}$) is simply related to the characteristic time τ with $\tau_{1/2} = \tau \, \mathrm{Ln}2$.

Considering that the experiments were performed at 10 Hz repetition rate and based on the above-defined criterion, a half-lifetime of 480 seconds (4800 pulses) was obtained for an incident pump energy of about 16 times above the lasing threshold. Excitation of the VECSOL with a pump energy of around four times above lasing threshold resulted in emission half-lifetime of 4200 seconds (42000 pulses).

The above-presented results were obtained for a sample prepared from a fresh solution, that is, a solution which was prepared a few hours before the experiment. We observed that by using an aged solution, prepared in advance and conserved under ambient light, at room temperature in a sealed container the degradations results were so different. In this respect, Figure 3.23 is comparing the above-obtained degradation curves for two different incident energies (based on a fresh solution) with degradation curves obtained at the same experimental conditions (the same pump spot size and cavity length) for a sample prepared from a two-week old solution of PMMA A15 doped with 1 wt. % of Rhodamine 640. For a sample prepared from a two-week old solution, the emission intensity dropped to half of its initial value after 45 seconds (450 pulses) at an excitation energy 16 times above the lasing threshold.

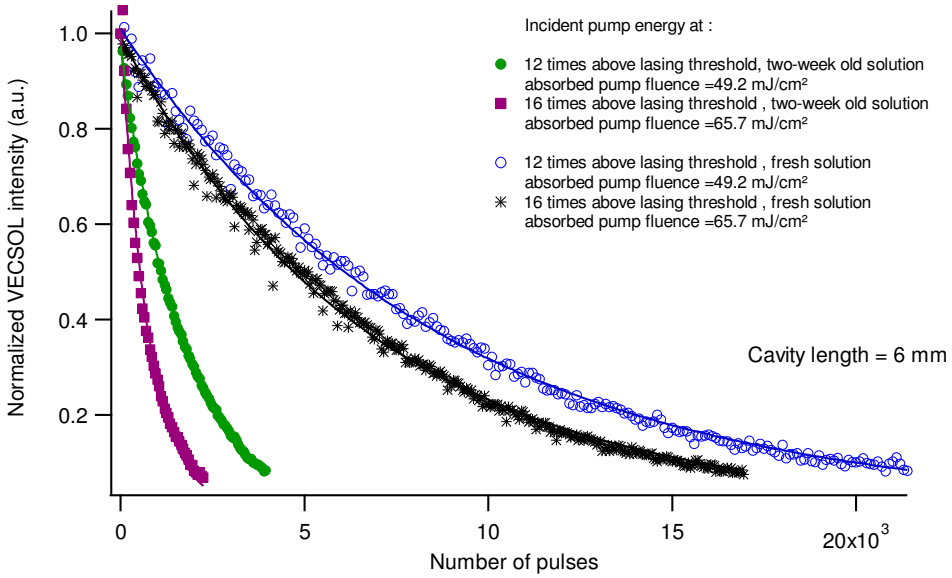

Figure 3.23 - Comparison between degradation curves of the VECSOL composed of a sample prepared once from an old and then based on a fresh solution.

The reason of the big difference seen during the degradation experiments for samples based on a fresh solution and an old solution is not completely understood. One highly-possible reason can be due to formation of peroxide as a result of a reaction between anisole and oxygen which is triggered by ambient light and is accelerated at high temperatures. We then assume that keeping solutions away from oxygen, in the dark and at low temperatures (in fridge) should considerably enhance the conservation capability for a given solution and thus a better lasing lifetime. To accredit this hypothesis, a systematic and detailed set of experiments are the subject of future studies. For the experiments carried out during this thesis, samples were realized from fresh solutions whenever possible within the same day that the solution was prepared.

3.3.6.3 VECSOL degradation curves under 7-ns-long pulse excitation regime

Similar measurements were carried out under 7-ns-long pulse excitation regime at 10 Hz repetition rate. Figure 3.24 is the comparison between the results of the experiment under this excitation regime and the degradation curve just presented in the above for an absorbed pump fluence of around 16 mJ.cm^{-2}. As one can see, in case of 7-ns-long pulse excitation regime the intensity dropped to half of its initial value after around 60,000 pulses, whereas, this happened after 40,000 pulses in case of 0.5-ns-long pulse excitation regime. Fitting the experimental data with a monoexponential gives degradation rates of

$(1/\tau) = 1\times10^{-4}$ (s^{-1}) versus $(1/\tau) = 2\times10^{-4}$ (s^{-1}) for 7-ns-long pulse and 0.5-ns-long pulse excitation regimes, respectively. The observed result is a bit unexpected since for a given energy the peak power associated with 0.5-ns-long pulse duration is 14 times higher than the peak power of a source with 7-ns-long pulse duration. Thus, we should expect about 14 times higher degradation rates under 0.5-ns-long pulse excitation regime in comparison to 7-ns-long pulse excitation regime. Our observation raises several questions on the origins of photodegradation (the influence of thermal issues, triplet state population and so on) which have to be elucidated via further systematic studies. The VECSOL emission lifetime order of magnitude is comparable to or even better than some reported values in the literature for thin-film-based organic lasers at normal condition and without taking special measures such as encapsulation which can lead to hundreds/thousands-fold improvement in lasing lifetimes [36].

Here, as an example similar to our experimental conditions, Oki et al. [147] have obtained half-lifetime of around 57000 shots for a pump fluence of $90\,\mu J/cm^2$ in a thin-film configuration (DFB based on Rhodamine6G in PMMA) pumped at 10 Hz repetition rate with the second harmonic of Nd:YAG laser.

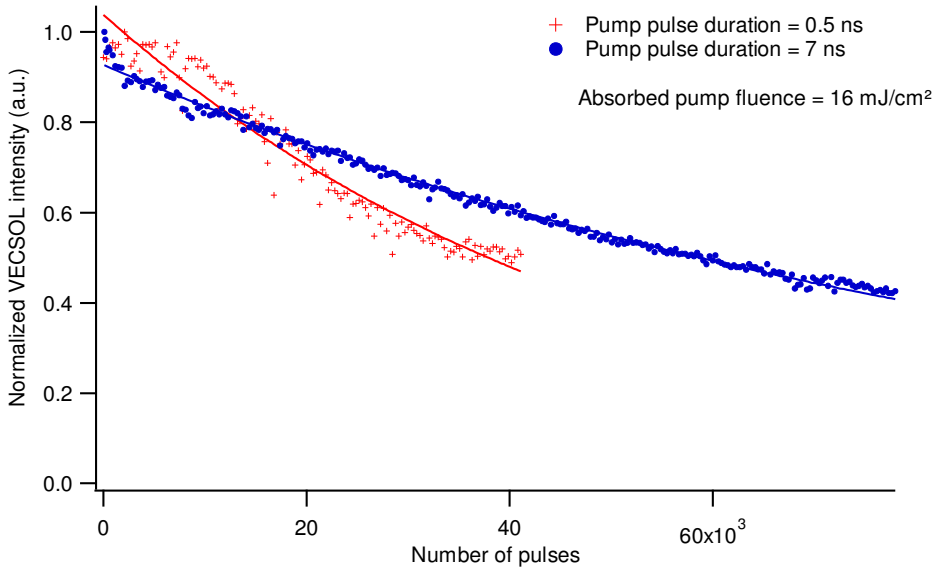

Figure 3.24 - Comparison between the VECSOL degradation curves under 7-ns-long pulse and 0.5-ns-long pulse excitation regimes at 10 Hz repetition rate.

Under 7-ns-long pulse excitation regime some strange behaviors were observed. It was seen that for very high incident pump fluences (hundreds of $mJ.cm^{-2}$) two degradation regimes were discernable (a very fast decaying slope in the beginning followed by a rather mild

steep). We noticed that upon termination of the fast degradation phase and entering the slow degradation regime, the VECSOL emission spatial profile evolved from a bright TEM_{00} beam to a ring-shaped profile with a dark region in the middle. Furthermore, we observed that upon starting the second degradation regime the emission intensity has a slight increase followed by a long-lasting decay. Further studies are under progress to quantify the above-described behavior observations.

In conclusion, within the above experiments we quantified degradation rates at different pump energy levels. We found out that in order to have better emission lifetimes fresh solutions must be used for sample preparation instead of the aged solutions. In addition, we saw that using a longer-pulse excitation regime led to a better emission lifetime at a given pump energy.

As a perspective, some other organic dyes such as Pyrromethene or Perylene have to be examined as based on the reports [31] these materials have shown to be very promising to enhance the emission lifetime to up to one or two orders of magnitude higher than the current results with Rhodamine 640.

The degradation studies and data processing were done by a Xin Zhang in the framework of a Master degree internship whom I would like to acknowledge here.

At the end, I would like to emphasize that the performed degradation studies are the very preliminary results. Further studies are under progress on this subject.

3.4 VECSOL dynamics comprehension toward optimized performance

After successful implementation of the VECSOL concept and the satisfactory preliminary results achieved hereby, in the following, we have carried out studies toward better understanding of the VECSOL dynamics via theory as well as the simulations. The analyses will help to understand how variations of different parameters such as cavity length or pump pulse duration would affect the emission behaviors. The results obtained in this way were used as a tool to improve the VECSOL performance by scavenging through and optimizing the VECSOL composing elements that eventually led to obtain the highest reported conversion efficiency within the organic laser family operating in thin film configuration.

3.4.1 Derivation of intramolecular and cavity rate equations applied to the VECSOL geometry

In this section, the intramolecular rate equations of a four-level system incorporated into a laser cavity followed by the cavity rate equation are developed to derive a set of coupled equations, known as the "Tang-Statz-de Mars" rate equations which would be useful to analyze the fundamental aspects of the realized VECSOL.

For this purpose, we start by derivation of the general rate equation which will be then applied to the VECSOL case. Deriving the first rate equation will help us following the evolution of the energy states taking part in laser action; the second equation will evidence the time-varying intensity or equivalently the number of photons propagating within a single laser mode before reaching steady-state.

Recall the simplified rate equations of a four level system, developed in the first chapter. They were as the following:

$$\left\{\begin{array}{l} N = N_{0,0} + N_{1,0} \\ \dfrac{dN_{0,0}}{dt} = -\sigma_{01(0,n)} I_p N_{0,0} + \sigma_{e(0,v)} I N_{1,0} + \dfrac{N_{1,0}}{\tau_{10}} \\ \dfrac{dN_{1,0}}{dt} = \sigma_{01(0,n)} I_p N_{0,0} - \sigma_{e(0,v)} I N_{1,0} - \dfrac{N_{1,0}}{\tau_{10}} \end{array}\right\} \qquad (3.30)$$

It should be noted that these equations correspond to a four-level system with several considerations. In derivation of these equations it is supposed that there is no triplet state population via ISC and no absorption from the first excited singlet state toward upper singlet state levels ($S_1 \rightarrow S_n$). In addition it is assumed there are no internal conversion (IC), quenching and photodegradation effects. These equations govern the case of single-mode laser (single frequency together with single spatial mode). However, what we observed in the case of VECSOL was a highly multimode emission. Therefore, in application of these equations to the VECSOL case that comes in the following, enough precautions should be taken.

Before to further proceed in this discussion, perhaps it would be easier to use simpler notations than what appeared in the above equations for absorption and emission cross sections. In the first chapter, for pedagogical reasons these parameters were introduced under the above-presented format. From now on, for sake of simplicity, a very simple four-level system with convenient notations as just presented in Figure 3.25 will be the basis of the equations and relations appearing hereafter in this context.

Pump wavelength	λ_p
Laser emission wavelength	λ_l
Absorption cross section at λ_p (cm^2)	σ_p
Emission cross section at λ_l (cm^2)	σ_{em}
Absorption cross section at λ_l (cm^2)	$\sigma_{abs} = \sigma_{em}$
Radiationless transition rates (1/s)	$\gamma_{3,2}$ $\gamma_{1,0}$
Excited – state lifetime (s)	τ
Emission intensity at λ_l (photons / s / cm^2)	I
Emission intensity at λ_p (photons / s / cm^2)	I_p

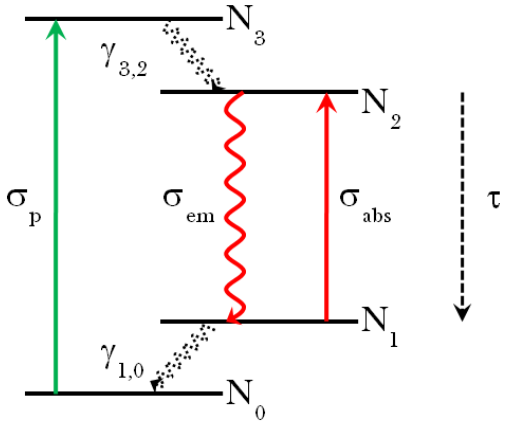

Figure 3.25 - Illustration of a four-level system with simplified notations in comparison to what presented earlier in chapter 1. The table is showing different parameters related to the various transitions in above presented system.

Given the above-illustrated four-level system, simplified in notations, the set of equations in (3.30) can be rewritten as the following:

$$\left\{\begin{array}{l} N = N_0 + N_2 \\ \dfrac{dN_0}{dt} = -\sigma_p I_p N_0 + \sigma_{em} I N_2 + \dfrac{N_2}{\tau} \\ \dfrac{dN_2}{dt} = \sigma_p I_p N_0 - \sigma_{em} I N_2 - \dfrac{N_2}{\tau} \end{array}\right\} \tag{3.31}$$

It should be reminded that these equations are obtained under the assumptions of $\gamma_{1,0}$ and $\gamma_{3,2} >> \tau^{-1}$ and thus, at a given time $N_1 \simeq 0$ and $N_3 \simeq 0$.
We continue our discussion by giving the following relation as a consequence of the set of equations described in (3.31)

$$\frac{dN_0}{dt} + \frac{dN_2}{dt} = \frac{dN}{dt} = 0 \tag{3.32}$$

This expression is always true since the total number of atoms in a closed system should be constant at a given time.
If $\Delta N(cm^{-3})$ is defined as the population difference between the energy levels of the laser transition, (i.e. $\Delta N \triangleq N_2 - N_1 \approx N_2$) then the last equation in (3.31) can be rewritten as the following:

$$\frac{d\Delta N}{dt} = \sigma_p I_p N - \left[\sigma_p I_p + \sigma_{em} I + \frac{1}{\tau}\right]\Delta N \tag{3.33}$$

A useful parameter for the following discussion is the effective loading time (τ_{eff}) of the gain medium under excitation. In order to obtain an expression of τ_{eff}, let us consider a "top-hat" pump profile as the following

$$I_p = \begin{cases} \text{Constant} & 0 < t < T_p \text{(pulse duration)} \\ 0 & \text{elsewhere} \end{cases} \tag{3.34}$$

With the above assumption, the analytical solution to equation (3.33) in a particular case of unsaturated condition when the laser intensity $I = 0$, will be in the form:

$$\Delta N(t) = \Delta N_0 \left(1 - e^{-\frac{t}{\tau_{eff}}} \right) \tag{3.35}$$

Where $\tau_{eff}(s)$ is defined as the characteristic time during which the N_2 energy state is getting populated when the emission intensity is assumed to be $I = 0$. ΔN_0 is the maximum non-saturated population inversion. From (3.33) these parameters are given by:

$$\tau_{eff} = \frac{1}{\sigma_p I_p + \frac{1}{\tau}} \tag{3.36}$$

$$\Delta N_0 = \sigma_p I_p N \tau_{eff} \tag{3.37}$$

By these notations, the equation (3.33) can be rewritten as:

$$\frac{d\Delta N}{dt} = \frac{1}{\tau_{eff}} \left[\Delta N_0 - \left(1 + \frac{I}{I_{sat}} \right) \Delta N \right] \tag{3.38}$$

where I_{sat} (Photons / s / cm^2) is the saturation intensity, that is, the intensity that passes through the gain medium and saturates the gain coefficient to half of its unsaturated value ($g_{local} = \sigma_{em} \Delta N$) and is given by:

$$I_{sat} = \frac{1}{\sigma_{em} \tau_{eff}} \tag{3.39}$$

Equation (3.33) simplified to (3.38) under the condition of constant pump profile, is one of the Tang-Statz-de Mars rate equations which accounts for the population inversion evolution in a four-level system gain medium under excitation in a pulsed regime.

To proceed with this argument and derive the cavity rate equation which shows the evolution of the intracavity laser intensity or the accumulated photons number inside the cavity, consider the VECSOL resonator comprising a gain medium with index n having a thickness d and two mirrors with reflectance R_1 and R_2 separated by distance L_{cav} (Figure 3.26).

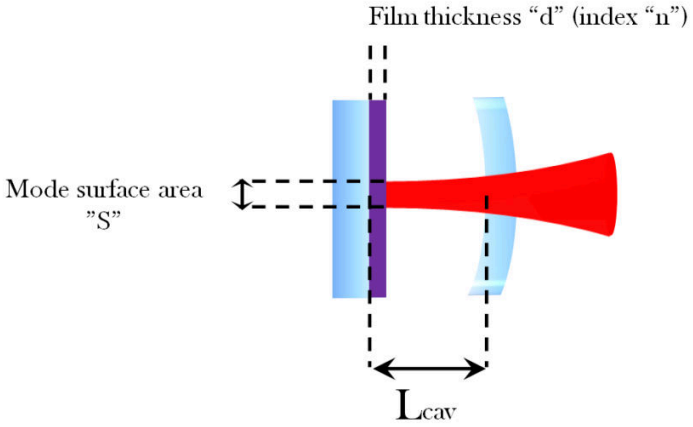

Figure 3.26 - Schematic representation of the VECSOL cavity with the corresponding designated notations for each composing element.

If μ (Photons / cm^3) is the density of laser photons in a volume limited by the mode surface area S (cm^2) over a distance dz (cm) and I (Photons / s / cm^2) is holding for the number of photons passing through the mode section with the light velocity c (in air) during time $dt(s)$, then we will have:

$$\mu S dz = I S dt \rightarrow I = \mu \frac{dz}{dt} \rightarrow I = \mu c \tag{3.40}$$

If the whole volume occupied inside the cavity by the laser mode is defined as V_{modal}, then we will find out that I (the intensity within a given laser mode) and q (the number of photons in this volume inside the cavity) are interchangeable terms since we have:

$$q = \mu V_{modal} = \frac{I}{c} V_{modal} \tag{3.41}$$

Since V_{modal} is occupying a hybrid region comprising the air and a gain medium of index n, then q can be decomposed into two distinguished terms as the following:

$$\begin{aligned} q &= \left(\frac{I}{c/n}\right)^{\text{Active volume}} \overbrace{Sd} + \left(\frac{I}{c}\right) S\left(L_{cav} - d\right) \\ &= \left(\frac{I}{c}\right) S \underbrace{\left[(n-1)d + L_{cav}\right]}_{L} = \frac{I}{c} V_{modal} \end{aligned} \tag{3.42}$$

This let us to introduce an optical path length L as indicated in the brackets and will be used later on as we proceed in this discussion.

q is a time-varying parameter. Let's for the moment forget about the contribution of the spontaneous emission in variation of q. With this assumption, the evolution of q, on one hand will depend on the cavity losses mainly imposed by the cavity out-coupling[13] and on the other hand, on the amplification achieved through stimulated emission process. These statements can be written as:

$$\frac{dq}{dt} = (Sd)(\sigma_{em} I)\Delta N - \frac{q}{\tau_{cav}} \tag{3.43}$$

Or through (3.41) , it can be equivalently expressed as:

$$\frac{dI}{dt} = \frac{cd}{L}(\sigma_{em} I)\Delta N - \frac{I}{\tau_{cav}} \tag{3.44}$$

where $\tau_{cav}(s)$ is the intracavity photon lifetime. The expression of τ_{cav} is as the following (see appendix 6 for calculation).

$$\tau_{cav} = -\frac{2L}{cLn\left[R_1 R_2 (1-T_i)^2\right]} \tag{3.45}$$

where R_1 and R_2 are the cavity mirror reflectivities and T_i is the cavity passive losses in a single-way beam trip.

Given that at the steady-state $(dq/dt) = (dI/dt) = 0$, then from (3.44) we can define $\Delta N_{ss}(cm^{-3})$ as the inverted population at steady-state as the following:

$$\Delta N_{ss} = \frac{L}{\sigma_{em}\tau_{cav} cd} \tag{3.46}$$

ΔN_{ss} can also be interpreted as the minimum required population inversion at threshold. Therefore, the equation (3.44) can be reconfigured under the general form of:

$$\frac{dI}{dt} = \frac{I}{\tau_{cav}}\left(\frac{\Delta N}{\Delta N_{ss}} - 1\right) \tag{3.47}$$

[13] The other losses could be due to material absorption or scattering.

Given that here we are not dealing with a continuous-wave laser, whatever happens during the oscillation buildup time is of great importance in our case. Therefore, we are particularly interested at the very initial conditions or the oscillation buildup origin. The laser oscillation builds up from the spontaneously-emitted photons. This fact is not considered at the equation being presented in (3.47). In fact, if we assume that $I = 0$ in (3.47), then logically one concludes that $(dI/dt) = 0$ at any time which is not physically true since the laser emission starts up from some "noises" which is spontaneous emission and equation (3.47) does not take it into account.

Therefore, in the following we try to reconsider this equation by taking into account the effect of the spontaneous emission. Of course, only the fraction of the spontaneous emission which is taking place within a cavity mode is the appropriate term that should be considered.

Based on quantum mechanics, the spontaneous emission rate within a given cavity mode is as probable as the stimulated emission rate by a single photon in the same mode [162].

The number of photons in a single cavity mode emitted per molecule via stimulated emission process during a second ($\sigma_{em} I$) can be expressed in the following way:

$$\sigma_{em} I = \kappa q \tag{3.48}$$

where $\kappa(1/s)$ is the probability of stimulated emission by one photon in a single cavity mode. By replacing q from (3.41) we will have:

$$\kappa = \sigma_{em} \frac{c}{V_{modal}} \approx \sigma_{em} \frac{c}{SL} \tag{3.49}$$

The approximation sign in (3.49) is because SL is the approximation of the modal volume (V_{modal}) for a cavity with small divergence ($S >> \lambda^2$ where λ is the oscillating wavelength). Upon putting $q = 1$ in (3.48) and considering that the total number of molecules in the active region is equal to $N_2(Sd)$, then the growth rate of q due to the spontaneous emission within the single cavity mode can be expressed as:

$$\left(\frac{dq}{dt}\right)_{\text{Spontaneous emission}} = \kappa N_2(Sd) = \left(\frac{cd}{L}\right)\sigma_{em} N_2 \tag{3.50}$$

Using (3.42) and considering the fact that $\Delta N = N_2 - N_1 \approx N_2$, then we will have:

$$\left(\frac{dI}{dt}\right)_{\text{Spontaneous emission}} = \left(\frac{c^2 d}{SL^2}\right)\sigma_{em}\Delta N \tag{3.51}$$

Addition of this term to the simplified rate equation found in (3.44), will provide the cavity rate equation taking into account all the contributive factors in the evolution of intracavity laser intensity within a single cavity mode as the following:

$$\begin{aligned}\frac{dI}{dt} &= \frac{I}{\tau_{cav}}\left(\frac{\Delta N}{\Delta N_{ss}} - 1\right) + \left(\frac{c^2 d}{SL^2}\right)\sigma_{em}\Delta N \\ &= \frac{1}{\tau_{cav}}\left[\frac{\Delta N}{\Delta N_{ss}}\left(I + \frac{c}{SL}\right) - I\right]\end{aligned} \tag{3.52}$$

Equations found in (3.33) and (3.52) represent the well-known Tang-Statz-de Mars rate equations, summarized in the following frame:

$$\boxed{\begin{aligned}\frac{d\Delta N}{dt} &= \sigma_p I_p N - \left[\sigma_p I_p + \sigma_{em} I + \frac{1}{\tau}\right]\Delta N \\ \frac{dI}{dt} &= \frac{1}{\tau_{cav}}\left[\frac{\Delta N}{\Delta N_{ss}}\left(I + \frac{c}{SL}\right) - I\right]\end{aligned}} \tag{3.53}$$

In the following, we have exploited this set of coupled equations to run a series of numerical simulations that describe the VECSOL emission behavior in regard with the obtained experimental results. It should be reminded that the equations developed in the above are governing the case of a single mode cavity and they are not fully adapted for the emission analysis of the VECSOL since we deal with a multimode emission from a coupled cavity made of an external resonator together with the microcavity formed by the gain medium. Therefore, the theory described in this section can be only useful for "very approximate" analysis of the observed emission characteristics.

3.4.2 VECSOL emission behavior simulations

In this part, the equations developed in the last section are used to run series of simulations which would help us to understand the observed behavior during experiments upon variation of different parameters (i.e. pump pulse duration or cavity length). To validate the model relevancy, in the beginning the model is confronted with the experimental results. Following this demonstration and approval, some theoretical cases are considered and in the end we will see how the model served as a tool for device performance optimization. Below, the necessary parameters, used in the simulations, are summarized in the given tables.

- Design parameters

Pump energy	0 to 17 μJ
Pump beam diameter	140 μm
Plane mirror reflectivity (R_1)	99.5%
Output coupler reflectivity (R_2)	98%
Cavity length (L)	5 mm[14]
Gain medium thickness	17-18 μm
Gain medium effective length (ℓ_{eff})	8.45 μm
Rhodamine 640 doping rate in PMMA	1 wt. %
Film absorption at pump wavelength (532 nm)	~ 80%
Single-way intracavity passive losses(T_{int})	1%
Pump wavelength	532 nm
Laser emission wavelength	640 nm

- Material parameters

Refractive index of the medium (n)	1.5
Number of dye molecules for 1 wt. % doping rate (N) per cm^3	1.22×10^{19}
Rhodamine 640 radiative lifetime (τ)	7.5 ns
Stimulated emission cross section (σ_{em}) in cm^2	2×10^{-16}
Absorption cross section at pump wavelength (σ_p) in cm^2	0.77×10^{-16}

[14] For all theoretical simulations in the following the cavity length is considered to be 5 mm, except in case of model validation (section 3.4.2.1), the cavity length is 4 mm to match the experimental condition.

- ✓ The effective length (ℓ_{eff}) is calculated based on the relation given in (3.21).

- ✓ Choice of τ: the value of 7.5 ns, appeared in the table, corresponds to the radiative emission lifetime of Rhodamine 640 in PMMA film measured by Ramon et al. [106].

- ✓ The absorption cross section at pump wavelength (σ_p) is calculated from the Beer-Lambert's law.

$$\sigma_p = \frac{-\mathrm{Ln}(T)}{NL} = -\frac{\mathrm{Ln}(0.2)}{(1.22\times10^{25})(m^3)\times(17\times10^{-6})(m)} = 0.77\times10^{-16}\,cm^2 \qquad (3.54)$$

where T is the transmission, L is the cavity length and N (see appendix 4 for estimation of N) is the number of dye molecules.

- ✓ Choice of σ_{em}: the value of σ_{em} is calculated from the Füchtbauer-Ladenburg equation:

$$\sigma_{em}(\lambda) = \frac{\phi_f f(\lambda)}{8\pi n^2 c\tau \int \frac{f(\lambda)}{\lambda^4} d\lambda} \qquad (3.55)$$

where λ is the wavelength, ϕ_f is the fluorescence quantum yield, $f(\lambda)$ is the fluorescence spectrum normalized to one, n is the medium refractive index, c is the speed of light in air and τ is the radiative lifetime.
For Rhodamine 640 in PMMA, by taking $\tau = 7.5$ ns, $n = 1.5$ and $\varphi_f \simeq 0.8$ (based on the values reported in [105] for other Rhodamine dyes in bulk PMMA) σ_{em} is estimated to be around 2×10^{-16} at 640 nm.

3.4.2.1 Model validation

Before applying the developed model to the study of some general cases, in the following we first validate our model by confronting it with the experimentally-obtained efficiency curves corresponding to two different pump pulse durations (0.5 ns and 7 ns), presented earlier in section 3.3.1.

Recall that the experiment was carried out on a 4-mm-long VECSOL comprising an ~18-µm-thick gain medium based on 1wt% of Rhodamine 640 dispersed in PMMA-A15 (see appendix 3 for more information on this PMMA type) and two cavity mirrors with $R_1 = 99.5\%$ and $R_2 = 98\%$.

Figure 3.27 is showing the experimentally obtained efficiency curve for the case of 7-ns-long pulse excitation. The model based on the given parameters in the above tables gives the solid line which is in rather good agreement with the experimental data. For sake of simplicity, the pump intensity profile for this simulation and the following ones is a top-hat intensity profile. Note that it is quite easy to obtain a perfect fit to the experimental data by letting σ_{em}, σ_p and T_{int} as fitting parameters. However, as the objective of the present section is to validate the experimental orders of magnitude, we fixed the values used for $\sigma_{em.}$ and σ_p (although, especially for $\sigma_{em.}$ this assumption is associated with a high degree of uncertainty) and used T_{int} as the only fitting parameter.

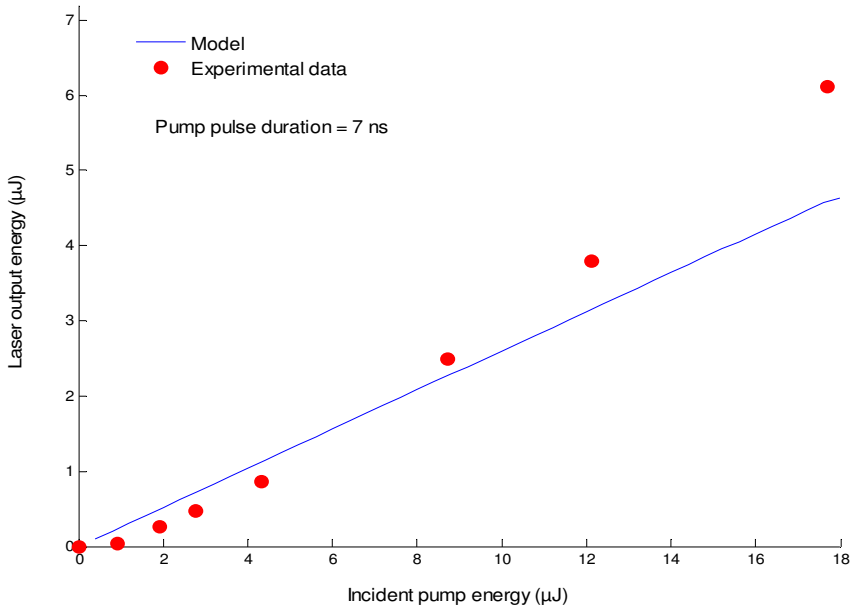

Figure 3.27 – Comparison between experimental VECSOL output energy and theoretical value based on the developed model as a function of incident pump energy. The graph corresponds to a cavity length of 4 mm and pump duration of 7 ns. The only fitting parameter is the roundtrip cavity loss which is set to 2%.

From the above curve the following parameters are deducible:

- ✓ Optical/optical experimental efficiency : 34,5%
- ✓ Theoretical efficiency : 25.7%
- ✓ Experimental slope efficiency (with respect to incident pump fluence) : 41.5%
- ✓ Theoretical slope efficiency : 26%

The same kind of comparison (without any other fitting parameter) is performed between theory and experiment for the case of 0.5-ns-long pulse duration (Figure 3.28). In this case, the fit shows to be proper and efficiencies turn out to be closer to reality.

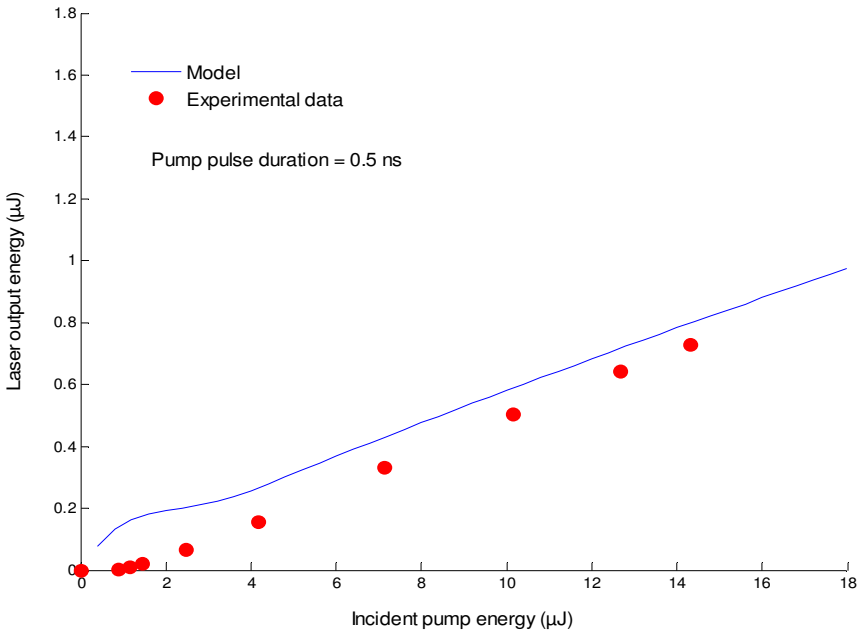

Figure 3.28 - Comparison between experimental VECSOL output energy and theoretical value based on the developed model as a function of incident pump energy. The graph corresponds to a cavity length of 4 mm and pump duration of 0.5 ns. The only fitting parameter is the roundtrip cavity loss which is set to 2%.

From the above curve the following parameters are deducible:

- ✓ Optical/optical experimental efficiency : 5%
- ✓ Theoretical efficiency : 5.5%
- ✓ Experimental slope efficiency (with respect to incident pump fluence) : 5.3%
- ✓ Theoretical slope efficiency : 4.85%

The anomalous behavior seen in the beginning of the theoretical model in Figure 3.28 is related to the top-hat pump intensity profile used for the simulations.

In both curves, the laser threshold and the slope efficiency tend to be underestimated (specially the threshold). However, with the only adjustable parameter of $T_{int} = 0.01$, we obtain a good order of magnitude for the efficiency values in two different experimental cases. This validates the relevance of the applied model for a better understanding of the influence of the different physical parameters on the emission behavior.

Let us now have a physical insight into difference observed between the two efficiencies. Given the above model verification, in the following we have modeled the emission transient behavior to understand different efficiency values obtained for two excitations regimes (0.5 ns and 7 ns).

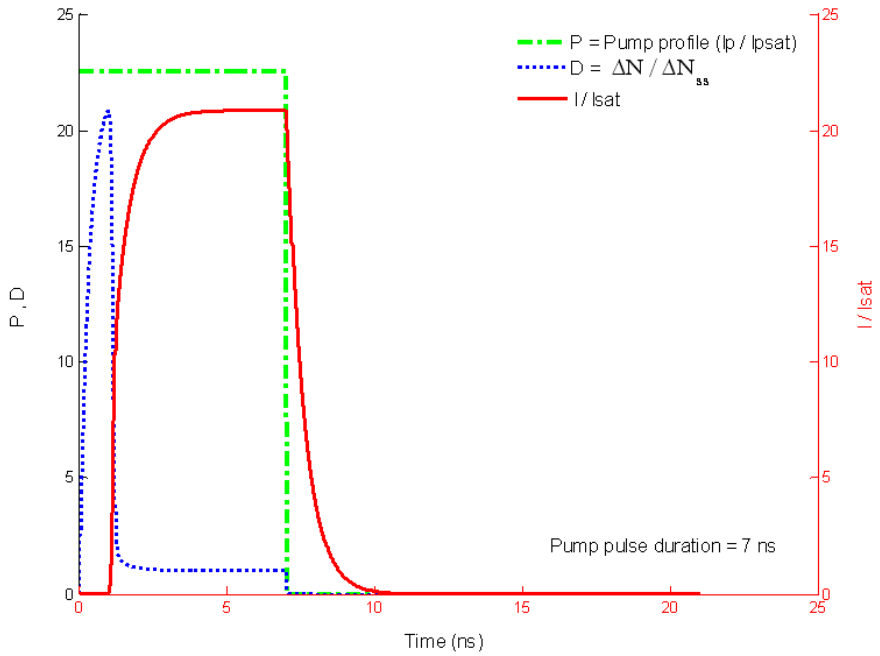

Figure 3.29 – Temporal analysis of a 4-mm-long VECSOL cavity under 7-ns-long pulse excitation regime. The amounts of P and D in the graph correspond to the experimental values.

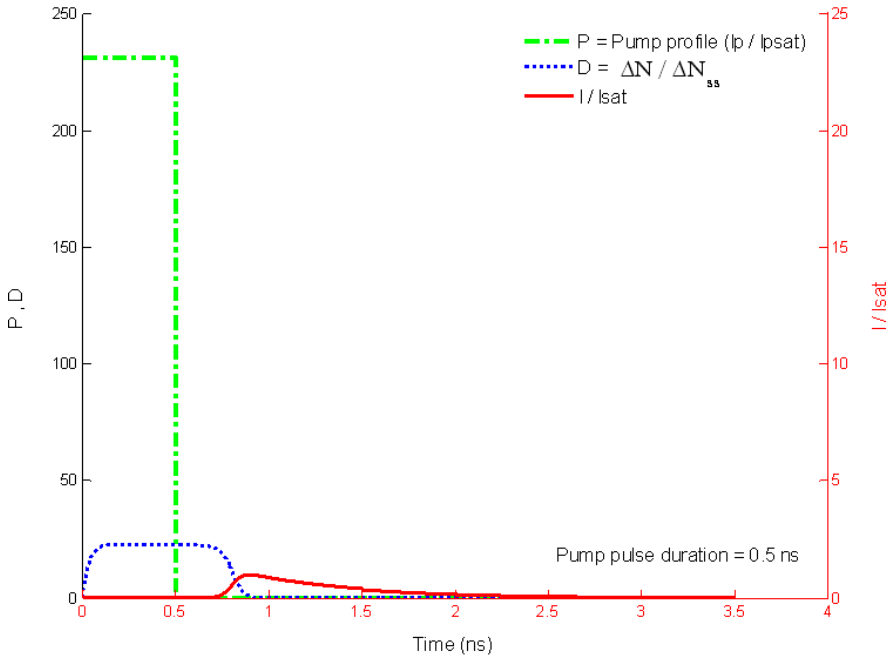

Figure 3.30 - Temporal analysis of a 4-mm-long VECSOL cavity under 0.5-ns-long pulse excitation regime. The amounts of P and D in the graph correspond to the experimental values.

In the above figures:

- Ip is the top-hat pump intensity profile.
- Ipsat is the saturation pump intensity and is given by:

$$\text{Ipsat} = \frac{1}{\sigma_p \tau} \tag{3.56}$$

  where σ_p (cm^2) is the absorption cross section at pump wavelength and τ is the radiative emission lifetime.
- ΔN is the inverted population and ΔN_{ss} is the minimum population inversion to reach the lasing threshold.
- I is the intracavity intensity.
- Isat is the saturation intensity ($I_{sat} = 1/\sigma_{em}\tau_{eff}$) which passes through the gain medium and saturates the gain coefficient to half its unsaturated value.
- P is the ratio of $Ip / Ipsat$.
- D is the ratio of $\Delta N / \Delta N_{ss}$.

  $D > 1$ represents the condition where the gain becomes superior to losses.

The above graphs are the temporal simulations which correspond to the experimental conditions where the cavity length was 4 mm. The values of P and D in the above-presented cases correspond to the values used for the measurements.
According to the model, by exciting the VECSOL with 7-ns-long pulses and 10 Hz repetition rate (Figure 3.29), the laser oscillation builds up in a rather short time with respect to the pump pulse duration. In this case steady state is reached before the pulse finishes and lasts till the end of the pulse which causes an efficient extraction of the stored energy during 7 ns and thus very high energy conversion efficiency. By pumping the cavity with 0.5-ns-long pulses and for the same cavity length (4 mm) (Figure 3.30), the laser intensity does not have enough time to build up since it barely reaches the I_{sat} value and thus, the inverted population will not be significantly depleted. As a consequence the stored energy will not be efficiently extracted. In this case the created population inversion lasts for ~ 0.25 ns after the end of the pump pulse and before the beginning of laser oscillation buildup since the excited-state lifetime (7.5 ns) [106] is longer than the pulse duration. When laser oscillation starts, the pump pulse has already terminated and the population inversion has a descending trend to zero and the steady sate will never be reached. Therefore, the conversion efficiency would be low in this case.

3.4.2.2 VECSOL output energy and efficiency vs. pump pulse duration

In the preceding section, the pump pulse time-dependant behavior of the VECSOL for two examined pulse durations of 0.5 ns and 7 ns were justified through temporal analysis achieved via Tang-Statz-de Mars rate equations applied to the VECSOL geometry. In the following, first, the same equations are used for theoretical calculation of the VECSOL output energy and then the VECSOL efficiency, when the pump pulse duration is varied in a continuous manner during 2.5 ns. For this purpose, a cavity length of 5 mm together with a constant pump peak power of 3 kW (corresponding to $P = (Ip / Ipsat) \simeq 26$) are considered.

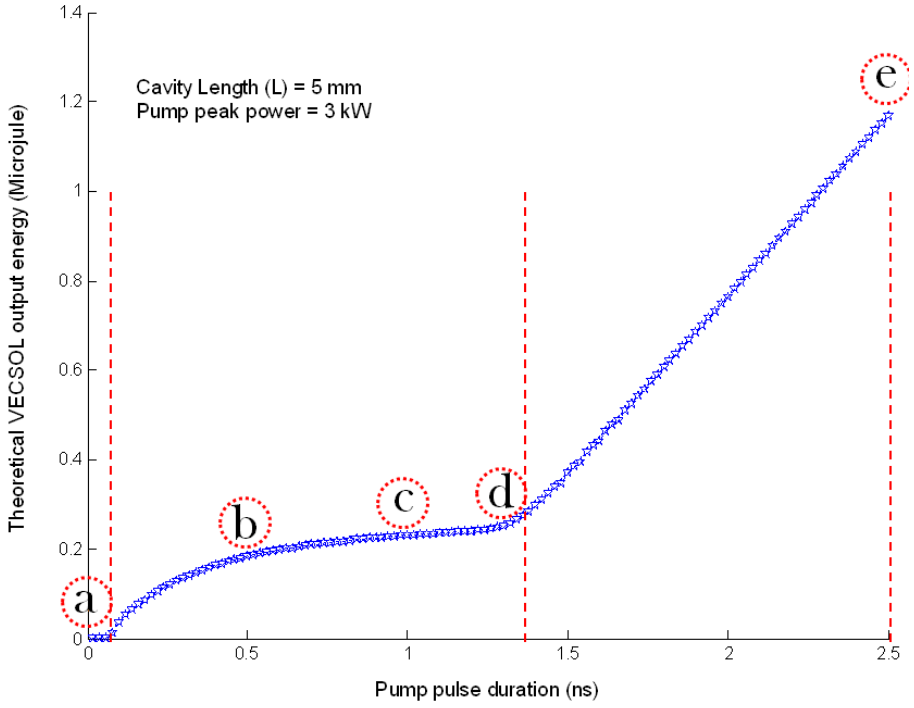

Figure 3.31 – Evolution of the VECSOL output energy versus pump pulse duration.

In the above figure, one can distinguish three different regimes. As we see in the very beginning the output energy is almost zero and then as the pulse duration increases it starts to grow in a nonlinear way when finally after a certain time the output energy increases linearly with the pump pulse duration.

This behavior can also be verified in terms of energetic efficiency, where the saturation toward the continuous-wave (CW) regime is clearly seen (Figure 3.32). It can be observed that for a 5-mm-long cavity, pulse durations longer than ~ 7 ns would not be very useful to improve the efficiency. However, as the oscillation buildup time is directly related to the cavity length L, the longer the cavity, the longer the pump pulse duration should be to obtain a good efficiency value.

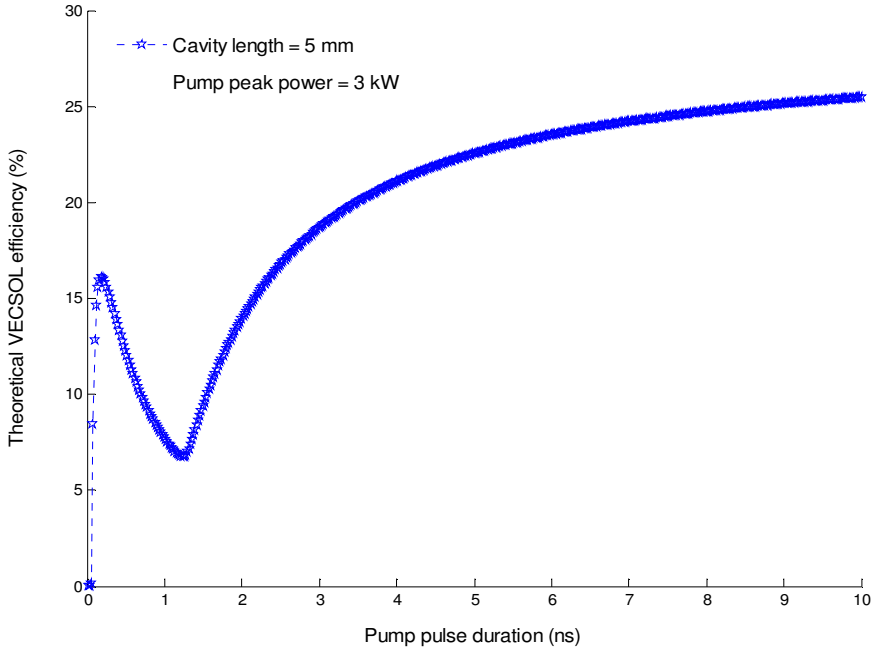

Figure 3.32 - Evolution of the VECSOL efficiency versus pump pulse duration.

In the very beginning, once the oscillation is built up, the VECSOL efficiency starts to increase. But within a pulse duration interval starting from below 0.1 ns to around 1.3 ns, the efficiency has a decreasing trend. From $Tp \simeq 1.3$ ns onward, the VECSOL behavior tends toward continuous-wave (CW) regime.

In order to understand the evolution of the output energy and efficiency with pump pulse duration, temporal analysis for five different pulse durations within 2.5 ns corresponding to different time spots, chosen within three observable regimes in Figure 3.31, are carried out and are sequentially presented in the following series of graphs (Figure 3.33).

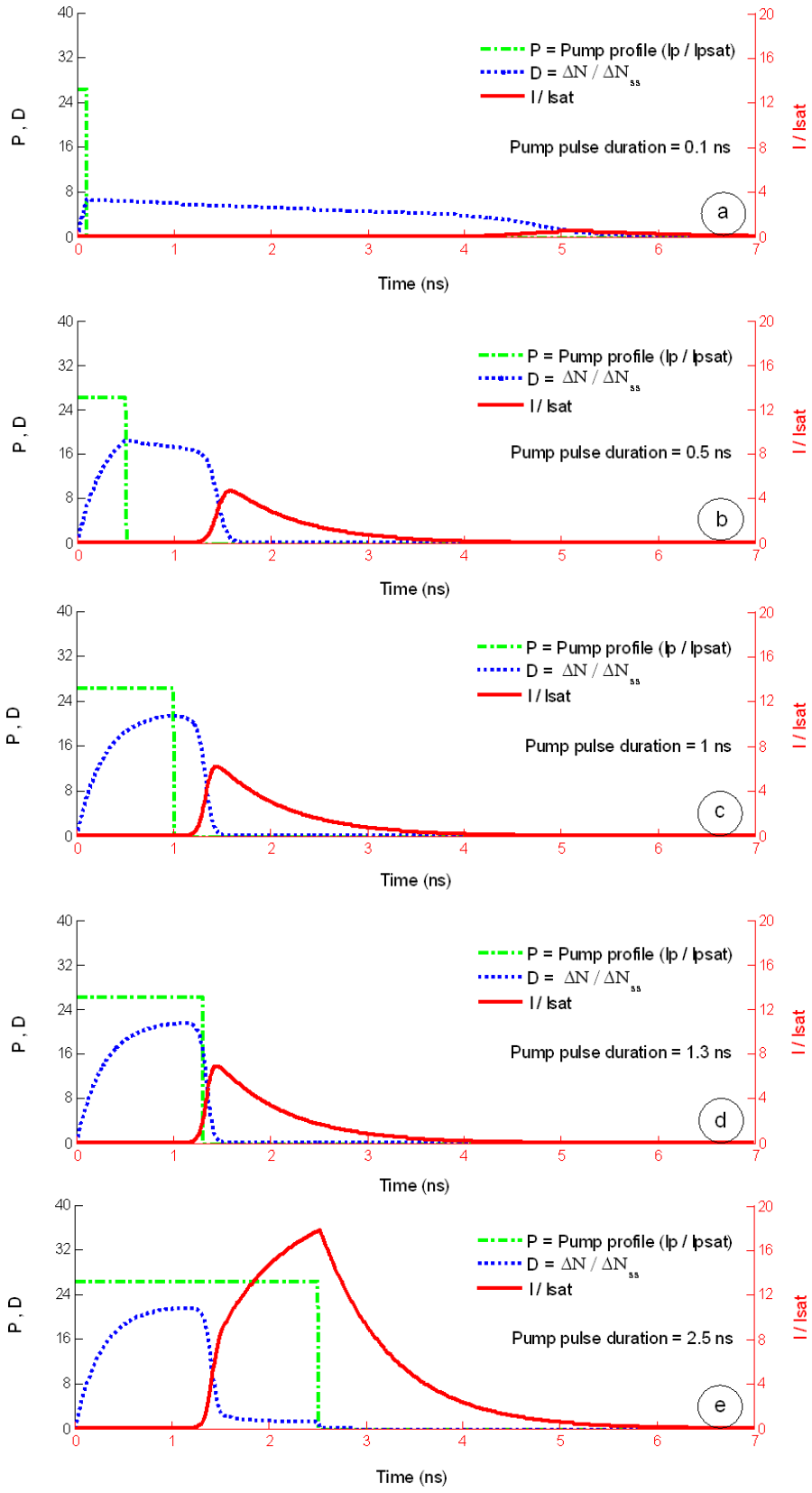

Figure 3.33 – Temporal analysis of the VECSOL for different pulse durations.

The first graph tagged with encircled “a” sign at the bottom right of the figure corresponds to a pump pulse duration of Tp = 0.1 ns. In this case, the created population inversion within 0.1 ns lasts for about 6 ns which is consistent with the 7.5 ns value taken for the radiative lifetime [106]. This case corresponds to the condition where $D \simeq 6$ which guarantees that stimulated emission is able to overcome the losses. However, as the gain is low and the time taken by a photon to travel through air is much longer than the time it takes to travel the gain region, the laser intensity does not grow sufficiently to reach the value of I_{sat}. The resulting laser pulse arrives much after the pump pulse duration, lasts quite a long time (≥ 1 ns) in comparison to the pump duration and is very small in intensity. Obviously, this regime is not useful in practice.

Cases “b” and “c”, correspond to Tp = 0.5 ns and Tp = 1 ns respectively. They represent a situation, within the curve of Figure 3.31, where I_{sat} is reached. However, as the oscillation builds up after the end of the pump pulse, the steady state will never be approached. In these cases, the inverted population will be consumed to create the laser pulse but it will never be replaced since the pump has already terminated. This situation continues till $Tp \simeq 1.3$ ns (case “d”) when the oscillation starts to build up within the pulse time period. From now on, if the pump pulse duration increases, oscillation buildup time will fall within the pump pulse duration. Thus, I_{sat} is reached during the pulse duration which causes the inverted population (ΔN) to decrease rapidly and clamp to the threshold value ($\Delta N = \Delta N_{ss}$). In this case, the laser intensity evolves toward a stationary value which corresponds to the steady state intensity in the continuous-wave (CW) regime.

3.4.2.3 VECSOL pulse width and output peak power vs. pump pulse duration

Following the above demonstration, it would be also interesting to see the evolution of the VECSOL emission pulse width as a function of the pump pulse duration and the associated peak power that can be obtained from our structure. Therefore, the same condition presumed for the above simulations are also considered here. That is, a 5-mm-long VECSOL cavity, excited at a pump peak power of 3 kW (Figure 3.34).

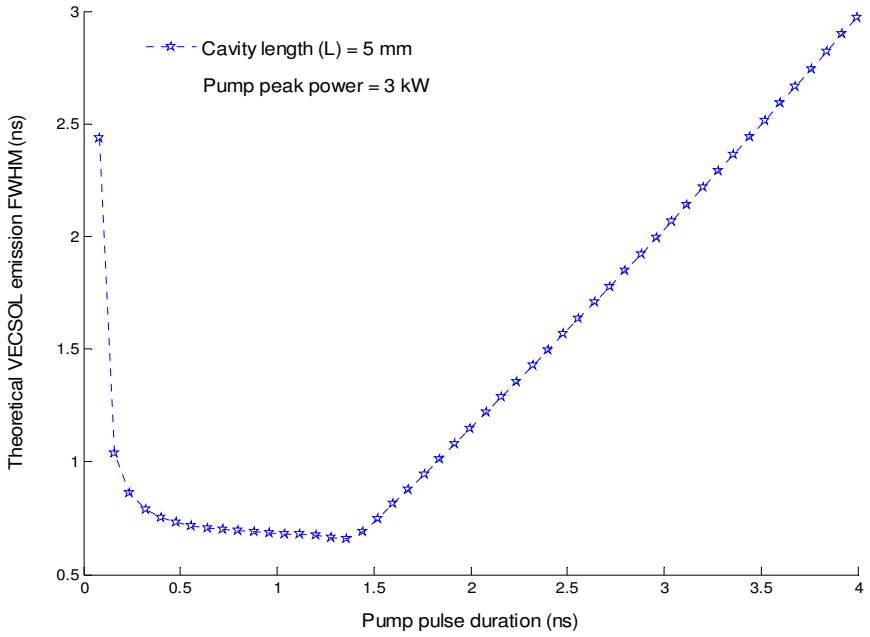

Figure 3.34 - Evolution of the VECSOL pulse width versus pump pulse duration

The pulse width starts from a high value when the oscillation is not built up yet and then reduces rapidly to below 1 ns till it reaches the pulse duration of $Tp \simeq 1.3$ ns. The fact that the for pump pulse durations up to 1.3 ns the pulse width reduces very fast is because that in this case the pulse starts to build up after the end of the pump pulse and grows very fast to I_{sat}. Therefore, the created inversion is rapidly depleted with the consequent of rapid ending of the laser pulse.

Based on temporal analysis in Figure 3.33, from $Tp \simeq 1.3$ ns, the oscillation starts to build up within the pump pulse and the pulse width increases along with pump pulse duration.

Now, it is interesting to wonder if during the regime where the VECSOL pulse width becomes shorter than the pump pulse duration, higher peak powers can be obtained or

not. As it is shown in Figure 3.35, the peak power is always increasing with Tp and thus, this region is not very useful for practical applications.

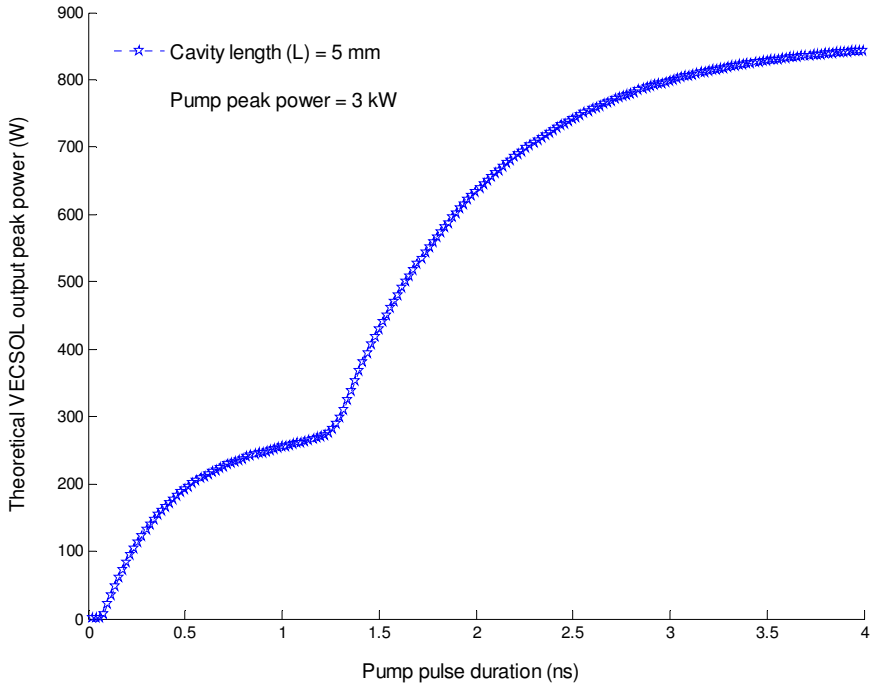

Figure 3.35 - Evolution of the VECSOL output peak power versus pump pulse duration

3.4.2.4 VECSOL efficiency vs. cavity length

Consequently, as the pump pulse duration has a major effect on defining the laser efficiency, similarly the cavity length is also a crucial parameter as it directly intervenes in the oscillation buildup time for a given pump pulse duration. The longer the cavity the longer it takes for the intracavity photons to travel in air (with no gain) in comparison to the very short time spent in the gain medium and thus, the buildup time is longer. This behavior is theoretically modeled for pump pulses of 7 ns and 0.5 ns (Figure 3.36). The model is compared to the experiments, where the VECSOL energy was measured as the cavity length was increased. In both cases the VECSOL energy dropped down as the cavity length was increased. But, it was observed that the energy reduces to zero for cavity lengths more than 6 mm in case of 0.5-ns-long pulse source whereas, in case of pumping with 7-ns-long pulse source, this happened after a cavity length of more than 30 mm. The collapse in the output energy by lengthening the cavity is equivalent to reducing the pulse duration at constant cavity length.

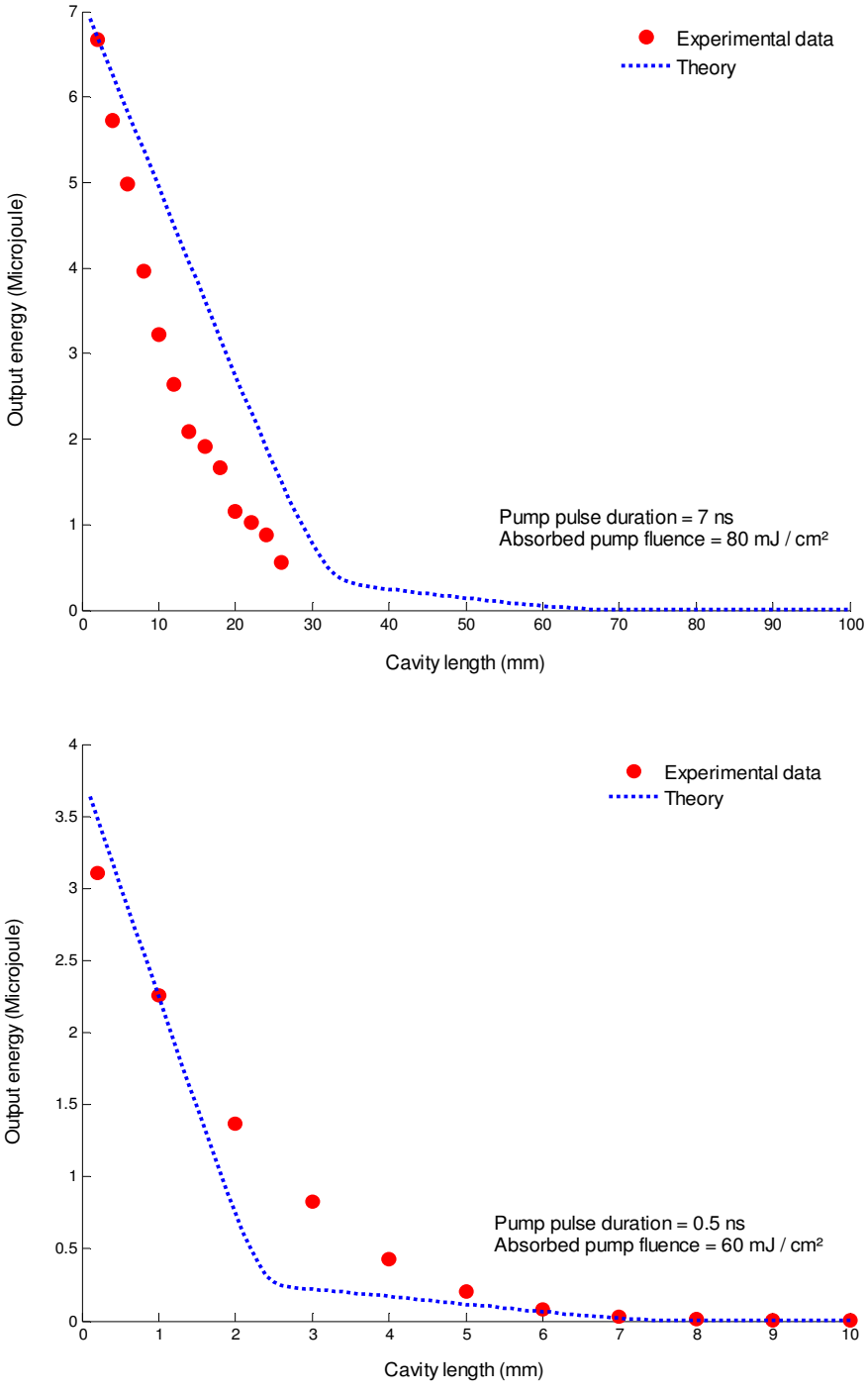

Figure 3.36 - VECSOL output energy dependency on cavity length for the pump pulse durations of 7 ns (top) and 0.5 ns (bottom). The only fitting parameter is the roundtrip cavity loss which is set to 2%.

In the above graphs, the two slopes which are seen in the theoretical curves can be explained in the same way as the two distinct regimes observed in Figure 3.31. The cavity length, for which there is a dramatic change in the slope, corresponds to the length where the laser pulse builds up right after the end of the pump pulse.

Following the above demonstration, we have modeled the VECSOL efficiency as a function of cavity length for three different pulse durations (Figure 3.37).

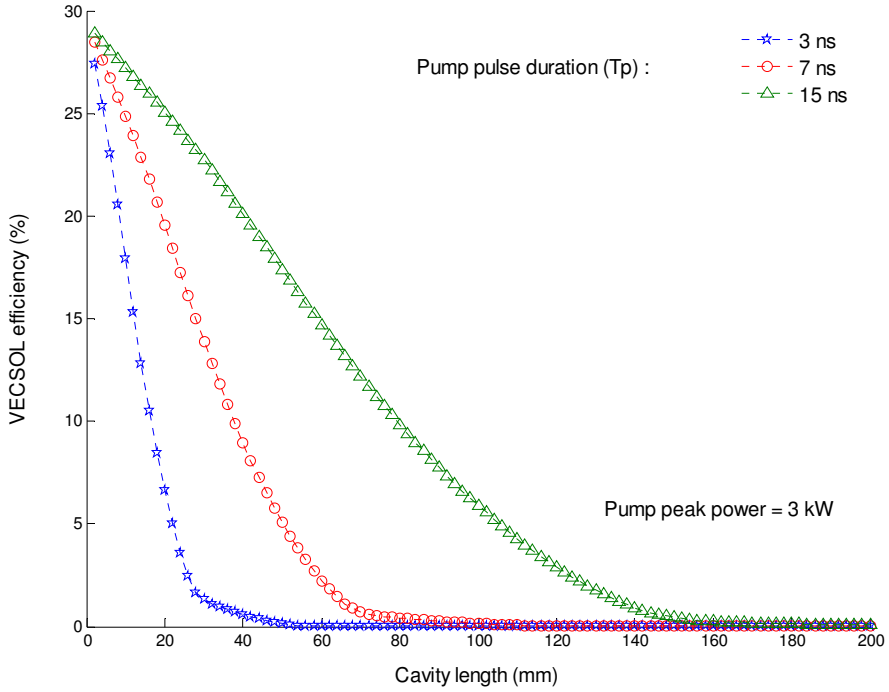

Figure 3.37 - Evolution of the VECSOL efficiency as a function of the cavity length for three different pump pulse durations.

As one can see, for a pump peak power of 3 kW, as the pump duration increases, the efficiency drops with a slower rate with respect to the cavity length. This is in fact because a long pulse offers a longer time spent near steady state regime, which enables using longer cavities.

This has an important consequence on the choice of the optimum pump source, depending on the room needed to insert optical components inside the cavity. For example, for a practical device incorporating a wavelength-selective element, a long-pulse pump source will be required.

Following the developed model validation with the preliminary-obtained results, in the next part we have used the model to optimize the VECSOL performance.

3.4.3 Optimizing VECSOL efficiency

Previously, we saw that higher efficiencies were obtained for longer pump pulse durations and shorter cavity lengths. Another criterion which would help to achieve the best lasing efficiency is to look for the optimum output coupler. The existence of an optimal output coupler is due to the fact that on one hand, one might expect an increase in the output signal intensity by decreasing the output coupler reflectivity and therefore the efficiency by reducing the mirror reflectivity. But, on the other hand this would also shorten the intracavity photon lifetime followed by a decrease in the output energy. Therefore, there is a compromise that must be respected in choosing the output coupler reflectance in order to have the best lasing performance. For this purpose the experiment was done for four different available output couplers (80%, 90%, 95% and 98%) and a cavity length fixed to 10 mm. We observed that among the examined output couplers, the highest efficiency was obtained for an output coupler of 95% reflectivity. The experimental data were then fitted by only one adjustable parameter (single-way cavity losses, $T_{int} = 0.01$). As it can be seen from Figure 3.38, the experiment and theory are in very good agreement with each other.

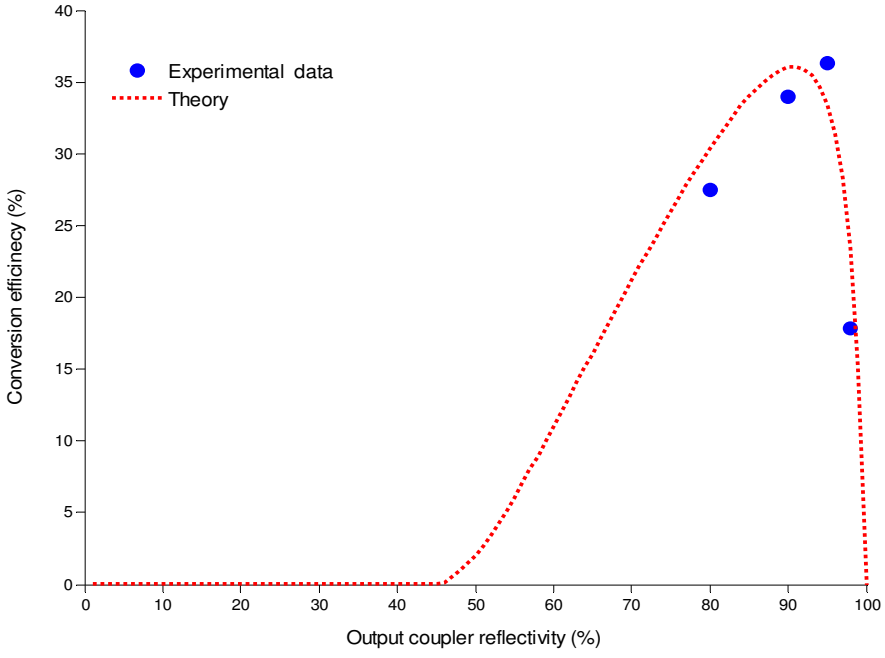

Figure 3.38 – Filled circles are the experimental data obtained for a 10-mm-long cavity length, 18-µm-thick gain medium and an incident pump fluence of $100\,mJ.cm^{-2}$. The dashed line is a model showing the evolution of the conversion efficiency by output coupler reflectivity variation from zero to hundred. The only fitting parameter is the roundtrip cavity loss which is set to 2%.

From these data, the output coupler of 98% reflectivity used in the first series of experiments was replaced by the optimized output coupler of 95% reflectivity and the VECSOL conversion efficiency was improved from 43% to 57% for a minimum possible cavity length of 1 mm (limited by the output coupler curvature and the increasing film thickness at the sample edge) when excited with pulses of 7-ns-long at 10 Hz repetition rate (Figure 3.39).

As mentioned before, the previously-obtained efficiency value of 43% which then improved also to 57% is up to now the efficiency record among the thin-film-based organic laser devices.

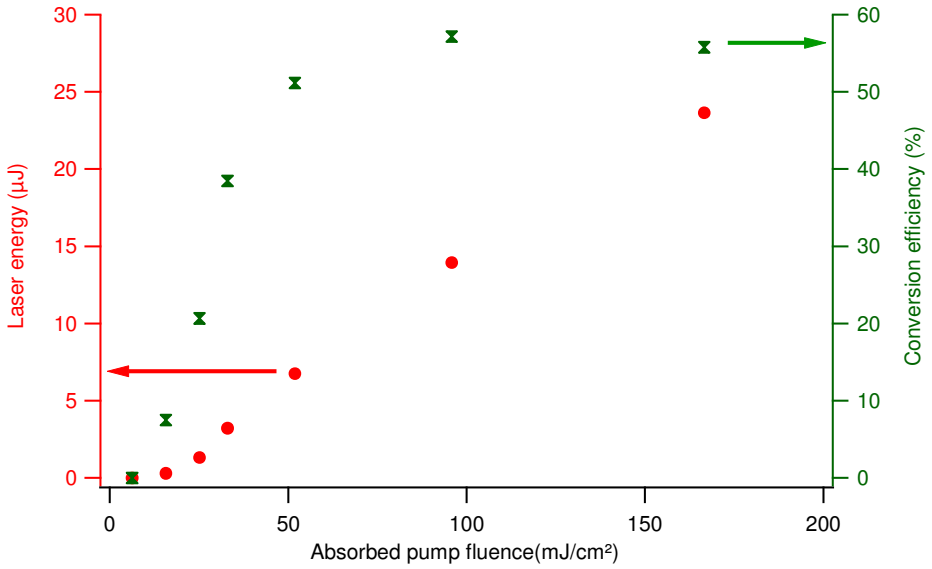

Figure 3.39 – (Left axis) Laser energy, (right axis) conversion efficiency as a function of the absorbed pump fluence for an optimum output coupler of 95% reflectivity, 1-mm-long cavity and 18-µm-thick gain medium. The small efficiency drop seen at the end could be due to degradation issues at the excitation density of more than 150 $mJ.cm^{-2}$. In this experiment, the pump beam had a spot size diameter of 180 µm .

In conclusion, the above-presented simulations gave us a better insight into the VECSOL dynamics thanks to the model which showed to be in good agreement with the experimental measurements.

Following this study, in the next part we have put a step forward to further enhance the VECSOL attractiveness (apart from its efficiency record) and for this purpose, we have shown the intracavity- frequency doubling that could be realized in VECSOL configuration.

3.5 Ultraviolet VECSOL (VESOUL) via intracavity frequency doubling

In this part, we are going to see how the open cavity of the VECSOL architecture together with a strong intracavity peak power can serve as the basis for realization of intracavity frequency doubling in a structure named VESOUL. The acronym stands for Vertical External cavity Surface-emitting Organic Ultraviolet Laser.
We start our discussion by presenting the objectives of the work, some of the existing works on this topic and then we continue by introducing some basic principles of the second harmonic generation followed by description of the resonator design and at the end, the characterization of the emission behavior achieved in this way.

3.5.1 Introduction

In the scope of realizing compact and tunable solid-state lasers, UV emission in the range extending from 200 to 400 nm is of great interest due to applications that it may find in different domains. Thus far, there have been reports of using UV laser light in various fields such as in spectroscopic studies of proteins, ionization spectrometry, chemical or biological hazard detection, laser-induced fluorescence spectroscopy, combustion diagnostics or photobiology [163]. So far, a number of approaches for obtaining coherent radiation in this wavelength region have been proposed and investigated.
One method has been through the direct UV radiation reported from rare-earth-doped crystals. The first of these devices with low and unstable laser performance was demonstrated in 1979 by Ehrlich et al. [164] in Ce: $LiYF_4$ crystal emitting at 325 nm and then in Ce: LaF_3 [165] crystal with emission at 286 nm by pumping the crystals with the 248 nm radiation of a KrF excimer laser. The efficiency of the Ce^{3+}-doped UV laser materials was then considerably improved up to 55% in Ce: $LiLuF_4$ [166] as a result of loss reduction in such materials coming from absorbing color centers [167].
Another method to obtain the UV emission has been through sum-frequency mixing from dye lasers [168], Ti-sapphire lasers, alexandrite or Cr-doped colquiriites [169]. In simple words, sum-frequency mixing is a process where two photons of frequencies ω_1 and ω_2 are served within a nonlinear process to generate another photon at frequency ω_3 with the condition of $\omega_3 = \omega_1 + \omega_2$. The process is said to be non-degenerate if the two interacting frequencies are different from each other whereas the term used in case of mixing two

identical frequencies, is called second harmonic generation that will be described later in detail. Within the above-described process, to have an emission in the UV region, two photons in the visible part of the spectrum must interact with each other.

Generally, all devices based on the techniques described in the above are expensive and barely transportable. As we mentioned earlier in the beginning of this chapter, solid-state lasers based on organic materials can be very promising alternatives as they offer a combination of broad tunability, inexpensive and compact devices. This especially becomes very true when the gain medium takes the form of a thin film prepared via simple deposition techniques (e.g. spin coating or ink-jet printing).

Within the category of organic solid-state lasers, one approach to achieve tunable UV emission is through the use of the UV-emitting organic materials in the traditional laser resonant structures. But in fact, to have the emission in the UV region, an excitation source in the deep-UV must be used which is highly deleterious to the organic material lifetime. Due to this limitation, there are few reports of organic lasers using the material approach for having emission wavelengths below 400 nm. Some examples of this kind are described in the following.

Within the category of thin-film devices, an example is the work of Berggren et al. [170] where a spin-casted film of an organic material (2-(4-biphenylyl)-5-(4-t-butyphenyl)-1,3,4-oxadiazole) known as PBD was incorporated within a DBR structure fabricated by pre-patterning a thermally-oxidized Si wafer. As a result, a laser emission peak at 392 nm was observed. Lower emission wavelength in the UV region was reported in 2000 by Zhu et al. [171] for Exalite 377E -doped sol-gel silica DFB laser with holographic grating. In that work, a continuous tuning range from 367 to 383 nm together with a slope efficiency of 4.4% was obtained when pumped by a pulsed nitrogen laser at 337 nm. The output energy dropped to 50% after 1200 pump shots for constant pump energy of 230 μJ at 0.5 Hz repetition rate. Another example of ultraviolet emission within the same category, is the work realized by Schneider et al. [39] reporting on a device based on thermally-evaporated film of novel spiro-linked material in a set of DFB structures with varying pitches from 200 to 225 nm created on thermally-grown silicondioxide layers (SiO_2) layers on silicon wafers. Consecutive pumping of the realized gratings with 500-ps-long pulses of a nitrogen laser ($\lambda_{pump} = 337\,\text{nm}$) led to discrete tunability from 377.7 nm (Λ = 200 nm) to 395 nm (Λ = 225 nm) defined by the grating pitch Λ. Furthermore, in order to reduce the cost of the device and future mass application in the spectroscopic domains, the authors could realize all plastic substrate based on a cyclic olefin copolymer (Topas 5013) fabricated through micromolding technique. In a very similar work to the previous one, again based on a spiro-linked compound, Spehr et al. [172] demonstrated a tunable ultraviolet organic

semiconductor laser with UV tunability range extended over 32 nm and the lowest emission wavelength at 361.9 nm in this case. Here again, the discrete tuning range was obtained thanks to segmented DFB gratings (spaced in steps of 5 nm from each other with varying pitch from 195 to 250 nm) created on a thermally-grown SiO_2 layer on top of a silicon wafer substrate.

In the category of external cavity devices based on organic materials emitting in the UV spectral region, there exists the work realized by Wu et al. [173] where the active medium was based on 20-mm-long slab of Exalite 376-doped silica material prepared from sol-gel process. The emission wavelength was centered at 364 nm. With an excitation energy of 10 mJ , output energy as high as 0.4 mJ was obtained (laser efficiency = 4%) which dropped to 50% after 2000 shots when pumped at 1 Hz by XeCl laser (λ_{pump} =308 nm). The authors have claimed that the output energy was revived after 10 min of pause in pumping process and then resuming back again.

Back to the above, the second approach that might seem realistic for achieving tunable UV emission could be through taking advantage of the high-efficient emission of the organic dyes in the visible part of the spectrum down to near UV and using this radiation to perform non-linear frequency conversion. For this purpose, high power density together with high beam quality at fundamental emission wavelength are required to succeed in realizing efficient frequency conversion (all these properties can be expressed by a single term, namely the spectral brightness($W.cm^{-2}.(sterad.\mathring{A})^{-1}$). This concept has been the basis of frequency doubling in liquid dye lasers for a long time [174].

An example of external frequency doubling in all-solid-state phase is the complex work realized by Chandra et al. [175] where a tunable UV radiation was obtained near 290 nm. The device was based on 15-mm-long Pyrromethene-doped plastic sample inserted inside a cavity with a grating and tuning mirror module and pumped by the second harmonic of Nd: YAG laser. The output tunable emission from this cavity (named as seed laser) was then sent into an amplifier consisting of a nonconfocal unstable resonator which contained a rotating disk of Pyrromethene-doped PMMA. Consequently, a high brightness and amplified beam was generated and then frequency doubled in a CLBO crystal. In that configuration, UV slope efficiency of 33% (45 mJ of UV was obtained for 180 mJ of the amplifier output) together with tunable radiation over 10 nm around 290 nm was obtained.

Another example of this type but in liquid phase is the hybrid system consisting of a distributed-feedback dye laser oscillator and an amplifier reported by Hoa et al. [176]. In such a structure, a tunable emission from two examined dye laser solutions of Couramin 153 (tuning range: 576 - 600 nm) and Rhodamine B (tuning range: 584 - 620 nm) in methanol was obtained via a DFB oscillator and then frequency doubled in a BBO crystal.

The frequency-doubled UV emission was then amplified in a single-pass geometry using a Ce-doped crystal excited by the fourth harmonic of Nd: YAG laser.

The above examples are two of the typical cases of frequency doubling demonstration in solution and bulk dye-doped materials [177].

To our knowledge, UV emission from a frequency-doubled organic solid-state laser has never been demonstrated in the family of organic solid-state thin film devices such as in DFB/DBRs and/or in microcavities with fast and easy-handled material processing. This is mainly because of the rather low available output powers in these devices added to the poor beam quality in the case of DFB and DBRs. Considering these difficulties and given that the realized VECSOL architecture is taking benefit of high intracavity peak brightness (several hundreds of Watts of output power obtained with 98% output coupler which means a few thousands of Watts of intracavity peak power together with a high beam quality ($M^2 = 1$)) along with an open resonator, therefore, it can be an ideal candidate for the realization of tunable ultraviolet laser through intracavity frequency doubling.

Before proceeding with this discussion, in order to understand the structure design and the experimental results achieved in this way, it is necessary to become familiar with some notions associated with nonlinear frequency conversion phenomenon. Therefore, the next section is aimed to fulfill this necessity.

3.5.2 Theoretical background

Frequency conversion is a useful technique to extend the frequency range of the available laser sources. This can be achieved through the use of nonlinear response of an optical medium in an intense radiation field. That is, when the response of the medium to an applied optical field depends in a nonlinear way to the field intensity. As a result of the force exerted by the electromagnetic field of light, the valence electrons displace from their normal orbits (in a classical point of view). This perturbation creates electric dipoles whose macroscopic manifestation is the medium polarization. If p represents the polarization of the medium induced by the electric field E of an optical field, the polarization can be developed in terms of the ascending field powers. That is:

$$p = \varepsilon_0 \chi^{(1)} E + \varepsilon_0 \left[\chi^{(2)} E^2 + \chi^{(3)} E^3 + ... \right] = p_{Linear} + p_{Nonlinear} \qquad (3.57)$$

where ε_0 is the free-space permittivity and $\chi^{(n)}$ is the n^{th}-order susceptibility[15].
For small field strengths the induced polarization p is linearly proportional to the applied electric field. That is:

$$p_{Linear} = \varepsilon_0 \chi^{(1)} E \qquad (3.58)$$

where $\chi^{(1)}$ is the first-order medium susceptibility. In linear optics, that is the $\chi^{(1)}$ factor which is a dimensionless value and determines the refractive index (n) of a dielectric medium through the following relation:

$$n = \sqrt{1 + 4\chi^{(1)}} \qquad (3.59)$$

If the medium is exposed to a high optical field, the response of the medium to the applied field will not be linear anymore. In this case the higher order nonlinear susceptibilities $\chi^{(n)}$ will intervene and create the nonlinear polarization term, $p_{Nonlinear}$, in (3.57). Among several nonlinear susceptibilities, in our case, we are particularly interested in the effect of the term $\chi^{(2)}(m.V^{-1})$ appearing in (3.57) as it is responsible for the second harmonic generation

[15] For sake of simplicity, the equation (3.57) is written based on scalar quantities. In reality, the polarization and the electric field must be considered as vectors. In this case the nonlinear susceptibility of order n, $\chi^{(n)}$, must be expressed as a tensor of rank (n+1).

(SHG) phenomenon. This can be justified by considering an incident electric field of $E(t) = E\cos(\omega t)$ with angular frequency of ω. Then the second polarization term, $p^{(2)}$, in (3.57) can be written as:

$$p^{(2)} = \varepsilon_0 \chi^{(2)} \left[E\cos(\omega t)\right]^2 = \varepsilon_0 \chi^{(2)} E^2 \left[\frac{1+\cos(2\omega t)}{2}\right] = \frac{1}{2}\varepsilon_0 \chi^{(2)} E^2 + \frac{1}{2}\varepsilon_0 \chi^{(2)} E^2 \cos(2\omega t) \qquad (3.60)$$

The first term in (3.60) is a constant term at frequency zero responsible for a phenomenon known as optical rectification where a static electric field is created inside the medium. The second term is the contribution of the polarization at frequency 2ω holding for SHG.
In the following, we have focused our special attention to some basic aspects of the SHG as in our case it was the phenomenon based on which the UV emission generated in the VESOUL architecture.

3.5.2.1 Second Harmonic Generation (SHG)

Second harmonic generation (SHG) is a process in which two photons of frequency ω are annihilated to create one photon of twice the frequency at 2ω (Figure 3.40).

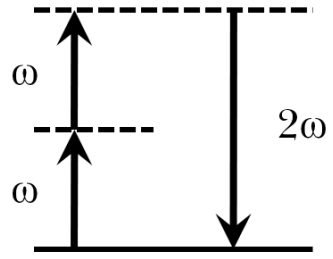

Figure 3.40 - Principle of SHG process leading to generation where two photons at fundamental frequency of ω are annihilated to generate a photon at frequency of 2ω.

SHG phenomenon must be viewed as a two-step process. Based on what was mentioned earlier, first, a polarization wave at the frequency of the second harmonic 2ω is produced and then through the second step process, the energy from the created polarization wave at 2ω is transferred to an electromagnetic wave at frequency of $2\nu = 2(\omega/2\pi)$. Evidently, an efficient energy transfer requires the polarization wave and second harmonic frequencies to have the same phase velocities. This fact demands satisfaction of the both momentum and energy conservation rules. The momentum conservation for collinear conversion, that is

when the wave vectors of the interacting waves $k^{(\omega)}$ and $k^{(2\omega)}$ are in the same direction, requires that $k^{(\omega)} + k^{(\omega)} = 2k^{(\omega)} = k^{(2\omega)}$ whereas the energy conservation rule implies that $\omega + \omega = 2\omega$. The two conservation rules lead to the phase-matching condition for the refractive index of the medium as $n^{(2\omega)} = n^{(\omega)}$. Since almost all materials have normal dispersion in a way that $n^{(2\omega)} > n^{(\omega)}$, then we have the phase velocity of the generated harmonic slower than the fundamental wave. The phase mismatch between the fundamental and the generated second harmonic waves for collinear beams is expressed as the difference in wave numbers:

$$\Delta k = k^{(2\omega)} - 2k^{(\omega)} = 2\pi\left(\frac{1}{\lambda^{(2\omega)}} - \frac{2}{\lambda^{(\omega)}}\right) = 2\pi\left(\frac{1}{\left(\frac{2c\pi}{n^{(2\omega)}2\omega}\right)} - \frac{2}{\left(\frac{2c\pi}{n^{(2\omega)}\omega}\right)}\right) \qquad (3.61)$$
$$= \frac{2n^{(2\omega)}\omega}{c} - \frac{2n^{(\omega)}\omega}{c} = \frac{2\omega}{c}\left(n^{(2\omega)} - n^{(\omega)}\right)$$

In perfect phase-matching condition we have $\Delta k = 0$ leading to $n^{(2\omega)} = n^{(\omega)}$.
By solving Maxwell's equations for both the fundamental and the generated second harmonic, we can obtain the SHG conversion efficiency as the power ratio between the generated harmonic and the incident fundamental wave as [159]:

$$\frac{P^{(2\omega)}}{P^{(\omega)}} = \tanh^2\left[\sqrt{l^2\kappa\left(\frac{P^{(\omega)}}{A}\right)}\frac{\sin(\Delta kl/2)}{(\Delta kl/2)}\right] \qquad (3.62)$$

where l is the nonlinear crystal length, $\kappa(W^{-1})$ is some constant for a given wavelength and a given nonlinear material and A is the fundamental incident beam cross-section area. For low conversion efficiencies, (3.62) can be approximated by the following simplified expression:

$$\frac{P^{(2\omega)}}{P^{(\omega)}} = l^2\kappa\frac{P^{(\omega)}}{A}\frac{\sin^2(\Delta kl/2)}{(\Delta kl/2)^2} \qquad (3.63)$$

Under phase-matched condition ($\Delta k = 0$), the equation in (3.63) becomes:

$$P^{(2\omega)} = l^2 \kappa \frac{(P^{(\omega)})^2}{A} \qquad (3.64)$$

Based on (3.64), we can observe that the generated power at the second harmonic grows with the square of the power at the fundamental frequency.

After this introductory part on the second harmonic generation, in the next part we will see how we can obtain the perfect phase-matching condition in a given nonlinear medium to achieve the maximum conversion efficiency.

3.5.2.2 Angular phase matching via crystal birefringence

One approach to achieve perfect phase-matching condition, that is $\Delta k = 0$, can be through index phase-matching thanks to the optical anisotropy of the propagating medium. Isotropic and centrosymmetric media are not suitable for this purpose since the elements of the second order susceptibility $\chi^{(2)}$, responsible for the SHG, cancel out in such media because of symmetry reasons.

To proceed, let's consider the simplest and the most encountered case of the uniaxial anisotropic crystal characterized by a particular direction known as the optical axis defining the crystalline symmetry axis. Imagine an electromagnetic incident plane wave with wave vector k normal to its wavefronts propagating into this crystal making an angle θ with the optical axis. The electric field of this wave, can be decomposed into two orthogonal components; one, oscillating normal to the optical axis which in the case is said to be ordinary polarized light and experiences the so-called ordinary refractive index of n_o and the other component vibrating parallel to the optical axis and is said to be extraordinary polarized light and is refracted with the θ-dependant extraordinary refractive index of $n_e(\theta)$. In an anisotropic material, this phenomenon leads to what is called "double refraction" or "birefringence".

For a given uniaxial crystal, depending on whether the birefringence, that is $\Delta n = n_e - n_o$, is positive or negative, the crystal is said to be positive or negative uniaxial respectively.

In three dimensions, the locus of the points representing the ordinary refractive index is a sphere surface since the light propagates with the same phase velocity in each direction while the angle-dependant extraordinary refractive index evolution follows an ellipsoidal locus because of the distinctive propagation directions for extraordinary-polarized light. This fact is demonstrated schematically in Figure 3.41 for a negative uniaxial crystal.

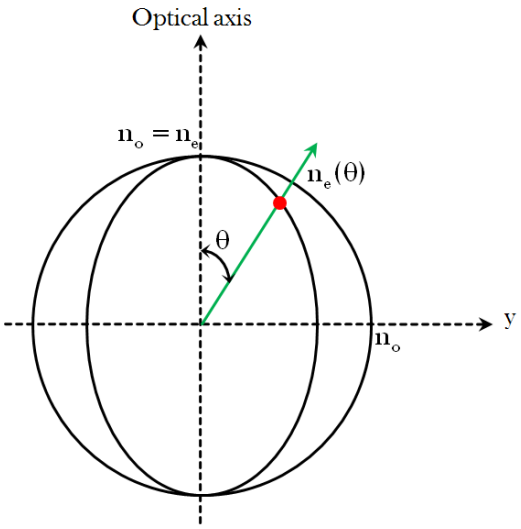

Figure 3.41 - Index surfaces made of a sphere and an ellipsoid, used to describe the refractive indices of the ordinary and extraordinary components respectively in a negative uniaxial crystal ($n_e \leq n_o$). The ordinary refractive index is independent of θ while the extraordinary component refractive index depends on the angle between the propagation direction and the optical axis.

The equation that describes the ellipsoid is given by:

$$\frac{1}{n_e(\theta)} = \frac{\sin^2(\theta)}{n_e^2} + \frac{\cos^2(\theta)}{n_o^2} \tag{3.65}$$

where n_e represents the extraordinary refractive index for $\theta = 90^\circ$. Obviously, the ordinary and extraordinary refractive indices become equal when $\theta = 0$ (propagation along the optical axis).

Recall that in the case of the second harmonic generation we reached the point where we said that in most materials, $n^{(2\omega)} > n^{(\omega)}$; for perfect phase-matching we must achieve the condition $n^{(2\omega)} = n^{(\omega)}$ or in other words, $\Delta k = 0$.

If the nonlinear crystal is oriented in such a way that the dispersion effect of the refractive index can be compensated by the crystal birefringence, then we will have $\Delta k = 0$ for a certain propagation direction. The angle between this particular direction and the optical axis of the crystal for which the phase-matching condition is achieved is called the phase-matching angle.

Depending on the polarization states of the fundamental wave and the generated harmonic, two types of phase-matching are distinguishable. In the first method, the incident fundamental wave contains only one polarization component, e.g. ordinary, whereas the

second harmonic contains the other polarization type, e.g. extraordinary. This is called type-I phase matching. The second method is called type-II phase matching in which the second harmonic is the contribution of two fundamental polarization type components (ordinary and extraordinary). For negative uniaxial crystal, that is when $\Delta n < 0$, the two methods for phase-matching are summarized as the following:

$$\begin{cases} n_o^{(\omega)} + n_o^{(\omega)} = 2n_e^{(2\omega)} & \text{(Type-I)} \\ n_o^{(\omega)} + n_e^{(\omega)} = 2n_e^{(2\omega)} & \text{(Type-II)} \end{cases} \tag{3.66}$$

To calculate the phase matching angle, consider the case of the SHG obtained through type-I phase-matching in a negative uniaxial crystal. Since for negative uniaxial crystal $\Delta n < 0$, one chooses the fundamental frequency to propagate as the ordinary wave and the second harmonic frequency as the extraordinary wave in order that the birefringence of the material can compensate for the dispersion. The phase-matching condition then becomes:

$$n_e^{(2\omega,\theta_m)} = n_o^{(\omega)} \tag{3.67}$$

where θ_m is the phase-matching angle. Then through (3.65) we have:

$$\frac{1}{\left(n_o^{(\omega)}\right)^2} = \frac{\sin^2(\theta_m)}{\left(n_e^{(2\omega)}\right)^2} + \frac{\cos^2(\theta_m)}{\left(n_o^{(2\omega)}\right)^2} \tag{3.68}$$

Replacing $\cos^2(\theta)$ with $1-\sin^2(\theta)$ and solve it for $\sin^2(\theta)$ gives the simplified form of (3.68) as:

$$\sin^2(\theta_m) = \frac{\left(\frac{1}{n_o^{(\omega)}}\right)^2 - \left(\frac{1}{n_o^{(2\omega)}}\right)^2}{\left(\frac{1}{n_e^{(\omega)}}\right)^2 - \left(\frac{1}{n_o^{(2\omega)}}\right)^2} \tag{3.69}$$

This equation shows how the crystal should be oriented to obtain the phase-matching condition. This fact is shown schematically in Figure 3.42 using the index surfaces. In this

figure θ_m is the phase matching angle between the wave propagation direction and the optical axis of the crystal and φ is the azimuth angle. Slight crystal disorientation from this specific angle causes a dramatic decrease in the generated harmonic intensity leading to an inefficient harmonic generation. In this case, the range of θ angles within which the generated harmonic intensity reduces from its maximum to zero is called the "crystal acceptance angle". Since the phase-matching angle is achieved for a certain fundamental wavelength, any change in this wavelength will require crystal realignment. Therefore, in a similar terminology, the term "crystal spectral acceptance" is defined as the range of wavelengths within which the generated harmonic intensity reduces from its maximum to zero without touching the crystal.

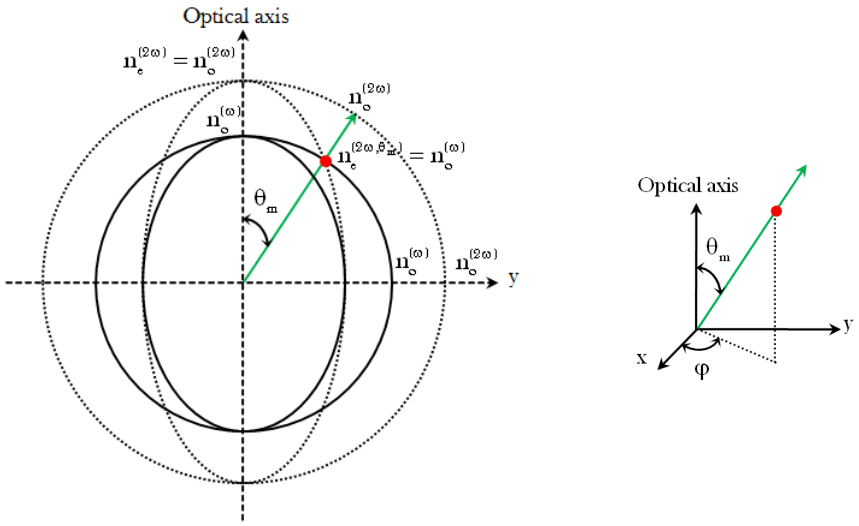

Figure 3.42 – (left) Index surfaces of the ordinary and extraordinary components in a negative uniaxial crystal ($n_e < n_o$) showing the phase matching angle, θ_m, for which $n_e^{(2\omega)} = n_o^{\omega}$. (right) is the demonstration of the azimuth angle, φ, in the xy plane.

In a nonlinear crystal even if the crystal is oriented at the calculated angle of $\theta_m \neq 90^\circ$ to achieve the perfect phase-matching condition, an issue that limits the efficient conversion by reducing the interaction length of the fundamental beam is the "spatial walk-off" phenomenon. This happens because the electrical displacement vector D and the electric field E are not parallel to each other in case of the beams with extraordinary polarization. Consequently, in case of collinear type-I phase matching obtained within a negative uniaxial crystal, the directions of the power flow (represented by the Poynting vector) between the ordinary fundamental wave and the extraordinarily-polarized generated second harmonic are not completely collinear and make a small angle with each other. This angle that lies within the plane defined by the crystal optical axis and the wave propagation direction k is called the walk-off angle (ρ) and is demonstrated in Figure 3.43 by using the index

surfaces. In this figure, the walk-off angle is the difference between the radial ordinary ray Poynting vector direction normal to index sphere surface and the extraordinary Poynting vector perpendicular to the surface of the extraordinary index ellipsoid of the second harmonic.

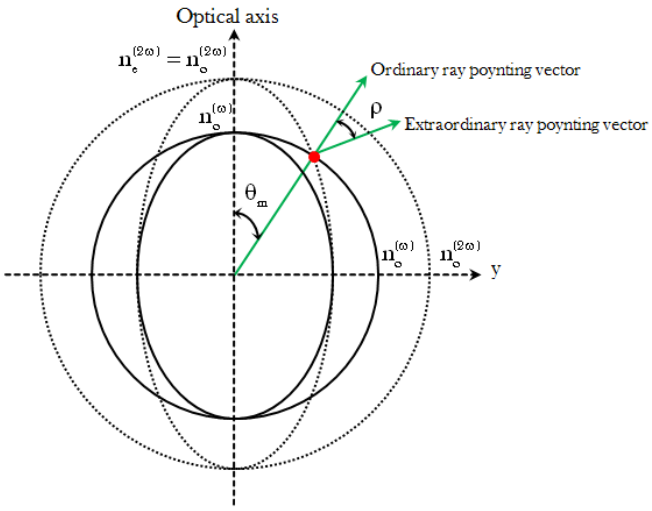

Figure 3.43 - Demonstration of the walk-off angle (ρ) as the difference between the ordinary and extraordinary poynting vector directions being normal to the sphere and ellipsoidal index surfaces respectively.

The walk-off phenomenon imposes a restriction on choosing the crystal length by the fact that after a certain length, the generated second harmonic walks out from the fundamental beam field and there would be no interaction between the two beams. Exceeding this particular amount in crystal length, will result in no further growth in the generated second harmonic intensity. Therefore, normally the crystal length is chosen as a trade-off between the walk-off and the conversion efficiency as we saw previously the crystal length also intervened in (3.62).

The walk-off effect is obvious for type-II phase matching as illustrated in Figure 3.44. However, it also exists to a lower extent in type-I phase matching [178].

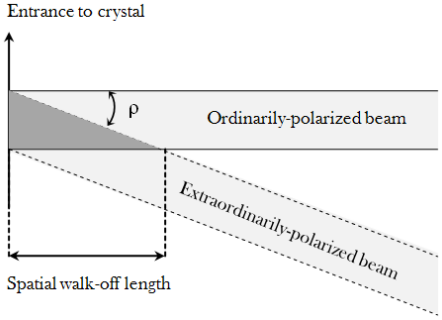

Figure 3.44 – Illustration of the walk-off phenomenon in type-II phase matching. ρ is the walk-off angle and the dark triangle is showing the region where the fields overlap with each other.

If the beam propagates at $\theta = 0$ and/or $\theta = 90$ the ordinary and extraordinary poynting vectors are collinear normal to the ellipsoid surface and thus the walk-off would be suppressed. These two particular cases are responsible for another type of phase matching known under the title of noncritical phase matching named because of the advantageous low angular sensitivity in these two conditions. In these cases, the phase matching is performed via temperature tuning of the crystal which is not the subject of discussion in this context.

With this brief introductory part on the fundamentals of second harmonic generation, we have the necessary tools to proceed with this chapter. We continue on this subject by presenting the modified VECSOL architecture exploited for UV generation via intracavity frequency conversion and we will finish by demonstration of some very interesting results obtained within this experiment.

3.5.3 All-solid-state tunable ultraviolet laser design

Earlier, in the beginning of this discussion, the existing challenges toward the realization of a compact tunable ultraviolet solid-state laser source based on thin films of the organic materials were discussed. Considering those difficulties and given that the realized VECSOL is taking benefit of high intracavity peak brightness along with an open resonator; therefore, it can be an ideal candidate for realization of tunable ultraviolet laser through intracavity frequency conversion.

On this basis, we are presenting a hybrid structure that we have named "VESOUL" standing for Vertical External-cavity Surface-emitting Organic Ultraviolet Laser. In such a structure, the VECSOL was modified in order to have the highest possible intracavity intensity in red region by using two highly-reflective ($R > 99.5\%$) cavity mirrors (Figure 3.45). The architecture comprises a non-linear crystal introduced into the VECSOL cavity for frequency conversion and a harmonic separator that couples out the UV emission and designed in such a way to prevent UV photons from reaching the organic medium. This is because the organic materials under optical excitation experience an irreversible photochemical degradation. The degradation rate could be further enhanced if these materials are exposed to the UV radiation since in this case the photons are more energetic.

In the following part, the experimental arrangement with details about each composing element used to realize such a design is discussed in detail.

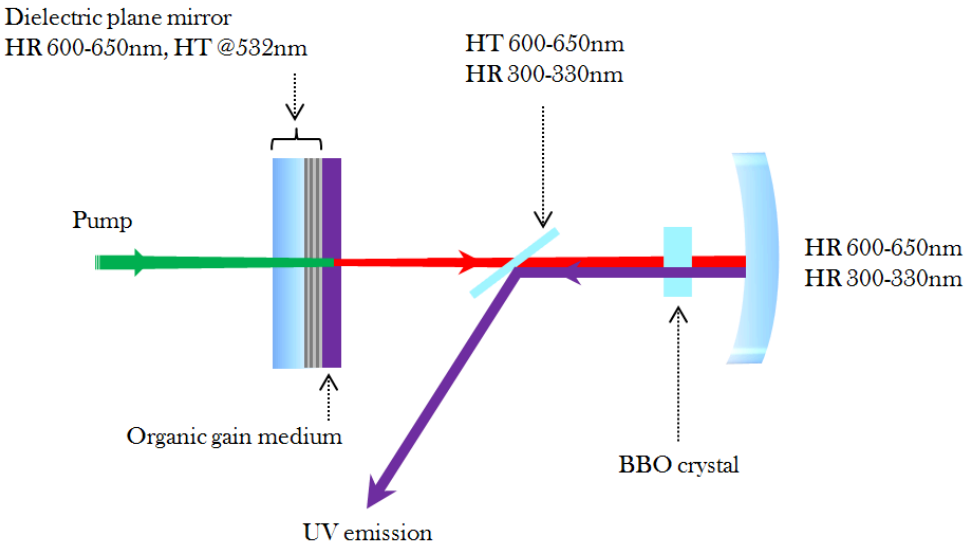

Figure 3.45 - Illustration of the modified VECSOL architecture for the purpose of UV beam generation via intracavity frequency doubling.

3.5.3.1 VESOUL experimental setup design

In order to implement the so-called VESOUL architecture, similarly to the VECSOL scheme, the plane mirror was designed in such a way to be highly transparent at the pump wavelength (T > 90% at 532 nm). As the intensity of the generated UV varies with the square of the fundamental (red) intensity ($I_{2\omega} \propto I_{\omega}^{2}$), the intracavity laser intensity at fundamental frequency was maximized by choosing highly-reflective mirrors (R >99.5%) in the range between 600-650 nm. In addition, for the reason that will be clarified in the following, the concave mirror was also designed to be reflective in the range of 300-330 nm. In terms of resonator geometry, generally the typical configuration for the purpose of intracavity harmonic generations is a folded cavity (Figure 3.46) due to existence of two waists. However this configuration leads to a longer cavity length and thus less efficiency as we observed that VECSOL efficiency dropped upon increase of the cavity length. Therefore, as the first try, we chose a plane active mirror similar to the one used for VECSOL and an end mirror with 150 mm radius of curvature providing a spot size diameter of ~ 180 µm at the crystal position for a ~ 10-mm-long cavity (the minimum possible length, considering the size of intracavity elements and their holding supports).

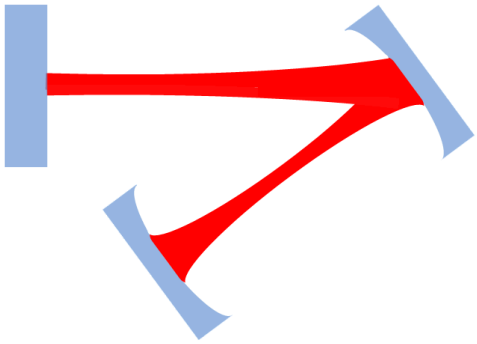

Figure 3.46 – Schematic representation of a folded cavity.

For outcoupling of the UV beam, the natural solution that comes to one's mind is the outcoupling directly through one of the cavity mirrors. The advantage of this method is the lowest possible cavity length that can be achieved in this way. As we saw earlier for the case of VECSOL, higher efficiency values were obtained for shorter cavity lengths. However, the high efficiency would last for a short term because of the very fast degradation rate caused by the energetic UV photons reaching the organic medium. Above all, we got informed by the mirror supplier (CVI) that technically, realization of a dielectric coating in such a way to be reflective for the red emission and transparent to the UV light was rather difficult and troublesome.

The strategy that we chose for outcoupling of the UV light while avoiding accelerated photodegradation induced by the UV photons was based on discriminating between fundamental and generated second harmonic through their distinctive polarizations. This could be achieved through type-I phase matching scenario. For type-I phase matching in a

negative uniaxial crystal, if the fundamental wave is considered to be ordinarily polarized; basically the generated second harmonic must have the extraordinary polarization type. To separate two polarization types, a specifically-designed dielectric coated plate was inserted inside the cavity at the Brewster angle. This plate had one side coating with high s-polarization reflectivity in a range between 300-330 nm to reflect out the generated UV beam and the other side facing the gain medium at the Brewster angle was highly transparent to let through the p-polarized red light in the range between 600-650 nm without losses. In this way, no UV photon could reach the gain medium. [16]

The adjustment of the specially-coated plate (harmonic separator) at the Brewster angle was achieved via a He-Ne laser sent through the cavity while crossing the harmonic separator inserted inside the cavity. Then the plate was continuously turned till reaching the Brewster angle at which the reflection of the p-polarized red light from the He-Ne laser became almost zero.

The BBO crystal was cut in such a way to realize type-I phase matching at 620 nm ($\theta = 38.9°, \varphi = 90°$). The crystal thickness was 3 mm. The crystal was placed inside the cavity in-between the harmonic separator and the output coupler, mounted on a support enabling several degrees of freedom for phase matching adjustment purposes.

To obtain the maximum efficiency, the whole setup was tried to be as compact as possible since as justified earlier, the efficiency would drop as the cavity length increases. The cavity length could be reduced to 10 mm limited by the size of the intracavity elements and the supports holding them. However, this length can be possibly reduced further by decreasing the actual size of the intracavity elements.

The whole structure was end-pumped with a beam of 532 nm at 10 Hz repetition rate generated by a flash-pumped Nd: YAG laser (SAGA 230, B.M.I., Thomson CSF) having 7 ns pulse duration. The beam was focused into a spot of 180-µm-large (measured by Spiricon beam analyzer) to match the cavity mode size. The solid gain medium was based on a film of 1 wt% of Rhodamine 640 dissolved in PMMA A15 solution and deposited directly onto the plane mirror via spin coating technique. In this way 85% of the pump beam could be absorbed by the film thickness. This thickness was precisely determined later on through measurement of the red emission free spectral range (FSR) and then using the related formula ($FSR = \lambda^2/2n\ell$). In this relation, the refractive index of the Rhodamine 640-doped PMMA was determined by the technique described in appendix 2

[16] This technique turns out to be unsuitable for "short" pump pulse durations (e.g. 0.5 ns). This is because of the limitation imposed on the cavity length under this pumping regime which only enables rather short cavity lengths (few mm) to be operational for laser emission and thus not having enough space for insertion of intracavity components.

and was measured to be around 1.52. On this basis, a film thickness of 21.5 µm was deduced

3.5.4 VESOUL emission characterization

In the following part, the performance characterizations of the UV emission in terms of the efficiency and the laser photostability are carried out and discussed in detail.

3.5.4.1 Efficiency curve

The input-output characteristic curves of the realized VESOUL are depicted in Figure 3.47.

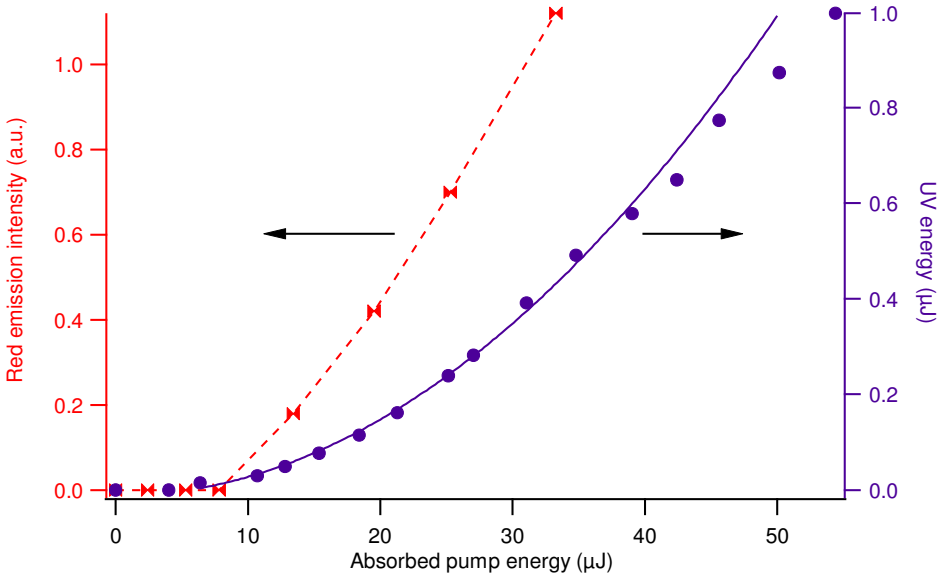

Figure 3.47 - (left) red laser emission (fundamental) as a function of the pump energy. The structure is not designed to produce red radiation, thus, the vertical axis represents the red emission intensity in an arbitrary unit from one of the leak sources. (right) UV output at 315 nm. The solid line is a parabolic fit to the experimental data.

The red and UV emissions are exhibiting linear and parabolic evolution vs. the pump energy, respectively, as expected. The UV output could be increased up to 1 µJ per pulse. An optical-to-optical conversion efficiency (UV energy divided by the absorbed pump energy at 532 nm) of 2% could be deduced in this way. For higher pump power levels, photodegradation induces a sublinear behavior of the laser output as it is also observable in

the last points of the above figure.

The spatial profile images of the UV emission together with a photo of the VESOUL architecture under operation are shown in Figure 3.48 and Figure 3.49 respectively.

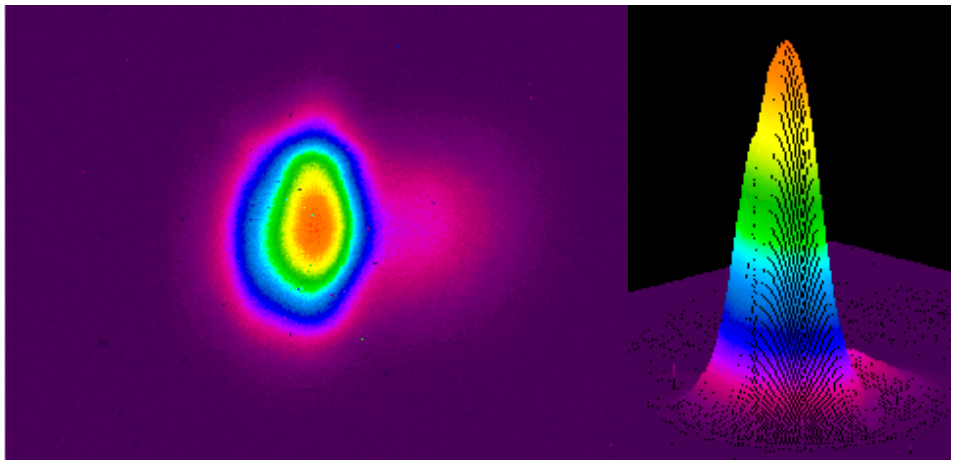

Figure 3.48 - Two dimensional (left) and three dimensional (right) images of the spatial UV mode profile. Slight profile asymmetry is supposed to be due small angular acceptance of the BBO crystal.

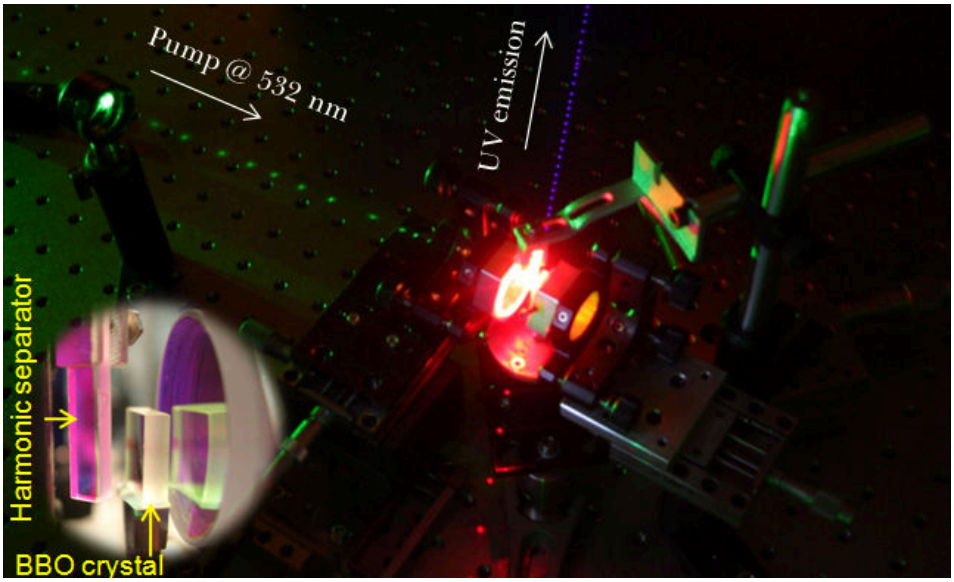

Figure 3.49 - Long-exposure time photograph of the VESOUL setup showing the pump beam (green) on the left, a red beam leaking from the dichroic plate toward the bottom and finally, on the top is the UV beam, became visible through fluorescence of a paper sheet. Inset is the cavity close up showing the BBO crystal and dichroic plate.

3.5.4.2 Emission spectrum

As mentioned earlier in the case of the VECSOL, the red emission spectrum (fundamental wavelength) is composed of several peaks due to the Fabry-Perot etalon effect imposed by the organic gain medium (Figure 3.50). This spectrum could be easily obtained thanks to the existence of numerous leaks within the architecture (i.e. through very weak transmission of the cavity mirrors and/or taking advantage of the dielectric plate coating imperfection reflecting very weak quantity of the red fundamental beam even at Brewster angle). In contrast, the UV spectrum exhibits a single peak with FWHM[17] below 0.5 nm, limited by the spectrometer resolution at disposal. This single mode operation is due to rather small acceptance angle (~ 0.5 nm) of the BBO crystal which allows only one of the red peaks to fulfill the phase matching condition at a given crystal angle (Figure 3.51). Albeit, it should be reminded that in both red and UV emissions, the narrowly-spaced longitudinal modes of the external cavity exist within each peak of the Fabry-Perot etalon. Upon tilting of the BBO crystal by a fraction of degree, the spectral acceptance curve could match any of the red peaks within the emission spectrum. In addition to second harmonic generation, emission peaks were also observed between two adjacent red maxima located in between the frequency-doubled peaks (e.g. 626 nm+632 nm $\rightarrow$ 314.5 nm) manifesting the non-degenerate sum-frequency mixing phenomenon. The second emission spectrum in Figure 3.50 is corresponding to UV emission tunable from 309.5 to 316 nm by discrete steps upon BBO orientation. Interestingly, as already demonstrated in case of VECSOL, the device showed continuous tunability between these values thanks to the non-homogeneous film thickness obtained during film deposition through spin coating. This effect was more noticeable when the pump excitation spot was scanned in a region near the sample edge as the thickness variation was more pronounced in this region. Combining all these effects (BBO adjustment to phasematch different emission peaks of the fundamental red emission and also scanning over the entire range of the sample from the center to the edge), made it possible to obtain a tunability range from 309 nm to 322 nm.

[17] FWHM=Full Width at Half Maximum.

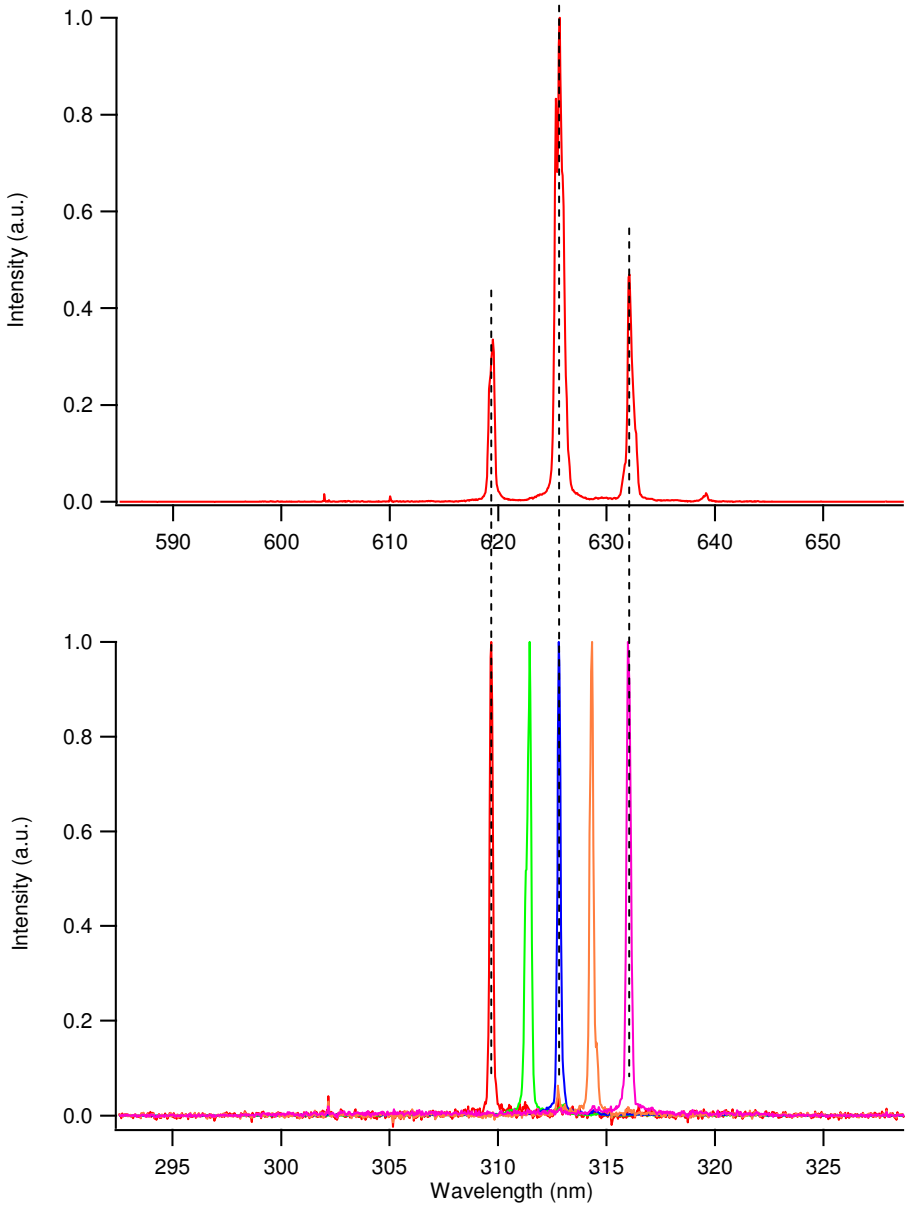

Figure 3.50 - Top: typical red emission spectrum of the VECSOL. Bottom: several individual UV peaks obtained for a given pump spot location on the organic layer, for different orientation of the BBO crystal.

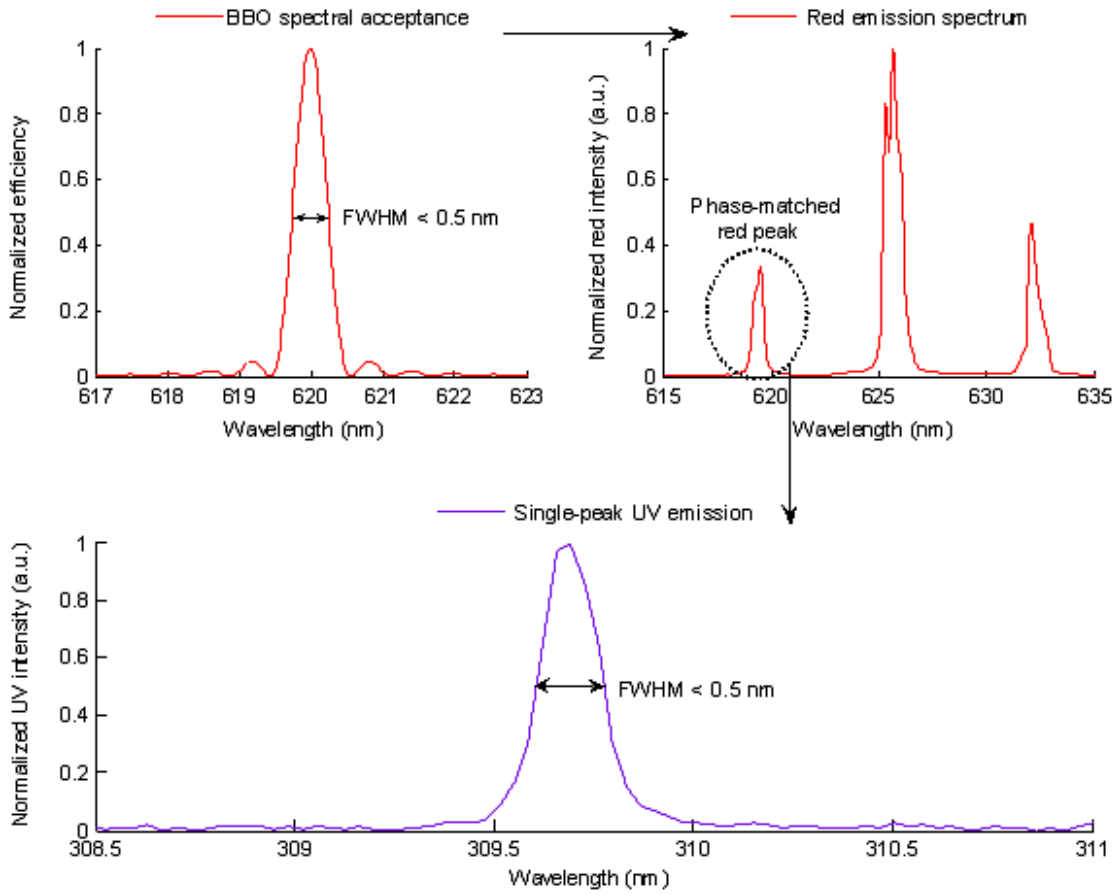

Figure 3.51 - (top-left) BBO spectral acceptance calculated from the crystal parameters (top-right) typical red emission spectrum. (bottom) single-peak UV emission spectrum obtained experimentally and justified theoretically as a result of the product of the red emission spectrum and the BBO spectral acceptance curve.

3.5.4.3 Photostability

As mentioned earlier, our strategy to design the VESOUL architecture was based on avoiding any UV-enhanced photodegradation. This signifies any further degradation other than normal irreversible photodegradation of the organic materials that can be induced by UV photons as they possess higher energy quantity than red photons. To prove our claim we carried out the photostability studies by pumping the realized architecture at pump energy level of approximately four times above lasing threshold (Figure 3.52).

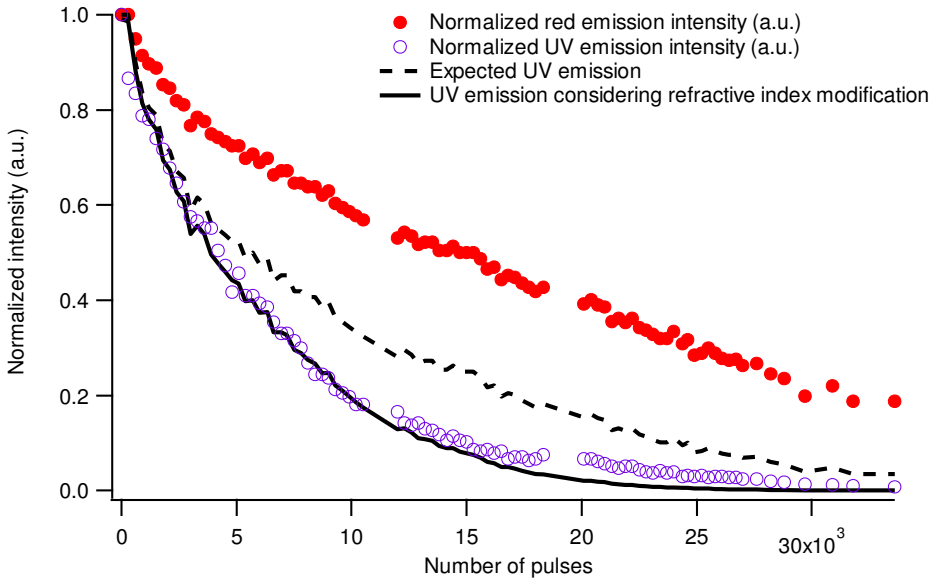

Figure 3.52 - Photodegradation curves. The dotted line is the expected UV intensity (square of the measured fundamental intensity). The solid line is the expected UV intensity calculated from the measured fundamental output with phase matching alteration due to refractive index change, deduced from the shift of laser wavelength vs. time.

From (3.64) we were expecting the time-varying UV energy to follow the trace of the squared red emission energy. But the preliminary result didn't fully comply with our expectation as the UV emission intensity decayed to half of its initial value after ~ 4470 pulses (void circles) which was ~ 1.5 times faster compared to the expected UV emission curve (dashed line obtained by tracing $(P^{(\omega)})^2$). Therefore, we got through the possible reasons to explain where the difference in behavior might come from and we found the answer in the slight blueshift occurred within the fundamental wavelength emission spectrum. In fact, when the excited spot within the gain medium undergoes the normal degradation during pumping, it causes the refractive index of the doped PMMA to shift towards the non-doped PMMA refractive index as the dyes gradually become bleached (Figure 3.53). This causes a spectral shift because the Fabry Perot etalon is index dependant.

A similar behavior was also seen and verified by Richardson et al. [36] in a DFB structure based on a conjugated polymer (poly[2-methoxy-5-(2′-ethylhexyloxy)-1,4-phenylene vinylene]). They attributed the refractive index modification to breaking of double bonds along the polymer backbone caused by photoinduced cross linking. However, in case of Rhodamine 640, the reason of this fact might be slightly different in nature since Rhodamine 640 is not a polymer and thus, it is not cross-linked.

Whatever the reason in behind, the change in the refractive index results in a spectral shift

of the fundamental red emission spectrum (governed by the Fabry-Perot etalon) that eventually leads to a phase mismatch and a reduced efficiency. This was verified by a slight tilt of the non-linear crystal which revived the UV energy and brought it back to its initial value before undergoing the phase mismatch condition (Figure 3.54).

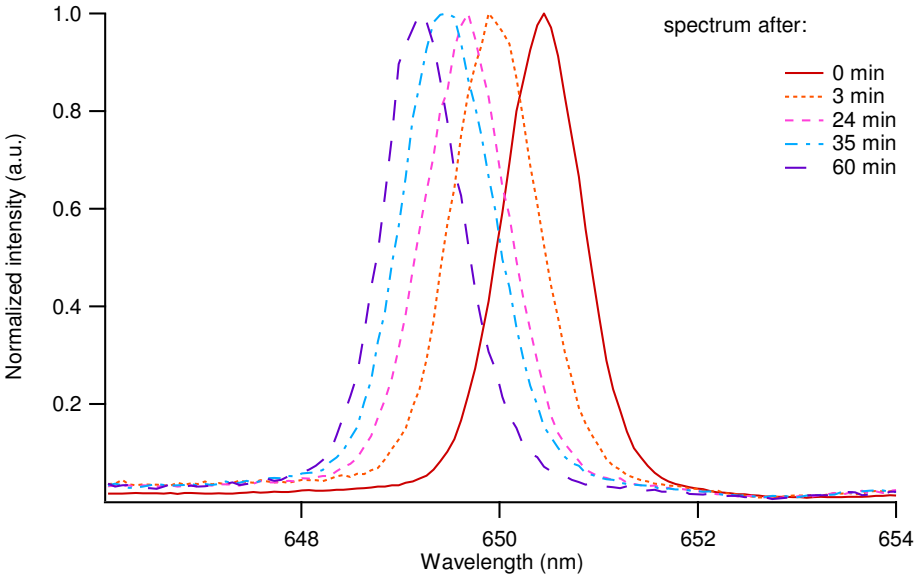

Figure 3.53 - VECSOL red emission spectral blueshift observed and demonstrated for one of the peaks within the multimode emission spectrum as a result of induced refractive index modification caused by photodegradation of the organic gain medium.

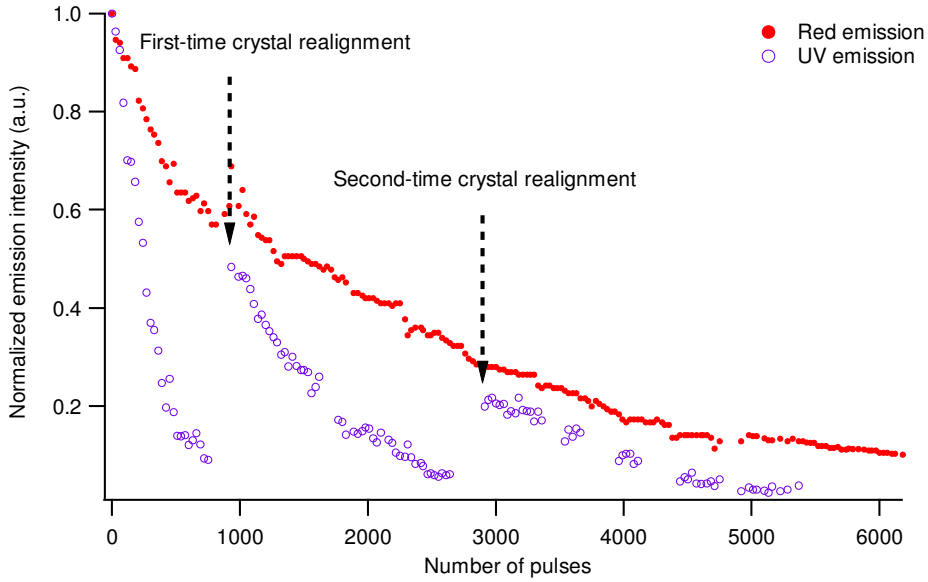

Figure 3.54 - Filled circles in red are showing the red emission (fundamental beam) degradation. Three discrete curves traced by hollow violet circles are showing the UV emission revived two times upon BBO crystal realignment. The curves are obtained for incident energy of 30 μJ and a cavity length of ~ 1.4 cm.

In order to prove our hypothesis on phase mismatch due to refractive index modification, we followed the described procedure in below.

As we saw, the red emission wavelength shifted by time due to refractive index modification resulted from photodegradation. This causes that phase-matched red peak to shift away from the narrow spectral acceptance band of the crystal (FWHM < 0.5 nm) and thus a decrease in UV efficiency due to phase mismatch. We plotted the UV intensity by taking into account the decrease in the UV efficiency caused by the reduced overlap between the shifted red peak and the spectral acceptance of the crystal. As a result, we obtained the solid line in Figure 3.52 which coincides almost perfectly with the experimental data.

It should be mentioned that the above procedure, taken to obtain the solid line, was all based on the experimental data and no fitting parameter was used.

3.6 Chapter conclusion

In this chapter, an external cavity laser based on a layer of dye-doped PMMA was presented and discussed. The structure design idea was rooted from inorganic Vertical External Cavity Surface Emitting Laser (VECSEL). Thus, the realized architecture was named VECSOL standing for Vertical External Cavity Surface-emitting Organic Laser.

The whole structure was end pumped at 532 nm in separate experiments by two pulsed sources at 10 Hz repletion rate but with different pulse durations of 0.5 ns and 7 ns. Based on preliminary experiments, the latter resulted in optical conversion efficiency of 43% while this was measured 6.3% for the other source. The emission showed to be multimode with peaks spacing corresponding to the free spectral range (FSR) of the Fabry-Perot etalon formed by the 18-μm -thick gain medium. Beam quality measurement revealed a perfectly diffraction-limited beam with $M^2 = 1$. A tuning range of 40 nm was achieved thanks to film thickness variation by going toward the sample edge. The structure power scalability was demonstrated for a typical case where the output energy became two times higher when the pump spot size doubled while keeping the pump fluence constant. The degradation rate showed to be constant before and after doubling the output energy. The laser emission photostability was studied for both cases of 0.5 and 7-ns-long pulse sources. This study was carried out based on a home-developed LabView program. We noticed that the degradation rates were highly dependent on the oldness of the used solution for sample preparation. Emission half-lifetime up to 10 times higher was observed for a sample prepared from a fresh solution than a sample made from a two-week old solution. Furthermore, VECSOL emission when excited by 7-ns-long pulse pump source showed to last for much longer time in comparison to the case when it excited with 0.5-ns-long pulses, evidencing the role of peak power in the photodegradation process.

Following the above-described characterization, theoretical analysis was performed based on Tang-Statz-de Mars rate equations for better understanding of the VECSOL emission dynamics, specially, the big difference seen in conversion efficiency values for two pump pulse durations. These analyses then helped to improve the structure performance and increase the VECSOL efficiency to 57% in an optimized geometry which up to date, it is the efficiency record among the reported conversion efficiencies for organic thin-film-based devices.

As observed during the experiment and then proved via modeling, the 7-ns-long pump pulse allowed having a few-cm-long cavity. Therefore, thanks to the open cavity and also the high intracavity intensity, the VECSOL emission centered at 650 nm could be extended

to the ultraviolet region through intracavity frequency doubling.

Using type-I phase matching, an optical conversion efficiency of 2% (UV energy divided by the absorbed pump energy at 532 nm) was obtained for the UV emission. A tunability range from 309 to 322 was obtained. The measured emission wavelengths are the lowest reported (up to date) in the family of organic thin-film-based devices.

In terms of photostability, the UV emission intensity dropped to half of its initial value after around 4500 shots at 10 Hz repetition in a cm-long cavity. This corresponds to a slightly higher degradation rate in comparison to what expected from the square of the fundamental output. However, we showed that this small difference could be fully explained by a fine wavelength shift during laser operation rather than by a UV-enhanced photodegradation as the structure was designed in such a way prevent UV photons to reach the gain medium.

The realized device with its attractive features can be very promising toward practical applications, notably due to its fabrication simplicity, high conversion efficiency and very good beam quality. For example, the last feature would allow easy injection of the emission beam into an optical fiber for applications where this is needed. The cost and size of the cavity makes it very interesting for in-situ spectroscopy applications (of course, once a more affordable, compact and cost effective pump source could be found). Further progress is underway by exploiting other organic materials and going deeper in understanding of device functionality.

Overall conclusion and perspectives

The aim of this thesis was to make a step forward in the field of organic solid-state lasers by addressing some issues that prevent these sources to be used in real applications. Let us very briefly summarize our results.

During this thesis, we first examined and characterized a novel organic small molecule (fvin) for laser applications. This deep red-emitting compound with its unique structural design evidenced a considerably reduced quenching in neat film configuration which is rarely seen in the family of organic devices. This material was examined in DFB configuration and laser emission was observed. This result shows the suitability of this material for realization of very low threshold devices thanks to high amount of absorption that can be achieved within a thickness of a few hundreds of nm. Furthermore, since this material is an organic semiconductor, it is promising for future electrical pumping, once the existing issues toward this goal are resolved.

In the second axis of this thesis, we started from scratch and then examined a novel external-cavity organic laser (called VECSOL) based on thin film of a classical dye (Rhodamine 640) doped into PMMA, with the aim of improved beam quality and increased lasing efficiency. Several characterization types (efficiency measurement, beam quality quantification, power scalability, tunability demonstration and photodegradation studies) were carried out in separate experiments for two different pump sources with different pulses durations (0.5 ns and 7 ns). A theoretical study of the emission dynamics was then performed. Simulations were carried out based on Tang-Statz-de Mars rate equations and validated by comparing with the experimentally-obtained results.

Following the experiments, we observed that a long-pulse excitation regime allows using a few-cm-long cavity. This feature together with high intracavity intensity was used to extend the emission wavelength to the ultraviolet part of the spectrum through intracavity frequency doubling. In this way, a successful realization of the lowest-achieved wavelength in the UV region for thin-film-based devices was demonstrated.

Fabrication simplicity, the efficiency record of this device (more than 50%) within the family of organic thin-film devices together with the diffraction-limited beam quality are appealing features which make this device an interesting candidate toward practical applications.

As this three-year-work comes to its end, it appears that there are still several works that can be done for device improvement functionality. For example:

Study of the VECSOL performance in several families of organic dyes, especially, in organic semiconductors (for instance, "fvin") with the perspective of future electrical pumping (although, the VECSOL threshold is far higher than those reported in planar DFB structure, making VECSOL not the ideal candidate for an early demonstration of electrical pumping).

A comprehensive degradation study is envisaged via the already-existing LabView program. This study includes examining the degradation issues (photochemical and thermal effects) in the VECSOL based on some other organic dyes such as Pyrromethene. According to very recent results obtained in our group, this material showed to be highly photostable with an emission that could last for several hours. The effect of oxygen on degradation is also the subject of future study which can be realized by comparative degradation studies in air and in an oxygen-free atmosphere.

As we saw during this thesis, the VECSOL tunability was possible thanks to film thickness variation by going toward the sample edge. Therefore, finding a systematic approach to have a controlled tunability of the emission wavelength is highly sought in the future studies.

Toward practical applications, a major problem is related to the pump source and a limit of the total device cost and portability which is imposed by the current sources. In this regard, the idea of laser diode pumping or LED pumping is very attractive and promising, following the recent results obtained by Samuel et al. [60] and also the advances in laser diode technology which have made possible the appearance of powerful blue-emitting laser diodes.

The VECSOL architecture with its very versatile structure makes it a tool that can be used to study and quantify photophysical parameters in organic dyes and, more interestingly, in organic semiconductors that are usually unknown (or known with rather poor accuracy). This would make the VECSOL an attractive tool to a broader community of organic photonics in a way that it can be useful to characterize materials for OLEDs and solar cells, for instance.

Appendix

Appendix 1: Some practical spectroscopic data relevant to the used laser dyes (Rhodamine 640 and DCM)

Rhodamine 640 and DCM are two of the very well-known laser dyes used within the realized work of this thesis. The later has a full chemical name of *"4-(dicyanomethylene)-2-methyl-6-(p-dimethylaminostyryl)-4H-pyran"* with the structure shown in the following figure (top). Rhodamine 640 has a full chemical name of "*9-(2-carboxyphenyl)-2,3,6,7,12,13,16,17-octahydro-1H,5H,11H,15H-xantheno [2,3,4-ij:5,6,7-i',j']diquinolizin-4-ium perchlorate*" and its structure is shown in the following figure (bottom). The consumed laser dyes were purchased from Exciton Inc.

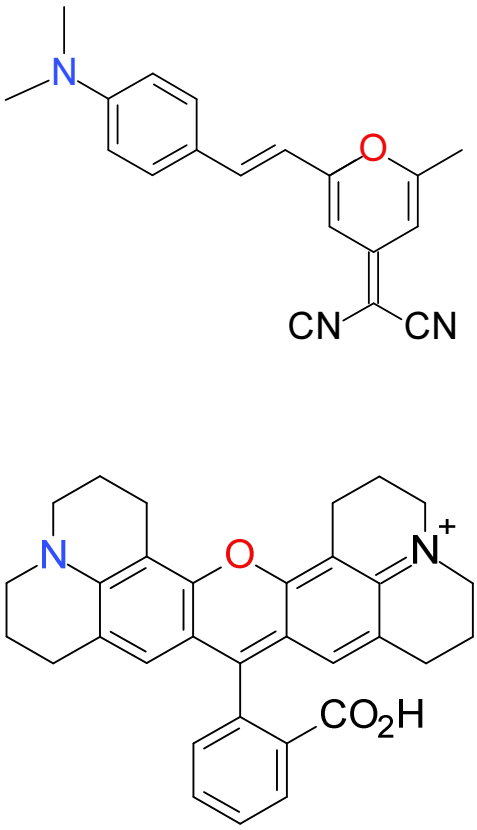

A 1. 1 – Chemical structures of DCM dye (top), Rhodamine 640 (bottom).

Concerning a dye molecule, two of the very useful parameters are the absorption and stimulated emission cross sections which are denoted as $\sigma_{abs}(cm^2)$ and $\sigma_{em}(cm^2)$, respectively. In the following, these parameters for different wavelengths are calculated from the absorption and emission curves measured experimentally in thin solid films of PMMA.

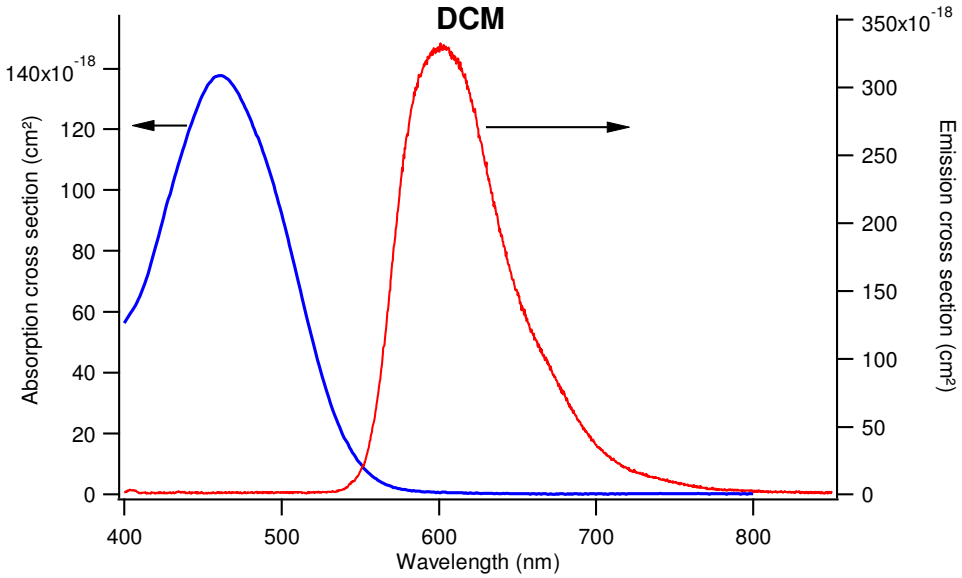

A 1. 2 – Absorption and emission curves of DCM-doped PMMA film and the corresponding cross sections for each curve.

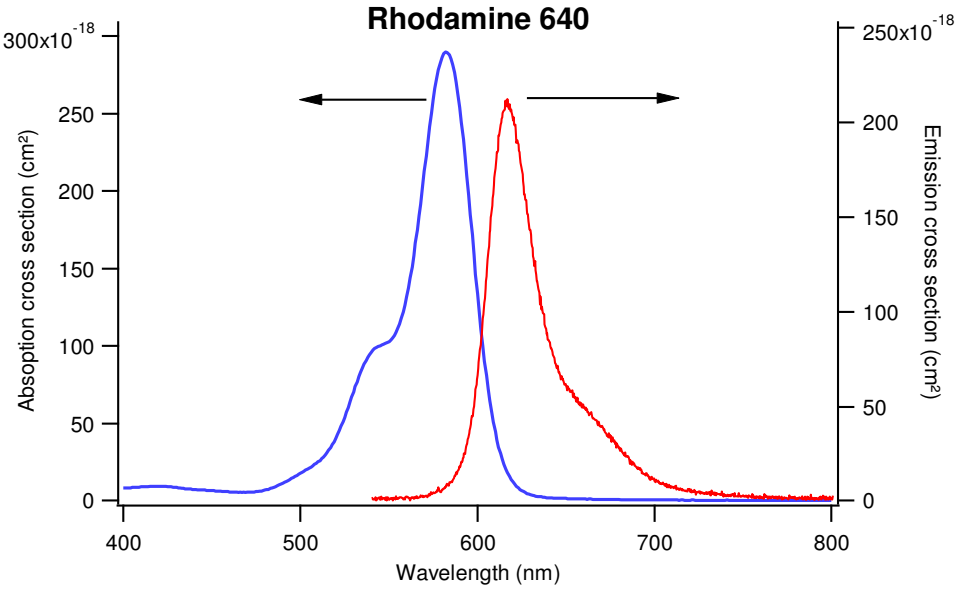

A 1. 3 - Absorption and emission curves of Rhodamine 640-doped PMMA film and the corresponding cross sections for each curve.

In the above graphs, the stimulated emission cross section is calculated from the well-known Füchtbauer-Ladenburg equation:

$$\sigma_{em}(\lambda) = \frac{\phi_f f(\lambda)}{8\pi n^2 c\tau \int \frac{f(\lambda)}{\lambda^4} d\lambda} \qquad \text{(A 1.1)}$$

where λ is the wavelength, ϕ_f is the fluorescence quantum yield, $f(\lambda)$ is the fluorescence spectrum measured experimentally and normalized to one, n is the medium refractive index, c is the speed of light in air and τ is the radiative lifetime.

For the relation given in (A 1.1), the refractive index of doped PMMA was measured experimentally to be around n=1.5 (see appendix 2). For DCM, the values of ϕ_f=0.76 and τ=2 ns were used based on Ref. [179]. For Rhodamine 640, a ϕ_f = 0.8 [105] and τ=7.5 ns [106] were considered.

For the calculation of absorption cross section the following procedure was taken.

First, dye-doped solutions of PMMA in anisole were prepared (doping rates were 5 wt. % and 1 wt. % for DCM and Rhodamine 640, respectively) and spin-casted on a glass slide. The film thicknesses were determined by the Alpha-Step IQ surface profiler (KLA Tencor). The absorbances of the realized films were measured by UV-Visible spectrophotometer Varian (Cary 100 series). Absorbance is expressed as $\alpha\ell$, with α being the absorption coefficient and ℓ the film thickness. The film transmission is written as $T = 10^{-\alpha\ell}$ (the transmission can also be expressed by a power function with an exponential base, that is, $T = e^{-\alpha\ell}$). The absorption coefficient can be easily determined through dividing the measured absorbance by the realized film thickness. To have the absorption cross section per dye molecule, the obtained absorption coefficient should be divided by the density of the dye molecules in the film. Using the relation (A 4.2) given in appendix 4, one can have a rough estimation of the density of the dyes in PMMA matrix as the following:

$$N = \frac{p\rho_{film} N_A}{M_{DCM}} = \frac{0.05 \times 1.2(g.cm^{-3}) \times 6.022 \times 10^{23}(mol^{-1})}{303(g.mol^{-1})}$$

$$= 1.19 \times 10^{20}(\text{DCM molecules} / cm^3)$$

$$N = \frac{p\rho_{film} N_A}{M_{Rhodamine\ 640}} = \frac{0.01 \times 1.2(g.cm^{-3}) \times 6.022 \times 10^{23}(mol^{-1})}{591(g.mol^{-1})} \qquad \text{(A 1.2)}$$

$$= 1.22 \times 10^{19}(\text{Rhodamine 640 molecules} / cm^3)$$

Given the above estimation about the density of dye molecules within a film of PMMA, the absorption cross section (cm^2) for different wavelengths can be easily obtained through division of the absorption coefficient α by the N value.

In the following tables, some of the useful spectroscopic properties of the DCM and Rhodamine 640 in solid matrices, found experimentally and/or reported in the literature, are summarized.

DCM								
Condition	λ_{max}^{abs} (nm)	λ_{max}^{em} (nm)	$\sigma_{abs}(cm^2)$	$\sigma_{em}(cm^2)$	τ (ns)	φ_f	$^{*}k_f$ $(s)^{-1}$	$^{**}k_{nr}$ $(s)^{-1}$
5 wt. % DCM in PMMA (measured by us)	460	600	@ $\lambda_{max} = 1.37\times10^{-16}$ @ 532 nm $= 2.86\times10^{-17}$	@ $\lambda_{max} = 3.3\times10^{-16}$	–	–	–	–
DCM in PMMA Ref. [179]	453	550	----	----	2	0.76	0.38	0.12
DCM in bulk PMMA Ref. [105]	460	570	@ $\lambda_{max} \simeq 5.1\times10^{-16}$ @ 532 nm $\simeq 8\times10^{-17}$	@ $\lambda_{max} \simeq 3.6\times10^{-16}$	1.31	0.66	0.5	0.25
Rhodamine 640								
1 wt. % Rhodamine 640 in PMMA (measured by us)	582	617	@ $\lambda_{max} = 2.9\times10^{-16}$ @ 532 nm $= 0.77\times10^{-17}$	@ $\lambda_{max} = 2.1\times10^{-16}$	–	–	–	–
1 wt. % Rhodamine 640 in PMMA Ref. [106]	580	630	----	-----	7.5	–	–	–
Rhodamine 640 in PMMA Ref. [180]	–	–	@ 527 nm $= 1.2\times10^{-16}$	@ $\lambda_{max} = 5.3\times10^{-16}$	4			

$^{*}k_f$ is the radiative rate constant and is defined as $k_f = \varphi_f/\tau$.

$^{**}k_{nr}$ is the nonradiative rate constant and is defined as $k_{nr} = k_f(\frac{1}{\varphi_f} - 1)$.

Appendix 2: Refractive index determination of doped PMMA

The following technique was used to measure the refractive index of the Rhodamine 640-doped PMMA film.

First, a layer of the doped PMMA was spin casted on a silica substrate (round shape with standard size of a mirror) under the same experimental condition as the VECSOL sample had been prepared (PMMA solution of the same viscosity, 1 wt. % doping rate and with the same spin speed). The film thickness ($\ell = 18.7\ \mu m$) was determined by Alpha-Step IQ surface profiler (KLA-Tencor Corp.). This sample was then inserted inside the spectrophotometer (Varian - Cary 100 series) and its transmission curve was monitored as a function of spectroscopic wavenumber ($1/\lambda$). As for long wavelengths the sample becomes transparent, the ~ 18-μm-thick film forms a Fabry-Perot etalon for the incident wavelengths leading to a sinusoidally-modulated transmission curve. This curve was fitted by a sinusoidal function as the following:

$$f(\tilde{\nu}) = A\tilde{\nu} + B + C\cos\left(\frac{2\pi\tilde{\nu}}{\Lambda} + \phi\right) \qquad (A\ 2.1)$$

where A, B and C are constant, $\tilde{\nu} = 1/\lambda$ is the spectroscopic wavenumber, $\Lambda = 1/(2n\ell)$ is the modulation period where $n\ell$ is the optical length with n being the refractive index and ℓ the film thickness.

Using the above-described procedure, a refractive index of $n = 1.520$ was deduced for the doped PMMA film in a rather precise manner.

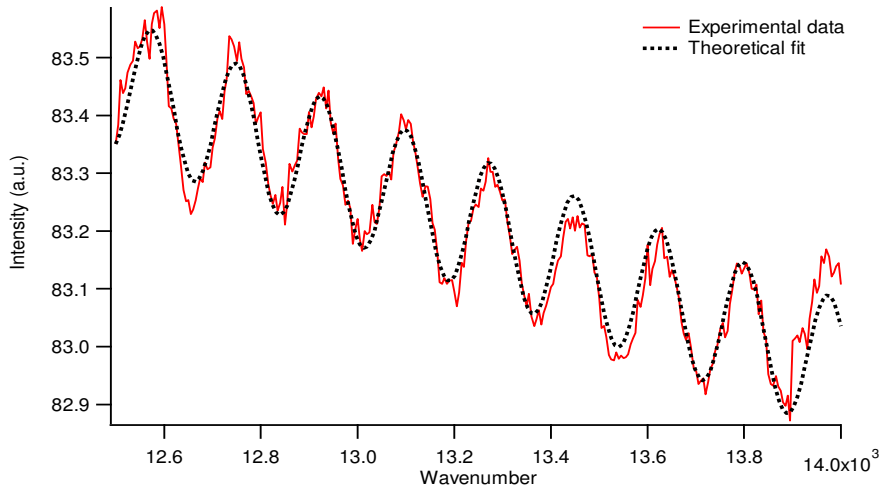

A 2. 1 – (solid line) transmission curve of a Fabry-Perot etalon formed by an ~18-μm-thick film of Rhodamine 640-doped PMMA. (dotted line) a fit to the experimental data to deduce the refractive index of a doped PMMA film.

Appendix 3: General information on the PMMA and spin speed curves

Poly (methyl methacrylate) known as PMMA is a transparent polymer which was used as the host matrix to embed the dye particles. Standard PMMA solutions in anisole with molecular weights (MW) of 495,000 and 950,000 were bought from MicroChem Corp. The latter is known under the commercial name of PMMA A15 which corresponds to 15 wt. % of dissolved PMMA in anisole and the former is recognized as PMMA A6 which is a solution with 6 wt. % of PMMA in anisole. The chemical structure of PMMA is shown in the following figure.

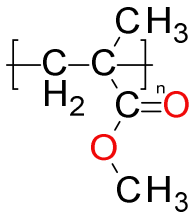

A 3. 1 – Chemical structure of Poly (methyl methacrylate) known as PMMA.

In the following the first two graphs are the spin speed curves provided with the bought products.

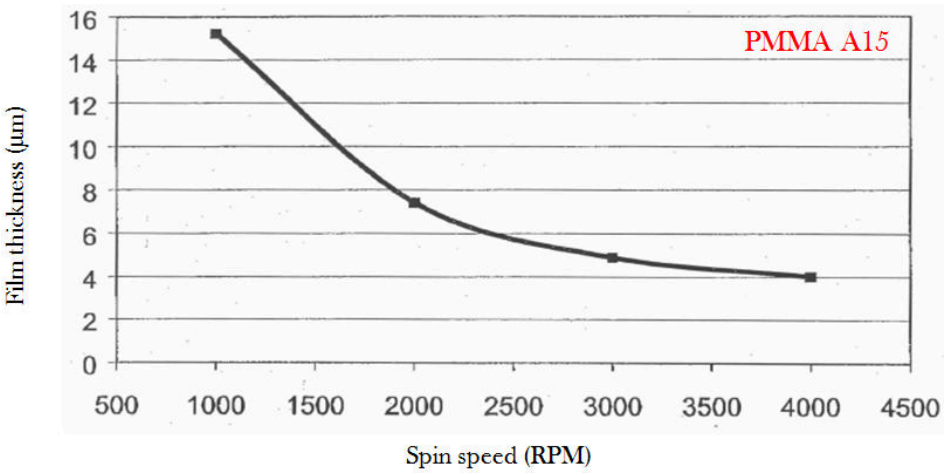

A 3. 2 – Spin speed curve of PMMA A15, provided by the MicroChem Corp.

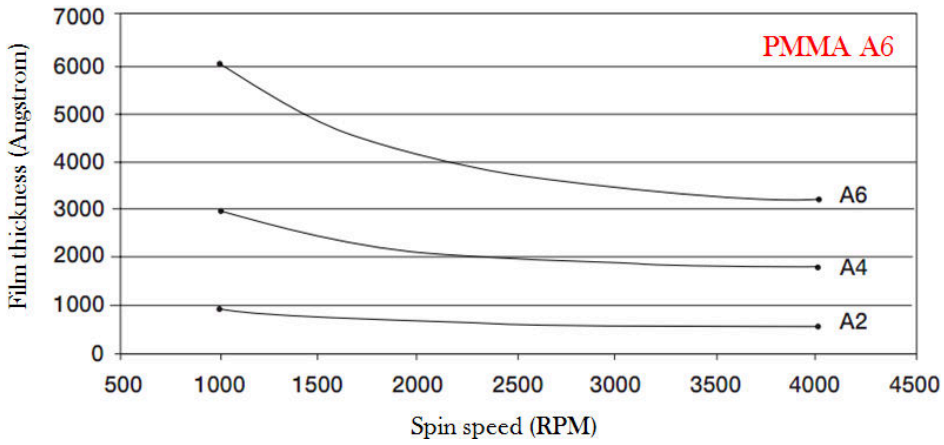

A 3. 3 - Spin speed curve of PMMA A6, provided by the MicroChem Corp.

To make an ~18-μm -thick film of Rhodamine 640-doped PMMA, the PMMA A15 type was used and the spin coater was programmed with the following recipe:

RPM 1 = 650	Ramp 1 = 1 Sec.	Time 1 = 30 Sec.
RPM 2 = 750	Ramp 2 = 3 Sec.	Time 2 = 15 Sec.
RPM 3 = 800	Ramp 3 = 3 Sec.	Time 3 = 15 Sec.
Ramp 4 = 30 Sec.		

The information in the first line of the above table means during one second the spin speed reaches 650 rounds per minute and keeps going at this speed during 30 seconds before starting the second phase.

In order to make ~600-nm-thick film of DCM doped PMMA (used for gain measurement and laser study in chapter 2), the less viscous PMMA type (PMMA A6) was used with the following spin speeds:

RPM 1 = 500	Ramp 1 = 1 Sec.	Time 1 = 1 Sec.
RPM 2 = 700	Ramp 2 = 1 Sec.	Time 2 = 1Sec.
RPM 3 = 1000	Ramp 3 = 1 Sec.	Time 3 = 40 Sec.
Ramp 4 = 30 Sec.		

The used recipes for the spin coater were obtained based on the spin speed curves and trial and error method.

As it can be seen in the above-given spin speed curves there is thickness gap from 600 nm

to around 4 μm . Therefore, for the experiment where the VECSOL single-peak operation was sought, a film thickness in this gap was required. For this purpose, the two PMMA types (PMMA A15 and PMMA A6) were mixed with equal weight ratio (50%-50%). The following curve is the corresponding spin speed curve obtained experimentally in the laboratory.

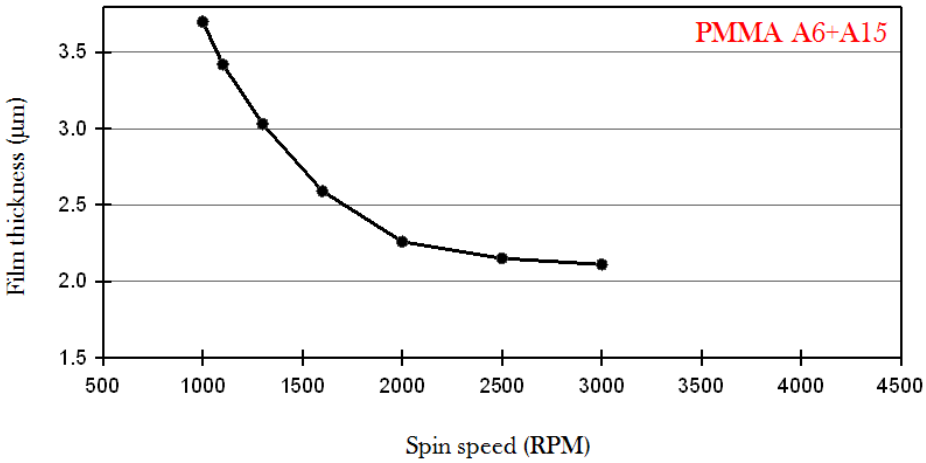

A 3. 4 - Spin speed curve of PMMA (A6+A15) in equal weight ratios obtained experimentally in our laboratory.

It should be noted that all the prepared samples were completely homogenous within a central zone with a gradually-increased thickness by going toward the edge.

Appendix 4: Estimation of Rhodamine 640 dye density in a film of PMMA

Estimation of the Rhodamine 640 dye density (N) in PMMA can be easily obtained through the following relation:

$$N(cm^{-3}) = \frac{\text{Rhodamine 640 total weight}}{\text{Rhodamine 640 molar weight}} \qquad \text{(A 4.1)}$$

This relation is expressed as the following:

$$N = \frac{p\rho_{film} N_A}{M_{Rhodamine\ 640}} \qquad \text{(A 4.2)}$$

where $N(cm^{-3})$ is the Rhodamine 640 dye density in the doped film, p is the doping rate (1 wt. % in our case), $N_A(mol^{-1}) = 6.022\times10^{23}$ is the Avogadro number, $M_{Rhodamine\ 640}(g/mol) = 591$ is the Rhodamine 640 molar weight and $\rho_{film}(g/cm^3)$ is the doped film density which is considered to be almost equal to non-doped PMMA film density ($\rho_{film}(g/cm^3) \approx \rho_{PMMA}(g/cm^3) \approx 1.2$ g/cm^3) as 1 wt. % of doping should not cause a big difference between doped and non-doped films.
Using the above information, the density of the Rhodamine 640 molecules is estimated to be $N = 1.22\times10^{19}$ (cm^{-3}).

Appendix 5: VECSOL dielectric mirror transmission curves

In the following, the first figure is the transmission curve of a typical dielectric output coupler (Altechna Inc.) with 200 mm curvature radius and ~ 98% reflectivity over the wavelength range of 600-680 nm measured by the UV-Visible spectrophotometer Varian (Cary 100 series).

The second curve corresponds to the transmission curve of a dielectric plane mirror from the same supplier with reflectivity of ~ 99.5% in the range of 620-660 nm. The curve in the inset of each graph is a zoom over the desired spectral region determining the highest reflectivity.

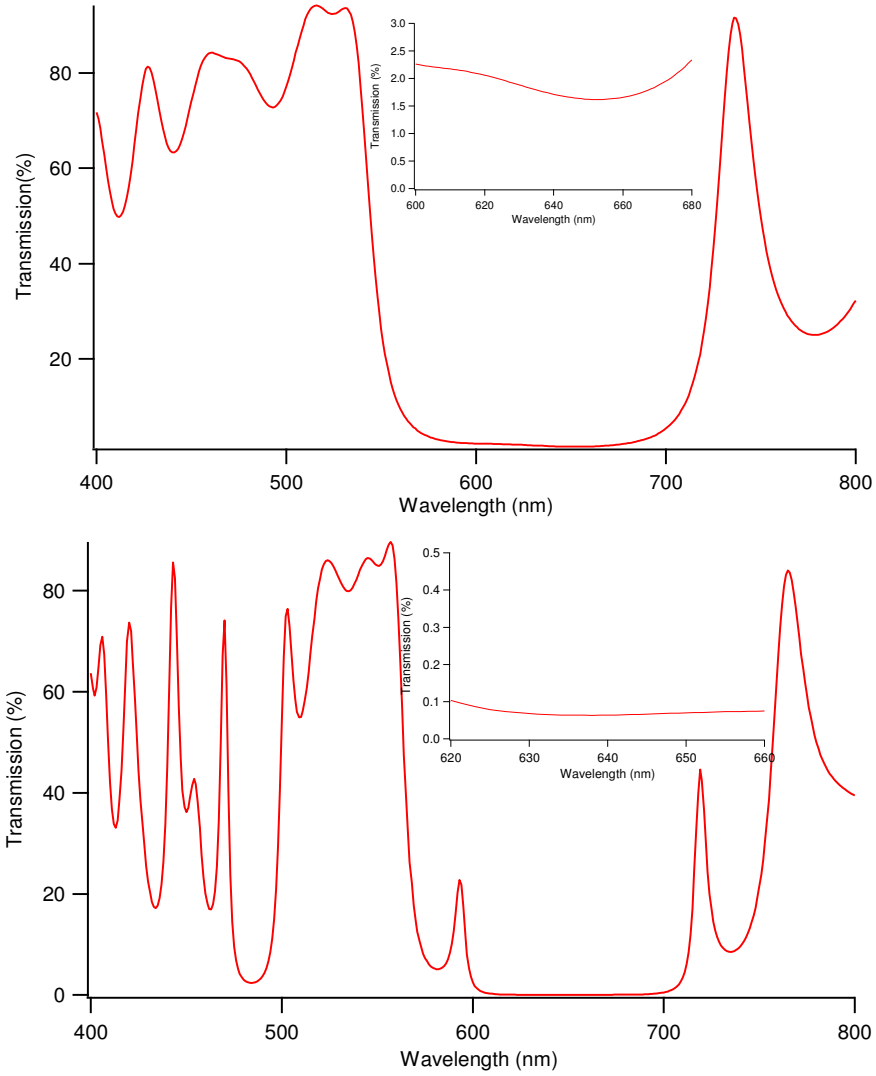

A 5. 1 –. (top) typical transmission curve of the VECSOL output coupler with 98% reflectivity within 600-680 nm. (bottom) typical transmission curve of the VECSOL plane mirror with 99.5% reflectivity within 620-660 nm. The insets are zooms over the interested regions.

Appendix 6: Calculation of the VECSOL intracavity photon lifetime

To obtain the intracavity photon lifetime (τ_{cav}), imagine a laser cavity where I_0 is representing the intracavity laser intensity in a transverse cross-section of the beam at time $t = 0$.

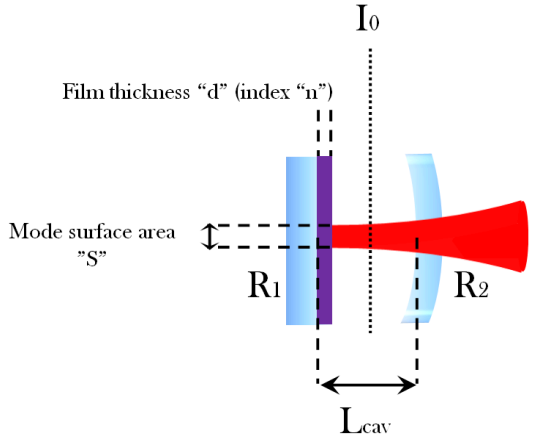

A 6. 1 – VECSOL cavity and the corresponding notations for each part.

The beam intensity at the same position after a round-trip inside the cavity at time $t = t_1$ will be:

$$I(t_1) = I_0 R_1 R_2 (1 - T_i)^2 \qquad \text{(A 6.1)}$$

where T_i is the cavity loss in single-way beam trip and R_1 and R_2 are the mirror reflectivities. Recall that I and q are proportional (relation 3.41), then equation (A 6.1) can also be expressed in terms of the number of intracavity photons where in this case q_0 is the number of photons at time $t = 0$ and so on. Therefore, the number of photons after m round-trip inside the cavity is given by:

$$q(t_m = \frac{2mL}{c}) = q_0 \left[R_1 R_2 (1 - T_i)^2 \right]^m \qquad \text{(A 6.2)}$$

where $L = (n-1)d + L_{cav}$ is the optical path length found in relation (3.42) and c is the light velocity.

The decay in q is exponential since after each round-trip inside the cavity a fixed number of photon would be lost. Then, relation (A 6.2) can be expressed as:

$$q(t_m) = e^{\left(-\frac{t_m}{\tau_{cav}}\right)} = e^{\left(-\frac{2mL}{c\tau_{cav}}\right)} \qquad \text{(A 6.3)}$$

where, τ_{cav} is representing the intracavity photon lifetime which can be interpreted as the time during which the number of supposedly fixed pack of photons imprisoned inside the cavity decays exponentially to zero by the rate of $1/\tau_{cav}$. From (A 6.2) and (A 6.3) τ_{cav} will be obtained as the following:

$$\begin{aligned} \tau_{cav} &= -\frac{2L}{cLn\left[R_1R_2(1-T_i)^2\right]} \\ &= -\frac{2\left[(n-1)d + L_{cav}\right]}{cLn\left[R_1R_2(1-T_i)^2\right]} \end{aligned} \qquad \text{(A 6.4)}$$

Bibliography

1. Sorokin, P.P. and J.R. Lankard, Stimulated Emission Observed From An Organic Dye Chloro-Aluminum Phthalocyanine. Ibm Journal Of Research And Development, 1966. 10(2): p. 162-&.
2. Peterson, O.G., S.A. Tuccio, and B.B. Snavely, Cw Operation Of An Organic Dye Solution Laser. Applied Physics Letters, 1970. 17(6): p. 245-&.
3. Fork, R.L., et al., Compression of optical pulses to six femtoseconds by using cubic phase compensation. Opt. Lett., 1987. 12(7): p. 483.
4. Eggeling, C., et al., Photobleaching of fluorescent dyes under conditions used for single-molecule detection: Evidence of two-step photolysis. Analytical Chemistry, 1998. 70(13): p. 2651-2659.
5. Soffer, B.H. and McFarlan.Bb, Continuously Tunable Narrow-Band Organic Dye Lasers. Applied Physics Letters, 1967. 10(10): p. 266-&.
6. Peterson, O.G. and B.B. Snavely, Stimulated Emission From Flashlamp-Excited Organic Dyes In Polymethyl Methacrylate. Applied Physics Letters, 1968. 12(7): p. 238-&.
7. Gromov, D.A., et al., Efficient Plastic-Host Dye-Lasers. Journal Of The Optical Society Of America B-Optical Physics, 1985. 2(7): p. 1028-1031.
8. Oconnell, R.M. and T.T. Saito, Plastics For High-Power Laser Applications - A Review. Optical Engineering, 1983. 22(4): p. 393-399.
9. Costela, A., et al., Laser performance of pyrromethene 567 dye in solid polymeric matrices with different cross-linking degrees. Journal Of Applied Physics, 2001. 90(7): p. 3159-3166.
10. Abedin, K.M., et al., 10 kHz repetition rate solid-state dye laser pumped by diode-pumped solid-state laser. Optics Communications, 2003. 218(4-6): p. 359-363.
11. Costela, A., et al., Studies on laser action from polymeric matrices based on trimethylsilyl methacrylate doped with pyrromethene 567 dye. Optics Communications, 2002. 201(4-6): p. 437-445.
12. Costela, A., et al., Solid-state dye lasers based on modified rhodamine 6G dyes copolymerized with methacrylic monomers. Journal Of Applied Physics, 1996. 80(6): p. 3167-3173.
13. Costela, A., et al., Solid-state dye laser based on coumarin 540A-doped polymeric matrices. Optics Communications, 1996. 130(1-3): p. 44-50.
14. Amatguerri, F., et al., Laser Action From A Rhodamine 640-Doped Copolymer Of 2-Hydroxyethyl Methacrylate And Methyl-Methacrylate. Optics Communications, 1995.

114(5-6): p. 442-446.
15. Canva, M., et al., Perylene-Doped And Pyrromethene-Doped Xerogel For A Pulsed-Laser. Applied Optics, 1995. 34(3): p. 428-431.
16. Nhung, T.H., et al., Stable doped hybrid sol-gel materials for solid-state dye laser. Applied Optics, 2003. 42(12): p. 2213-2218.
17. Tessler, N., G.J. Denton, and R.H. Friend, Lasing from conjugated-polymer microcavities. Nature, 1996. 382(6593): p. 695-697.
18. Koschorreck, M., et al., Dynamics of a high-Q vertical-cavity organic laser. Applied Physics Letters, 2005. 87(18).
19. DiazGarcia, M.A., et al., "Plastic" lasers: Comparison of gain narrowing with a soluble semiconducting polymer in waveguides and microcavities. Applied Physics Letters, 1997. 70(24): p. 3191-3193.
20. Persano, L., et al., Low-threshold blue-emitting monolithic polymer vertical cavity surface-emitting lasers. Applied Physics Letters, 2006. 89(12).
21. Stagira, S., et al., Single-mode picosecond blue laser emission from a solid conjugated polymer. Applied Physics Letters, 1998. 73(20): p. 2860-2862.
22. Zavelani-Rossi, M., et al., Single-mode tunable organic laser based on an electroluminescent oligothiophene. Applied Physics Letters, 2001. 79(25): p. 4082-4084.
23. Persano, L., et al., Monolithic polymer microcavity lasers with on-top evaporated dielectric mirrors. Applied Physics Letters, 2006. 88(12).
24. Dumarcher, V., et al., Polymer thin-film distributed feedback tunable lasers. Journal Of Optics A-Pure And Applied Optics, 2000. 2(4): p. 279-283.
25. Mele, E., et al., Polymeric distributed feedback lasers by room-temperature nanoimprint lithography. Applied Physics Letters, 2006. 89(13).
26. Suganuma, N., et al., Organic polymer DBR laser by softlithography. Journal Of Photopolymer Science And Technology, 2002. 15(2): p. 273-278.
27. Frolov, S.V., et al., Cylindrical microlasers and light emitting devices from conducting polymers. Applied Physics Letters, 1998. 72(22): p. 2811-2813.
28. Dou, S.X., et al., Polymer microring lasers with longitudinal optical pumping. Applied Physics Letters, 2002. 80(2): p. 165-167.
29. Berggren, M., et al., Solid-state droplet laser made from an organic blend with a conjugated polymer emitter. Advanced Materials, 1997. 9(12): p. 968-&.
30. Hermes, R.E., et al., High-Efficiency Pyrromethene Doped Solid-State Dye-Lasers. Applied Physics Letters, 1993. 63(7): p. 877-879.
31. Faloss, M., et al., Toward millions of laser pulses with pyrromethene- and perylene-doped xerogels. Applied Optics, 1997. 36(27): p. 6760-6763.

32. Rodriguez, M., et al., A Simple Rotating System To Avoid Early Degradation Of Solid-State Dye-Lasers. Measurement Science & Technology, 1995. 6(7): p. 971-978.
33. Persano, L., et al., Rapid prototyping encapsulation for polymer light-emitting lasers. Applied Physics Letters, 2009. 94(12).
34. Vannahme, C., et al., All-polymer organic semiconductor laser chips: Parallel fabrication and encapsulation. Optics Express. 18(24): p. 24881-24887.
35. Herrnsdorf, J., et al., Flexible blue-emitting encapsulated organic semiconductor DFB laser. Optics Express. 18(25): p. 25535-25545.
36. Richardson, S., et al., Improved operational lifetime of semiconducting polymer lasers by encapsulation. Applied Physics Letters, 2007. 91(26).
37. Woggon, T., S. Klinkhammer, and U. Lemmer, Compact spectroscopy system based on tunable organic semiconductor lasers. Applied Physics B-Lasers And Optics, 2010. 99(1-2): p. 47-51.
38. Oki, Y., et al., Spectroscopic applications of integrated tunable solid-state dye laser. Optical Review, 2005. 12(4): p. 301-306.
39. Schneider, D., et al., An ultraviolet organic thin-film solid-state laser for biomarker applications. Advanced Materials, 2005. 17(1): p. 31-+.
40. Woggon, T., S. Klinkhammer, and U. Lemmer, Compact spectroscopy system based on tunable organic semiconductor lasers. Applied Physics B-Lasers And Optics. 99(1-2): p. 47-51.
41. Lu, M., et al., Plastic distributed feedback laser biosensor. Applied Physics Letters, 2008. 93(11).
42. Yang, Y., G.A. Turnbull, and I.D.W. Samuel, Sensitive Explosive Vapor Detection with Polyfluorene Lasers. Advanced Functional Materials. 20(13): p. 2093-2097.
43. Richardson, S., et al., Chemosensing of 1,4-dinitrobenzene using bisfluorene dendrimer distributed feedback lasers. Applied Physics Letters, 2009. 95(6).
44. Rose, A., et al., Sensitivity gains in chemosensing by lasing action in organic polymers. Nature, 2005. 434(7035): p. 876-879.
45. Kuriki, K., et al., High-efficiency organic dye-doped polymer optical fiber lasers. Applied Physics Letters, 2000. 77(3): p. 331-333.
46. Sheeba, M., et al., Multimode laser emission from dye doped polymer optical fiber. Applied Optics, 2007. 46(33): p. 8089-8094.
47. Tang, C.W. and S.A. Vanslyke, Organic Electroluminescent Diodes. Applied Physics Letters, 1987. 51(12): p. 913-915.
48. Garnier, F., et al., An All-Organic Soft Thin-Film Transistor With Very High Carrier Mobility. Advanced Materials, 1990. 2(12): p. 592-594.

49. Kozlov, V.G., et al., Study of lasing action based on Forster energy transfer in optically pumped organic semiconductor thin films. Journal Of Applied Physics, 1998. 84(8): p. 4096-4108.
50. McGehee, M.D. and A.J. Heeger, Semiconducting (conjugated) polymers as materials for solid-state lasers. Advanced Materials, 2000. 12(22): p. 1655-1668.
51. Stehr, J., et al., A low threshold polymer laser based on metallic nanoparticle gratings. Advanced Materials, 2003. 15(20): p. 1726-+.
52. Andrew, P., et al., Photonic band structure and emission characteristics of a metal-backed polymeric distributed feedback laser. Applied Physics Letters, 2002. 81(6): p. 954-956.
53. Reufer, M., et al., Low-threshold polymeric distributed feedback lasers with metallic contacts. Applied Physics Letters, 2004. 84(17): p. 3262-3264.
54. Wallikewitz, B.H., et al., A Lasing Organic Light-Emitting Diode. Advanced Materials. 22(4): p. 531-+.
55. Gwinner, M.C., et al., Integration of a Rib Waveguide Distributed Feedback Structure into a Light-Emitting Polymer Field-Effect Transistor. Advanced Functional Materials, 2009. 19(9): p. 1360-1370.
56. Kozlov, V.G., et al., Structures for organic diode lasers and optical properties of organic semiconductors under intense optical and electrical excitations. Ieee Journal Of Quantum Electronics, 2000. 36(1): p. 18-26.
57. Segal, M., et al., Excitonic singlet-triplet ratios in molecular and polymeric organic materials. Physical Review B, 2003. 68(7).
58. Giebink, N.C. and S.R. Forrest, Temporal response of optically pumped organic semiconductor lasers and its implication for reaching threshold under electrical excitation. Physical Review B, 2009. 79(7).
59. Gartner, C., et al., The influence of annihilation processes on the threshold current density of organic laser diodes. Journal Of Applied Physics, 2007. 101(2).
60. Yang, Y., G.A. Turnbull, and I.D.W. Samuel, Hybrid optoelectronics: A polymer laser pumped by a nitride light-emitting diode. Applied Physics Letters, 2008. 92(16).
61. Yang, Y., I.D.W. Samuel, and G.A. Turnbull, The Development of Luminescent Concentrators for Pumping Organic Semiconductor Lasers. Advanced Materials, 2009. 21(31): p. 3205-+.
62. Voss, T., D. Scheel, and W. Schade, A microchip-laser-pumped DFB-polymer-dye laser. Applied Physics B: Lasers and Optics, 2001. 73(2): p. 105.
63. Rabbani-Haghighi, H., et al., Laser operation in nondoped thin films made of a small-molecule organic red-emitter. Applied Physics Letters, 2009. 95(3).

64. Riechel, S., et al., Very compact tunable solid-state laser utilizing a thin-film organic semiconductor. Optics Letters, 2001. 26(9): p. 593-595.
65. Turnbull, G.A., et al., Operating characteristics of a semiconducting polymer laser pumped by a microchip laser. Applied Physics Letters, 2003. 82(3): p. 313-315.
66. Wang, G., Infrared Dye Laser-Excited By A Diode Laser. Optics Communications, 1974. 10(2): p. 149-153.
67. Riedl, T., et al., Tunable organic thin-film laser pumped by an inorganic violet diode laser. Applied Physics Letters, 2006. 88(24).
68. Sakata, H. and H. Takeuchi, Diode-pumped polymeric dye lasers operating at a pump power level of 10 mW. Applied Physics Letters, 2008. 92(11).
69. Vasdekis, A.E., et al., Diode pumped distributed Bragg reflector lasers based on a dye-to-polymer energy transfer blend. Optics Express, 2006. 14(20): p. 9211-9216.
70. Sakata, H., et al., Diode-pumped distributed-feedback dye laser with an organic-inorganic microcavity. Applied Physics B-Lasers And Optics, 2008. 92(2): p. 243-246.
71. Sakata, H. and H. Takeuchi, Green-emitting organic vertical-cavity laser pumped by InGaN-based laser diode. Electronics Letters, 2007. 43(25): p. 1431-1433.
72. Cohen-Tannoudji, C., B. Diu, and F. Laloe. 1st ed. 2006: Wiley-Interscience.
73. Guymont, M., Structure De La Matière - Atomes, Liaisons Chimiques Et Cristallographie. 2003: Belin.
74. Valeur, B., Molecular Fluorescence: Principles and Applications. 1st ed. 2001: Wiley-VCH. 250.
75. Klessinger, M. and J. Michl, Excited States and Photo-Chemistry of Organic Molecules. 1995: p. 537.
76. Wardle, B., Principles and Applications of photochemistry. 1 ed. 2009: Wiley.
77. Auweraer, M.V.d., Photophysics and Photochemistry of Molecular Materials, B-KUL-H06D5A.
78. Marling, J.B., D.W. Gregg, and L. Wood, Chemical quenching of the triplet state in flashlamp-excited liquid organic lasers. Vol. 17. 1970: AIP. 527-530.
79. Bornemann, R., U. Lemmer, and E. Thiel, Continuous-wave solid-state dye laser. Optics Letters, 2006. 31(11): p. 1669-1671.
80. Kranzelbinder, G. and G. Leising, Organic solid-state lasers. Reports On Progress In Physics, 2000. 63(5): p. 729-762.
81. Berggren, M., et al., Organic lasers based on Forster transfer. Synthetic Metals, 1997. 91(1-3): p. 65-68.
82. Schneider, D., et al., Laser threshold reduction in an all-spiro guest-host system. Applied Physics Letters, 2004. 85(10): p. 1659-1661.

83. Nagawa, M., et al., Organic solid-state distributed feedback dye laser with a nonmorphological modification grating. Applied Physics Letters, 2000. 77(17): p. 2641-2643.
84. Kozlov, V.G., et al., Laser action in organic semiconductor waveguide and double-heterostructure devices. Nature, 1997. 389(6649): p. 362-364.
85. Schneider, D., et al., Wavelength-tunable organic solid-state distributed-feedback laser. Applied Physics B-Lasers And Optics, 2003. 77(4): p. 399-402.
86. Holzer, W., et al., Spectroscopic and travelling-wave lasing characterisation of Gilch-type and Horner-type MEH-PPV. Synthetic Metals, 2004. 140(2-3): p. 155-170.
87. McGehee, M.D., et al., Semiconducting polymer distributed feedback lasers. Applied Physics Letters, 1998. 72(13): p. 1536-1538.
88. Riechel, S., et al., A nearly diffraction limited surface emitting conjugated polymer laser utilizing a two-dimensional photonic band structure. Applied Physics Letters, 2000. 77(15): p. 2310-2312.
89. Wegmann, G., et al., Laser emission from a solid conjugated polymer: Gain, tunability, and coherence. Physical Review B, 1998. 57(8): p. R4218.
90. Zavelani-Rossi, M., et al., Organic laser based on thiophene derivatives. Synthetic Metals, 2003. 139(3): p. 901-903.
91. Schneider, D., et al., Organic solid-state lasers based on sexiphenyl as active chromophore. Journal Of Applied Physics, 2005. 98(4).
92. Schneider, D., et al., Deep blue widely tunable organic solid-state laser based on a spirobifluorene derivative. Applied Physics Letters, 2004. 84(23): p. 4693-4695.
93. Johansson, N., et al., Solid-state amplified spontaneous emission in some spiro-type molecules: A new concept for the design of solid-state lasing molecules. Advanced Materials, 1998. 10(14): p. 1136-+.
94. Salbeck, J., M. Schorner, and T. Fuhrmann, Optical amplification in spiro-type molecular glasses. Thin Solid Films, 2002. 417(1-2): p. 20-25.
95. Forget, S., et al., Red-emitting fluorescent organic light emitting diodes with low sensitivity to self-quenching. Journal Of Applied Physics. 108(6).
96. Okamoto, K., Fundamentals of Optical Waveguides. 2nd ed. 2005: Academic Press.
97. McGehee, M.D., et al., Amplified spontaneous emission from photopumped films of a conjugated polymer. Physical Review B, 1998. 58(11): p. 7035-7039.
98. Xia, R.D., et al., Fluorene-based conjugated polymer optical gain media. Organic Electronics, 2003. 4(2-3): p. 165-177.
99. Calzado, E.M., et al., Amplified spontaneous emission in polymer films doped with

a perylenediimide derivative. Applied Optics, 2007. 46(18): p. 3836-3842.
100. Ribierre, J.C., et al., Amplified spontaneous emission and lasing properties of bisfluorene-cored dendrimers. Applied Physics Letters, 2007. 91(8).
101. Thompson, J., et al., Amplified spontaneous emission in the near infrared from a dye-doped polymer thin film. Synthetic Metals, 2004. 143(3): p. 305-307.
102. Liu, X., et al., Low-threshold amplified spontaneous emission and laser emission in a polyfluorene derivative. Applied Physics Letters, 2004. 84(15): p. 2727-2729.
103. Ishow, E., et al., Multicolor Emission of Small Molecule-Based Amorphous Thin Films and Nanoparticles with a Single Excitation Wavelength. Chemistry Of Materials, 2008. 20(21): p. 6597-6599.
104. Brouwer, H.J., et al., Stimulated emission from vacuum-deposited thin films of a substituted oligo(p-phenylene vinylene). Applied Physics Letters, 1998. 73(6): p. 708-710.
105. Tagaya, A., et al., High gain and high power organic dye-doped polymer optical fiber amplifiers: Absorption and emission cross sections and gain characteristics. Japanese Journal Of Applied Physics Part 1-Regular Papers Short Notes & Review Papers, 1997. 36(5A): p. 2705-2708.
106. Ramon, M.C., et al., A characterization of Rhodamine 640 for optical amplification: Collinear pump and signal gain properties in solutions, thin-film polymer dispersions, and waveguides. Journal Of Applied Physics, 2005. 97(7).
107. Costela, A., et al., Amplified spontaneous emission and optical gain measurements from pyrromethene 567 - doped polymer waveguides and quasi-waveguides. Optics Express, 2008. 16(10): p. 7023-7036.
108. Goudket, H., et al., Importance of dye host on absorption, propagation losses, and amplified spontaneous emission for dye-doped polymer thin films. Applied Optics, 2006. 45(29): p. 7736-7741.
109. Karnutsch, C., Low trheshold organic thin-film laser devices. 2007, KIT: Karlsruhe.
110. Kogelnik, H. and C.V. Shank, Stimulated Emission In A Periodic Structure. Applied Physics Letters, 1971. 18(4): p. 152-&.
111. Holzer, W., et al., Corrugated neat thin-film conjugated polymer distributed-feedback lasers. Applied Physics B-Lasers And Optics, 2002. 74(4-5): p. 333-342.
112. Riechel, S., et al., Laser modes in organic solid-state distributed feedback lasers. Applied Physics B-Lasers And Optics, 2000. 71(6): p. 897-900.
113. Kallinger, C., et al., A flexible conjugated polymer laser. Advanced Materials, 1998. 10(12): p. 920-+.
114. Zavelani-Rossi, M., et al., Laser dynamics in organic distributed feedback lasers. Applied Physics Letters, 2006. 89(18).

115. Tsiminis, G., et al., Low-threshold organic laser based on an oligofluorene truxene with low optical losses. Applied Physics Letters, 2009. 94(24).
116. Namdas, E.B., et al., Low Thresholds in Polymer Lasers on Conductive Substrates by Distributed Feedback Nanoimprinting: Progress Toward Electrically Pumped Plastic Lasers. Advanced Materials, 2009. 21(7): p. 799-+.
117. Tsutsumi, N. and T. Ishibashi, Organic dye lasers with distributed Bragg reflector grating and distributed feedback resonator. Optics Express, 2009. 17(24): p. 21698-21703.
118. Dyer, P.E., R.J. Farley, and R. Giedl, Analysis Of Grating Formation With Excimer-Laser Irradiated Phase Masks. Optics Communications, 1995. 115(3-4): p. 327-334.
119. Karnutsch, C., et al., Improved organic semiconductor lasers based on a mixed-order distributed feedback resonator design. Applied Physics Letters, 2007. 90(13).
120. Gouedard, C., et al., Generation Of Spatially Incoherent Short Pulses In Laser-Pumped Neodymium Stoichiometric Crystals And Powders. Journal Of The Optical Society Of America B-Optical Physics, 1993. 10(12): p. 2358-2363.
121. Lawandy, N.M., et al., Laser Action In Strongly Scattering Media (Vol 368, Pg 436, 1994). Nature, 1994. 369(6478): p. 340-340.
122. Hide, F., et al., Laser emission from solutions and films containing semiconducting polymer and titanium dioxide nanocrystals. Chemical Physics Letters, 1996. 256(4-5): p. 424-430.
123. Frolov, S.V., et al., Stimulated emission in high-gain organic media. Physical Review B, 1999. 59(8): p. R5284-R5287.
124. Cao, H., et al., Random laser action in semiconductor powder. Physical Review Letters, 1999. 82(11): p. 2278-2281.
125. Cao, H., et al., Spatial confinement of laser light in active random media. Physical Review Letters, 2000. 84(24): p. 5584-5587.
126. Frolov, S.V., et al., Laser-like emission in opal photonic crystals. Optics Communications, 1999. 162(4-6): p. 241-246.
127. Yoshino, K., et al., Amplified spontaneous emission and lasing in conducting polymers and fluorescent dyes in opals as photonic crystals. Applied Physics Letters, 1999. 74(18): p. 2590-2592.
128. Ramachandran, H., Mirrorless lasers. Pramana-Journal Of Physics, 2002. 58(2): p. 313-323.
129. Polson, R.C. and Z.V. Vardeny, Random lasing in human tissues. Applied Physics Letters, 2004. 85(7): p. 1289-1291.
130. Anni, M., et al., Far-field emission and feedback origin of random lasing in

oligothiophene dioxide neat films. Applied Physics Letters, 2003. 83(14): p. 2754-2756.
131. Stabile, R., et al., Organic-based distributed feedback lasers by direct electron-beam lithography on conjugated polymers. Applied Physics Letters, 2007. 91(10).
132. Lu, M., et al., Vertically emitting, dye-doped polymer laser in the green (lambda similar to 536 nm) with a second order distributed feedback grating fabricated by replica molding. Optics Communications, 2008. 281(11): p. 3159-3162.
133. Stroisch, M., et al., Organic semiconductor distributed feedback laser fabricated by direct laser interference ablation. Optics Express, 2007. 15(7): p. 3968-3973.
134. Tsutsumi, N. and A. Fujihara, Tunable distributed feedback lasing with narrowed emission using holographic dynamic gratings in a polymeric waveguide. Applied Physics Letters, 2005. 86(6).
135. Karnutsch, C., et al., Low threshold blue conjugated polymer lasers with first- and second-order distributed feedback. Applied Physics Letters, 2006. 89(20).
136. Heliotis, G., et al., Emission characteristics and performance comparison of polyfluorene lasers with one- and two-dimensional distributed feedback. Advanced Functional Materials, 2004. 14(1): p. 91-97.
137. Barlow, G.F., et al., Design and analysis of a low-threshold polymer circular-grating distributed-feedback laser. Journal Of The Optical Society Of America B-Optical Physics, 2004. 21(12): p. 2142-2150.
138. Bauer, C., et al., A surface-emitting circular grating polymer laser. Advanced Materials, 2001. 13(15): p. 1161-+.
139. Vasdekis, A.E., et al., Low threshold edge emitting polymer distributed feedback laser based on a square lattice. Applied Physics Letters, 2005. 86(16).
140. Meier, M., et al., Laser action from two-dimensional distributed feedback in photonic crystals. Applied Physics Letters, 1999. 74(1): p. 7-9.
141. Samuel, I.D.W., E.B. Namdas, and G.A. Turnbull, How to recognize lasing. Nature Photonics, 2009. 3(10): p. 546-549.
142. Schneider, D., et al., Ultrawide tuning range in doped organic solid-state lasers. Applied Physics Letters, 2004. 85(11): p. 1886-1888.
143. Tsutsumi, N., A. Fujihara, and D. Hayashi, Tunable distributed feedback lasing with a threshold in the nanojoule range in an organic guest-host polymeric waveguide. Applied Optics, 2006. 45(22): p. 5748-5751.
144. Klinkhammer, S., et al., A continuously tunable low-threshold organic semiconductor distributed feedback laser fabricated by rotating shadow mask evaporation. Applied Physics B-Lasers And Optics, 2009. 97(4): p. 787-791.
145. Gorrn, P., et al., Elastically Tunable Self-Organized Organic Lasers. Advanced

Materials. 23(7): p. 869-+.
146. Heliotis, G., et al., Blue, surface-emitting, distributed feedback polyfluorene lasers. Applied Physics Letters, 2003. 83(11): p. 2118-2120.
147. Oki, Y., et al., Fabrication of a distributed-feedback dye laser with a grating structure in its plastic waveguide. Applied Optics, 2002. 41(24): p. 5030-5035.
148. Schutte, B., et al., Continuously tunable laser emission from a wedge-shaped organic microcavity. Applied Physics Letters, 2008. 92(16).
149. Tulek, A. and Z.V. Vardeny, Studies of polymer microring lasers subject to uniaxial stress. Applied Physics Letters, 2007. 91(12).
150. Polson, R.C. and Z.V. Vardeny, Directional emission from asymmetric microlaser resonators of pi-conjugated polymers. Applied Physics Letters, 2004. 85(11): p. 1892-1894.
151. Lebental, M., et al., Inferring periodic orbits from spectra of simply shaped microlasers. Physical Review A, 2007. 76(2).
152. Lebental, M., et al., Directional emission of stadium-shaped microlasers. Physical Review A, 2007. 75(3).
153. Garcia-Moreno, I., et al., Materials for a Reliable Solid-State Dye Laser at the Red Spectral Edge. Advanced Functional Materials, 2009. 19(16): p. 2547-2552.
154. Yee, K.C., T.Y. Tou, and S.W. Ng, Hot-press molded poly(methyl methacrylate) matrix for solid-state dye lasers. Applied Optics, 1998. 37(27): p. 6381-6385.
155. Cazeca, M.J., et al., Epoxy matrix for solid-state dye laser applications. Applied Optics, 1997. 36(21): p. 4965-4968.
156. Schulzgen, A., et al., Near diffraction-limited laser emission from a polymer in a high finesse planar cavity. Applied Physics Letters, 1998. 72(3): p. 269-271.
157. Kuznetsov, M., et al., High-power (>0.5-W CW) diode-pumped vertical-external-cavity surface-emitting semiconductor lasers with circular TEM00 beams. Ieee Photonics Technology Letters, 1997. 9(8): p. 1063-1065.
158. Reilly, M.A., et al., Optical gain at 650 nm from a polymer waveguide with dye-doped cladding. Applied Physics Letters, 2005. 87(23).
159. Koechner, W., Solid-state laser engineering: (Springer Science, 2006).
160. Okhotnikov, O.G., Semiconductor Disk Lasers: Physics and Technology. 1st ed. 2010: Wiley-VCH.
161. Popov, S., Dye photodestruction in a solid-state dye laser with a polymeric gain medium. Applied Optics, 1998. 37(27): p. 6449-6455.
162. YARIV, A., Quantum Electronics. 3rd ed. 1989: Wiley.
163. Dubinskii, M.A., Ultraviolet spectroscopy and UV lasers (Practical spectroscopy). 1st ed, ed. P. Misra. 2002: CRC Press.

164. Ehrlich, D.J., P.F. Moulton, and R.M. Osgood, Ultraviolet Solid-State Ce-Ylf Laser At 325 Nm. Optics Letters, 1979. 4(6): p. 184-186.
165. Ehrlich, D.J., P.F. Moulton, and R.M. Osgood, Optically Pumped Ce-Laf3 Laser At 286-Nm. Optics Letters, 1980. 5(8): p. 339-341.
166. Rambaldi, P., et al., Efficient and stable pulsed laser operation of Ce: LiLuF4 around 308 nm. Optics Communications, 1998. 146(1-6): p. 163-166.
167. Lim, K.S. and D.S. Hamilton, Optical Gain And Loss Studies In Ce3+-Ylif4. Journal Of The Optical Society Of America B-Optical Physics, 1989. 6(7): p. 1401-1406.
168. Stokes, E.D., et al., A high efficiency dye laser tunable from the UV to the IR. Optics Communications, 1972. 5(4): p. 267.
169. Balembois, F., et al., Tunable picosecond UV source at 10 kHz based on an all-solid-state diode-pumped laser system. Applied Physics B-Lasers And Optics, 1997. 65(2): p. 255-258.
170. Berggren, M., et al., Light amplification in organic thin films using cascade energy transfer. Nature, 1997. 389(6650): p. 466-469.
171. Zhu, X.L. and D. Lo, Distributed-feedback sol-gel dye laser tunable in the near ultraviolet. Applied Physics Letters, 2000. 77(17): p. 2647-2649.
172. Spehr, T., et al., Organic solid-state ultraviolet-laser based on spiro-terphenyl. Applied Physics Letters, 2005. 87(16).
173. Wu, S.X. and C.S. Zhu, All-solid-state UV dye laser pumped by XeCl laser. Optical Materials, 1999. 12(1): p. 99-103.
174. Hirth, A., K. Vollrath, and J.Y. Allain, Production of high power tunable UV laser emission by second-harmonic generation fro, a rhodamine 6G dye laser. Optics Communications, 1977. 20(3): p. 347.
175. Chandra, S., et al., Tunable ultraviolet laser source based on solid-state dye laser technology and CsLiB6O10 harmonic generation. Optics Letters, 1997. 22(4): p. 209-211.
176. Hoa, D.Q., et al., A hybrid laser system consisting of a frequency-doubled, narrow-line-width, distributed-feedback dye laser oscillator and a high saturation-fluence Ce: LiCaAlF6 crystal amplifier. Applied Physics Letters, 2003. 82(20): p. 3391-3393.
177. Jiang, Y.G., et al., Tunable ultraviolet solid-state dye laser based on MPMMA doped with pyrromethene 597. Laser Physics Letters. 8(1): p. 38-41.
178. Boyd, G.D. and D.A. Kleinman, Parametric Interaction Of Focused Gaussian Light Beams. Journal Of Applied Physics, 1968. 39(8): p. 3597-&.
179. Bondarev, S.L., et al., Fluorescence and Electronic Structure of the Laser Dye DCM in Solutions and in Polymethylmethacrylate. Journal of Applied Spectroscopy, 2004. 71(2): p. 194.

180. Berger, G.A., M. Kempe, and A.Z. Genack, Dynamics of stimulated emission from random media. Physical Review E, 1997. 56(5): p. 6118-6122.

Laser operation in nondoped thin films made of a small-molecule organic red-emitter

Hadi Rabbani-Haghighi,[1] Sébastien Forget,[1,a)] Sébastien Chénais,[1] Alain Siove,[1] Marie-Claude Castex,[1] and Elena Ishow[2]
[1]*Laboratoire de Physique des Lasers, UMR 7538, Université Paris, 13/CNRS, 93430 Villetaneuse, France*
[2]*Laboratoire de Photophysique et Photochimie Supramoléculaires et Macromoléculaires, UMR-CNRS 8531, ENS Cachan, F-94235 Cachan, France*

(Received 16 April 2009; accepted 18 June 2009; published online 21 July 2009)

Stimulated emission in small-molecule organic films at a high dye concentration is generally hindered by fluorescence quenching, especially in the red region of the spectrum. Here we demonstrate the achievement of high net gains (up to 50 cm^{-1}) around 640 nm in thermally evaporated nondoped films of 4-di(4′-*tert*-butylbiphenyl-4-yl)amino-4′-dicyanovinylbenzene, which makes this material suitable for green-light pumped single mode organic lasers with low threshold and superior stability. Lasing effect is demonstrated in a distributed Bragg resonator configuration, as well as under the form of random lasing at high pump intensities. © *2009 American Institute of Physics*. [DOI: 10.1063/1.3182820]

Organic optoelectronics is a very active field of research, partly driven by the rapid developments of organic light-emitting diodes and photovoltaic cells. In this context, solid-state organic lasers open the way to many applications (sensing, telecommunications…), due to their ability to produce coherent radiation over the whole visible spectrum, together with low-cost fabrication techniques on possibly large areas. While huge challenges remain to be solved in order to achieve direct electrical pumping of organic semiconductors, recent reports have shown the interest of an "indirect" electrical driving strategy, in which a small solid-state laser,[1] a laser diode,[2] or a light-emitting diode[3] is used as an optical pump source. Stimulated emission and lasing have been observed in numerous conjugated polymers[4,5] as well as in some small-molecule-based organic materials.[6,7] The latter are especially attractive as they exhibit a well-defined molecular structure and can be thermally evaporated, which provides an accurate control over the layer thickness and a better film quality. However, stimulated emission in small-molecule materials is generally hindered in nondoped films due to strong dipole-dipole coupling between excited-state molecules and $\pi-\pi$ stacking (overlap of the π orbitals) between neighboring conjugated segments, which can both lead to significant luminescence quenching.[8] To limit self-quenching, the emitter is generally introduced at low concentrations in a polymeric or small-molecule organic matrix.[9] Nonetheless, the realization of a single mode organic waveguide lasers requires high absorption over a short distance, which cannot be readily achieved with low-doped layers. This absorption problem can be bypassed in host-guest blends: in such systems, the host strongly absorbs light and subsequently transfers its excitation to the guest through a Förster energy transfer mechanism.[10] In this case the pump radiation is generally in the ultraviolet, which is detrimental to the photostability of the laser and sets limits in the choice of the pump source.

So far lasing in small-molecule neat films has been demonstrated in materials such as sexiphenyls,[11] oligothiophenes,[7] or spiro derivatives.[12] However, the reported emission wavelength lies essentially in the violet or the blue part of the spectrum, with some rare exceptions in the orange-red.[9] Indeed, long-wavelength emission is generally achieved with extended π-conjugated planar structures, in which the probability to observe $\pi-\pi$ stacking (and luminescence quenching) is therefore stronger. In the present work amplified spontaneous emission (ASE) and laser operation in a distributed Bragg reflector-type cavity (DBR) is demonstrated in neat films of an organic dye [4-di(4′-*tert*-butylbiphenyl-4-yl)amino-4′-dicyanovinylbenzene,[13] named *fvin* in the following] in the deep red part of the spectrum (650 nm), pumped at 532 nm.

The molecular structure of the fvin molecule is depicted in the inset of Fig. 1. Femtosecond transient absorption spectroscopy studies have evidenced the formation of a quite distorted geometry in the excited state with regard to the ground state. This leads to a large Stokes shift of up to 170 nm, with the consequence that red emission is achieved with a relatively short conjugation length, which limits intermolecular $\pi-\pi$ aggregation. The large Stokes shift is also favorable to obtain a true four-level system with very low reabsorption losses (see Fig. 1). Quenching is also highly reduced here by the steric hindrance exerted by the bulky *tert*-butylphenyl substituents and twisting of the triphenylamino group. These geometrical characteristics allowed us to obtain amorphous materials (T_g=86 °C) with no microc-

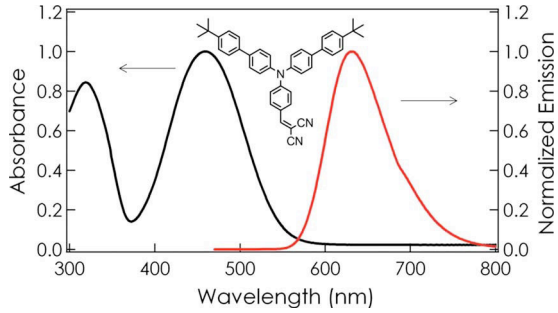

FIG. 1. (Color online) fvin emission and absorption spectrum in neat film. Inset: structure of the molecule.

a)Electronic mail: sebastien.forget@univ-paris13.fr.

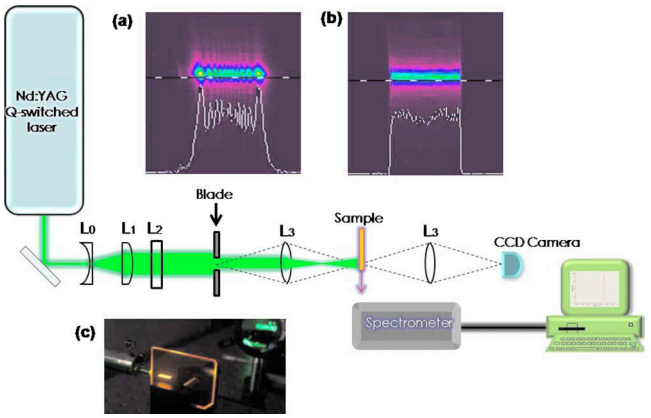

FIG. 2. (Color online) Experimental setup. Inset: (a) stripe intensity profile on the sample when the razor blade is set at 10 mm of the sample without imaging lens and (b) with imaging lens (see text). (c) is a photograph of the pumped sample with the collection fiber on the left.

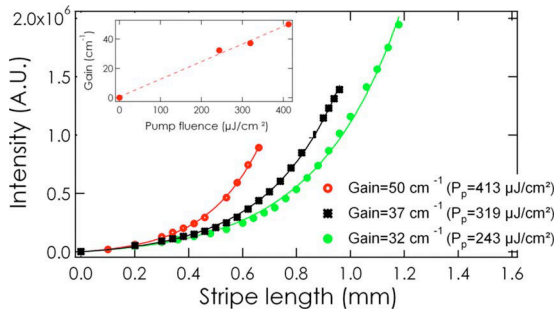

FIG. 3. (Color online) Net gain (gain minus losses) measurement with the VSL method. Inset: net gain vs pump fluence.

rystallized areas, which would limit the lasing capabilities because of the induced optical losses at the domain boundaries.[11]

The fvin neat film was realized on silica substrates through thermal evaporation under a 10^{-6} mbar pressure. No visible scattering was observed and the film optical quality was excellent as expected when resorting to the thin film evaporation process. The film thickness was monitored by means of a quartz microbalance in the evaporator machine to be 600 nm. Neat films absorbed as much as 84% of the incident light at 532 nm, in the tail of the absorption band. Since the refractive index is 1.82 at 633 nm (determined by ellipsometry), single mode waveguiding is expected.

The variable stripe length (VSL) method[14] was employed to measure the net gain coefficient. In this technique, ASE is detected from the diamond-cleaved edge of the sample for different pump excitation lengths. The luminescence was collected via an optical fiber and sent to a spectrometer SPEX 270-M (grating 150 or 1200 lines/mm, corresponding to a resolution of 8 or 1 nm, respectively) followed by an Andor technologies DH 720 charge coupled device camera.

The experimental setup is depicted in Fig. 2. The 532 nm pump beam was produced by a Nd:YVO_4 Q-switched laser (PowerChip, Teem Photonics) with frequency doubling through single-pass in a lithium triborate crystal. The pulse duration at 532 nm was 500 ps with a repetition rate of 10 Hz, and the pulse energy could be varied up to 20 μJ. The beam was expanded by an afocal telescope (L_0 and L_1) and focused with a cylindrical L_2 lens to form a thin stripe (320 μm full width at $1/e^2$, measured by a Spiricon camera). After selecting only the central part of this line to provide a uniform excitation intensity onto the sample, an adjustable sharp edge blade positioned on a translation stage enabled to vary the length of the stripe. In order to avoid the complex intensity modulation due to Fresnel diffraction effects after the blade edge,[15] the latter were optically conjugated through a 1:1 imaging system. We thus managed to produce an intensity profile of the imaged pump stripe with abrupt edges (as shown in the inset of Fig. 2), provided that the imaging lens had a large enough numerical aperture to collect the high spatial-frequency information contents of the far-field diffraction pattern. In practice, a 10 cm focal length lens with a diameter of 1 in. was chosen as a good compromise between the desired edge sharpness and the image degradation due to spherical aberration.

Figure 3 shows the ASE intensity versus the pump stripe length for different pump fluences. We clearly observed a superlinear increase in the emission with the excitation length, which can be well fitted with the following expression:

$$I(L) = \frac{\eta_{\text{spont}}}{g-\alpha}[e^{(g-\alpha)L} - 1],$$

where I is the ASE intensity, L the stripe length, g is the optical gain, α represents the passive losses (self-reabsorption and waveguide losses), and η_{spont} is the power density of spontaneous emission emitted into the stripe solid angle.

In this expression, the gain saturation is neglected, which is reasonable as only short pump stripes are considered. The amount of losses α were experimentally measured with a similar method[14] and were estimated to be around 10 cm^{-1}. We obtained a maximum optical gain of 50 cm^{-1} for a pump fluence of 413 $\mu\text{J/cm}^2$, which ranges among the highest reported for red-emitting neat films of small molecules. The maximum emission wavelength is in the deep red part of the spectrum, around 660 nm and the ASE threshold is 22 $\mu\text{J/cm}^2$, which is the lowest reported ASE "threshold" as defined by McGehee *et al.*[16] for neat films made of small-molecule organic red emitters. Moreover, pumping in the green instead of UV induces excellent ASE stability: 80% of initial ASE intensity (just above threshold) was still measured after 10^5 pulses at 10 Hz.

For the sake of comparison, we used the well-known DCM dye in the same single mode waveguide configuration since it exhibits similar absorption and emission spectral characteristics. Contrarily to fvin, DCM is very sensitive to quenching, which limited us to a 5 wt % doping in polymethyl methacrylate (PMMA) matrix (Microchem Inc., $M_w = 4.95 \times 10^5$ g mol^{-1}). The sample was prepared by spin coating the DCM-PMMA anisole solution on silicon substrates at a spin speed of 1000 rpm to obtain a 600-nm-thick film. In this case only 15% of the pump beam at 532 nm was absorbed. With the VSL method, an optical gain of 40 cm^{-1} was measured at the maximum pump fluence (413 $\mu\text{J/cm}^2$).

For a similar absorbed pump power, the gain in DCM is then higher than in fvin. However, as the film thickness was fixed to ensure single mode waveguiding, it is noticeable that a higher gain is obtained with fvin for the same incident pump power.

The fvin capabilities in a laser cavity were tested upon appending a DBR resonator to the waveguide. To obtain a

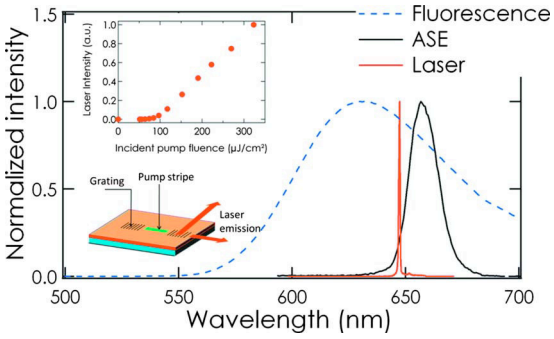

FIG. 4. (Color online) Fluorescence, ASE and laser spectrum in the DBR configuration. Inset: laser chip design (here the pump stripe length is 2 mm).

periodic modulation of the film thickness, we used a very simple all-optical method based on direct laser ablation through a phase mask.[17] We used an ArF excimer laser ($\lambda = 193$ nm, energy per pulse$=300$ μJ, repetition rate of 10 Hz) to illuminate a phase mask: the diffracted orders interfere in the vicinity of the mask, creating an interference pattern with a pitch that can be shown to be, under the conditions of this work, the same as the period of the mask.[17] Local ablation of the organic material is obtained for illumination times around one minute (several hundreds of pulses).

The optimal pitch Λ for a Bragg grating is given by the Bragg formula $2n_{\text{eff}}\Lambda = m\lambda$, where n_{eff} is the effective index of the waveguide and m is the Bragg order. Here, we used a mask with a 1090 nm period, leading to laser emission at the $m=6$ order (chosen here because the mask was readily available; lower thresholds are expected for lower order gratings). The periodicity of the grating extends over several millimeters with a modulation depth of 200 nm. The grating structure appears under an atomic force microscope to be smooth, and free of groove defects.

We used a DBR configuration in which two Bragg gratings (with the same 1090 nm pitch) facing each other were engraved in a PMMA layer before the evaporation of a 695-nm-thick fvin layer (see inset in Fig. 4). The pump stripe (active region) was located between the two mirrors. The laser spectrum peaks at 647 nm as expected from the Bragg formula with $n_{\text{eff}}=1.82$. The polarization of the laser beam was parallel to the layer (TE). A typical curve showing the variation in the laser intensity with pump power is shown on Fig. 4 (inset). The lasing threshold is relatively high (60 $\mu\text{J}/\text{cm}^2$) because of the high order Bragg configuration.

Interestingly, we also observed that under high pump fluences, lasing can occur without any resonator, under the form of *random lasing*, a phenomenon that has been already observed in some films of conjugated polymer and small molecules.[18] Indeed, we observed that the ASE spectrum, for fluences higher than typically 0.3 mJ/cm^2, was highly structured, exhibiting multiple narrow peaks with a spectral width limited here by the spectrometer resolution (1 nm). The physical origin of the feedback still remains unclear in this system and is under study.

In summary, we have demonstrated single mode laser action in a thermally evaporated neat film of a red-emitting dye at 647 nm with a very simple DBR patterning technique. The optical gain was measured for different pump powers with the variable stripe length method and a maximum value of 50 cm^{-1} was obtained. In order to obtain more accurate fits, a simple way to avoid the complex intensity modulation provided by Fresnel diffraction on the edges of the slit was presented. The fact that fvin molecule exhibits optical gain and ASE with a threshold as low as 22 $\mu\text{J}/\text{cm}^2$ in a neat film configuration shows that quenching effects are tremendously reduced compared to classical dyes such as DCM or rhodamine, in which emission is totally suppressed in neat films. Consequently, in a single mode waveguide configuration, a higher gain can be obtained for the same pump power in a neat film of fvin than in a doped film of DCM. Laser operation in the red (at 647 nm) was demonstrated with a DBR resonator fabricated with a very simple technique. At last, random lasing with coherent feedback was observed for pump fluences exceeding ~ 0.3 mJ/cm^2.

The present results give very favorable implication for the use of fvin material as red-emitting organic laser material with a pumping wavelength in blue or green region.

We acknowledge the ANR ("Bachelor" project) and the Université Paris 13 (BQR credits) for funding this work. We thank M. Lebental for loaning us the DCM sample used for these experiments. We thank P. Sebbah for fruitful discussions on random lasers and D. Ades for assistance in making the PMMA films.

[1] S. Riechel, U. Lemmer, J. Feldmann, S. Berleb, A. G. Muckl, W. Brutting, A. Gombert, and V. Wittwer, Opt. Lett. **26**, 593 (2001).
[2] T. Riedl, T. Rabe, H. H. Johannes, W. Kowalsky, J. Wang, T. Weimann, P. Hinze, B. Nehls, T. Farrell, and U. Scherf, Appl. Phys. Lett. **88**, 241116 (2006).
[3] Y. Yang, G. A. Turnbull, and I. D. W. Samuel, Appl. Phys. Lett. **92**, 163306 (2008).
[4] W. Holzer, A. Penzkofer, H. Tillmann, and H. H. Horhold, Synth. Met. **140**, 155 (2004).
[5] M. D. McGehee, M. A. Diaz-Garcia, F. Hide, R. Gupta, E. K. Miller, D. Moses, and A. J. Heeger, Appl. Phys. Lett. **72**, 1536 (1998).
[6] M. Zavelani-Rossi, G. Lanzani, S. De Silvestri, M. Anni, G. Gigli, R. Cingolani, G. Barbarella, and L. Favaretto, Appl. Phys. Lett. **79**, 4082 (2001).
[7] M. Zavelani-Rossi, G. Lanzani, M. Anni, G. Gigli, R. Cingolani, G. Barbarella, and L. Favaretto, Synth. Met. **139**, 901 (2003).
[8] J. Cornil, D. Beljonne, J. P. Calbert, and J. L. Bredas, Adv. Mater. (Weinheim, Ger.) **13**, 1053 (2001).
[9] V. Bulović, V. G. Kozlov, V. B. Khalfin, and S. R. Forrest, Science **279**, 553 (1998).
[10] V. G. Kozlov, V. Bulovic, P. E. Burrows, and S. R. Forrest, Nature (London) **389**, 362 (1997).
[11] D. Schneider, T. Rabe, T. Riedl, T. Dobbertin, M. Kroger, E. Becker, H. H. Johannes, W. Kowalsky, T. Weimann, J. Wang, and P. Hinze, J. Appl. Phys. **98**, 043104 (2005).
[12] H. Nakanotani, S. Akiyama, D. Ohnishi, M. Moriwake, M. Yahiro, T. Yoshihara, S. Tobita, and C. Adachi, Adv. Funct. Mater. **17**, 2328 (2007).
[13] E. Ishow, A. Brosseau, G. Clavier, K. Nakatani, P. Tauc, C. Fiorini-Debuisschert, S. Neveu, O. Sandre, and A. Leaustic, Chem. Mater. **20**, 6597 (2008).
[14] M. D. McGehee and A. J. Heeger, Adv. Mater. (Weinheim, Ger.) **12**, 1655 (2000).
[15] L. Dal Negro, P. Bettotti, M. Cazzanelli, D. Pacifici, and L. Pavesi, Opt. Commun. **229**, 337 (2004).
[16] M. D. McGehee, R. Gupta, S. Veenstra, E. K. Miller, M. A. Diaz-Garcia, and A. J. Heeger, Phys. Rev. B **58**, 7035 (1998).
[17] P. E. Dyer, R. J. Farley, and R. Giedl, Opt. Commun. **115**, 327 (1995).
[18] R. C. Polson and Z. V. Vardeny, Phys. Rev. B **71**, 045205 (2005).

Highly efficient, diffraction-limited laser emission from a vertical external-cavity surface-emitting organic laser

Hadi Rabbani-Haghighi, Sébastien Forget, Sébastien Chénais,* and Alain Siove

Laboratoire de Physique des Lasers, Université Paris 13 / CNRS, 93430 Villetaneuse, France
**Corresponding author: sebastien.chenais@univ-paris13.fr*

Received February 19, 2010; revised May 10, 2010; accepted May 19, 2010;
posted May 20, 2010 (Doc. ID 124206); published June 4, 2010

We report on a solid-state laser structure functioning as the organic counterpart of a vertical external-cavity surface-emitting laser (VECSEL) design. The gain medium is a poly(methyl methacrylate) film doped with Rhodamine 640, spin casted onto the high-reflectivity mirror of a plano–concave resonator. Upon pumping by 7 ns pulses at 532 nm, a diffraction-limited beam ($M^2 = 1$) was obtained, with a conversion efficiency of 43%; higher peak powers (2 kW) could be attained when resorting to shorter (0.5 ns) pump pulses. The spectrum was controlled by the thickness of the active layer playing the role of an intracavity etalon; tunability is demonstrated at over and up to 20 nm.

OCIS codes: 140.2050, 140.3580, 160.4890, 230.5750, 250.7270.

Organic solid-state lasers offer the potential of low-cost, compact, and broadly tunable coherent sources over the whole visible spectrum [1]. They may find applications in the fields of, e.g., polymer optical fiber telecommunications [2], bio/chemo-sensing [3], or spectroscopy [4]. In the perspective of achieving direct [5] or indirect [6] electrical pumping of organic semiconductors, most recent studies have dealt with low-loss resonator structures, such as distributed feedback resonators [7,8] or microcavities [9,10]. In the meantime, less attention has been paid to the question of optimizing conversion efficiency, beam quality, and power scaling capability. Low-threshold operation and high output power are indeed incompatible statements in a single device: whereas weak output coupling and small active volume are desirable for low-threshold lasing, achieving high output power leads to an optimal transmission for the output coupler [11] and requires keeping the pump fluence at a low level to cope with photobleaching and thermal issues. Furthermore, low-loss compact resonators do not generally provide diffraction-limited beams [12].

A combination of high efficiency, high output power, and high beam quality is achievable with external resonators. A typical external-cavity organic laser consists of a thick (approximately millimeters to centimeters) dye-doped polymeric sample prepared by, e.g., radical polymerization [13] or the sol-gel technique [14], which has to be polished to optical quality prior to its insertion in an open stable resonator. Preparation of such samples is complex and not compatible with organic semiconductor processing techniques. As a simpler alternative, it has been proposed to spin coat an organic film directly onto one of the mirrors [15–17]. However, pumping with femtosecond pulses not only limited the cavity length to a few micrometers, making this type of device very similar in nature to microcavity lasers, but also led to modest efficiencies (1.7%) [17].

In this Letter, we report on a vertical external-cavity surface-emitting organic laser [VECSOL, upon analogy with the vertical external-cavity surface-emitting laser (VECSEL) structure [18]]. It consists of an organic poly(methyl methacrylate) (PMMA) film doped with Rhodamine 640, spin casted onto the high-reflectivity mirror of a plano–concave resonator, pumped in the nanosecond regime. It shares the same general properties as VECSELs: diffraction-limited output, high efficiency, power scaling capability upon a simple increase of pump spot size (hence without higher photodegradation), possibility of long (cm) cavities enabling the insertion of intracavity elements, such as spatial or spectral filters. It is compatible with organic semiconductors and hence with a potential of future electrical driving.

The resonator consisted of a highly reflective plane dielectric mirror ($R > 99.5\%$ in the range of 600–660 nm) and a 200 mm radius-of-curvature output coupler ($R = 98\%$ at 600–680 nm). The two mirrors were transparent ($T > 90\%$) at 532 nm. A 17-μm-thick film of PMMA ($M_w = 9.5 \times 10^5$ g mol^{-1}) doped by 1 wt% of Rhodamine 640 was spin coated directly onto the plane mirror, allowing 80% of incident radiation at 532 nm to be absorbed in a single pass. The laser cavity was end pumped (Fig. 1) with a pump beam diameter of 140 μm. Two pump sources were used: a "long-pulse" Nd:YAG laser (Saga 230, B.M. Industries, Thomson CSF) emitting 7 ns (FWHM) pulses and a "short-pulse" Nd:YVO_4 laser (PowerChip, Teem Photonics) with a pulse duration of 0.5 ns. Both sources had a 10 Hz repetition rate and were frequency doubled

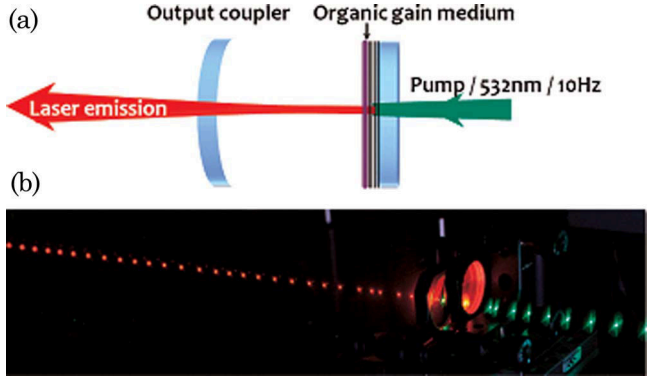

Fig. 1. (Color online) (a) Schematic representation of the plano–concave VECSOL resonator (see text for details). (b) Long-exposure time photo of the working VECSOL.

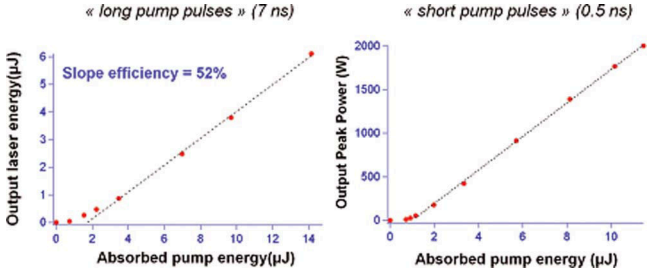

Fig. 2. (Color online) Output laser energy (left) and output peak power (right) versus absorbed pump energy under 7 ns and 0.5 ns pumping, respectively. The dashed line is a linear fit to the experimental data.

through a single pass in a lithium triborate crystal. Laser output energy was monitored with a calibrated photodiode and the emission spectrum detected by a spectrometer (1200 lines/mm grating, 1 nm resolution) followed by a DH720 CCD camera (Andor Technologies).

In the following, the thresholds and slope efficiencies are given with respect to the absorbed energy. The laser characteristic curve for long-pulse pumping is shown in Fig. 2 (left) for a 4 mm long cavity. A clear lasing threshold is visible at 1.8 μJ (11.7 μJ/cm^2) with maximum output energy of 6 μJ (peak power of 870 W). An optical-to-optical efficiency of 43% was measured, corresponding to a power slope efficiency of 52%, or 63% expressed in quantum efficiency. This ranges among the highest reported conversion efficiencies for an organic laser [19] and, to our knowledge, the highest for a thin-film based dye laser. The laser beam was linearly polarized parallel to the pump beam polarization. A typical emission spectrum above threshold is shown in Fig. 3. It consists of several evenly spaced peaks, separated by 7.5 nm, which corresponds to the free spectral range of the Fabry–Perot etalon formed by the thick active layer itself. This filtering of the cavity modes by the active layer was verified by spin coating 10- and 5.6-μm-thick films, which yielded peaks separated by the expected 13 nm and 22 nm spacings, respectively. Interestingly, tunability could be achieved here over the whole free spectral range of the etalons by taking advantage of the unwanted thickness growth observed at the edges of the mirror, due to the high viscosity of the PMMA solution needed to obtain

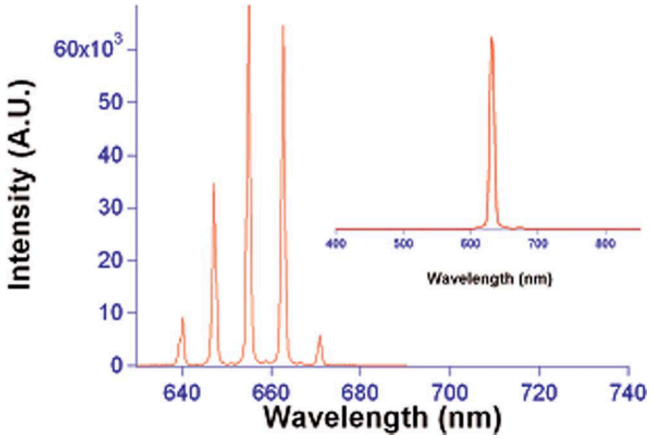

Fig. 3. (Color online) Typical emission spectrum of a 17-μm-thick active layer. Inset, single-peak laser operation achieved for a 2.35 μm layer.

such thick samples. This corresponded to wavelength tunability of around and above 20 nm for the 5.6 μm sample. Single-peak (but yet highly multimode) operation was obtained by using a 2.35-μm-thick sample, as shown in the inset of Fig. 3. However, tunability could not be achieved in this case because of the perfect thickness uniformity of the sample, realized with a lower molar mass PMMA.

Under "short-pulse" pumping (0.5 ns), the laser threshold was lowered to 0.95 μJ (6.2 mJ/cm^2). The output peak power reached the value of 2 kW for an absorbed pump fluence of 75 mJ/cm^2, while in this case maximum output energy was 0.7 μJ (Fig. 2, right). The conversion and slope efficiencies were 6.3% and 7%, respectively. The conversion efficiency is significantly higher than in previously reported external-cavity thin-film dye lasers [17] thanks to the fulfillment of two requirements: the pump intensity is higher than the pump saturation intensity (~MW/cm^2 for organic dyes) by 1 or 2 orders of magnitude for the "long-pulse" and "short-pulse" pump, respectively, which guarantees that a large fraction of the total population can be inverted in a timescale shorter than the radiative lifetime; the pulse width is long enough to let the laser field build up from spontaneous emission. With the 7 ns pump pulse, steady state is reached within the pulse, as an output energy of 6 μJ emitted from an active area comprising ~3.10^{12} molecules corresponds to an average of 6 photons emitted per molecule and per pulse; with 0.5 ns pumping, every molecule emits an average of 0.7 photon/pulse, as oscillation buildup is not over when pumping terminates.

A remarkable feature of VECSOLs is that the length of the cavity can be increased up to ~6 cm for "long-pulse" pumping (7 ns) and 1 cm for "short-pulse" (0.5 ns) pumping, which enables the insertion of intracavity optical components. This is in contrast with previously reported external-cavity organic semiconductor lasers, where the use of femtosecond pulses for pumping restricted the cavity length to a few micrometers [17] because of the need for a small oscillation buildup time.

Beam quality was quantified by measuring the M^2 factor (Fig. 4) for both pump sources: the output was diffraction limited ($M^2 = 1$). A typical image of the TEM$_{00}$ beam profile is depicted in the inset of Fig. 4, with two images of other TEM$_{nm}$ Hermite–Gaussian modes that are observable upon fine misalignment of the laser cavity.

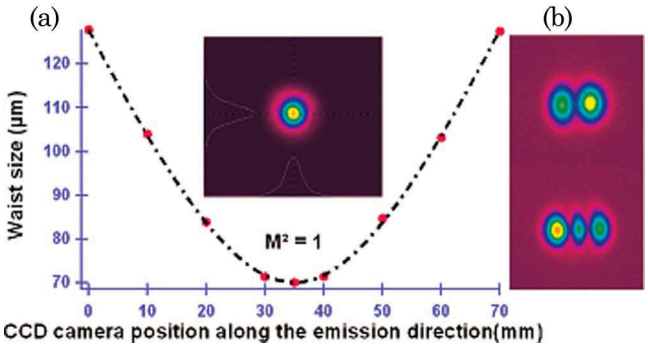

Fig. 4. (Color online) (a) Spatial evolution of the output beam profile along the emission direction. The dotted line is a fit to the experimental data with $M^2 = 1$. Inset, TEM$_{00}$ laser beam profile. (b) TEM$_{10}$ and TEM$_{20}$ images of the VECSOL emission obtained by fine misalignment of the VECSOL cavity.

Finally, photostability was investigated at fixed absorbed pump fluence above threshold (15.3 mJ/cm^2). Under "long-pulse" pumping, the output emission decreased to half its initial value after ~140000 pulses against ~5000 shots with "short-pulse" pumping. This is consistent with a one-order-of-magnitude difference in intracavity peak powers. These values are common for solid-state dye lasers [20]. The plane mirror could be translated without misalignment to maintain stable lasing performance during hours of operation. After the whole sample was degraded, simple rinsing in acetone prior to spin casting yielded a fresh active mirror without loss of performance.

In summary, laser emission from a VECSOL based on PMMA doped with Rhodamine 640 was studied. The efficiency was highly dependent on the pump pulse duration: with a 7 ns pump pulse at 532 nm, output energy (6 μJ), power slope efficiency (52%), and conversion efficiency (43%) were higher than those obtained with 0.5 ns pulse pumping, for which, in contrast, higher peak powers (2 kW) were measured. A long-pulse pumping regime allows better photostability and enables lasing with cavity lengths up to 6 cm. The spectrum shows multiple peaks due to the etalon effect of the active layer; tunability could be obtained at over and up to 20 nm upon playing on thickness variations observed at the edge of the sample. The laser emission was perfectly diffraction limited ($M^2 = 1$) for both pump lasers. The VECSOL design is an interesting alternative to traditional low-loss resonators when organic lasers have to meet practical applications requiring a stable, high-quality, and powerful beam.

The authors acknowledge financial support from the ANR (JC/JC call, "BACHELOR" project) and Paris 13 University (BQR credits).

References

1. I. D. W. Samuel and G. A. Turnbull, Chem. Rev. **107**, 1272 (2007).
2. J. Zubia and J. Arrue, Opt. Fiber Technol. **7**, 101 (2001).
3. A. Rose, Z. G. Zhu, C. F. Madigan, T. M. Swager, and V. Bulovic, Nature **434**, 876 (2005).
4. Y. Oki, S. Miyamoto, M. Maeda, and N. J. Vasa, Opt. Lett. **27**, 1220 (2002).
5. T. Rabe, P. Gorrn, M. Lehnhardt, M. Tilgner, T. Riedl, and W. Kowalsky, Phys. Rev. Lett. **102**, 137401 (2009).
6. Y. Yang, G. A. Turnbull, and I. D. W. Samuel, Appl. Phys. Lett. **92**, 163306 (2008).
7. M. D. McGehee, M. A. Diaz-Garcia, F. Hide, R. Gupta, E. K. Miller, D. Moses, and A. J. Heeger, Appl. Phys. Lett. **72**, 1536 (1998).
8. H. Rabbani-Haghighi, S. Forget, S. Chenais, A. Siove, M. C. Castex, and E. Ishow, Appl. Phys. Lett. **95**, 033305 (2009).
9. N. Tessler, G. J. Denton, and R. H. Friend, Nature **382**, 695 (1996).
10. L. Persano, A. Camposeo, P. Del Carro, E. Mele, R. Cingolani, and D. Pisignano, Appl. Phys. Lett. **89**, 121111 (2006).
11. A. E. Siegman, *Lasers* (University Science Books, 1986).
12. G. Heliotis, R. D. Xia, G. A. Turnbull, P. Andrew, W. L. Barnes, I. D. W. Samuel, and D. D. C. Bradley, Adv. Funct. Mater. **14**, 91 (2004).
13. I. Garcia-Moreno, A. Costela, V. Martin, M. Pintado-Sierra, and R. Sastre, Adv. Funct. Mater. **19**, 2547 (2009).
14. M. Canva, P. Georges, J. F. Perelgritz, A. Brum, F. Chaput, and J. P. Boilot, Appl. Opt. **34**, 428 (1995).
15. A. Schulzgen, C. Spiegelberg, M. M. Morrell, S. B. Mendes, B. Kippelen, N. Peyghambarian, M. F. Nabor, E. A. Mash, and P. M. Allemand, Appl. Phys. Lett. **72**, 269 (1998).
16. S. Stagira, M. Zavelani-Rossi, M. Nisoli, S. DeSilvestri, G. Lanzani, C. Zenz, P. Mataloni, and G. Leising, Appl. Phys. Lett. **73**, 2860 (1998).
17. M. Zavelani-Rossi, G. Lanzani, M. Anni, G. Gigli, R. Cingolani, G. Barbarella, and L. Favaretto, Synth. Met. **139**, 901 (2003).
18. M. Kuznetsov, F. Hakimi, R. Sprague, and A. Mooradian, IEEE Photonics Technol. Lett. **9**, 1063 (1997).
19. V. G. Kozlov, V. Bulovic, P. E. Burrows, and S. R. Forrest, Nature **389**, 362 (1997).
20. A. Costela, I. Garica-Moreno, J. M. Figuera, F. Arnat-Guerri, R. Mallavia, M. D. Santa Maria, and R. Sastre, J. Appl. Phys. **80**, 3167 (1996).

Tunable ultraviolet vertically-emitting organic laser

Sébastien Forget, Hadi Rabbani-Haghighi, Nordine Diffalah, Alain Siove, and Sébastien Chénais[a)]

Laboratoire de Physique des Lasers, Université Paris 13/CNRS, 99 avenue Jean-Baptiste Clément, 93430 Villetaneuse, France

(Received 4 January 2011; accepted 8 March 2011; published online 28 March 2011)

A solid-state organic thin-film laser with intracavity frequency doubling is reported. Tunable ultraviolet emission from 309 to 322 nm is achieved from a vertical external cavity surface-emitting organic laser, with 2% efficiency (1 μJ at 315 nm). The laser comprises a poly(methyl methacrylate) layer doped with Rhodamine 640, spun-cast onto a plane mirror, a remote concave mirror, a nonlinear crystal, and a dichroic separator. The output is spectrally narrow (<0.5 nm full width at half maximum) and tunable through phase-matching selection of the fundamental radiation lasing modes. These results highlight a low-cost and portable alternative to tunable UV laser sources, useful for spectroscopic applications. © *2011 American Institute of Physics*. [doi:10.1063/1.3571558]

Tunable UV (200–400 nm) laser sources are of fundamental interest in many fields such as atmospheric spectroscopy, ionization spectrometry, chemical or biological hazard detection, laser-induced fluorescence spectroscopy, combustion diagnostics, or photobiology.[1]

For most of these applications, portable and low-cost devices are desirable. Tunable UV radiation has been demonstrated using nonlinear optical conversion, either by optical parametric oscillation[2] or by sum-frequency mixing from dye lasers,[3] Ti-sapphire lasers, alexandrite or Cr-doped colquiriites.[4] It may also be obtained directly from rare-earth-doped crystals pumped by Nd laser harmonics.[5] All these systems are expensive and hardly transportable.

In the other hand, a combination of broad tunability, low cost, and compactness can be achieved with organic solid-state lasers.[6] This is especially true when the gain medium takes the form of a thin film, since its deposition onto the substrate (by, e.g., spin casting or ink-jet printing) can be a high-throughput and cost-effective process, balancing the drawbacks of a finite lifetime. Furthermore, many demonstrations of lasing in organic semiconductors have presented the possibility for realizing electrically-pumped lasers;[7] while this goal has not yet been reached, recent reports of diode-pumping[8] and light-emitting diode-pumping[9] suggested that cheap tunable optically-pumped lasers may become a reality.

However, tunability of organic pi-conjugated systems is limited to the visible spectrum, and extending the remarkable properties of organic lasers to lower wavelengths is fundamentally restricted to the near-UV domain. UV dyes are indeed inefficient light emitters in virtue of their low quantum yield of fluorescence;[10] furthermore the deep-UV optical excitation needed to obtain lasing in the UV results in a very fast photodegradation. Therefore, among a few reports of organic lasers below 400 nm,[11] the lowest wavelength obtained to date directly from an organic thin-film laser is 361 nm.[12]

We propose an alternative way to reach the UV domain with an organic thin-film device, while not compromising photostability: it consists in using intracavity frequency conversion in an open resonator. Whereas frequency doubling is standard in liquid dye lasers to obtain tunable UV light,[13] it has been up to now mostly unexplored in solid-state dye lasers, presumably because available intensities are too weak. External frequency doubling has been reported from a bulk dye-doped rotating plastic disk laser,[14] but has never been demonstrated in a thin-film organic laser.

We have based the design of an efficient frequency-doubled organic laser on two simple building principles: (1) the laser beam at the fundamental wavelength must have high peak brightness, i.e., high peak power and high beam quality; and (2) the resonator must be open to enable intracavity mixing, upon insertion of an efficient nonlinear crystal inside the cavity. Neither condition is met in traditional organic thin-film laser structures, such as distributed feedback or microcavity lasers.[12,15,16] It has been proposed to mix an organic nonlinear chromophore with an active lasing dye within the same structure, however, the concept requires complex poling techniques and has been only demonstrated with a liquid dye.[17]

In this letter, we propose a hybrid structure composed of a red-emitting thin-film open-resonator laser comprising a beta barium borate (BBO) crystal phase-matched for frequency doubling and a harmonic separator. This architecture derives from the vertical external cavity surface-emitting organic laser (VECSOL concept) recently demonstrated in our group.[18] The VECSOL is the organic counterpart of the vertical external cavity surface-emitting laser (VECSEL) (Refs. 19 and 20) and is made up of a thin layer of a dye-doped polymer spun-cast onto a high-reflectivity mirror, and a remote concave output coupler closing the cavity. The structure is optically pumped by a frequency doubled Nd:YAG laser (532 nm, 10 Hz, 7 ns). The pump spot diameter on the organic sample was set to 180 μm to match the fundamental cavity mode size. High conversion efficiencies were obtained (up to 57%, corresponding to intracavity peak powers of several tens of kilowatt), together with excellent beam quality ($M^2=1$). The open cavity of VECSEL makes it the ideal structure for intracavity frequency mixing.[20]

The VECSOL setup was modified as illustrated in Figs. 1 and 2. The BBO crystal (section 10×10 mm^2) was cut for

[a)]Author to whom correspondence should be addressed. Electronic mail: sebastien.chenais@univ-paris13.fr.

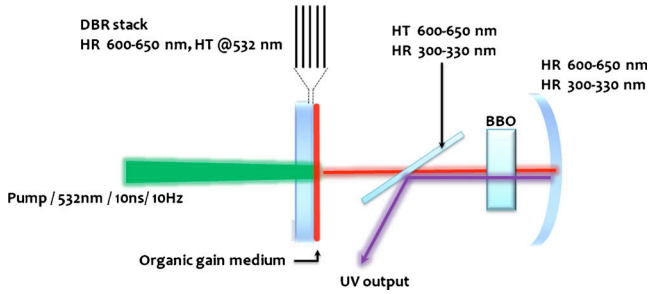

FIG. 1. (Color online) Experimental setup.

type-I phase matching at 620 nm ($\Theta = 38.9°$, $\phi = 90°$). The thickness of the crystal was 3 mm, determined as a trade-off between conversion efficiency and walk-off.

The laser medium was a 21.7-μm-thick film made of 1-wt. % Rhodamine 640 in poly(methyl methacrylate) (PMMA, molar weight 9.5×10^5) spun cast onto the highly-reflective (R = 99.5% @600–650 nm) plane mirror. All experiments were performed in air at room temperature. The sample absorbed 85% of the incident pump power. In order to maximize intracavity peak power for the fundamental radiation, the two cavity mirrors were chosen to be highly reflective in the 600–650 nm range, and the concave mirror (curvature radius R = 150 mm) was also coated for high reflectivity in the 300–330 nm range to enable conversion of the red beam in both propagating directions. Since the VECSOL efficiency drops as the cavity length increases (as an effect of the increasing oscillation buildup time[18]), the length of the cavity was here set to 10 mm, which was the minimum value practically achievable given the size of intracavity elements. The setup remains extremely compact (see photo in the inset of Fig. 2) and could be further miniaturized.

A dichroic plate was inserted at Brewster angle inside the cavity, with one side having a high *s*-polarization reflectivity coating in the 300–330 nm range and a high *p*-polarization transmission coating in the 600–650 nm range. The role of this plate was to allow a type-I phase matching scenario by forcing the red beam to be *p*-polarized, to guarantee outcoupling of the UV beam, while ensuring that UV photons never meet the organic film. This avoids any UV-enhanced photodegradation, and decouples degradation issues from UV generation.

The input-output characteristics of the source are shown in Fig. 3; the red and UV emissions exhibit a linear and

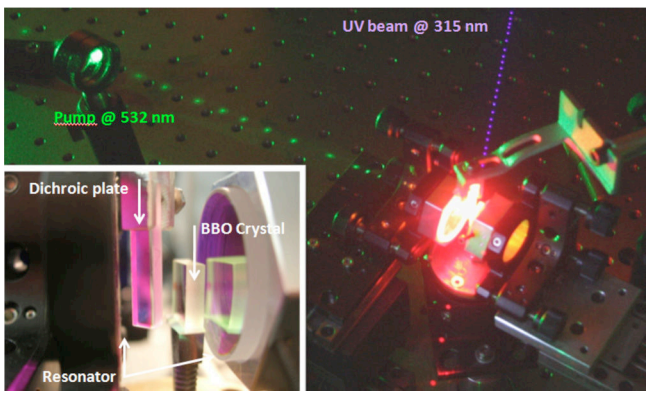

FIG. 2. (Color online) Long-exposure photograph of the setup showing the pump beam (left), a red beam leaking from the dichroic plate (bottom) and the UV beam, visible through fluorescence of a paper sheet (on top). Inset: close up of the cavity.

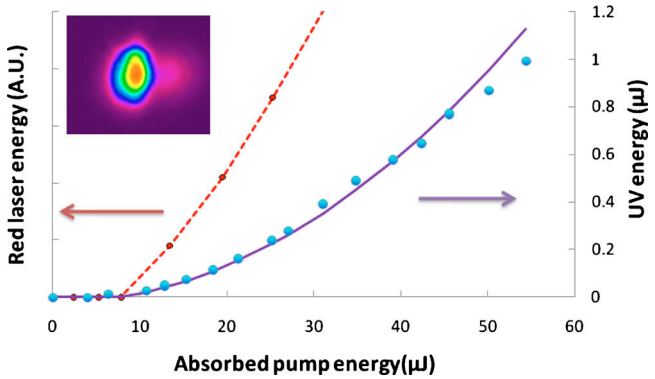

FIG. 3. (Color online) Left: red (fundamental) laser emission as a function of the pump energy. The structure is not designed to produce red radiation, thus the vertical axis represents one of the leaks in arbitrary units. Right: UV output at 315 nm. The full line is a parabolic fit. Inset: UV beam profile.

parabolic evolution versus pump power, respectively, as expected when pump depletion is negligible. The UV output is 1 μJ per pulse, corresponding to a peak power of 250 W; the optical-to-optical conversion efficiency (UV energy divided by the absorbed pump energy) is 2%. This is similar to the maximum conversion efficiency of 2% obtained at 338 nm in an inorganic intracavity frequency-doubled VECSEL with GaInP quantum wells running in the cw mode.[20] For higher pump power levels, photodegradation induces a sublinear behavior of the laser output (see Fig. 3) and a reduced lifetime. The spatial profile of the UV beam is shown in the inset of Fig. 3. The fundamental laser beam is diffraction-limited, and the slight anisotropy of the UV spot is linked to the small angular acceptance of BBO.

The red output spectrum is controlled by the subcavity formed by the organic film acting as a Fabry–Perot filter (see Fig. 4); it comprises several peaks spaced by 6 nm, corresponding to the free spectral range of a 21.7-μm-thick etalon. Each peak contains many modes of the external cavity, which cannot be resolved with a standard spectrometer. The UV spectrum, in contrast, exhibits a single peak (with a spectral width below 0.5 nm—limited by our spectrometer reso-

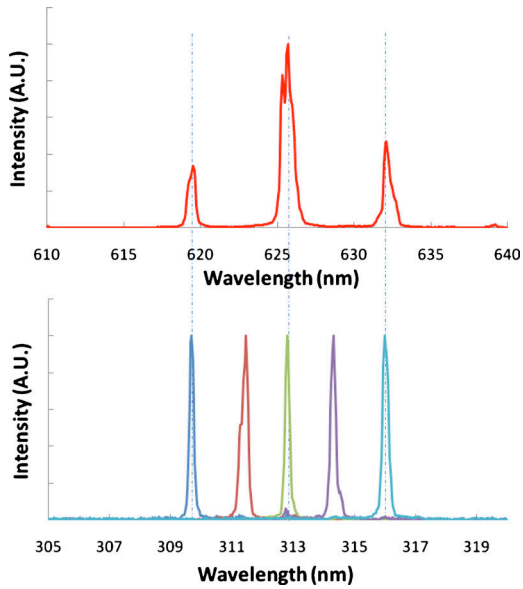

FIG. 4. (Color online) Top: typical spectrum of the laser. Bottom: several individual UV peaks obtained for a given pump spot location onto the organic layer, for different orientations of the BBO crystal.

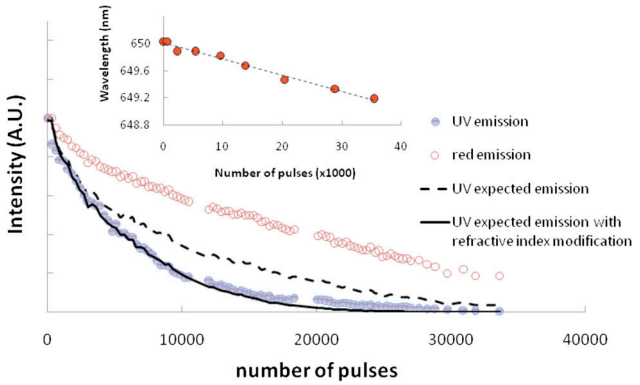

FIG. 5. (Color online) Photodegradation curves. The dotted line is the expected UV intensity (square of measured fundamental intensity). The solid line is the expected UV intensity calculated from the measured fundamental output with phase matching alteration due to refractive index changes, deduced from the shift of laser wavelength vs time (inset).

lution), because the spectral acceptance of the nonlinear process (also on the order of 0.5 nm) allows only one of the red peaks to fulfill the phase-matching condition at a given crystal angle. Upon tilting the BBO crystal by a fraction of degree, it is straightforward to make the spectral acceptance curve matching any of the red peaks. Moreover, we observed nondegenerate sum-frequency mixing occurring between two adjacent red peaks (for example, 626 nm+632 nm =314.5 nm), which leads to additional UV peaks located in-between frequency-doubled lines. In Fig. 4, a typical series of spectra is shown corresponding to a given position of the pump spot onto the sample; it corresponds to an UV emission tunable by discrete steps upon BBO orientation from 309.5 to 316 nm. Interestingly, the device is also continuously tunable between these values in virtue of the nonperfect thickness homogeneity of the film, especially near the edges where the spin-casting process causes the film to be thicker than at the center.[18] It was then possible to obtain continuous tunability from 309 to 322 nm, by combining a scan of the pump spot location to a fine control of BBO orientation.

At last, we studied the laser photostability at a pump energy level fixed at four times the laser threshold (see Fig. 5). More than 5100 shots were observed before the UV intensity dropped to half its initial value. It can be seen in Fig. 5 that the UV output does not vary with time as the square of the fundamental red energy, as it should be the case since the dichroic plate protects the sample from a direct UV degradation. We relate this effect to the slight blueshift observed on the fundamental output (see inset of Fig. 5) induced by refractive index modifications in the sample. A shift from 650 to 649.2 nm was measured within one hour of operation (36 000 pulses). As the dye molecules degrade, the index of refraction decreases toward the lower index of undoped PMMA, causing the resonance condition of the Fabry–Perot etalon to shift, and the lasing wavelength accordingly, inducing a phase mismatch. Taking into account the wavelength shift in the spectral acceptance of BBO, we predicted a UV emission behavior from the red emission that fits correctly the experimental data (see Fig. 5).

A slight realignment of the nonlinear crystal brings the UV energy back to a higher value which confirms that the accelerated degradation rate is only due to phase matching issues. An active tracking system could then easily be implemented to restore the expected degradation profile. The UV emission lifetime can therefore be considered as only limited by the lifetime of the red dye, which can be extremely high (millions of pulses) in red dyes. The extended lifetime is at the cost of a deriving wavelength, which is not necessarily a problem in applications such as biology where spectral signatures are broad.

In conclusion, we demonstrated an ultraviolet organic thin-film laser tunable between 309 and 322 nm, based on intracavity sum-frequency mixing of Rhodamine 640 in PMMA by an inorganic BBO frequency converter. The device is based on the VECSOL concept, which produces high-brightness beams and offers an open cavity allowing for the implementation of intracavity nonlinear conversion. UV energies in the microjoule range were obtained with 2% conversion efficiency. The spectrum of the UV output contains a single peak (<0.5 nm full width at half maximum), as the spectral acceptance of BBO plays the role of a narrowband filter on the multiple-peak spectrum of the fundamental red laser. Wavelength tuning was obtained through phase-matching control (upon BBO orientation, by discrete steps) as well as through layer thickness control (uncontrolled fluctuations near the edges), resulting in a continuous tuning range of 13 nm.

The authors acknowledge the Agence Nationale de la Recherche ("Bachelor" project, Young researchers program, grant 07JCJC0029) for funding this work.

[1]M. A. Dubinski and P. Misra, *Ultraviolet Spectroscopy and UV Lasers*, 1st ed. (CRC, New York, 2002), Vol. 30.
[2]D. J. Armstrong and A. V. Smith, IEEE J. Sel. Top. Quantum Electron. **13**, 721 (2007).
[3]E. D. Stokes, F. B. Dunning, R. F. Stebbings, G. K. Walters, and R. D. Rundel, Opt. Commun. **5**, 267 (1972).
[4]F. Balembois, M. Gaignet, F. Louradour, V. Couderc, A. Barthelemy, P. Georges, and A. Brun, Appl. Phys. B: Lasers Opt. **65**, 255 (1997).
[5]M. F. Joubert and R. Moncorgé, Opt. Mater. **22**, 95 (2003).
[6]I. D. W. Samuel and G. A. Turnbull, Chem. Rev. **107**, 1272 (2007).
[7]J. Clark and G. Lanzani, Nat. Photonics **4**, 438 (2010).
[8]T. Riedl, T. Rabe, H. H. Johannes, W. Kowalsky, J. Wang, T. Weimann, P. Hinze, B. Nehls, T. Farrell, and U. Scherf, Appl. Phys. Lett. **88**, 241116 (2006).
[9]Y. Yang, G. A. Turnbull, and I. D. W. Samuel, Appl. Phys. Lett. **92**, 163306 (2008).
[10]B. Valeur, *Molecular Fluorescence* (Wiley, Weinheim, 2001).
[11]M. Berggren, A. Dodabalapur, R. E. Slusher, and Z. Bao, Nature (London) **389**, 466 (1997).
[12]T. Spehr, A. Siebert, T. Fuhrmann-Lieker, J. Salbeck, T. Rabe, T. Riedl, H. H. Johannes, W. Kowalsky, J. Wang, T. Weimann, and P. Hinze, Appl. Phys. Lett. **87**, 161103 (2005).
[13]A. Hirth, K. Vollrath, and J. Y. Allain, Opt. Commun. **20**, 347 (1977).
[14]S. Chandra, T. H. Allik, J. A. Hutchinson, J. Fox, and C. Swim, Opt. Lett. **22**, 209 (1997).
[15]H. Rabbani-Haghighi, S. Forget, S. Chenais, A. Siove, M. C. Castex, and E. Ishow, Appl. Phys. Lett. **95**, 033305 (2009).
[16]D. Schneider, T. Rabe, T. Riedl, T. Dobbertin, M. Kroger, E. Becker, H. H. Johannes, W. Kowalsky, T. Weimann, J. Wang, P. Hinze, A. Gerhard, P. Stossel, and H. Vestweber, Adv. Mater. (Weinheim, Ger.) **17**, 31 (2005).
[17]A. Barsella, F. May, J. P. Vola, A. Fort, S. Sanaur, A. J. Attias, M. Lefebvre, and E. Rosencher, J. Opt. Soc. Am. B **25**, 196 (2008).
[18]H. Rabbani-Haghighi, S. Forget, S. Chénais, and A. Siove, Opt. Lett. **35**, 1968 (2010).
[19]M. Kuznetsov, F. Hakimi, R. Sprague, and A. Mooradian, IEEE Photonics Technol. Lett. **9**, 1063 (1997).
[20]J. E. Hastie, L. G. Morton, A. J. Kemp, M. D. Dawson, A. B. Krysa, and J. S. Roberts, Appl. Phys. Lett. **89**, 061114 (2006).

Eur. Phys. J. Appl. Phys. **xx**, xx (2011)
DOI: 10.1051/epjap/2011110123

THE EUROPEAN PHYSICAL JOURNAL
APPLIED PHYSICS

Regular Article

Analytical study of Vertical External-Cavity Surface-emitting Organic Lasers

H. Rabbani-Haghighi[a], S. Forget, A. Siove, and S. Chénais

Laboratoire de Physique des Lasers, Université Paris 13/CNRS, 99 avenue Jean-Baptiste Clément, 93430 Villetaneuse, France

Received: 24 March 2011 / Received in final form: 8 July 2011 / Accepted: 14 September 2011
Published online (Inserted later) – © EDP Sciences 2011

Abstract. In this paper we report a detailed study of emission dynamics of an organic solid-state laser structure so-called VECSOL standing for Vertical External-Cavity Surface-emitting Organic Laser recently developed in our group. An optical-optical efficiency of 43% and 6.3% was reported for a 4-mm-long cavity incorporating 18-μm-thick film of Poly(methyl methacrylate) (PMMA) doped with 1 wt.% of Rhodamine 640 when pumped with 7-ns-long and 0.5-ns-long pulses respectively. In order to understand the difference seen in lasing efficiency as a function of different parameters such as cavity length or pump pulse duration, *Tang-Statz-deMars* cavity rate equations are used to model the emission behavior in a pulsed regime. Based on this model, conversion efficiency could be optimized practically to values as high as 57%. Furthermore, some characteristics of this laser architecture such as lasing lifetime (up to 140000 pulses at two times above lasing threshold), wavelength tuning (over 40 nm) and the system power scalability with potential operation up to mJ level are investigated.

1 Introduction

Organic semiconductor lasers based on polymers and small molecules have been an intense field of research in recent years [1–3]. This is mainly due to wide spectral tunability and simple processing techniques of organic materials (e.g., via spin coating or thermal evaporation) which has led to compact, tunable and inexpensive solid-state laser sources with potential applications in different fields such as spectroscopy [4,5], bio/chemo sensing [6,7] and short-haul data telecommunications via plastic optical fibers [8]. There are numerous reports of such devices under optical pumping in different laser configurations such as distributed feedback resonators [9], vertical microcavities [10,11] and external-cavity resonators [12]. In the perspective of having compact organic laser sources which integrate the pump and the laser cavity in a small-volume device, there have been several achievements through indirect electrical pumping of organic solid-state lasers via Light-Emitting Diodes [13] or nitride diode lasers [14,15] by means of somehow sophisticated electronic circuitry systems for the pump source to make it operate in a pulsed regime. This indirect excitation approach has been chosen since realization of direct electrically-pumped organic semiconductor laser is hindered by several heavy constraints like low charge-carrier mobility of organic semiconductor materials as well as several loss mechanisms such as electrode losses and polaronic absorption [16–18]. Therefore, optically-pumped organic semiconductor lasers are of foremost importance.

Among several existing laser architectures for optically-pumped organic lasers, the external-cavity resonators are of great interest to provide efficient output power extraction possibility, excellent beam quality and power scalability. Nonetheless, in most cases the organic amplifying medium addressed in reports concerning this kind of laser architecture is prepared by complicated and long processes such as sol-gel [19] or radical polymerization [20] techniques which sometimes may take up to several days or weeks. Zavelani-Rossi et al. [21] have proposed an external-cavity model based on spin-coated neat films of electroluminescent oligothiophenes. However based on this report regarding the cavity length ($\sim$6 μm) and the low output energy, it would rather be classified as a microcavity.

Recently, we have reported on a very simply-built external-cavity organic laser, so-called *V*ertical *E*xternal-*C*avity *S*urface-emitting *O*rganic *L*aser (VECSOL), which has brought together a combination of high output powers, excellent efficiency as well as good beam quality in a single device [22]. The laser architecture was basically inspired from the traditional inorganic *V*ertical *E*xternal-*C*avity *S*urface-*E*mitting *L*aser (VECSEL) and consisted of a highly reflective dielectric plane mirror ($R > 99.5\%$ within the range of 600–660 nm) onto which an amorphous film ($\sim$18-μm-thick) of Poly(methyl methacrylate) (PMMA) doped with 1 wt.% of Rhodamine 640 was directly deposited through spin-coating process.

[a] e-mail: hadi.rabbani@univ-paris13.fr

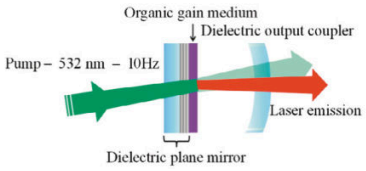

(a)

Fig. 1a. (Color online) Experimental setup of the VECSOL cavity under optical pumping.

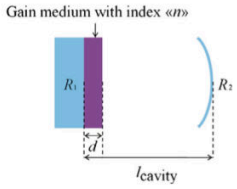

(b)

Fig. 1b. (Color online) Schematic representation of different cavity parameters (see text).

A meniscus output coupler of 98% reflectivity within the range of 600–680 nm closed the cavity (Fig. 1a). The whole setup was end-pumped by a frequency-doubled Nd:YAG laser at 532 nm. In this configuration and for a typical case of 4-mm-long laser cavity, a diffraction-limited laser emission ($M^2 = 1$) with an optical-optical efficiency as high as 43% and 6.3% was obtained for 7-ns-long and 0.5-ns-long pump pulses, respectively, under 10 Hz repetition rate excitation regime. Lasing was observed for cavity lengths up to 60 mm in case of pumping with 7-ns-long pulses whereas this was limited to 10 mm for 0.5-ns-long pump pulses. A noticeable feature of the VECSOL architecture is its open cavity, allowing intra-cavity frequency doubling and consequently UV emission from an organic thin-film device [23].

In the present article we perform a detailed study of the VECSOL performance through experiment followed by theoretical modeling via application of the *Tang-Statz-deMars* rate equations in a pulsed regime [24]. This may help to understand how variations of different parameters such as cavity length or pump pulse duration would affect emission behaviors. Furthermore, VECSOL performance optimization is carried out by inspecting among different resonator elements and then wavelength tuning, photostability and power scalability are demonstrated in the last part.

2 Theoretical background

Consider an amplifying gain medium (index n) of thickness "d" and a pumped region of cross-sectional area "S" inserted between two mirrors with R_1 and R_2 reflectivities to build a laser cavity with an optical length of $L = (n-1)d + l_{\text{cavity}}$, where l_{cavity} is the physical length of the cavity (Fig. 1b). The cavity rate equations over the $S \cdot L$ volume (mode volume) showing the evolution of the output laser intensity and the population inversion would be the following [24]:

$$\frac{\mathrm{d}I}{\mathrm{d}t} = \frac{1}{\tau_{\text{cav}}}\left[\frac{\Delta N}{\Delta N_{\text{th}}}\left(I - \frac{c}{SL}\right) - I\right], \quad (1)$$

$$\frac{\mathrm{d}\Delta N}{\mathrm{d}t} = \frac{1}{\tau_{\text{eff}}}\left[\Delta N_0 - \Delta N\left(1 + \frac{I}{I_{\text{sat}}}\right)\right], \quad (2)$$

where I is the laser intensity in photonic unit (photons/s/m^2) and c is denoting the speed of light. $\Delta N = N_2 - N_1$ is defined as the population inversion (m^{-3}) in a four-level system between the low excited-state and one of the ground-state vibronic levels, depending on the emission wavelength. is the population inversion at threshold.

τ_{cav} is the photon lifetime inside the cavity and is derived as

$$\tau_{\text{cav}} = \frac{-2L}{c \cdot \text{Ln}\left[R_1 R_2 \left(1 - T_i\right)^2\right]}, \quad (3)$$

with T_i representing the single-pass cavity passive losses due to gain medium absorption, diffusion or mirror scattering.

τ_{eff} is described as the effective non-saturated excited-state lifetime as it determines the excited-state filling time when $I = 0$:

$$\tau_{\text{eff}} = \frac{\tau}{1 + \frac{I_p}{I_{p_{\text{sat}}}}}, \quad (4)$$

with τ, I_p and $I_{p_{\text{sat}}}$ symbolizing the singlet excited-state radiative lifetime, the pump intensity (assumed to be constant during the pump pulse duration) and saturation pump intensity respectively. I_{sat} is defined as the laser saturation intensity and ΔN_0 stands for the non-saturated population inversion with N showing the density of molecules in the active region:

$$\Delta N_0 = \frac{N\frac{I_p}{I_{p_{\text{sat}}}}}{1 + \frac{I_p}{I_{p_{\text{sat}}}}}. \quad (5)$$

It should be mentioned that the theory, which is introduced here to be used for the following simulations, holds for a four-level system operating in a single-mode regime. It does not take into account the existence of a microcavity formed by the organic film which was shown to control the emitted spectrum. It also neglects intramolecular as well as intermolecular phenomena that occur once the molecules are in the excited state such as quenching or triplet state absorption which make this system more complex than a true four-level system. In the following part we investigate the observed VECSOL emission characteristic behavior and then explain this behavior through some simulations.

3 VECSOL dynamics analysis

Before starting the analysis, it should be reminded that a rectangular-shaped pump profile is used for the modeling purpose. Based on simulations which apply the cavity

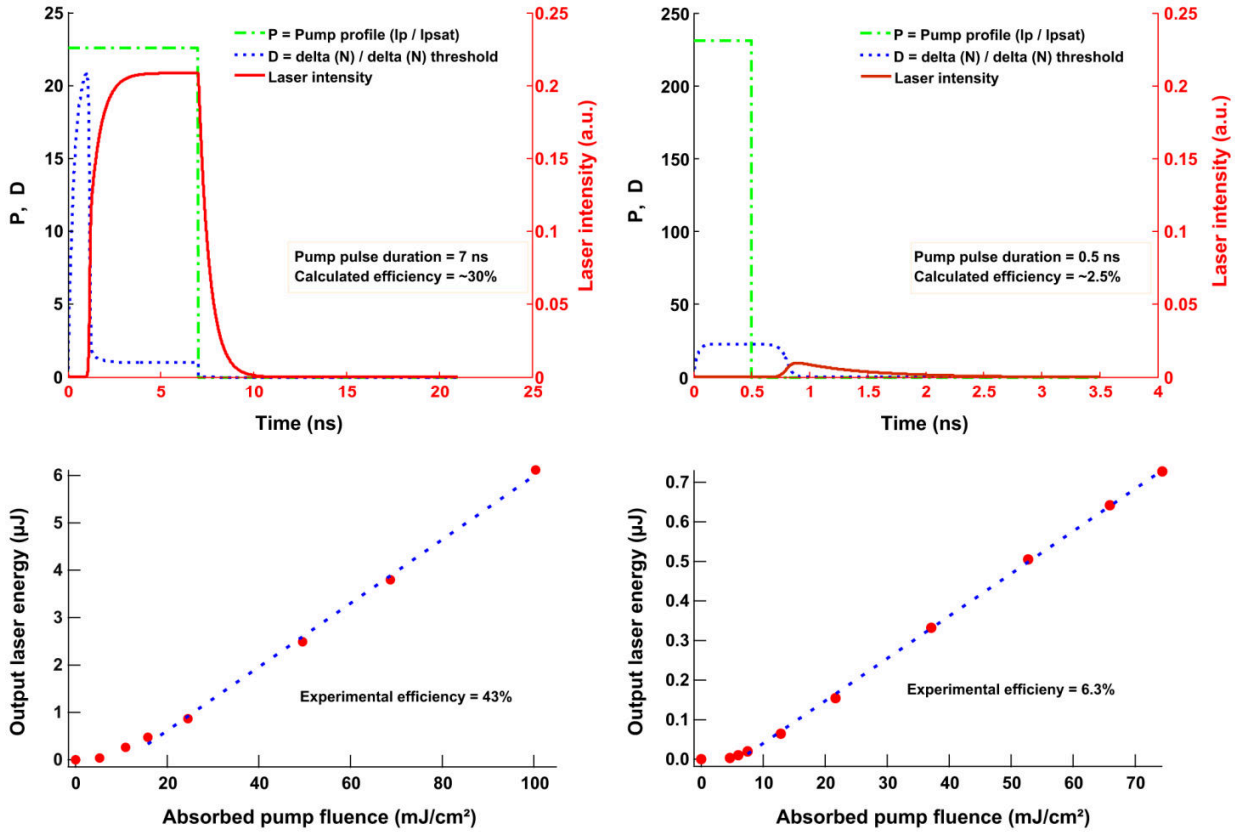

Fig. 2. (Color online) Oscillation buildup time simulations for 7-ns-long pump pulse (left) and 0.5-ns-long pump pulse (right) and below are the corresponding experimental efficiency curves for each case. In practice as well as for the modeling, the cavity is 4-mm-long. The only fitting parameter for the simulations is the roundtrip passive loss which is considered 2%.

rate equations to a typical case of 4-mm-long VECSOL with $R_1 = 99.5\%$ and $R_2 = 98\%$ and an amplifying gain medium of $\sim$18-μm-thick, in case of exciting the cavity with 7-ns-long pulses and 10 Hz repetition rate, the laser oscillation builds up in a rather short time with respect to the pump pulse duration (Fig. 2). In this case the steady state is reached before the pulse finishes and would last till the end of the pulse which causes an efficient extraction of the pump energy during 7 ns and thus very high conversion efficiency. In case of pumping the cavity with 0.5-ns-long pulses and for the same cavity length, the population inversion is also created in a fraction of a ns after excitation but the laser field does not have enough time to exceed the cavity losses within the pulse time period. In this case the created population inversion lasts for $\sim$0.25 ns after the end of the pump pulse and before the beginning of laser oscillation buildup since the excited-state lifetime (7.5 ns) [25] is longer than the pulse duration. When the laser oscillation starts, the pump pulse has already terminated and the population inversion has a descending trend to zero and the steady state will never be reached. Therefore, the conversion efficiency would be low in this case even if a rather high output peak power could be obtained. A comparison between the experimental conversion efficiencies (43% and 6.3% corresponding to 7-ns-long and 0.5-ns-long pump pulses respectively) confirms the above-described analysis. Theoretical calculation of the efficiency values follows the same trend as a function of pump pulse duration but with a difference (30% instead of 43% and 2.5% instead of 6.3%) which is likely to be due to model limits introduced previously and above all, neglect of the existing microcavity for the simulations.

The pulse-duration-dependent VECSOL behavior can also be justified numerically by estimating the number of absorption/emission cycles that each molecule experiences within the pump pulse duration. In the case of 7-ns-long pulses, the output energy of 6 μJ obtained from an excited region containing $\sim 3\times10^{12}$ molecules would mean an average number of six photons emitted per molecule and per pulse. This can be interpreted as the case where each molecule undergoes an average of 6 absorption/emission cycles during 7 ns. When the pulse duration is 0.5 ns, the output energy of 0.7 μJ corresponds to an average photon number of 0.7 per molecule during the pulse time. This validates the conclusion taken from Figure 2 that steady state is reached for 7-ns-long pulses whereas it is not the case for 0.5-ns-long pump pulses.

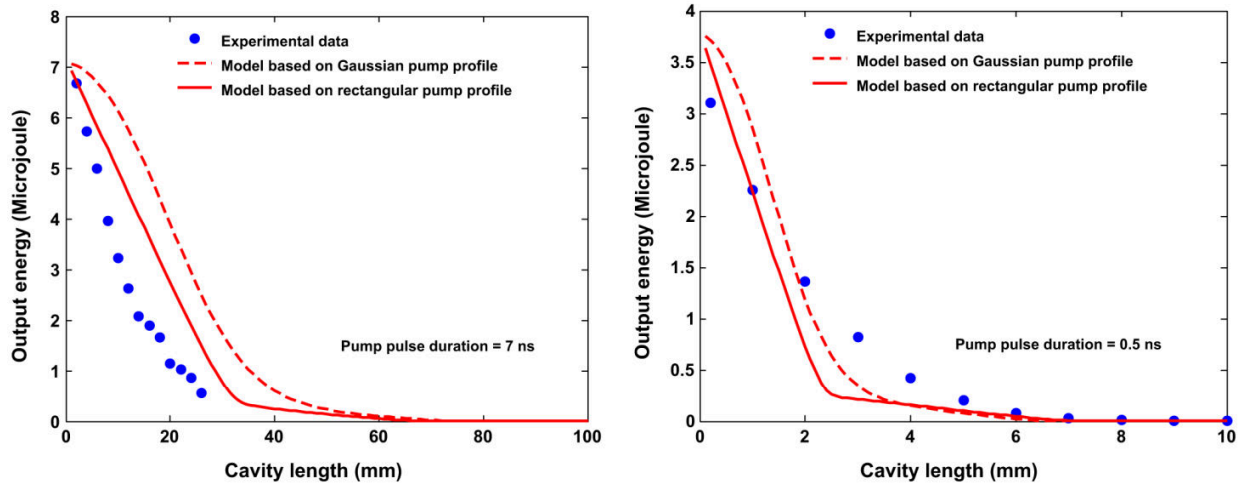

Fig. 3. (Color online) VECSOL output energy dependency on cavity length for two different pump pulse durations (7 ns and 0.5 ns). The only fitting parameter is the roundtrip passive loss which is considered 2%.

Consequently, as the pump pulse duration has a dramatic effect on the laser efficiency, similarly the cavity length is an important parameter as it directly intervenes in the oscillation buildup time for a given pump pulse duration. This behavior is theoretically modeled for pump pulses of 7 ns and 0.5 ns and for sake of comparison each time for two different cases of Gaussian and rectangular pump profiles (Fig. 3). In both cases the VECSOL energy drops down as the cavity length increases. The collapse of output energy by lengthening the cavity could be explained in a similar way as shortening the pump pulse duration by an increase of the oscillation buildup time with respect to pump duration and therefore a decrease of the efficiency.

4 VECSOL performance optimization

These results can now serve as a basis to find out the optimum parameters for lasing action in order to achieve the highest possible output energy. One of the criteria which would help to achieve the best lasing efficiency is to look for the optimum output coupler. This is due to the fact that one might expect an increase in the output signal intensity and therefore the efficiency by reducing the mirror reflectivity but this would also shorten the intra-cavity photon lifetime followed by a decrease in the output energy. In this case there is compromise that must be respected in choosing the output coupler in order to have the best lasing performance. Based on the previous simulations, the highest conversion efficiency is obtained for an output coupler of 95% reflectivity. This is also shown experimentally for four different available output couplers (80%, 90%, 95% and 98%) and a cavity length fixed to 10 mm (Fig. 4). As it is seen, the experimental data and the simulation are in good agreement. From these data, the output coupler of 98% reflectivity used in reference [22] was replaced by the optimized output coupler of 95% reflectivity and the VECSOL conversion efficiency was improved from 43% to 57% for a cavity length of 1 mm when excited with pulses of 7-ns-long at 10 Hz repetition rate (Fig. 5).

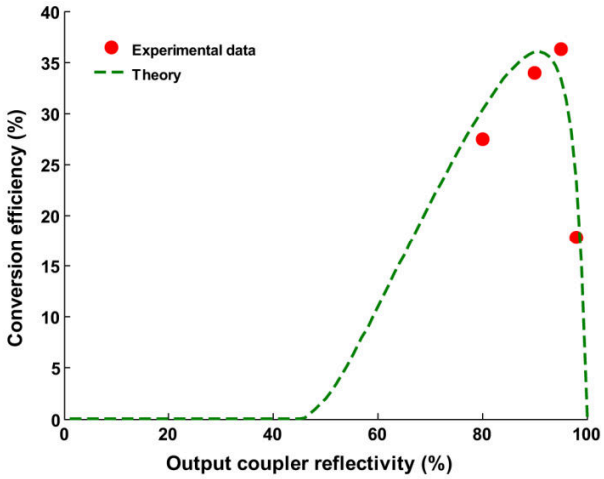

Fig. 4. (Color online) Filled circles are the experimental data obtained for 10-mm-long cavity length, 18-μm-thick gain medium and an incident pump fluence of 100 mJ/cm^2. The dashed line is a model showing the evolution of the conversion efficiency by output coupler reflectivity variation in a range from 0 to 100. The only fitting parameter is the roundtrip cavity loss which is set to 2%.

5 VECSOL emission characterization

VECSOL emission spectrum is a result of a Fabry-Perot etalon formed by the organic gain medium which is coupled to the external cavity. It consists of several peaks, with 7.8 nm distance between the peaks which corresponds

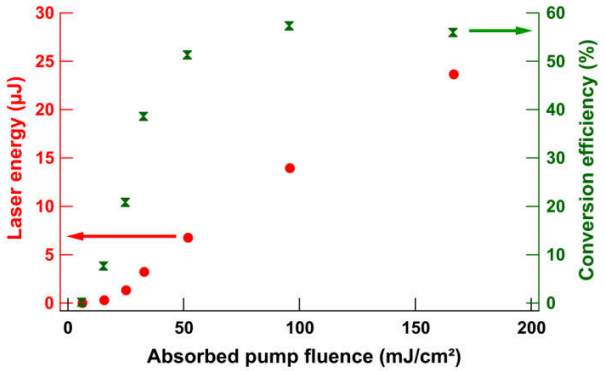

Fig. 5. (Color online) (Left axis) Laser energy, (right axis) conversion efficiency as a function of the absorbed pump fluence for an optimum output coupler of 95% reflectivity, 1-mm-long cavity and 18-μm-thick gain medium. The small efficiency drop seen at the end could be due to degradation issues at this excitation intensity.

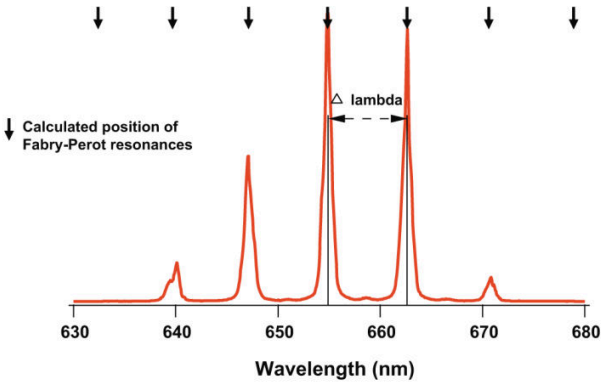

Fig. 6. (Color online) Typical VECSOL emission spectrum of an 18-μm-thick gain medium. Small arrows pointing down are indicating the position of Fabry-Perot peaks obtained by simulation.

to the free spectral range of the ∼18-μm-thick etalon ($\Delta\lambda = \frac{\lambda^2}{2nl}$ with n the refractive index of the medium, l the film thickness and λ the emission wavelength) (Fig. 6). Each of these peaks is containing the external-cavity modes with a free spectral range that would be decreased as the cavity length increases. The free spectral range corresponding to a 1-mm-long cavity is a fraction of nm. Therefore the external-cavity modes are not resolved with the resolution (0.5 nm) of the spectrometer (SPEX 270M) at disposal. By modulating the rotation speed during the spin-coating process and by using lower density PMMA it is possible to reduce the film thickness in order to have only one mode of the Fabry-Perot etalon under the gain spectral region of the organic material. Single-peak laser operation was observed for 2.35-μm-thick film which still contains the external-cavity modes inside of it (Fig. 7).

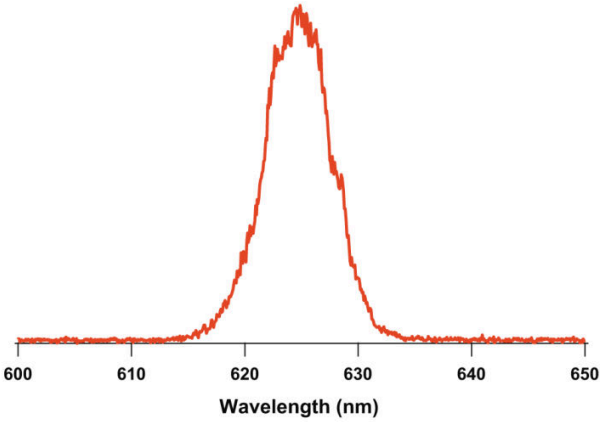

Fig. 7. (Color online) Single-mode laser operation obtained for a 2.35-μm-thick film. This peak comprises several external-cavity modes but the observation is limited by spectrometer resolution. However, the external-cavity mode competition can still be seen on the top of this peak.

6 Tunability

Certainly, among the most interesting features of the VECSOL emission is the wavelength tuning achieved thanks to clever use of film thickness variation obtained via spin coating by going toward the sample edge. The intrinsic characteristic of the films realized through spin coating is a flat zone in the middle and then a gradual increase as it goes toward the edge. This fact is verified experimentally by measuring the deposited film thickness with a profilometer from the center to the edge on a standard-size plane mirror (diameter = 25.4 mm) (Fig. 8). For the purpose of wavelength tuning demonstration, a sample 2.35-μm-thick sample was prepared to operate in single-mode regime. When the coated plane mirror moved transversely to the pump beam, as it approached to the edge, a tuning range of around $\Delta\lambda = 40$ nm (from 615 nm to 655 nm) could be obtained, limited by the gain spectrum and the mirror reflectivities (Fig. 9).

7 Laser emission lifetime and power scalability

In terms of stability, the VECSOL was irradiated at 10 Hz repetition rate by two pump sources with 7-ns and 0.5-ns pulse durations. As it is seen in Figure 10 the laser energy reduced to half of its initial value after 140000 pulses in case of pumping with 7-ns-long pump pulses whereas this happened after 5000 pulses when the VECSOL is pumped by 0.5-ns-long pulses and an absorbed pump fluence of ∼15 mJ/cm^2 in both cases. The higher degradation rate in the case of pumping with 0.5-ns-long pulses might be mainly due to higher absolute pump power which is ∼20 times higher in this case. The lasing lifetimes are comparable (or even far better, given the high pump fluence used in our case) to values reported in the literature for organic thin-film devices [26].

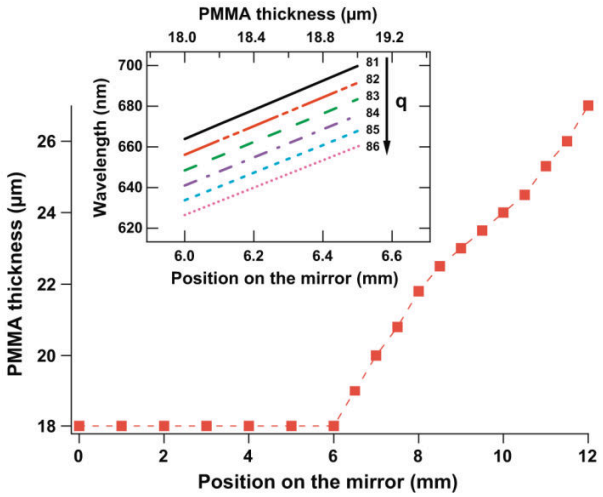

Fig. 8. (Color online) PMMA thickness variation as it goes toward the sample edge for an 18-μm-thick film. The inset is the simulation showing the peak wavelengths in a Fabry-Perot when the film thickness varies as a function of the position on the mirror. q numbers are representing the Fabry-Perot resonance modes residing within the Rhodamine 640 gain region.

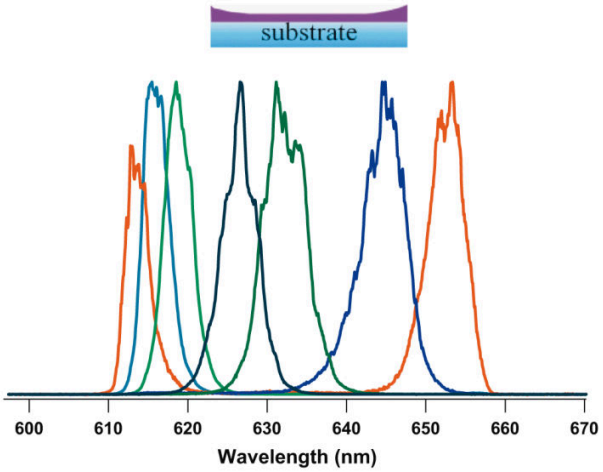

Fig. 9. (Color online) Tunability obtained over 40 nm from 615 nm to 655 nm for 2.35-μm-thick film due to film thickness variation. (Inset) Schematic representation of film thickness variation by going toward sample edges.

Another interesting feature of the VECSOL is the power scalability or in other words the possibility of increasing the output power or energy without decreasing the laser lifetime. As an example, we were interested to show that the output energy is doubled when the VECSOL is pumped by incident energy twice higher, while the incident pump fluence and consequently the degradation rate are kept constant. For this purpose, we started the experiment with an output coupler of 98% reflectivity with 50 mm radius of curvature. The TEM_{00} fundamental mode waist radius corresponding to this curvature

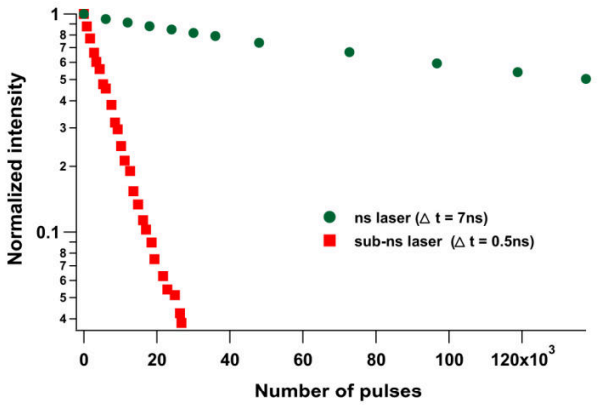

Fig. 10. (Color online) VECSOL normalized intensity versus the number of pump pulses for two different pump pulse durations of 0.5 ns and 7 ns and a pump fluence of $\sim$15 mJ/cm^2 in both cases.

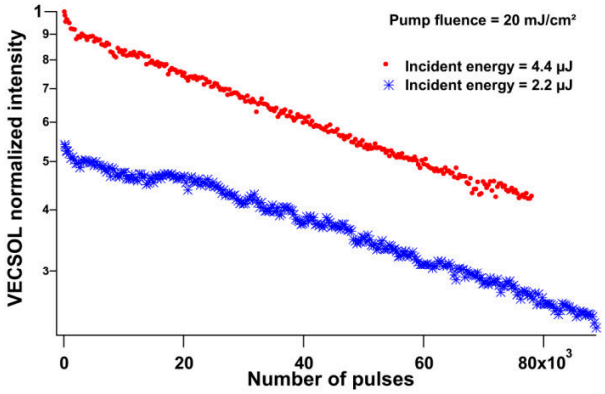

Fig. 11. (Color online) VECSOL power scaling demonstration for two typical incident energies.

is 52 μm. Therefore, a pump waist radius of 60 μm was chosen in order to have only a predominant pump area over the TEM_{00} fundamental cavity mode and not the higher-order transverse modes. In another case, the pump waist size of 85 μm was chosen in order to enlarge the pump surface area by a factor of 2. So the output coupler was replaced with an output coupler of 98% reflectivity and 200 mm radius of curvature to match this pump size and the fundamental TEM_{00} cavity mode (having in this case 75 μm waist size) together. The experimental results depicted in Figure 11 show identical degradation rates in accordance with our expectation for an incident pump fluence of 20 mJ/cm^2, which is roughly two times above lasing threshold in the case of 7-ns-long pump pulses.

It would be also useful to estimate the maximum attainable output energy of the VECSOL at the same pump fluence with a maximum pump beam diameter of 4 mm for example (for higher diameters, the beam spatial quality is likely to be disturbed by thermal effects) and a relevant output coupler that could match this pump beam size

to TEM_{00} fundamental mode. In this condition, output energy of ∼1 mJ would be achievable while preserving a low degradation rate.

8 Conclusion

In conclusion we have explored through simulations and experiments, the VECSOL emission behavior (based on film of PMMA doped by 1 wt.% of Rhodamine 640) in terms of lasing efficiency when the cavity length or the pump pulse duration was varied (7 ns and 0.5 ns). We observed that higher laser efficiency was directly related to longer pump pulse durations or similarly shorter cavity lengths due to shorter oscillation buildup time with respect to pump pulse duration. The realized simulations paved the way to improve VECSOL lasing efficiency to values as high as 57% by utilizing the optimum output coupler. The spectrum was controlled by the Fabry-Perot and a single-peak lasing operation could be achieved by reducing gain medium thickness to 2.35 μm. Wavelength tuning over 40 nm (615–655 nm) was obtained thanks to thickness variation of the gain medium realized by the spin-coating process. In terms of photostability, we demonstrated half lasing lifetime after 140000 pulses in normal condition when the VECSOL was pumped by 7-ns-long pulses. Finally, power scalability was an added value feature of the VECSOL architecture that will open the way toward high-energy organic lasers based on thin films.

The authors are grateful to Manal Yewakim for valuable assistance on the film thickness measurements, and the French National Research Agency (ANR, Young Researchers Program, Grant # 07JCJC0029), for financial support.

References

1. N. Tessler, Adv. Mater. **11**, 363 (1999)
2. M.D. McGehee, A.J. Heeger, Adv. Mater. **12**, 1655 (2000)
3. I.D.W. Samuel, G.A. Turnbull, Chem. Rev. **107**, 1272 (2007)
4. T. Woggon, S. Klinkhammer, U. Lemmer, Appl. Phys. B: Lasers Opt. **99**, 47 (2010)
5. Y. Oki et al., Opt. Rev. **12**, 301 (2005)
6. M. Lu et al., Appl. Phys. Lett. **93**, 131922 (2008)
7. Y. Yang, G.A. Turnbull, I.D.W. Samuel, Adv. Funct. Mater. **20**, 2093 (2010)
8. K. Kuriki et al., Appl. Phys. Lett. **77**, 331 (2000)
9. H. Rabbani-Haghighi et al., Appl. Phys. Lett. **95**, 033305 (2009)
10. N. Tessler, G.J. Denton, R.H. Friend, Nature **382**, 695 (1996)
11. L. Persano et al., Appl. Phys. Lett. **88**, 121110 (2006)
12. I. Garcia-Moreno et al., Adv. Funct. Mater. **19**, 2547 (2009)
13. Y. Yang, G.A. Turnbull, I.D.W. Samuel, Appl. Phys. Lett. **92**, 163306 (2008)
14. T. Riedl et al., Appl. Phys. Lett. **88**, 241116 (2006)
15. H. Sakata, H. Takeuchi, Appl. Phys. Lett. **92**, 113310 (2008)
16. M. Reufer et al., Appl. Phys. Lett. **84**, 3262 (2004)
17. T. Rabe et al., Phys. Rev. Lett. **102**, 137401 (2009)
18. B.K. Yap et al., Nature Mater. **7**, 376 (2008)
19. W.T. Hu et al., Appl. Opt. **36**, 579 (1997)
20. A. Costela et al., Appl. Phys. B: Lasers Opt. **76**, 365 (2003)
21. M. Zavelani-Rossi et al., Synt. Met. **139**, 901 (2003)
22. H. Rabbani-Haghighi et al., Opt. Lett. **35**, 1968 (2010)
23. S. Forget et al., Appl. Phys. Lett. (in press)
24. O. Svelto, *Principles of Lasers*, 5th edn. (Springer, New York, 2010)
25. M.C. Ramon et al., J. Appl. Phys. **97**, 073517 (2005)
26. V. Navarro-Fuster et al., Appl. Phys. Lett. **97**, 171104 (2010)